



HAL
open science

Two-mode giant optical non-linearity with a single quantum dot in a photonic waveguide

Hoai Anh Nguyen

► **To cite this version:**

Hoai Anh Nguyen. Two-mode giant optical non-linearity with a single quantum dot in a photonic waveguide. Optics [physics.optics]. Université Grenoble Alpes, 2016. English. NNT: 2016GREAY036 . tel-01360549v2

HAL Id: tel-01360549

<https://theses.hal.science/tel-01360549v2>

Submitted on 13 Apr 2017

HAL is a multi-disciplinary open access archive for the deposit and dissemination of scientific research documents, whether they are published or not. The documents may come from teaching and research institutions in France or abroad, or from public or private research centers.

L'archive ouverte pluridisciplinaire **HAL**, est destinée au dépôt et à la diffusion de documents scientifiques de niveau recherche, publiés ou non, émanant des établissements d'enseignement et de recherche français ou étrangers, des laboratoires publics ou privés.

THÈSE

Pour obtenir le grade de

DOCTEUR DE LA COMMUNAUTE UNIVERSITE GRENOBLE ALPES

Spécialité : **Physique / Physique de la matière condensée et du rayonnement**

Arrêté ministériel : 7 août 2006

Présentée par

Hoai Anh NGUYEN

Thèse dirigée par **Jean-Philippe POIZAT**

préparée au sein de l'**Institut Néel**
dans l'**École Doctorale de Physique de Grenoble**

Two-mode giant optical non- linearity with a single quantum dot in a photonic waveguide

Thèse soutenue publiquement le **12 Mai 2016**,
devant le jury composé de :

Dr. Bernhard URBASZEK

Directeur de Recherche au Laboratoire de Physique et Chimie des Nano-Objets (Rapporteur)

Prof. Brahim LOUNIS

Professeur au Laboratoire Photonique, Numérique et Nanosciences (Rapporteur)

Dr. Philippe GRANGIER

Directeur de Recherche au Laboratoire Charles Fabry (Président)

Prof. Darrick CHANG

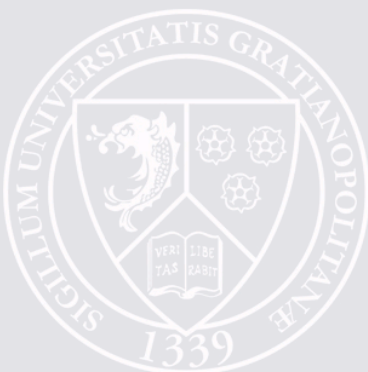
Professeur au Instituto de Ciencias Fotónicas (Membre)

Dr. Jean-Michel GERARD

Directeur de Recherche au CEA/INAC/PHELIQS (Membre)

Dr. Jean-Philippe POIZAT

Directeur de Recherche à l'Institut Néel (Directeur)



Acknowledgement

Over the last three years and two months, I have had a privilege of working along-side great colleagues and scientists. This thesis would not be possible without all the contribution of my colleagues in NPSC joint team between Institut Néel and CEA Grenoble.

I would like to acknowledge most importantly my supervisor, Dr. Jean-Philippe Poizat, for all of his supports, his advices and his enthusiasm in every single step of my PhD. We have met and discussed for almost every working day during my PhD, which has made the work much more easier. Thank to his knowledge and expertise, every problem and difficulty in the measurement and in the theory was pointed out and solved efficiently. I appreciate also all the 'non-scientific' discussions and activities that we have had.

I would also like to acknowledge Dr. Julien Claudon, Dr. Jean-Michel Gérard and their team, first of all for fabricating such amazing trumpets and second of all, for all the valuable insightful discussions and meetings that we had.

I would like to thank Dr. Thomas Grange for his theoretical support. The model that he developed has helped us a lot in verifying the experimental results as well as in understanding better the system.

The experimental results I obtained could have been much more challenging without the wonderful Labview program made by Edouard Wagner. I appreciate all the time and efforts that he spent on making such a big and sophisticated program to run smoothly with his amazing programming skill.

I would like to thank Dr. Pierre-Louis de Assis, who taught me a lot when I first arrived here. I spent the my initial PhD period with him in the laboratory, to build and improve the giant non-linearity set up. His guidance helped me a lot to overcome many difficulties at the first stages of the measurement.

I want to thank Dmitrii Tumanov, my lab-mate, for all the measurements that we have done together. He has been always a great working partner with his skills and also his kindness. I would also like to thank all of my colleagues in NPSC team and my PhD friends in the open space for the fruitful scientific discussion, extensive help, friendship and enjoyable moments during my time in Grenoble.

I would like to thank Prof. Nguyen Van Hieu, for his support over the years of my study. His enthusiasm has always been a big motivation for me. I would also like to express my grateful to Dr. Le Si Dang, for bringing me the opportunity to work in one of the best scientific institutions in the world. It has been a great pleasure to know such a very nice human being and also a great scientist like him. I thank him for his advice, encouragement and for everything that he has done for me.

My PhD could not have been done successfully without the help from the administrative office of PLUM (Nano) department, as well as all the engineers and the service staff of Institut Néel.

I would like to thank all of my Vietnamese friends in Grenoble, my football teammates and my tennis partners. I appreciate every joyful and also 'painful' moment that we have spent together.

Finally, I extremely grateful to my little family and my parents. Their countless, continuous love and support have kept me on track and pushed me forward over the years of my PhD.

Contents

Contents	ii
List of Figures	viii
1 Introduction	1
1.1 Context	1
1.2 One-dimensional optical system	2
1.3 Single-photon source	2
1.4 Optical giant non-linearity and all-optical switch	4
1.4.1 Single-mode giant non-linearity	4
1.4.2 Two-mode giant non-linearity: all-optical transistor and switch	4
1.5 Motivation of this Thesis	6
1.6 Thesis outline	6
2 A quantum dot embedded in a photonic wire	9
2.1 Self-Assembled InAs quantum dots	10
2.1.1 Overview	10
2.1.2 Quantum dot discrete energy levels and optical excitation methods	11
2.1.3 Multi-excitonic states in a quantum dot	14
2.1.3.1 Fine-structure splitting	15
2.2 Interaction of a quantum dot with light in a photonic wire	16
2.2.1 Quantum emitter coupled to a photonic nanostructure	16
2.2.2 Resonant structures	17
2.2.2.1 Pillar micro-cavity	18
2.2.2.2 Photonic crystal cavity	19
2.2.3 Non-resonant waveguide structures	20
2.2.3.1 Photonic crystal waveguide	20
2.2.4 Fiber-like photonic wire	21
2.2.4.1 An infinite cylindrical photonic wire	22
2.2.4.2 Influence of quantum dot lateral position on β factor	24

2.2.5	Extraction efficiency enhancement in a finite photonic wire	25
2.2.5.1	Tapering of the photonic wire top facet	26
2.2.6	Photonic trumpet	28
2.2.6.1	Fabrication process	28
2.2.6.2	Sample summary	29
2.3	Chapter summary	30
3	Photoluminescence spectroscopy	31
3.1	Experimental setup	32
3.1.1	Optical source	33
3.1.2	Cryogenics	33
3.1.3	Spectrometer	33
3.2	Photoluminescence spectroscopy	34
3.2.1	Photoluminescence spectra	34
3.2.2	Photoluminescence power dependence	35
3.2.2.1	Identification of exciton and biexciton from the same quantum dot	37
3.2.2.2	Biexciton binding energy	42
3.2.3	Spectral drift	43
3.2.4	Time-resolved photoluminescence measurement	45
3.2.4.1	Experimental setup	45
3.2.4.2	Time-resolved photoluminescence spectroscopy	46
3.3	Chapter summary	47
4	Single-mode giant non-linearity	49
4.1	Giant non-linearity of a one-dimensional atom	50
4.1.1	Introduction	50
4.1.2	Bloch equation of a coherent field interacting with a one-dimensional atom	51
4.1.2.1	Evolution of the fields and the interference between incoming and scattering fields	52
4.1.2.2	Impact of β factor and spectral broadening on the reflectivity of the one-dimensional two-level system	56
4.1.2.3	Effect of spectral diffusion	56
4.1.2.4	Coherent and incoherent scatterings of a two-level atom	58
4.2	Resonant excitation spectroscopy	60
4.2.1	Experimental setup	61
4.2.2	Cross-polarized detection	62
4.2.2.1	Quarter-wave plate	65

4.2.2.2	Laser extinction ratio	66
4.2.2.3	Optical sources	66
4.2.2.4	Experimental procedure	67
4.2.2.5	Reflectivity in cross-polarization scheme	69
4.2.3	Resonant excitation spectroscopy	70
4.2.3.1	The effect of an additional ultra-weak non-resonant laser on resonant excitation spectra	71
4.2.3.2	Saturation of a two-level system	73
4.2.3.3	Calibration of input and output powers	75
4.3	Ultra-low power single-mode giant non-linearity	76
4.3.1	A quantitative evaluation of all experimental parameters	76
4.3.1.1	A non-circular symmetry at the waist where the quantum dots locate	78
4.3.1.2	Polarizations of the excitonic dipoles with respect to the sample axes	79
4.3.2	Single-mode giant non-linearity	80
4.3.2.1	Broad-band operation properties in single-mode giant non- linearity	81
4.3.2.2	Single-mode giant non-linearity of an ideal system in cross- polarization scheme	82
4.3.2.3	Coherent versus incoherent scattering	83
4.4	Chapter summary	84
5	Two-mode giant non-linearity	85
5.1	Introduction	87
5.1.1	Dressed states	87
5.1.1.1	Rabi oscillations of the atomic system	87
5.1.1.2	A two-level atom interacts with a quantized field: Dressed states approach	88
5.1.2	Observation of dressed states	90
5.1.2.1	Mollow triplet	91
5.1.2.2	Autler-Townes doublet	92
5.1.3	Dressed states of a three-level system via Bloch equations	93
5.1.4	Two-mode giant non-linearity with a quantum dot three-level system - Autler-Townes splitting approach	99
5.1.5	Two-mode giant non-linearity with a quantum dot three-level system - population switch approach	100
5.1.6	Evaluation of all-optical switch performances	101

5.1.7	Electromagnetically induced transparency versus Autler-Townes splitting	102
5.2	Experimental setup	105
5.2.1	Experimental procedure	106
5.3	Two-mode giant-nonlinearity: Autler-Townes splitting approach	107
5.3.1	Autler-Townes splitting	107
5.3.2	Autler-Townes splitting as a function of control laser power	109
5.3.3	A full scan over two excitonic fine-structure dipoles	112
5.3.4	Autler-Townes optical switch	115
5.3.4.1	Probe reflection as a function of control power	115
5.3.4.2	Enhancement of probe reflection	116
5.3.4.3	Probe laser switching contrast	119
5.3.4.4	Probe reflectivity for an ideal system in Autler-Townes approach	120
	Ideal probe reflectivity in co-polarized excitation scheme	121
5.3.4.5	Optical switch with laser background	122
5.4	Two-mode giant non-linearity: Population switch approach	123
5.4.1	Reflection measurement	124
5.4.2	Ultra-low power optical switch	125
	Probe reflectivity for different probe laser powers	127
5.4.2.1	Observation of Autler-Townes splitting at high control laser power	128
5.4.2.2	Probe reflectivity with optimum parameters	131
	Ideal reflectivity in cross-polarized excitation	132
	Ideal reflectivity in co-polarized excitation	132
5.5	Contributions of coherence and incoherence in total probe reflectivity	133
5.5.1	Autler-Townes splitting approach	134
5.5.2	Population switch approach	135
5.6	Switching time	135
5.7	A comparison with state of the art giant non-linearity	136
5.7.1	Single-mode giant non-linearity	136
5.7.2	Two-mode giant non-linearity	137
5.8	Chapter summary	140
6	Summary and Perspectives	141
	Appendix A Fitting method for the unknown parameters of the quantum dot-waveguide system	145

Appendix B Observation of suspended and giant trumpets	149
B.1 Suspended trumpet	149
B.2 Giant trumpet	150
B.3 Photoluminescence spectra of quantum dots embedded in a suspended trumpet	150
B.4 Resonant excitation spectra of suspended trumpet	152
Appendix C An alternative to counteract the temporal spectral drift	155
References	159

List of Figures

1.1	Illustration of a one-dimensional atom	3
2.1	Conduction and valence band energies in a quantum dot	10
2.2	TEM image of the cross section of the quantum dot structure	11
2.3	Schematic of energy levels for a InAs/GaAs quantum dot	11
2.4	A Schematic of non-resonant excitation strategies	12
2.5	Schematics of resonant excitation methods	13
2.6	Schematic multi-particle states of a single QD	14
2.7	Fine-structure splitting illustration	15
2.8	Illustrations of the structure of a pillar micro-cavity	18
2.9	Illustrations of the structure of photonic crystal cavity	19
2.10	Illustration of Photonic crystal waveguide	21
2.11	Scanning electron microscope images of fiber-like photonic wire	21
2.12	Schematic guided modes for for an emitter embedded into a cylindrical photonic wire	22
2.13	Dependence of spontaneous emission rate on the diameter of the photonic wire	23
2.14	Sketch that describes a QD at an random position	24
2.15	β for different cylindrical wire diameters	24
2.16	Sketch of photon collection from a finite photonic wire	25
2.17	Schematics of two approaches for the top facet of the photonic wire	26
2.18	Trumpet fabrication process	28
2.19	Scanning electron microscope images of the trumpets	29
3.1	Photoluminescence experimental setup	32
3.2	PL spectra of a single InAs QD embedded in GaAs photonic wire	34
3.3	Power dependence of exciton and biexciton spectra	36
3.4	Radiative biexciton-exciton decay cascade	38
3.5	PL spectra of X and XX fitted with two Gaussian functions	38
3.6	Half-wave plate	39

3.7	Polarization dependence PL spectra	40
3.8	The evolution of H and V polarization dipoles as a function of the half-wave plate's angle	40
3.9	Photoluminescence spectra showing charged exciton	41
3.10	Photoluminescence spectra of the other quantum dots	42
3.11	Biexciton binding energy for free-standing trumpets	43
3.12	PL spectra of a pair of X and XX lines taken at different time scales	44
3.13	Emission energy drift as a function of time	44
3.14	Time-resolved PL experimental setup	45
3.15	Time-resolved PL spectra	46
4.1	Scheme of an atom-one dimensional continuum system	50
4.2	Scheme of field propagations inside a one-dimensional waveguide	52
4.3	Calculated reflection power and reflectivity	56
4.4	Illustration of spectral diffusion	57
4.5	Coherent and incoherent scattering rate	60
4.6	Resonant excitation experimental setup	61
4.7	Illustration of cross-polarized detection	63
4.8	Simple sketches of cross-polarized detection configurations -	64
4.9	Configuration of the resonant excitation in cross-polarization scheme	65
4.10	A picture of the setup	66
4.11	Resonant excitation scheme	67
4.12	Data collection procedure	68
4.13	Resonant excitation spectrum with a single resonant laser	71
4.14	Resonant excitation spectra with and without a non-resonant laser.	72
4.15	Dependence of resonance intensity on the non-resonant laser power	73
4.16	Typical resonant excitation spectra for both two excitonic dipoles	74
4.17	Resonant excitation as a function of resonant laser	74
4.18	Calibration of the incoming and reflected powers	76
4.19	The trumpet used in this study	77
4.20	SEM images of the sample	78
4.21	Cross-section of the waist diameter of the trumpet	79
4.22	Polarizations of excitonic dipoles	80
4.23	Reflection intensity and reflectivity of the system	81
4.24	Reflection and reflectivity for both two exciton dipoles	82
4.25	Calculated reflectivity for a perfect system	83
4.26	Coherent versus incoherent scattering	84
5.1	Simple sketches describing the goal of this chapter	87

5.2	An electromagnetic field coupled to a two-level quantum emitter	89
5.3	Scheme of the dressed states of the atom and excitation field system	91
5.4	The second laser beam couples the transition and leads to the formation of the Mollow triplet.	91
5.5	Pump-Probe experiment of a three-level system, AT doublet.	92
5.6	Energy evolution of the dressed states as a function of the pump laser detuning δ_C	93
5.7	A cascade three-level system coupled with two different fields	94
5.8	Absorption as a function of detuning	98
5.9	A scheme of two-mode giant non-linearity for a QD three-level cascade system	99
5.10	A scheme of two-mode giant non-linearity for a QD three-level cascade system in a reversed approach	100
5.11	Electromagnetically induce transparency	102
5.12	Absorption spectra of transition $ 1\rangle \longleftrightarrow 2\rangle$ at zero detuning of the control field	103
5.13	Experimental setup of the two-mode giant non-linearity measurement	105
5.14	Illustration of two-laser scan process	106
5.15	Probe laser scans over X_x state	107
5.16	Two-dimensional map showing Autler-Townes splitting	108
5.17	Probe reflectivity at different detunings of the control laser	109
5.18	Two-laser scan with different powers of control laser powers	110
5.19	Probe reflected intensity at zero detuning of control laser	111
5.20	Probe reflection of X transitions, theory and experimental plots - 1	113
5.21	Probe reflection of X transitions, theory and experimental plots - 2	114
5.22	Probe laser reflectivity when the control laser is ON and OFF	115
5.23	Probe reflection intensity as a function of the control laser.	116
5.24	Schema of a four level system that explains the enhancement in probe reflection	117
5.25	Calculated probe reflection intensity as a function of control power, for different angle θ	118
5.26	Probe laser switching contrast as a function of control laser power	119
5.27	Probe reflectivity for optimized parameters of the system in cross-polarized configuration	120
5.28	Ideal probe reflectivity in co-polarized excitation configuration	121
5.29	Probe reflection and switching contrast as the presence of laser background	122
5.30	Configuration of the population switch geometry	123
5.31	Two-laser scan in the population switch experiment	124
5.32	Probe reflected intensity as a function of the control laser power	125

5.33	Reflectivity of the probe laser in 4 orders of magnitude of the control laser power	126
5.34	Calculated probe reflectivity for different probe powers	128
5.35	Two-dimensional map of the Autler-Townes splitting obtained in the reversed situation (population switch)	129
5.36	Autler-Townes splitting for different control laser power in reversed approach	130
5.37	Illustration of the population switch in cross-polarized detection scheme . .	131
5.38	Calculated probe reflectivity in co-polarized excitation	132
5.39	Calculated probe reflectivity in co-polarized excitation	133
5.40	Calculated coherent and incoherent contribution in the total probe reflectivity in Autler-Townes splitting approach	134
5.41	Calculated coherent and incoherent contribution in the total probe reflectivity in population switch approach	135
A.1	Two-laser scan in Autler-Townes approach with a probe beam coupled to $0 \longleftrightarrow X$ transition	147
A.2	Calculated probe reflectivity for different homogeneous broadenings	148
B.1	Scanning electron microscope views of suspended trumpets	149
B.2	SEM images of giant trumpets	150
B.3	PL spectra from QDs embedded in a suspended photonic wire	151
B.4	Exciton and biexciton lines of a quantum dot embedded in suspended trumpet	151
B.5	Exciton and biexciton power dependence of QD in suspended trumpet . . .	151
B.6	Biexciton Binding energy as a function of exciton energy for both two samples	152
B.7	Photoluminescence spectrum of a quantum dot embedded in a suspended trumpet	153
B.8	Resonant excitation spectra of the quantum dot embedded in a suspended trumpet and a giant trumpet	154
C.1	Experimental setup with the presence of an intense fiber laser	155
C.2	Resonant spectra without and with the presence of the intense fiber laser .	156
C.3	Fitted resonant spectra with the presence of the intense fiber laser	157

Chapter 1

Introduction

1.1 Context

Tremendous progress in semiconductor optics has opened up various types of potential applications over the past decades. In the domain of quantum information science, one way to encode information is in the quantum state of single photons. Photons are the elementary constituents of light [1]. A single photon is a clean quantum system in which quantum information can be encoded in many ways and transported over long distances. A single photon is a non-classical state of light and it can not be described in term of classical electric field. Realizing bright sources of non-classical light states is one of the critical issues for quantum communication [2] and quantum information processing [3,4] potential applications.

From the classical point of view, for decades, optics have been proved to be the most efficient method of conveying information from one point to another, since light beams can be easily transmitted in parallel in free space or and do not suffer from crosstalk. In optical fiber, multiple independent optical signals can be carried using frequency-division multiplexing technique. Nowadays, the high-bandwidth internet connections also operate optically.

In the field of computing, the fundamental component of a computing circuit is a transistor. The present-day computers possess electronic transistors. Those transistors are reaching the bandwidth limitations of silicon electronics and printed metallic tracks [5]. That has raised up the demands for an alternative advanced solution. A all-optical switch is such a promising candidate. An optical switch is the optical analog of a transistor, allowing light to govern the transmission of light. Such technology has the potential to exceed the speed of electronics, while consuming less power. That brings the opportunity for optical technology to go beyond being not only a way for ultrafast data transmission, but also capable of performing data processing. Thus, it may give rises to the design

of a all-optical or a electro-optical hybrid computer. Since photons do not interact in vacuum, an optical transistor must employ an operating non-linear medium to mediate photon-photon interactions. The biggest challenge in this technology is the strength of the optical nonlinearities that couple optical fields. Strong light-matter interaction is required to realize a switch at a ultra-low level of power. The ultimate power limit for an ideal switch is a single photon and achieving this limit has been an important object in the field of optical and quantum computing.

1.2 One-dimensional optical system

As stated above, a ultra-low switching power is the critical issue in investigating any optical transistor device. An optimum device should possess optimum light input-coupling and output-collection efficiencies. In this case, techniques must be developed so that a single photon sent into the system has 100% possibility to interact with the non-linear quantum emitter and at the same time, every photon emitted by the emitter has to be successfully collected at the output of the device. Such a device can be realized using a one-dimensional structure. One-dimensional optical system is a system where the propagation of an electromagnetic field inside it is confined in a single dimension, as described in Fig. 1.1. A quantum emitter placed inside that structure has the highest probability to couple with the single spatial mode of the field. That concept was proposed by Kimble in 1995 [6] and is called “one-dimensional atom”. One dimensional system is one of the key features in many fields of semiconductor optics for quantum information science. Such a system increases not only the coupling of a light source with a quantum emitter, but also the collection of the light emitted from the emitter with optimum efficiency. Various types of one-dimensional system have been conducted in the last ten years. The most common systems will be discussed later in this thesis.

1.3 Single-photon source

One of the most attracting fields in quantum optics in the last years is the development of single-photon sources. Single-photon sources are light sources that emit light as single photons and they are capable of emitting only one photon after each triggering signal. The realization of “on-demand” single-photon devices have brought a huge impact and would revolutionize the field of quantum information processing [7, 8], quantum computation [3] and quantum cryptography [9]. The first single-photon device was demonstrated by Kimble et. al. in 1977 [10] via sodium atoms. Other schemes have also been reported using single molecules [11] or nitrogen vacancy (NV) centers in diamond [12]. Among these sources, semiconductor quantum dots (QDs) show particular properties suitable for

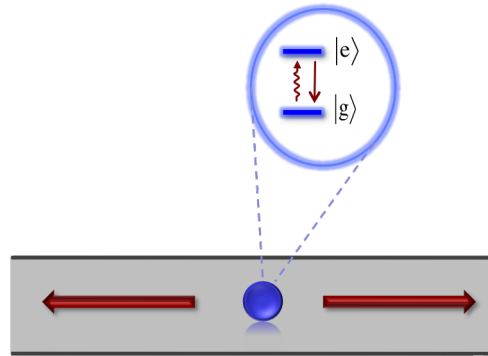


Figure 1.1 – Illustration of a one-dimensional atom: an atom as a two-level quantum emitter is placed inside a one-dimensional photonic structure. The light propagation is restricted to this one-dimensional geometry where the photons can scatter only back or forth. As a result, the light-matter interaction is optimized.

realizations of single-photon sources and also non-linear quantum optics applications [13, 14]. A semiconductor QD can be considered as an artificial atom [15], a strong confinement of the carriers in all three directions of space results in discrete energy levels. Like real atoms, QDs can emit single photons [16] or entangled-photon pairs [17]. These properties make semiconductor QDs very promising to implement quantum functionalities in a solid state system. As mentioned above, for any potential QD based single-photon source, the efficiency of the source, which is defined as the probability to collect a photon when the QD is excited is the key figure of merit. For quantum communication and quantum information applications, a near-unity efficiency is desired [18].

Unfortunately, QDs inside a bulk semiconductor material emit light in all directions. In addition, the QD is surrounded by a high refractive index material, which causes internal reflections at the semiconductor-air interface. All that results in a probability to collect photons emitted from a single QD of just a few percents. Therefore, techniques must be developed to enable an efficient photon collection.

To overcome that issue, the general idea is to couple the quantum emitter to a well-defined optical channel in a one-dimensional structure to optimize the coupling. Several approaches have been proposed over the last years. The most common approach is inserting the QDs in a photonic structure like photonic wires [19, 20], photonic crystals [21] or micro-cavities [22]). J. Claudon and his co-workers demonstrated an efficient, on-demand and pure single-photon source based on an InAs QD embedded in a GaAs photonic wire, with an extraction efficiency up to 0.75 [23]. In [22], the authors reported a single-photon source with a collection of 0.79 photon per excitation pulse. The detailed explanations of those structures will be given in the next chapter.

1.4 Optical giant non-linearity and all-optical switch

It turns out that these one-dimensional single-photon sources can be used as well the other way around to couple a propagating electromagnetic field to a single quantum emitter with optimal efficiency. In this situation, the probability for the single quantum object to absorb a photon fed into the structure is maximal. A single quantum emitter is a non-linear optical medium [24], where the interaction of one photon with the medium can block the reflection of a second incoming photon, owing to the saturation effect of the two-level system [25]. One can then take advantage of the one-dimensional property of a photonic structure to achieve giant non-linearity. The non-linearity is giant because ideally, only a single-photon is needed to saturate a single two-level emitter. Optical giant non-linearity at the single-photon level can be applied in various types of applications in quantum information and computation [26, 27]. It can also enable all-optical gates and switches for classical optical signal processing [28, 29]. Therefore, single-photon giant non-linearity has been the subject studied by several groups in photonic engineering. The main goal is to achieve a non-linearity signature at the lowest possible excitation power level.

1.4.1 Single-mode giant non-linearity

Single-mode giant non-linearity is obtained using a non-linear quantum medium to control and modify the reflectivity (or transmissivity) of an incoming electromagnetic field. In 2007, D. Englund et.al. demonstrated a giant optical non-linearity from QDs in photonic crystal cavities with a few average cavity photon numbers [30], but the input coupling efficiency into the cavity was reported to be only 1.8%. V. Loo et.al. reported a giant non-linearity on a system with a single QD embedded in a micro-cavity [14], where only 8 photons per excitation pulse were needed at the entrance of the structure to achieve the non-linear threshold. Recently, A. Javadi and coworkers demonstrated the giant non-linearity of a QD in a photonic-crystal waveguide at the level of less than one photon per lifetime [31], although the coupling efficiency of the excitation beam and the waveguide was 23% in this report. Apart from semiconductor QDs, strong light-matter non-linear interaction has also been reported with superconducting transmon qubit [32], ultra-cold atom gas [33, 34].

1.4.2 Two-mode giant non-linearity: all-optical transistor and switch

The ideal of investigating two-mode giant non-linearity is to be able to control light by only light at single-photon level. Among various possible applications, a realization of single-photon all-optical transistor has been a subject that attracted many interests. Optical transistor is a device that switches or amplifies optical signals [35]. This device is an optical analog of the electronics transistor that forms the basis of modern electronic

devices. An optical transistor provides a significant advantage that it can help reduce the power consumption compared with electronics transistor because of the absence of capacitance in the connections between individual optical logic gates. In electronics, the transmission lines need to be charged to the signal voltage. The capacitance of a transmission line is proportional to its length and it is the one of the main energy losses in electronic logic. In optical communication, this loss can be avoided. In addition, optical transistor can be directly linked to fiber-optics cables whereas electronics requires coupling via photodetectors and light emitting diodes (LEDs) or lasers.

Photons inherently do not interact with each other, thus in vacuum, direct photon-photon interactions are absent. Nonetheless, optical signals can influence each other in non-linear media. One of the fundamental issues that has limited this technology is the strength of the optical non-linearity that couple the signal and the control fields. The question is how to achieve this non-linearity at the level of a single photon. The main difficulty is to ensure that the coupling field will interact with the emitter with a close to unity probability. The ultimate optical transistor is a single-photon transistor: it is a device in which the propagation of a single signal photon is under the control of the presence or absence of a single gate photon. All-optical switches and transistors have been proposed to be the basic requirements for both classical and quantum optical information processing and quantum networking [4, 7, 36].

Several schemes have been proposed to implement all-optical transistors. Two-mode giant non-linearity has been efficiently realized using ultra-cold atom, most of the approached have relied on electromagnetically induced transparency (EIT) [37–39] and Rydberg blockade to create large nonlinearities [33, 40]. Such a system demonstrated a all-optical switch with a gate pulse that contains only one incoming photon on average to reduce the transmission of a subsequent target pulse [33]. The non-linearity have been obtained at the single-photon level. However, in this type of approach, a strong control field is always required to provide EIT effect.

Another promising method to reduce optical switching energies is to exploit the strong atom-light interactions between a QD and a photonic crystal cavity. In the strong coupling regime, the cavity-QD system can exhibit a large non-linear optical response at low optical powers [25, 41–43].

Io-Chun Hoi et.al. demonstrated an efficient interaction between two microwave fields using a superconducting transmon qubit, strongly coupled to an open transmission line [32]. Alternatively, a single-photon transistor can also be realized by coupling emitters and propagating surface plasmons confined to a conducting nanowire. Ideas and concepts have been proposed in [44–46].

All of those approaches will be discussed in detail in the last chapter of this thesis.

1.5 Motivation of this Thesis

Technical methods enabling efficient interaction between single photons and a quantum emitter have been emerging as one of the fundamental investigation fields of modern quantum optics. Among several proposals that have been demonstrated in the photonic engineering community, two-mode optical giant-nonlinearity has not been done efficiently in optics, especially with semiconductor QDs. Therefore, this thesis aims at an experimental realization of two-mode giant non-linearity, using a one-dimensional atom with an InAs QD embedded in a GaAs photonic wire. Photonic wire represents the combination of efficient, broadband spontaneous emission control and good coupling to standard optics in the far-field. Those excellent features pave a way to obtain a ultra-low power all-optical switch.

1.6 Thesis outline

Followed by this introduction, this thesis is organized in 4 upcoming main chapters:

Chapter 2 describes in details the system under study with InAs QDs embedded in a vertical GaAs trumpet-like photonic wire (PW). This chapter begins with general descriptions of the fabrication, structures and properties of self-assembled InAs QDs, including the fine structure splitting of an excitonic transition. The chapter continues with discussing the enhancement of light-matter interaction by coupling the QDs inside a one-dimensional photonic structure. The most common structures will be presented and discussed, including the one using in this thesis.

Chapter 3 presents the experimental results of basic optical characterizations of self-assembled InAs QDs embedded in a PW. The high resolution micro-photoluminescence experimental setup is described. The identification of the different emission transitions from the same QD is then demonstrated. This chapter also presents a time-resolved photoluminescence measurement, which gives the information of the lifetime of the single QD embedded in the PW environment.

Chapter 4 demonstrates the single-mode giant non-linearity results. The non-linearity effect is based on the saturation of a QD two-level system. The chapter begins with a theoretical model considering a two-level system placed inside a one-dimensional waveguide. The model includes also the imperfections of the system. The chapter then continues with explaining the experimental setup and procedure. The non-linearity is realized based on reflectivity measurement. The resonant fluorescence measurement is carried out by scanning a laser across the excitonic frequency of the QD. The power dependence plot shows the non-linearity behavior in which the reflectivity drops down towards above saturation of the two-level system. This giant-nonlinearity is observed at the level of very few photons

per lifetime.

Chapter 5 presents the main result of this thesis on two-mode giant non-linearity, realizing an all-optical switch. The measurements are carried out by considering a QD three-level system, where the biexciton transition is taken into account together with the exciton transition to form a cascade scheme. In this experiment, two transitions of the three-level system are coupled to two different laser beams. One beam plays the role of a probe beam while the other plays the role of a control beam. We study how the transmission of the probe beam on one transition is modified when the control beam is introduced to the other transition. Two different approaches are considered, by coupling the probe beam either with the lower or upper transition. The first case is based on the dressed approach, whereas the second one is based on population effect. The chapter firstly introduces an ideal three-level model to theoretically describe two-mode giant non-linearity. Then it is followed by the detailed experimental methods and results. The results indicate that two-mode giant non-linearity is achieved at the level of just a few tens of photons per emitter lifetime, realizing an ultra-low power all-optical switch.

Chapter 6 concludes the thesis and discusses future perspectives.

Chapter 2

A quantum dot embedded in a photonic wire

This chapter will give a detailed presentation of the sample studied in this thesis. The first section will give an overview, fabrication and properties of semiconductor quantum dot (QD) in general and for InAs QD in particular. The following section will discuss the enhancement of the light-emitter interaction efficiency by coupling the QD inside a photonic nanostructure. Different coupling approaches will be summarized and discussed before going into details of the QD-photonic waveguide system using in this thesis.

Contents

2.1	Self-Assembled InAs quantum dots	10
2.1.1	Overview	10
2.1.2	Quantum dot discrete energy levels and optical excitation methods	11
2.1.3	Multi-excitonic states in a quantum dot	14
2.2	Interaction of a quantum dot with light in a photonic wire . .	16
2.2.1	Quantum emitter coupled to a photonic nanostructure	16
2.2.2	Resonant structures	17
2.2.3	Non-resonant waveguide structures	20
2.2.4	Fiber-like photonic wire	21
2.2.5	Extraction efficiency enhancement in a finite photonic wire . . .	25
2.2.6	Photonic trumpet	28
2.3	Chapter summary	30

2.1 Self-Assembled InAs quantum dots

2.1.1 Overview

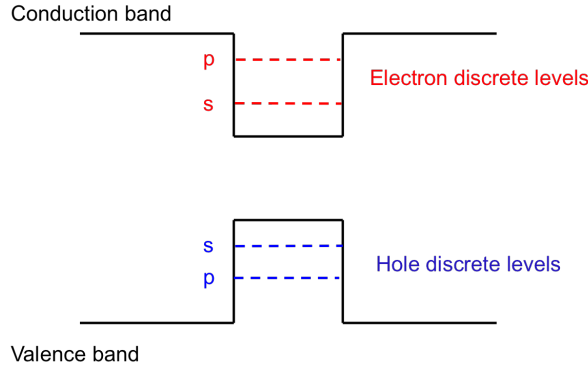


Figure 2.1 – Conduction and valence band energies in a QD - The confinement potential energy in the growth direction results in a series of quantized energy levels. A ladder of discrete energy levels in the QD are labeled as s, p, d... similar to the classification of atomic states.

A semiconductor quantum dot (QD) is a droplet of a semiconductor material embedded in a matrix of another semiconductor material of larger band gap. The most basic property of the QDs is that electrons and holes in QDs are confined in all three dimensions. This property makes QDs being considered as zero-dimensional (“0D”) structures. A result of confinement is the complete quantization or discretization of a confined charge carrier energy spectrum. A QD is able to sustain trapped states for both electrons in the conduction band and holes in the valence band at cryogenic temperature (Fig. 2.1). The properties of quantized energy spectrum and complete localization resemble the behaviors of electrons in an atom. Although each QD consists of tens of thousands of atoms, it still has optical properties similar to single atoms due to the quantum confinement of electrons to a nanometer length scale. For this reason, a QD can be considered as a semiconductor “artificial atom”. Excitons are quasi particles composed of a negatively charged electron and a positively charged hole. Owing to attractive Coulomb force, an electron and a hole form an exciton which can be spatially confined inside the QD. Excitons can recombine either radiatively or non-radiatively. When an electron and a hole are trapped in the ground states of respectively the conduction and the valence band of the QD, the decay mode is mainly a radiative recombination.

The QDs used in this study are self-assembled InAs QDs embedded in GaAs (Fig. 2.2). These InAs QDs are grown by molecular beam epitaxy (MBE), using a strain-induced self-assembly method (“Stranski-Krastanov” growth mode). This method uses the relief of elastic energy when two materials with a large lattice mismatch form an epitaxial structure. A monolayer of InAs is first deposited on a GaAs substrate. The

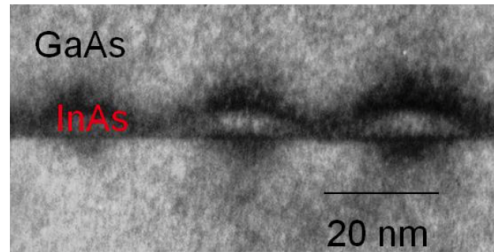


Figure 2.2 – TEM image of the cross section of the quantum dot structure - Self-assembled InAs/GaAs QDs are grown by Stranski-Krastanov method, strained InAs islands based on the wetting layer in GaAs matrix [47].

growth mode is two-dimensional and coherent with GaAs substrate, which is referred as the “wetting layer”. The InAs crystal has a lattice parameter 7% larger than the one of GaAs. When the thickness of the wetting layer is further increased to a certain value, the strain accumulated in the InAs layer is elastically relaxed through the generation of three-dimensional InAs islands, which are the QDs. Their dimensions are about a few tens of nanometer (20 ~ 30 nm) in diameter and 2 ~ 3 nm in height. In order to protect the QDs from oxidation and to prevent interactions with surface states, the QDs are finally capped with a GaAs layer. In this manner, we have self-assembled QDs on the top of a thin InAs wetting layer [48].

2.1.2 Quantum dot discrete energy levels and optical excitation methods

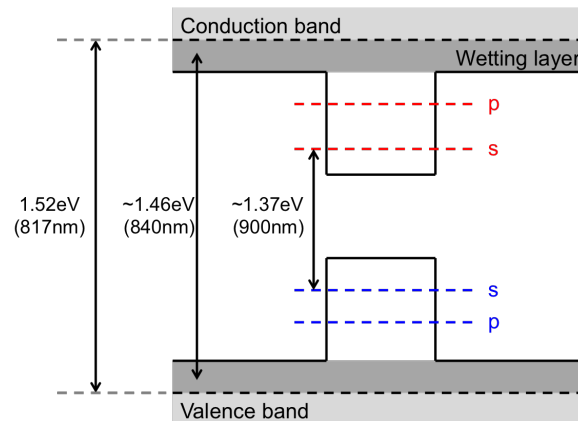


Figure 2.3 – Schematic of energy levels for a InAs/GaAs quantum dot - The band gap of GaAs at liquid helium temperature is about 1.52 eV, the energy of the wetting layer is below the GaAs band gap energy at about 1.46 eV, the s-shell recombination energy is around 1.37 eV.

Fig. 2.3 illustrates the energy levels of conduction and valence bands in a InAs/GaAs QD. Optical excitation of a QD can be performed in several ways. The first way is

above-band excitation. In this case, the excitation energy is above the band gap of the material surrounding the QD. The band gap of GaAs at low temperature is 1.52 eV, corresponding to a wavelength of 817 nm. This excitation generates electrons and holes in the regions surrounding the QD. Some fractions of these charge carriers are captured by the wetting layer, which is a two-dimensional quantum well. The carriers then relax into QD excited states via emission of phonons. When an electron reaches its ground state within the conduction band, the only remaining decay path is the inter-band transition to the valence band. A transition can occur only if the valence band has a un-occupied state (a hole). This transition is primarily radiative with a lifetime in the order of 1 ns [49]. This process is called “photoluminescence” (PL) of the QD.

The second method is wetting layer excitation. In this method, the excitation laser energy is chosen slightly below the band gap of the surrounding material (GaAs in our case), within the wetting layer continuum. This excitation can create the carriers directly in the wetting layer. Such excitation is still non-resonant and does not depend highly on the particular wavelength used, but it helps decreasing the time required for particles to relax within the conduction and valence band (a few 10 ps time scale [50, 51]). In the case of excitation of a QD placed inside a GaAs photonic waveguide, wetting layer excitation also has an important advantage of preventing unwanted heatings of GaAs and allowing the exciting light to propagate within the photonic wire without being absorbed. In our study, we will use this approach when performing non-resonant excitation experiments.

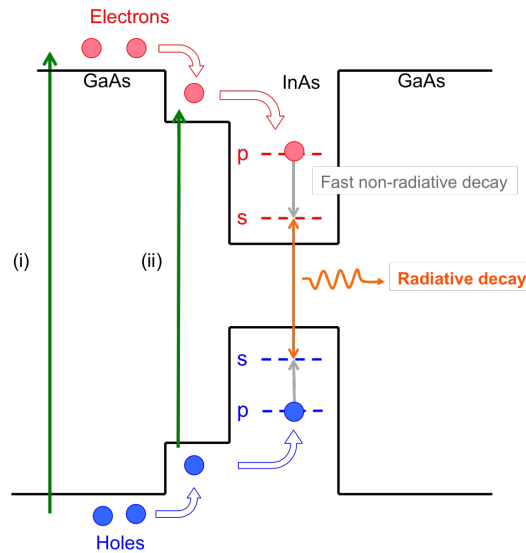


Figure 2.4 – A Schematic of non-resonant excitation methods - (i) Above band gap excitation. (ii) Wetting layer excitation. After the excitation, the generated electrons and holes are trapped by the QD potential well. Once inside the QD, the carriers then relax quickly from excited states to the ground states of the QD via phonon emission. The carriers at their ground states then recombine via inter-band transition from conduction band to valence band and emit a photon after a characteristic lifetime of about 1 ns.

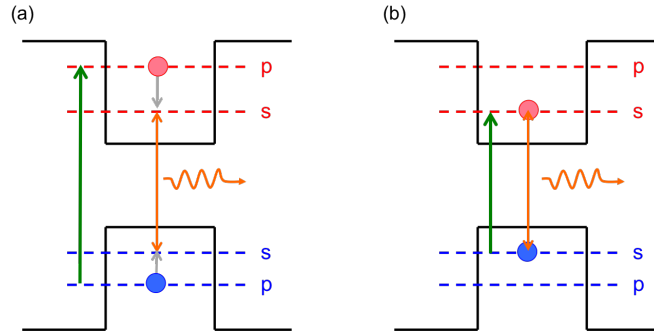


Figure 2.5 – Schematics of resonant excitation methods - (a) p-shell quasi-resonant excitation: the excitation source is turned to higher excited states of the QD. A single electron-hole pair is created directly inside the QD, and can relax to the ground state with 10 ps. (b) s-shell resonant excitation: the excitonic ground state is directly probed. Thus, it requires less pump power compared with p-shell excitation.

Together with non-resonant excitation, a QD can be excited by quasi-resonant and resonant excitations. Quasi-resonant excitation can be performed by tuning the laser on resonance with a higher excited state of the QD (electron and hole in their p-shell levels), which is described in Fig. 2.5(a). This way, a single electron-hole pair is generated directly inside the QD. Due to the nature of this process, only fast carrier relaxation from higher shells into the s-shell has to be considered. Quasi-resonant excitation can also be proceeded through excitation of an longitudinal optical (LO) phonon above the QD fundamental transition energy. In this approach, it is not so difficult to spectrally filter the excitonic ground-state emission with the scattered laser light (the bulk GaAs LO phonon energy for the same system under this study was reported to be $E_{LO} = 36$ meV [52]). The excited state has rapid relaxation time, therefore it is expected to have a broad emission linewidth. Quasi-resonant excitation also requires higher excitation power compared with above-band and wetting layer excitations since the absorption cross-section of a single QD is small. After relaxation into the s-shell, each generated electron-hole pair delivers a single photon. Thus, quasi-resonant excitation features a reduced perturbation of the QD environment and can therefore enhance the coherent properties of emission [53]. In general, this kind of excitation is used commonly in realization of indistinguishable photons [22]. In practice, to perform a quasi-resonant excitation, photoluminescence excitation (PLE) is normally carried out. [52].

The ultimate pumping process is a direct resonant excitation into the s-shell of the QD, in which excitonic ground states are directly probed (see Fig. 2.5(b)). This scheme possesses the same advantages as the quasi-resonant excitation, that it creates a single electron-hole pair. However, in this case, no additional relaxation process is needed before the radiative recombination process. In other words, only photon emission process occurs. In s-shell resonant excitation, the excitation laser frequency has to be exactly the same

as the emission frequency. That is the reason why this scheme has not been commonly used for implementation of single photon sources. The scattered light from the laser is a serious problem in this type of experiment. In our study, to overcome this problem, we will perform this strict resonant excitation using the cross-polarization technique to suppress the back-scattered laser background, which will be shown in chapter 4.

2.1.3 Multi-excitonic states in a quantum dot

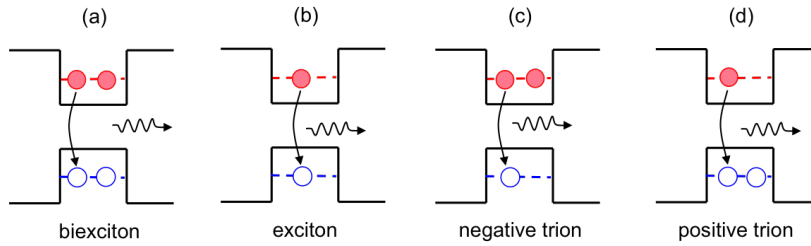


Figure 2.6 – Schematic multi particle states of a single quantum dot - Considering the s-shell radiative recombination, four types of excitonic quasiparticles exist due to Pauli exclusion principle.

QDs can contain multiple electrons and/or holes, which leads to additional transitions besides the single neutral excitons. The occupation of the QD shells follows Pauli's principle, the ground state of a QD can be occupied by only a maximum of two electrons or two holes of opposite spins. That creates four types of excitonic quasi-particles that are described in Fig. 2.6: the neutral exciton (one electron and one hole), the biexciton (two electrons and two holes), the negative trion (two electrons and one hole) and the positive trion (one electron and two holes), the two last quasi-particles are called charged excitons. In the first case, one single exciton (X) occupies the QD and its recombination generates a photon at energy $\hbar\omega_X$. This emission energy depends on the discrete levels of the electron and the hole. In the second case, two pairs of electron-hole occupy the QD, this state is called biexciton (XX). Its emission frequency ω_{XX} corresponds to the transition from XX to X . It is shifted by Coulomb and exchange interactions with respect to ω_X . In the two first cases (Fig. 2.6(a)-(b)), it is possible to observe two luminescence lines corresponding to exciton and biexciton. The energy difference is called biexciton binding energy, this binding energy changes between different QDs depending on the degree of carrier confinement. The binding energy can be positive or negative (see section 3.2.2.2 for an experimental demonstration) and its amplitude can vary from a few meV to a few tens of meV [54]. The two last cases (Fig. 2.6(c)-(d)) consist of one exciton plus an additional charge (electron or hole to form respectively either negative trion (X^-) or positive trion (X^+)). As for the XX , the presence of the additional charge makes the emission energies of charged excitons different from the neutral X . Therefore it is possible

to observe spectrally a PL spectrum which corresponds to the recombination of a charged exciton.

2.1.3.1 Fine-structure splitting

Each of the excitonic levels consists of a multiplet of states corresponding to different spin configurations of the carriers. The electron and hole may have either parallel or anti-parallel spins. The spins are coupled by the anisotropic exchange interaction, giving rise to the fine structure [55].

The lowest energy exciton is composed of the electron spin ($s = \pm\frac{1}{2}$) and the heavy-hole angular momentum ($j = \pm\frac{3}{2}$), consequently producing four exciton states $M = \pm 2$ and $M = \pm 1$ [56]. States with $M = \pm 2$ can not couple to the light field, therefore they are optically inactive and denoted *dark* excitons. States with $M = \pm 1$ couple to the light field and are denoted *bright* excitons. Independent of the given confinement symmetry electron-hole exchange interaction causes a dark-bright splitting. The exchange interaction mixes the dark states forming a dark doublet ($|2\rangle \pm |-2\rangle$). Additional lowering of the confinement symmetry produces a non-degenerate bright doublet ($|1\rangle \pm |-1\rangle$). While emission lines involving pure states are circularly polarized, the two bright states usually produce linear polarization lines along the crystal directions are thus directly observable in a luminescence experiment [56]. The energy difference between these lines is called exciton fine-structure splitting (FSS).

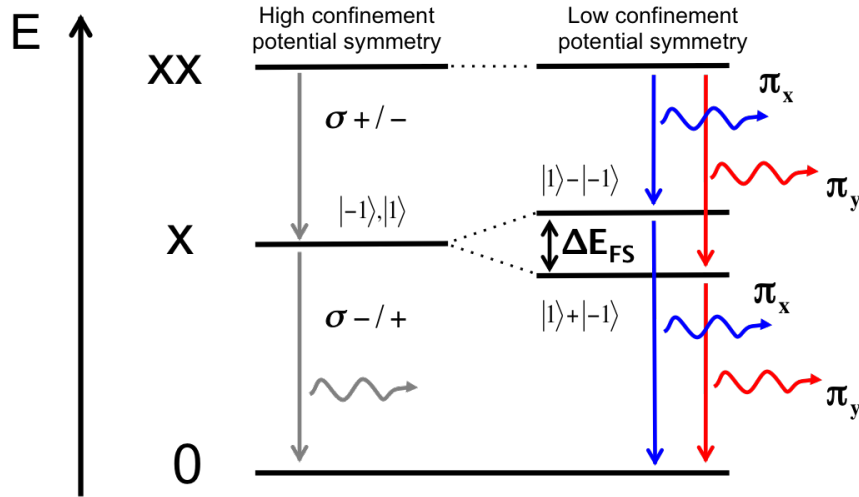


Figure 2.7 – Illustration of biexciton-exciton cascade. At high confinement potential symmetry, the exciton bright state is a pure state and emits circularly polarized light σ_{\pm} . When the confinement potential symmetry is lowered, the exciton bright states are mixed and produce a bright doublet with linear polarizations.

For the negatively charged trion X^- , the two s-electrons must have opposite spins due

to the Pauli exclusion principle, whereas both spin orientations are allowed for the hole. As a consequence, there is no FSS. The situation is the same for the positively charged trion X^+ . The transient matrix elements for the decay of a trion to a single electron or hole are circularly polarized with the helicity depending on the spin of the additional carrier, they have no corresponding dark states. The additional carrier in trions may be prepared in a spin eigenstate, and therefore trions are particularly relevant for spin physics. The XX ground state is not split by the exchange interaction, since the net spin of the involved electrons and holes is 0. However, the XX to X decay involves two allowed transitions with the final states being the bright states of the X . Therefore, the FSS is reproduced in the biexciton to exciton decay. The $XX - X$ radiative decay cascade is described in Fig. 2.7. Several experimental reports have been made on In(Ga)As/(Al)GaAs showing different values of FSS [57–64]. The typical FSS of InAs/GaAs QDs is in the range from a few tens of μeV to about 200 μeV [57–59].

It has been shown that the FSS can be reduced by annealing process [60,61], by apply external electric fields [65], or by growing QDs in the higher symmetry (111) substrates [66,67]. The $XX - X$ radiative cascade in a QD therefore has been proposed as a source of triggered polarization-entangled photon pairs. The suppression of FSS is the critical issue in realizing polarization entangled photon pairs, which are an important resource in quantum optics and quantum information applications [7, 17, 68–70]. Entanglement requires two indistinguishable decay paths with different polarizations. This is only be possible for vanishing FSS.

2.2 Interaction of a quantum dot with light in a photonic wire

2.2.1 Quantum emitter coupled to a photonic nanostructure

The first chapter has presented various potential applications using semiconductor QD as a quantum emitter, such as single-photon sources or all-optical transistors. The efficiency of the device is the key figure of merit. The crucial challenge is to maximize the coupling of an incoming light to the emitter as well as the efficient collection of the emission. Therefore, optimizing the interaction between light and matter has been an essential task in quantum optics. For a bulk InAs QD, the size of the QD is much smaller than the emitter wavelength, thus, it emits light in all directions. In addition, the large refractive index of GaAs causes internal reflections at the semiconductor-air interface. As a result, a very small fraction of light can be finally extracted (just a few percent). To enhance light-matter interaction, one can couple the emitter to a well-defined mode of an optical field. In this approach, photonic nanostructure appears to be a suitable candidate. Such

kind of structure has the ability to tailor an electromagnetic field on a length scale that is a fraction of the optical wavelength. Moreover, photonic nanostructures with excellent optical properties can be fabricated with modern nano-fabrication techniques [71]. An ideal light-matter interface requires that a single atom interacts only with a single optical channel. Such an “one-dimensional atom” can be achieved by controlling the spontaneous emission (SE) of the atom. In general, the main factor that characterizes the performance of a quantum emitter embedded in a photonic structure is the SE rate of the emitter into a given mode of the structure, normalized by the total SE rate, namely the β -factor. β represents the fraction of the emitted photons coupled into the given mode compared to the total emission into all available modes.

For the realization of a real source of single-photon, one has to take into account a second factor which is the extraction efficiency ε_C . It corresponds to the probability of a photon to escape from the structures. Similarly, concerning the giant non-linearity experiment, the input-coupling efficiency, which is the coupling rate of an incoming photon into the structure, is also a critical parameter.

Several approaches have been proposed and demonstrated experimentally to enhance the controlling of SE by using a photonic structure. The following sections will give a brief overview of the two commonly used structures and then present the one that is used in this thesis.

2.2.2 Resonant structures

The first strategy is to use a resonant optical microcavity [72]. The light-matter interaction can be improved by placing the emitter inside a high quality microcavity and taking advantage of cavity quantum electrodynamics to control SE of the QD. Resonating light in a cavity provides a way of increasing light-matter interaction since the coupling to one localized mode can be strongly enhanced compared to all other modes. The cavities can have very small mode volumes, which enhances the interaction strength [71]. Resonant SE control is based on Purcell effect [73], in which the enhancement of SE rate into the cavity mode is governed by the Purcell factor,

$$F \propto \frac{Q}{V} \quad (2.1)$$

with Q is the quality factor of the mode and V is the mode volume. Q and V are the two figures of merit that define the performance of a emitter-cavity system. Achieving a high Purcell factor thus requires a cavity able to confine electromagnetic field over small volumes V and at the same time having a high Q (which means long photon-storage time) [74–76]. Given the Purcell factor F , the fraction of photons emitted in the mode β is [77],

$$\beta = \frac{F}{F + 1} \quad (2.2)$$

thus a cavity with large Purcell factor will have a close to unity β .

One important physical quantity is the QD-cavity coupling strength g , it describes the coherent interaction between the QD optical transition and the confined cavity mode. Thus, the objective for a QD-cavity device is to increase the coupling strength. A system is in the strong-coupling regime if the amplitude of g is higher than both $\kappa/4$ and $\gamma/4$, with κ is the cavity damping rate and γ is the dephasing rate (including γ_{SP} the SE rate of the QD outside the cavity mode and γ^* the pure dephasing rate) [77].

In general, Purcell effect leads to an acceleration of SE rate. It basically reduces the QD excited state lifetime hence its sensitivity to pure dephasing is reduced. Purcell factor can also be defined as $F = \frac{\Gamma}{\gamma_{SP}}$ [78], where $\Gamma = \frac{2g^2}{\kappa}$ is the emission rate in the cavity mode. A large Purcell factor is usually required to obtain $\frac{\Gamma}{2} \gg \gamma^*$ [77], so that the contribution of pure dephasing can be negligible. This is a favorable condition for emitting indistinguishable single photons [22].

2.2.2.1 Pillar micro-cavity

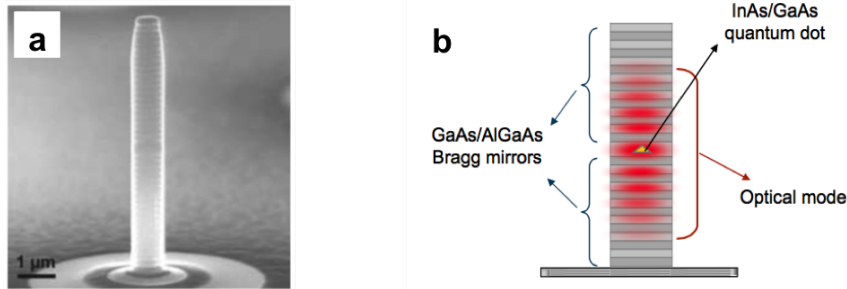


Figure 2.8 – Illustrations of the structure of a pillar microcavity - (a) SEM image of the pillar microcavity described in [79]. (b) Sketch of a typical Qd-Pillar cavity system [80], a layer of self-assembled InGaAs QDs is embedded into a cavity and is sandwiched between two-distributed Bragg mirrors, inducing the confinement in lateral and vertical directions.

In this context of resonant cavity, one popular approach is to use pillar micro-cavities [81]. A pillar microcavity consists of two Bragg mirrors made of many alternating layers. Two Bragg mirrors have different refractive indices n_1 and n_2 , with the thickness $\lambda/4n_i$ ($i = 1,2$). A space between such two Bragg mirrors creates a highly localized cavity mode, where the QDs are located (Fig. 2.8). This cavity mode induces the confinement of light in the vertical direction. The lateral confinement can be obtained by etching a cylindrical micropillar with a typical diameter of a few μm [80]. A maximal light-matter interaction is achieved when the QD is located at a maximum of the cavity mode intensity and the

QD transition frequency matches the cavity frequency $\omega_{QD} = \omega_{cavity}$.

The fabrication of such a system can be carried out using far-field in-situ optical lithography to position a single QD in a spectrally resonant pillar microcavity with an accuracy as high as 50 nm [81]. In particular, this technique firstly maps the QD of desired energy and possesses large emission intensity from a layer of many QDs. Then the pillar microcavity is defined around the chosen QD and the position of the QD is ensured to be at the maximum of the pillar fundamental mode. This step is repeated as many times as desired for different QDs, so that one can fabricate many optimally coupled QD-pillar cavities on a single wafer [80].

Regarding this pillar microcavity approach, O. Gazzano and co-workers at *LPN/CNRS in Paris* reported a very bright single-photon source with a QD embedded in a pillar microcavity [22] with a collection efficiency up to 0.79 photon per excitation pulse. Also from the same group, V. Loo and coworkers demonstrated single-mode giant non-linearity using a similar structure [14]. The quality factor Q and the input-coupling rate reported in this worked were respectively $3 \cdot 10^4$ and 95%.

2.2.2.2 Photonic crystal cavity

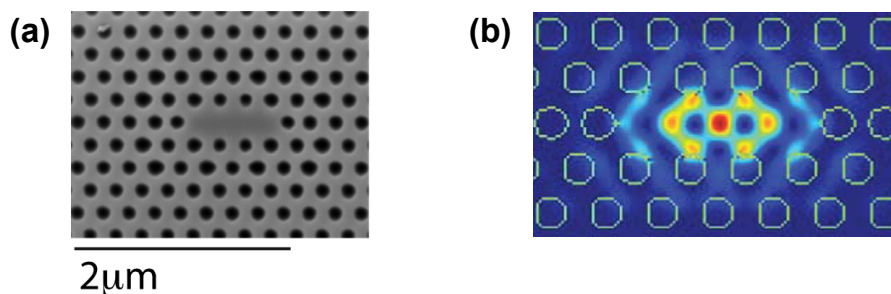


Figure 2.9 – Illustrations of the structure of photonic crystal cavity. (a) Scanning electron micrograph of the photonic crystal cavity in [82] showing a three-hole (L3) structure. (b) Simulated electric field intensity of the photonic crystal cavity [30].

Another approach to confine light in a cavity is to use photonic crystal [83]. Highly localized cavity modes can be obtained by introducing defects in photonic crystal (PC) membranes to induce light confinement. A design of a high- Q PC cavity is plotted in Fig. 2.9(a). The base structure is composed of a triangular lattice of air “rods”. The structure of the cavity is made with three missing air rods in a line. As a result, light can be confined by Bragg reflection for the in-plane direction, the z direction is confined by total internal reflection [82, 83]. Such a structure is one of the most successful PC cavity designs and is called three-hole defect cavity or $L3$ cavity. The electric field of the fundamental mode of a $L3$ cavity is shown in Fig. 2.9(b) [30]. Experimental result of single-mode giant non-linearity using a single QD embedded in a $L3$ PC cavity has been reported in [30]

where the authors demonstrated a cavity with quality factor $Q \approx 10^4$. The non-linearity in reflection can be obtained at the level of less than 1 intracavity photon number inside the cavity. However, the input-coupling rate of the system is just less than 2%.

2.2.3 Non-resonant waveguide structures

In the approach using a resonant structure, it has been shown that Purcell effect is a resonant effect, the associated drawback is the requirement of an energy matching between the cavity mode and the quantum emitter emission line. The operation bandwidth of the cavity is therefore limited (below 1nm for a cavity with $Q > 10^3$ operating at the 1 μm wavelength range on resonance). Thus resonant structures are restricted to monochromatic emitters.

Apart from Purcell factor enhancement, the non-resonant SE control approach provided by a one-dimensional photonic waveguide appears as an appealing alternative [84–86].

2.2.3.1 Photonic crystal waveguide

To overcome the fact that the QD-cavity system can only operate within a narrow bandwidth, PC waveguide was proposed as a candidate. In this structure, an efficient mode guiding is ensured by a tight lateral confinement of this mode by photonic bandgaps. The photonic waveguide can be highly dispersive which may be employed for enhancing light-matter interaction by taking advantage of slow light propagation [86]. The difference between a high- Q cavity and a waveguide is that in this case, photons are transferred directly to the propagating mode of the waveguide, which potentially gives rise to a larger overall efficiency of the source. Importantly, the coupling enhancement is not limited to a narrow spectral bandwidth as in a cavity.

A waveguide can be defined in a PC membrane [86, 87] as shown in Fig. 2.10. It is composed of a slow-light section, which is coupled on both sides to weakly dispersive sections. The slow-light section features a low group velocity in order to increase light-matter interaction. This enhanced coupling will allow the efficient channeling of single photons from a QD into the PC waveguide mode.

In [31], A. Javadi et.al. reported a single-photon giant non-linearity with a quantum dot in a PC waveguide with the inferred coupling efficiency $\beta \approx 96\%$. An operation bandwidth of $\Delta\lambda = 20$ nm was demonstrated in [86], which already outperformed the structures based on narrow bandwidth cavities. Concerning the input coupling efficiency, this PC waveguide possessed an efficiency of 23% [31].

In the following part of this section, we will demonstrate another non-resonant approach to control SE: a fiber-like, vertical photonic nanowire. This approach has been

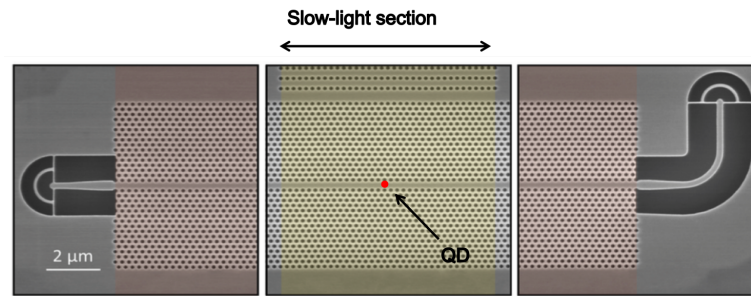


Figure 2.10 – Illustration of Photonic crystal waveguide. Scanning-electron micrograph of the photonic crystal waveguide [31]. A QD is placed in the central part of the slow-light section. Each end of the structure is coupled to regular bridge waveguides and out-coupling gratings.

chosen for giant non-linearity realization in this thesis.

2.2.4 Fiber-like photonic wire

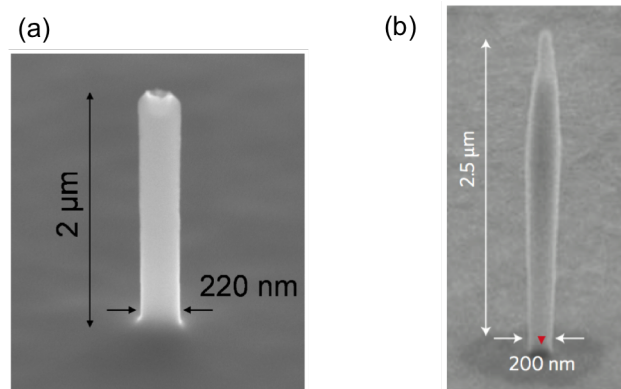


Figure 2.11 – (a) scanning electron microscope images of fiber-like GaAs photonic wire [88]; (b) a single-photon source based on needle-like photonic wire made of GaAs embedding InAs QDs [19].

In the last ten years, single-photon sources relying on a InAs QD embedded in a GaAs photonic nanowire have been proposed [19, 88, 89] (Fig. 2.11). The photonic nanowire geometry is well adapted to efficient collection of light. This structure features no cavity and relies on a geometrical screening of radiation modes rather than resonant effects to ensure a large coupling between the QD and the guided mode [89]. Photonic nanowires are relatively simple dielectric structures, made of a high refractive index material, surrounded by a cladding with a low refractive index. They were pointed out to have a broadband and efficient SE control [88, 90, 91]. In practice, this geometry was reported to feature a β factor up to 96% and exceeds 90% over a $\Delta\lambda = 250$ nm broad operation bandwidth around $\lambda = 900$ nm and a first lens external coupling efficiency of 75% [23].

2.2.4.1 An infinite cylindrical photonic wire

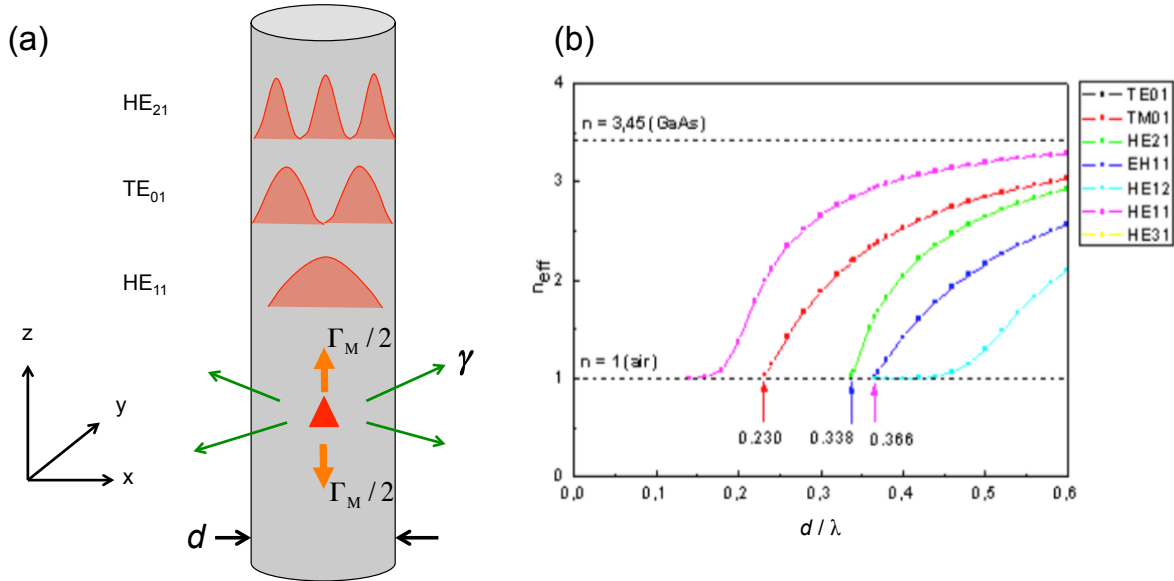


Figure 2.12 – Schematic guided modes for an emitter embedded into a cylindrical photonic wire - (a) Depending on the diameter d of the photonic wire, the emitter is supported by various optical guided modes. Γ_M is the fraction of the guided modes and γ corresponds to the unguided modes. (b) effective index as a function of reduced diameter calculated for the first guided modes [47].

We firstly consider the case in which a QD is embedded in an infinite cylindrical photonic wire (PW) with diameter d as displayed in Fig. 2.12(a). The PW is made of GaAs (refractive index $n=3.45$) and surrounded by air or vacuum ($n=1$). The structure provides a confinement of the optical field inside the PW in the two lateral dimensions (x and y) and therefore the mode propagates freely in the third direction (z). Depending on the diameter of the PW, the emitter is coupled to one or several guided modes that are supported by the structures (HE_{mn} , EH_{mn} , TE_{mn} , TM_{mn}). At the same time, it is also coupled to a continuum of free-space modes that are called radiative mode.

To define the SE coupling rate of the waveguide, as shown in Fig. 2.12(a), we denote Γ_M the decay rate into the target guided mode and γ the decay rate into all other modes (the radiative mode and other possible guided modes). We thus have $\Gamma_{Tot} = \Gamma_M + \gamma$ is the total decay rate of the emitter. The desired mode in this case is the vertical mode at the center of the wire axis and the QD is assumed to locate at this center position. The relevant figure of merit of the one-dimensional photonic waveguide is the β factor describing the SE rate into the desired mode over the total emission rate,

$$\beta = \frac{\Gamma_M}{\Gamma_{Tot}} = \frac{\Gamma_M}{\Gamma_M + \gamma} \quad (2.3)$$

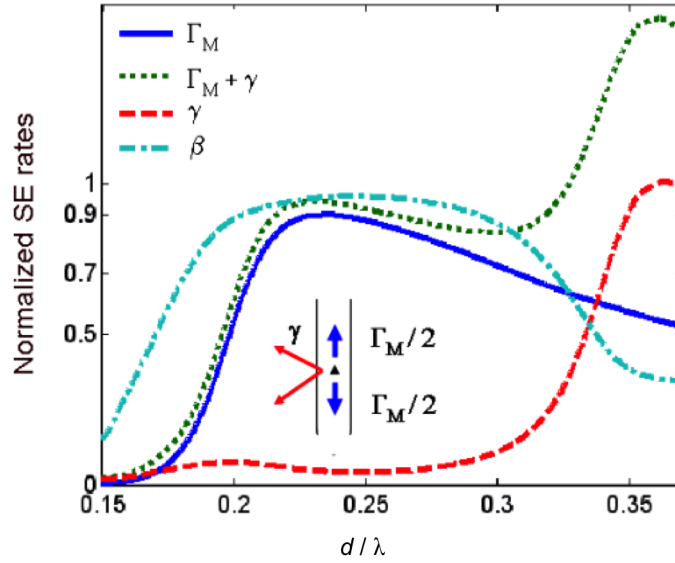


Figure 2.13 – Dependence of spontaneous emission rate on the diameter of the photonic wire - The case is considered for a QD located at the center of the wire. Blue-solid curve shoes the emission Γ_M into the fundamental mode HE_{11} . Dark-red curve represents the amount of leaky modes. Dash-dotted curve indicate the evolution of γ factor for the fundamental mode when the diameter changes [47].

Therefore, for the waveguide to have a high β factor, the decay rate into all the unwanted modes γ has to be minimized. Fig. 2.12(b) shows a plot of the effective refractive index n_{eff} of the system as a function of reduced diameter d/λ (λ is the wavelength of the emitter, which is 950 nm in this case) [47]. In the small diameter range ($d < 0.18\lambda$), the effective index of the dielectric wire is close to 1, indicating that the mode is completely deconfined in the surrounding air. Increasing the diameter, n_{eff} increases rapidly for the fundamental guided mode HE_{11} . At the diameter $d > 0.23\lambda$, new guided mode starts to show up (TE_{01}). However, as shown in Fig. 2.12(a), it features zero amplitude on the wire central axis and can be neglected for an on-axis emitter. For a diameter larger than 0.338λ , other modes with non-zero components on the wire axis appear (HE_{21} , HE_{12} , HE_{31} , ...) and their effective indices tend toward the refractive index of GaAs ($n = 3.45$) (see the thesis of Nitin Malik [47] for more details).

Here, we consider Γ_M is the decay rate into the fundamental guided mode HE_{11} . By choosing a proper wire diameter, one could optimize spontaneous emission coupling rate into this mode. Fig. 2.13 [47] describes the evolution of SE rates as a function of the wire diameter, for a QD at the center of the wire. The fraction β exceeds 90% when the wire diameter d is in the range $0.2\lambda - 0.29\lambda$, which is about 200-300 nm for a QD emits at $\lambda = 950\text{nm}$. The coupling reaches the maximum value 95% for $d = 0.24\lambda$. The large tolerance for the high SE coupling rate indicates that broadband operation control can be achieved

for that one-dimensional structure.

2.2.4.2 Influence of quantum dot lateral position on β factor

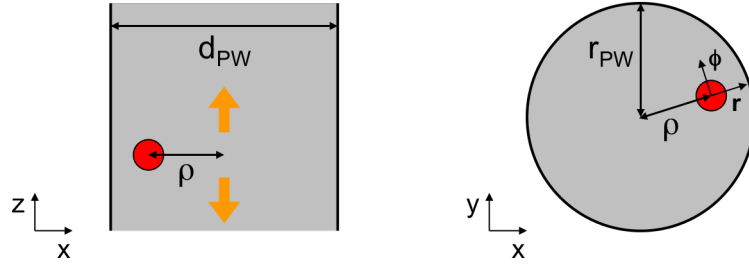


Figure 2.14 – Sketch that describes the situation for a QD at an random position inside the wire: considering a QD located at a position ρ away from the center axis of the PW. The calculation of SE coupling rate β as a function of ρ is carried out for two orthogonal directions ϕ and r .

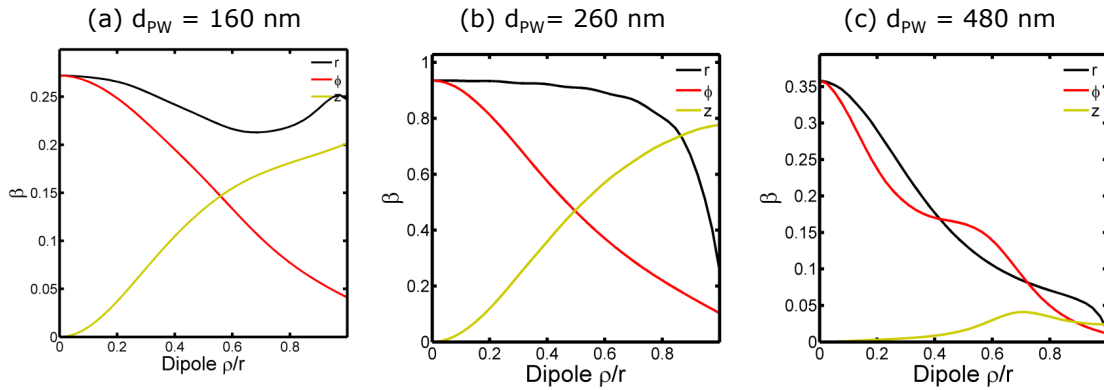


Figure 2.15 – Calculating results for the SE rate into HE_{11} guided mode for three different diameters of a cylindrical photonic wire: (a) $d_{PW}=160$ nm, the wire diameter is too small to obtain a good β even for an on-axis QD. For the off-axis QD, different behaviors of β factor are observed for two orthogonal directions pointing out in Fig. 2.14 ; (b) $d_{PW}=260$ nm, $\beta > 0.9$ is predicted for QDs locating at the center of the PW; (c) $d_{PW}=480$ nm, increasing the diameter of the PW results in the appearance of other guided modes, therefore β factor into HE_{11} mode decreases.

So far, we have just considered β -factor for the case of a QD located on the central axis of the PW. This section will briefly give the calculation results of the SE coupling rate for a QD located in a off-axis position. The calculation was done by Niels Gregersen (DTU Fotonic, Denmark). The situation is described in Fig. 2.14, the QD is located at the position ρ from the center of the wire. The results of β for three different wire diameters are shown in Fig. 2.15, where β is plotted as a function of the ratio between the distance of the QD from the axis and the wire radius. $\rho/r = 0$ correspond to an on-axis QD. One

can see that β changes drastically when a QD is located off-axis. And the behaviors are different for two orthogonal-oriented dipoles ϕ and r . It should be noted that a QD inside the PW with a waist diameter around 500 nm (Fig. 2.15(c)) approximately corresponds to the case that will be studied in this thesis.

2.2.5 Extraction efficiency enhancement in a finite photonic wire

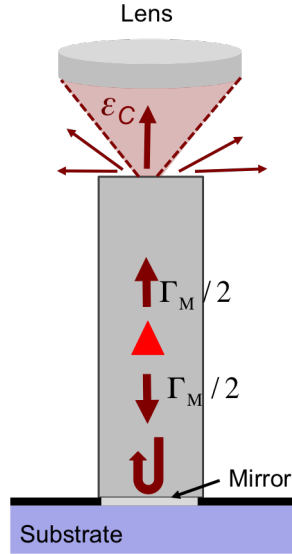


Figure 2.16 – Sketch of photon collection from quantum emitter embedded inside a finite photonic wire: A mirror is integrated at the bottom to reflect upward the emission going to the bottom of the wire. The light exiting the top of the wire will be collected by an optical lens.

We have seen in the previous section that β factor into the fundamental guided mode can reach values close to unity. In practice, we have to consider a finite PW which stands on a substrate (Fig. 2.16). The photons emitted from the QD are collected at the top facet. To realize a real single-photon source, all the guided photons must be collected at one output of the PW. In principle, there are two main factors that could affect the global extraction efficiency.

Firstly, since the photons are guided equally into upward and downward directions of the mode, the collection efficiency will be reduced by a factor of 2. We assume that the PW has a “semi-open” symmetry, which means the reflectivity of the upper facet is suppressed and only the reflection of the bottom is taken into account. Therefore, if we place a mirror at the bottom of the PW and set the position of the QD in a way to obtain the interference between the field reflected back and the field emitted upward [47], the fraction of emitted light traveling to the top facet can be maximized. It has been shown that by putting a planar gold-silica mirror at the bottom of the PW, the modal reflectivity

can be reached more than 95% [23].

The second factor which affects the global efficiency is the fraction of the light exiting the wire that is collected by a first lens, which is denoted as ε_C (see Fig. 2.16). According to [23, 47], the first lens external efficiency ϵ , has the form

$$\epsilon = \frac{\beta(1 + |r|)^2}{2(1 + \beta|r|)} \varepsilon_C \quad (2.4)$$

The parameter ϵ is the figure of merit for the global efficiency of the one-dimensional system. To have a large ϵ , high ε_C is required, which means that a low divergence of the output beam is necessary. However, for the PW with small diameter, the fundamental mode waist is narrow. As a result, the tightly confined HE_{11} photons leaving a real, finite wire through a flat top facet are diffracted with a high angle into free space. That leads to a wide far-field radiation pattern. It prevents an efficient collection of light with standard optics. In order to increase the collection rate, one has to reduce the output beam divergence by expanding the mode waist [92]. There are two possibilities to achieve this mode expansion, by either decreasing or increasing the top diameter of the PW.

2.2.5.1 Tapering of the photonic wire top facet

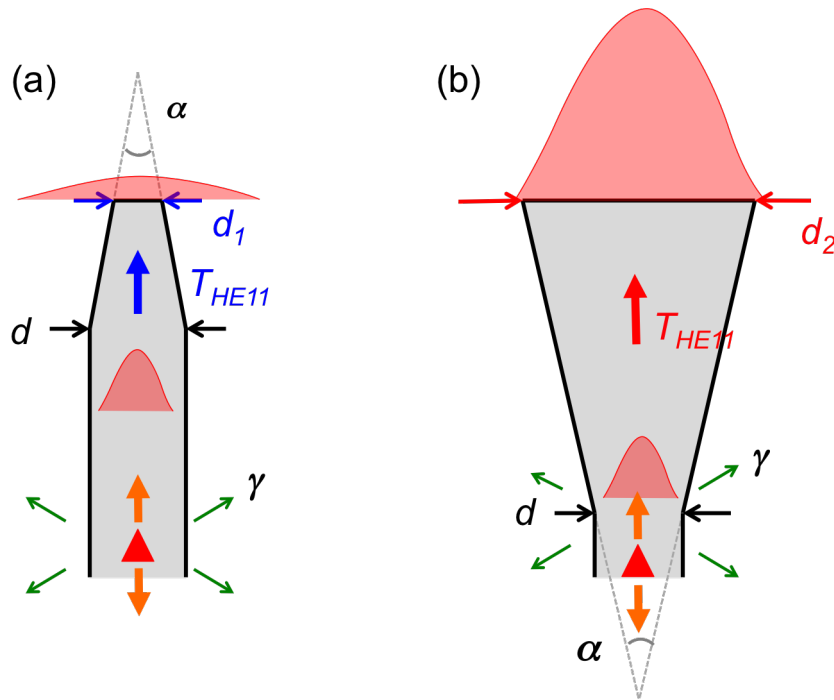


Figure 2.17 – Schematics of two approaches for the top facet of the photonic wire -
 (a) Sketch of a needle-like taper design photonic wire. (b) Schematic of the inverted trumpet-like taper design photonic wire. The diameter of the cylindrical part in both two cases is d . $T_{HE_{11}}$ denotes the modal transmission along the taper section.

The first approach decreases the diameter of the PW at the upper end, thus featuring a conical tapering of opening angle α [19, 88, 89, 93, 94] (Fig. 2.17(a)). As the fundamental mode propagates forward, the radius of the PW decreases and forms a needle-like taper PW. For a small angle α , this ensures the adiabatic conversion of the HE₁₁ mode into a strongly deconfined mode, which represents a narrower and less diffraction output mode. $T_{HE_{11}}$ represents the modal transmission, which corresponds to the propagation of HE₁₁ along the tapered section. It has been shown in [23] that $T_{HE_{11}}$ depends drastically on the angle α in this needle type taper ($T_{HE_{11}} \approx 60\%$ for $\alpha = 5^\circ$ and $\approx 50\%$ for $\alpha = 7.5^\circ$). This device features a measured efficiency of 0.72 combined with a very clean single photon emission with $g^{(2)}(\tau=0)$ of 0.008 [19].

However, the needle taper design encounters several weaknesses. Firstly, the fabrication of the regular conical tapering with an opening angle $\alpha \leq 5^\circ$ is quite challenging using the top-down approach [19]. Secondly, although such a taper design expands the guided mode outside the PW to obtain a directive far-field emission, the emission still remains poorly matched to a Gaussian free-space beam [23].

The limitations of the needle-like design lead us to the second geometry, which is sketched in Fig. 2.17(b). The bottom part of the structure is similar to the first geometry. However, the upper part features a trumpet-like taper with an opening angle α . As the diameter of the PW increases, the lateral size of the mode also increases progressively, but the mode remains confined inside the structure. Concerning the performance of this second geometry compared with the needle-like design, according to [23], the needle-like taper suffers from significant non-adiabatic losses of $T_{HE_{11}}$ when increasing the angle α from 0° to 10° , that results in free-space emission into the surrounding air before reaching the taper end. Meanwhile, the trumpet-like taper design ensures a nearly perfect adiabatic expansion of HE₁₁ for $\alpha < 5^\circ$, leading to $T_{HE_{11}} > 0.994$. The modal transmission $T_{HE_{11}}$ is maintained above 0.95 when increasing α up to 15° . Since the far-field emission is essentially governed by the scattering of HE₁₁ when it reaches the top facet, so the high value of $T_{HE_{11}}$ is a critical parameter. The figures of merit of the efficiency of the taper design are the total transmission ε_C into the collection lens and the transmission T_g into a Gaussian beam. For a PW with a fixed height, it has been calculated that for the trumpet design PWs, ε_C and T_g increase with the angle α and reach the optimal value $T_g = 0.97$ for $\alpha = 11.5^\circ$, which corresponds to the top diameter $d_2 = 2.6 \mu\text{m}$. For the needle-like PW, ε_C and T_g decrease drastically with α and the maximum value for T_g is just 0.43. This means that the trumpet design of the PW is much more favorable for light propagating in the mode HE₁₁ to be collected when escaping from the top facet of the PW.

2.2.6 Photonic trumpet

Because of the outstanding β factor and high collection efficiency, trumpet-like PW (trumpet for short) is chosen for the giant non-linearity experiment in this study. It should be noted that the trumpet under study is not integrated with a mirror at the bottom. The following parts will briefly introduce the sample fabrication process and the description of sample structure.

2.2.6.1 Fabrication process

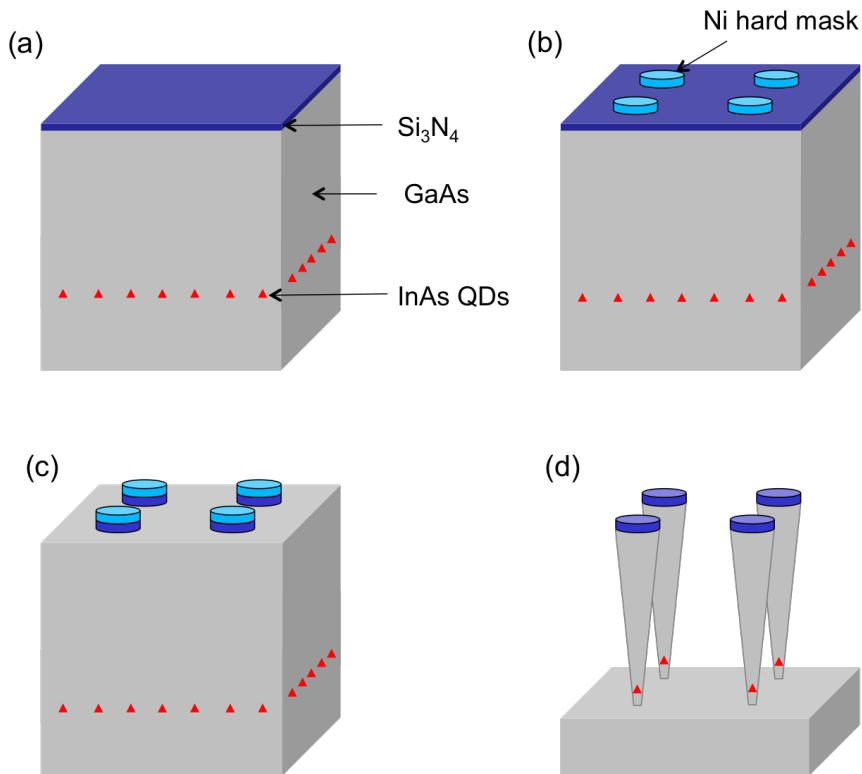


Figure 2.18 – An illustration of the trumpet fabrication steps: (a) Deposition of anti-reflection coating layer Si_3N_4 on top of a planar GaAs wafer, (b) Nickel deposition, which defines the top shape of the trumpet, (c) Reactive ion etching (RIE) with Si_3N_4 layer and (d) RIE to form the inverted trumpet shape.

The fabrication of the sample was carried out by E. Dupuy and N. S. Malik in the group of J. Claudon and J-M. Gérard from the same Nanophysics et Semiconductors (NPSC) joint team, CEA/INAC/SP2M. The main fabrication steps are illustrated in Fig. 2.18. The device is made out of a planar structure grown by molecular beam epitaxy on a GaAs wafer, in which a single layer of InAs self-assembled QDs is located in a GaAs matrix. To make sure all the incoming light could enter the structure with highest efficiency, a layer of anti-reflection coating made of 115 nm-thick Si_3N_4 is deposited on the top facet using

plasma-enhanced chemical vapor deposition (Fig. 2.18(a)). The inverted trumpet-shape is then obtained through a top-down approach. Using electron-beam lithography, a Nickel hard mask is defined and consists in arrays of circular disks with diameter ranging from $1\ \mu\text{m}$ to $4\ \mu\text{m}$ with $10\ \text{nm}$ steps (Fig. 2.18(b)). The following step is the reactive ion etching (RIE) process to transfer the pattern of the mask into firstly the anti-reflection coating layer (Fig. 2.18(c)) and then into the GaAs wafer. By a careful control of the chemical recipe of the etching process, the conical shape with high aspect ratio and smooth sidewalls is formed. Finally, the remaining Ni mask is removed in a diluted nitric acid solution (Fig. 2.18(d)). To suppress spurious surface effects, the wire sidewalls were passivated and covered with a $20\ \text{nm}$ thick Si_3N_4 layer [95, 96]. This fabrication process is applied for a non-mirror sample. For a trumpet with integrated metallic mirror at the bottom, a more sophisticated fabrication is required to deposit the mirror into the structure [23, 47].

2.2.6.2 Sample summary

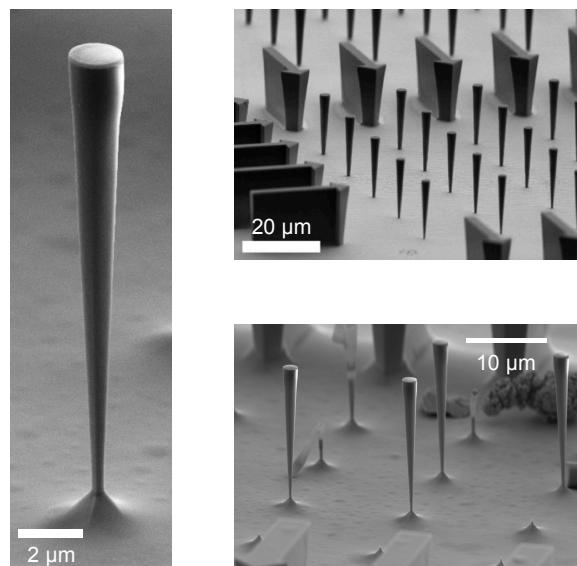


Figure 2.19 – Scanning electron microscope images of the trumpets - The sample contains several arrays of trumpets with top diameter ranging from $1\ \mu\text{m}$ to $4\ \mu\text{m}$ with the a step of $10\ \text{nm}$. The opening angle is fixed at 5° .

Fig. 2.19 shows SEM images of the photonic trumpets, a series of trumpets with top diameters varying by a $10\ \text{nm}$ step is obtained. The height of the trumpets is about $17.2\ \mu\text{m}$, the QD layer locates $0.8\ \mu\text{m}$ above the waist, each trumpet is estimated to contain approximately 100 QDs.

2.3 Chapter summary

This chapter gave an overview about the samples that are used in this thesis. General properties, applications, and multi-exciton levels of self-assembled InAs QDs was presented. Several approaches in addressing efficient coupling between the emitter and photonic environment have been demonstrated in details. The trumpet-like photonic wire structures was shown to have several advantages in studying the giant non-linearity for all-optical switch applications. The last sections discussed the fabrication processes of GaAs photonic wires embedding InAs QDs and the short summary of the samples was presented.

Chapter 3

Photoluminescence spectroscopy

Photoluminescence (PL) spectroscopy is a fundamental study when investigating semiconductor QDs. This chapter will firstly present the experimental setup, where we perform a high resolution micro-PL measurement. The full characterization of the PL spectra will be then presented and discussed, firstly with the PL power dependence, then with the polarization resolved measurement. Evidences will be shown to identify the exciton and the biexciton transition from the same QD, based on the fine structure splitting of the exciton level of the QD. The following section will discuss about the spectral drift of the QD emission. Finally, time-resolved PL measurement is then performed to study the relaxation process and measure the lifetime of the single InAs QD embedded in the GaAs photonic wire.

Contents

3.1	Experimental setup	32
3.1.1	Optical source	33
3.1.2	Cryogenics	33
3.1.3	Spectrometer	33
3.2	Photoluminescence spectroscopy	34
3.2.1	Photoluminescence spectra	34
3.2.2	Photoluminescence power dependence	35
3.2.3	Spectral drift	43
3.2.4	Time-resolved photoluminescence measurement	45
3.3	Chapter summary	47

3.1 Experimental setup

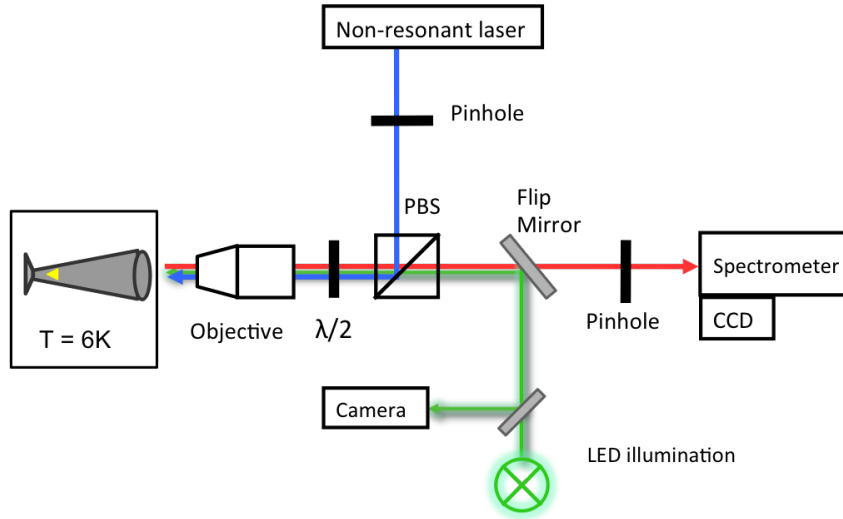


Figure 3.1 – Non-resonant micro-photoluminescence experimental setup - The measurement is performed at 6K. The QDs are excited by a non-resonant laser. The photons emitted from the QDs are collected by a CCD camera placed at the output of a spectrometer.

Fig. 3.1 shows the experimental setup. The laser excites the sample in one direction, and the light emitted from the sample is collected in the opposite direction. The sample is placed on a cold finger in vacuum inside a Helium-flow cryostat. The laser is directed to pass through a pin hole with a diameter $20 \mu\text{m}$. The pin hole helps to spatially filter the elliptical shape of a laser beam. For that reason, all the lasers that are used in this study are aligned to pass through that pin hole. The laser beam is then directed to a polarizing beam splitter (PBS). The purpose of placing a PBS but not a normal beam splitter is to establish the cross-polarized detection, which will be used and demonstrated more clearly in the next chapters. The laser beam reflects on the PBS and then passes through a half-wave plate. With a half-wave plate in front of the sample, we can rotate the polarization of the incoming beam, as well as the linear polarizations of the light emitted from the QDs.

The laser beam is focused on top of the trumpet by a microscope objective. We can choose either an objective with numerical aperture (NA) = 0.4 (Olympus LMPL) or NA = 0.75 (ZEISS LD Plan_NEOFLUAR). The working distances of the NA 0.4 and 0.75 objectives are respectively 8.1 mm and 2.2 mm. Photoluminescence (PL) measurement is performed by wetting layer excitation method, as explained in section 2.1.2. The laser wavelength is at 825 nm, which is slightly below the band gap energy of GaAs at 6K (1.52 eV - 817 nm). At this energy, the laser excites the wetting layer of the QD and the light can propagate within the photonic wire without being absorbed. The beam reaches the

QD level and is absorbed and re-emitted by the QDs. Part of the light emitted from the QDs travels toward the top facet of the trumpet, exits the trumpet and is collected by the same objective. The light then passes through the PBS to the detection system. To spatially select only the light going out of the trumpet, the top facet of the trumpet is imaged on a second pin hole. The output of this pin hole is then directed to the 1.5m-focal-length spectrometer. At the output of the spectrometer, the light is detected by a charge coupled device (CCD) camera.

To be able to visualize the trumpets and the position of the optical beam, the sample is illuminated with a LED lamp. The sample is imaged on a small camera (Watek WAT-902) and is displayed on a screen.

3.1.1 Optical source

The laser used in PL spectroscopy is a continuous-wave (CW) diode laser, controlled by Thorlabs ITC 502 controller. To prevent the unwanted back reflection, which may cause a number of instabilities to the excitation beam (like intensity noise, frequency shifts, mode hopping or even the possibilities of damaging the laser), an optical isolator is put just after the laser. Optical isolator is a magneto-optic device that preferentially transmits light along a single direction and shields upstream optics from back reflections.

To precisely control the focus and the position of the laser beam on the sample, the microscope objective is mounted on a 3-dimensional translation stage (Nanomax-312D/M). The Nanomax offers a positioning in three directions, including coarse adjustment of 4 nm with 10 μm precision, plus 300 μm of fine adjustment with 1 μm precision. In addition, it can also be controlled by piezoelectric actuators, with 20 μm travel at 20 nm accuracy.

3.1.2 Cryogenics

Optical properties of QDs are studied at cryogenic temperature. The sample is mounted on a sample holder, which is kept inside a continuous helium flow cryostat (by Oxford Instruments). The cryostat is placed on a 2-axis translation stage, with the precision of 10 μm . The stage helps to perform the initial adjustments of the sample position. The temperature inside the cryostat can be modified by a heater controlled by the temperature controller ITC 601, which can tune the temperature from 3.5 K up to room temperature with accuracy of 0.1 K.

3.1.3 Spectrometer

The CCD camera we use is the PIXIS: 100B from Princeton Instruments. It is a fully integrated, low noise camera with a 1340×100 pixels format. The working temperature of the camera is -70°C . This camera offers very low electronics noise and a very high quantum

efficiency in the near-infrared region, up to more than 80% at 900nm. The spectrometer we use is a Jobin-Yvon THR1500, with a focal length of 1.5 m. It has a grating with 1200 grooves/mm, blazed at 750 nm, which offers a spectral resolution of about 0.0088 nm at 930 nm ($\approx 12.3 \mu\text{eV}$). The movement of the grating can be rotated by a motor controlled by computer.

3.2 Photoluminescence spectroscopy

3.2.1 Photoluminescence spectra

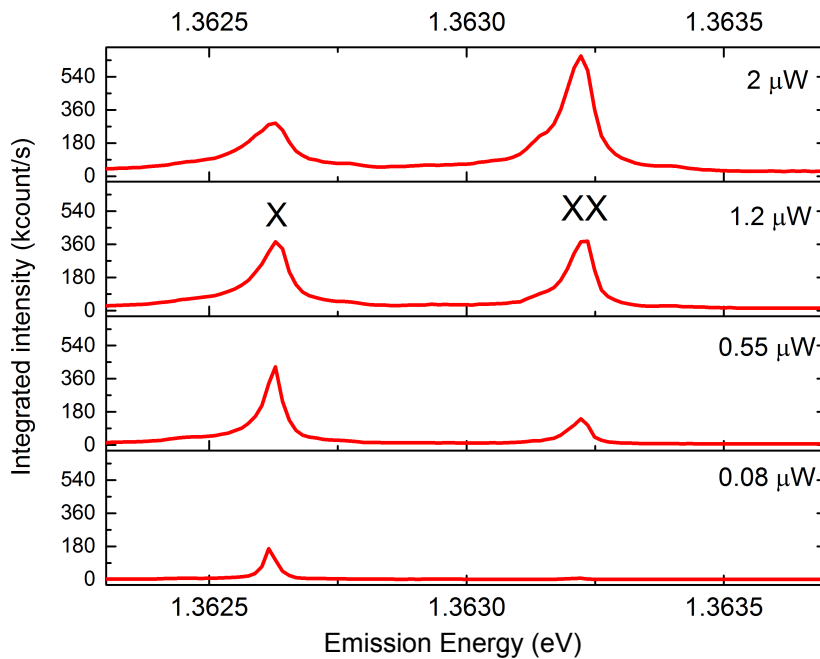


Figure 3.2 – PL spectra of a single InAs QD with different excitation powers - The integration time for every spectrum is 1 s. The spectra of X and XX transitions are shown when the excitation power increases from low power, where we see only the emission of the X transition, to higher power, where the intensity of the X transition increases and saturates, while the XX transition starts to dominate the spectra.

PL measurement is performed at 6K, the temperature can be controlled either by the temperature controller at a fixed set point, or by adjusting the amount of He flowing into the cryostat by a needle integrated in the He transfer tube. PL spectra are taken with Winspec (an integrated spectroscopy package for cameras and spectrographs, by Princeton Instruments). In addition, PL spectra can also be recorded by a home-made Labview program (developed by Edouard Wagner), which has integrated all the necessary functions from Winspec. To select the preferred wavelength range, the grating inside the spectrometer can be rotated remotely by another Labview program.

Fig. 3.2 shows a typical PL spectra of a self-assembled InAs QD embedded in the trumpet. The QD emits photons in the near-infrared region (900-930 nm). Each subgraph shows a PL spectra with different excitation powers, from 0.08 μW to 2 μW . In the low excitation limit, the QD occupation probability is low, resulting in an emission spectrum dominated by a single exciton (X). With increasing the excitation power, the biexciton XX line starts to show up. The X line saturates when the XX emission begins to dominate the spectrum. The linewidth of the emission is about 30 μeV . Performing the non-resonant PL on different QDs from the same trumpet or different trumpets gives the linewidth in the range from a few ten of μeV to more than 100 μeV .

Chapter 2 has discussed about the β factor, which represent the coupling efficiency between the QDs and the guided mode of the PW. In fact, one trumpet contains many QDs. The β factor related to each QD depends strongly on the position of that QD with respect to the central axis of the trumpet. That is why in the PL spectra, several emission lines which come from many different QDs can be observed. Normally, the QDs closer to the central axis of the trumpet exhibit stronger PL than QDs located further away, owing to a large coupling β to the guided mode of the trumpet. In addition, if a QD is located close to the center, it will be coupled better to the excitation beam, because the laser beam is also guided to propagate along the central optical axis of the PW and benefits from the guided mode. As a consequence, it will require less power to saturate the QD that is closer to the center. In the case in Fig. 3.3, just about a few hundreds nW is needed to saturate the QD in this wetting layer PL excitation. Although the non-resonant laser has the wavelength of 825 nm, which is not properly guided by the mode with the highest efficiency, but the level of excitation power is still significantly smaller than that in bulk QDs. The power required to excite bulk InAs QDs has been reported to be in a range from less than 1 mW to a few mW [97–99].

3.2.2 Photoluminescence power dependence

The PL emitted by a QD can be described by a simple model considering a two-level system consisting of a ground state and an excited state. Due to spin degeneracy, the excited state can contain up to two excitations. Thus, there are three possibility: an empty dot, a dot with one excitation (X) and a dot with two excitations (XX). The rate equations describing the transitions are:

$$\frac{dn_{XX}}{dt} = \Gamma n_X - \frac{n_{XX}}{\tau_{XX}} \quad (3.1)$$

$$\frac{dn_X}{dt} = \Gamma n_0 - \frac{n_X}{\tau_X} + \frac{n_{XX}}{\tau_{XX}} - \Gamma n_X \quad (3.2)$$

$$\frac{dn_0}{dt} = -\Gamma n_0 + \frac{n_X}{\tau_X} \quad (3.3)$$

where n_0 , n_X and n_{XX} are respectively the probabilities that the QD being in ground, X and XX states. The times τ_X and τ_{XX} are respectively the radiative lifetimes of X and XX . The quantity Γ is the pumping rate. Neglecting the possible contribution of higher levels and the creation of charged excitons allows the assumption $n_0 + n_X + n_{XX} = 1$. Hence Eq. 3.2 becomes

$$\frac{dn_X}{dt} = -\frac{n_X}{\tau_X} + \frac{n_{XX}}{\tau_{XX}} - \Gamma(1 - 2n_X - n_{XX}) \quad (3.4)$$

In steady state regime, $\frac{dn_X}{dt} = 0$ and $\frac{dn_{XX}}{dt} = 0$, we then have

$$n_X = \frac{\Gamma}{\frac{1}{\tau_X} + \Gamma + \Gamma^2 \tau_{XX}} \quad (3.5)$$

$$n_{XX} = \frac{\Gamma^2 \tau_{XX}}{\frac{1}{\tau_X} + \Gamma + \Gamma^2 \tau_{XX}} \quad (3.6)$$

The X and XX emission intensities depend on the pumping rate as followings

$$I_X \propto \frac{n_X}{\tau_X} = \frac{\Gamma}{1 + \Gamma \tau_X + \Gamma^2 \tau_X \tau_{XX}} \quad (3.7)$$

$$I_{XX} \propto \frac{n_{XX}}{\tau_{XX}} = \frac{\Gamma^2 \tau_X}{1 + \Gamma \tau_X + \Gamma^2 \tau_X \tau_{XX}} \quad (3.8)$$

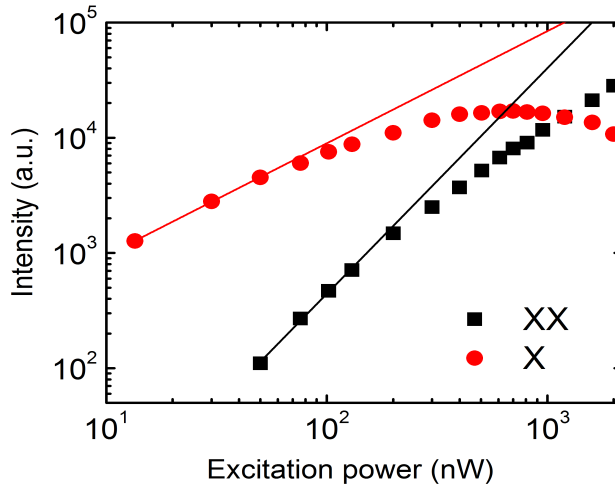


Figure 3.3 – Integrated intensity of X and XX as a function of excitation power - The solid lines show the fitting. At low excitation power, the X emission intensity follows the linear dependence, while the XX emission intensity follows the quadratic dependence on the power.

In the low pumping rate limit (excitation power well below saturation power of the transition), one could see that X and XX intensities have respectively linear and quadratic dependences on the pumping rate. The integrated PL intensities of the X and XX transitions as a function of the excitation power are shown in Fig. 3.3. This dependence is plotted in log-log scale. The black and red straight lines are the fit lines for X and XX intensities at low excitation power. The fits show the exponents 0.97 and 1.96 for X and XX , respectively. This indicates that at low excitation limit, the intensity of the exciton $I_X \propto P^{0.97}$ and the intensity of the biexciton $I_{XX} \propto P^{1.96}$, with P is the excitation power of the laser.

Taking into account the saturation power for the X and XX transitions, one could see from Fig. 3.3 that the PL intensity of the XX line is slightly higher than that of the X line at saturation. This difference is due to the influence of dark X states. Dark X state has been introduced in section 2.1.3.1. In a QD, X states are split by the electron-hole exchange interaction into higher-energy bright X states and lower-energy dark X states with respective angular momentum of $J_z = \pm 1$ and $J_z = \pm 2$ [100, 101]. It has been demonstrated that if the energy splitting between bright X and dark X states is rather large ($\Delta E \gg k_B T$ with k_B is the Boltzmann constant and T is the temperature), dark X can not transit back to bright X . Thus dark X is stored until recombining nonradiatively, leading to a reduced excitonic light emission. By contrast, for XX state, there is no non-radiative recombination channel. As a result, the PL saturation intensity of X is less than that of the XX .

3.2.2.1 Identification of exciton and biexciton from the same quantum dot

When studying the PL spectroscopy of a single QD, it is important to identify a pair of X and XX transitions which are emitted from the same QD. Furthermore, in the next chapters, the study will be based on a three-level ladder system which involves the X and XX levels from a single QD. Therefore, among several emission lines in the PL spectra, it is crucial to be able to point out a pair of X and XX from the same QD.

Firstly, one can rely on the fine structure splitting (FSS) of the X state. Fig. 3.4(a) shows the $XX-X$ -ground state radiative cascade. X transition contains two orthogonal-polarized levels X_x and X_y . Therefore, XX level has two possible recombination channels through either X_x or X_y . The presence of ΔE_{FS} leads to distinguishable recombinations for the XX and X cascades and creates a pair of polarization-correlated photons. As a result, the PL spectra is composed of two doublets with the two components linearly polarized along perpendicular directions. Those doublets can be described spectrally by the energy scheme in Fig. 3.4(b). The PL spectra of X and XX contains two peaks that are split in energy by ΔE_{FS} .

In principle, due to the asymmetry, each QD has its own fine structure and the splitting

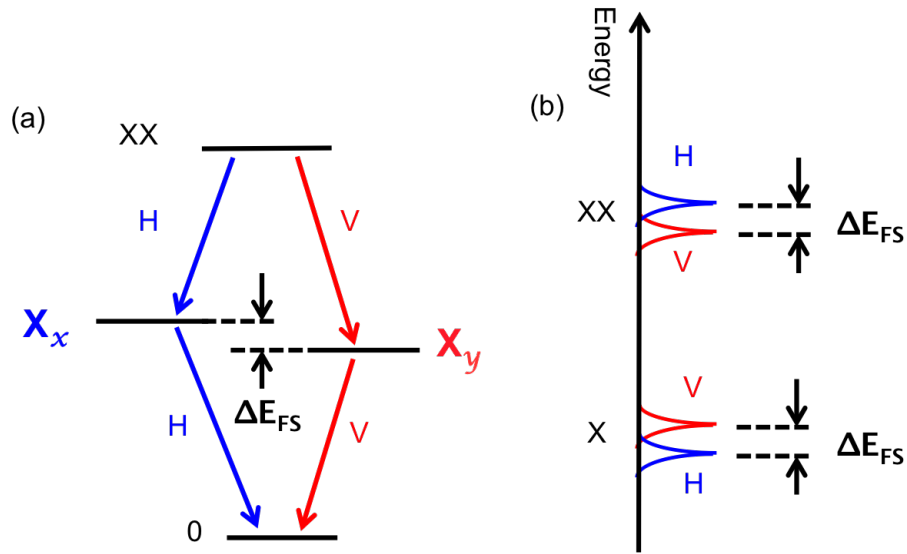


Figure 3.4 – (a) Radiative biexciton-exciton decay cascade - PL are composed of doublets with the two components linearly polarized along perpendicular directions, and has energy splitting ΔE_{FS} , which results from anisotropy in electron-hole pair exchange interaction. (b) Energy scheme showing the expected emission spectra of X and XX levels. Each spectrum contains a doublet which are split by ΔE_{FS} . H and V dipole energies in X spectrum are reversely positioned with respect to those in XX spectrum.

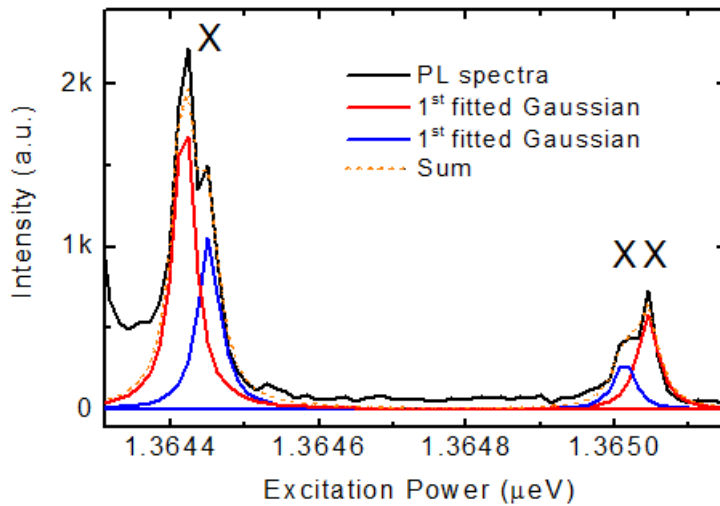


Figure 3.5 – PL spectra of X and XX lines fitted with two Gaussian functions - The FSS energy can be defined by the every difference between two fitted peaks, which is 25 eV in this case. the X and XX lines have the same splitting, which is an evidence that they are originated from the same QD

ΔE_{FS} differs from QD to QD. Taking a closer look at the PL peaks, Fig. 3.5 shows that each of X and XX lines actually contains two peaks. These peaks can be fitted with Gaussians functions as the red and blue curves. The peaks in X and XX lines both are split by the same amount $25 \mu eV$. Normally, the FSS is comparable to the inhomogeneous linewidth of the excitonic emission measured with this non-resonant excitation. The fact that an emission line contains FSS means that we can identify it to be a neutral QD, because charged QD do not exhibit FSS [64]. This is the first argument implying that this X and XX emission lines are originated from the same QD.

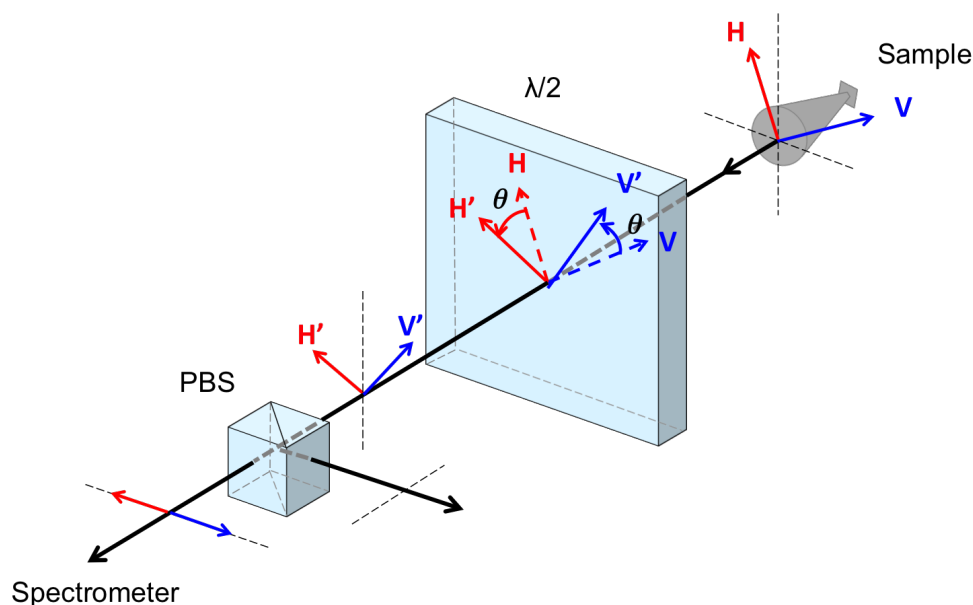


Figure 3.6 – Polarization sensitive measurement - By rotating the half-wave plate ($\lambda/2$), the two linear-polarization FSS dipoles of the QD is also rotated. The intensity detected for each dipole depends on the position of the wave plate.

The second argument is based on polarization-sensitive measurement of the PL emission. The polarizations of the emission can be rotated by putting a half-wave plate in front of the sample. It should be noted that the non-resonant wetting layer excitation is not a polarization sensitive excitation. So that rotating the polarization of an incoming laser does not affect the QD emission. Fig. 3.6 shows how the output beam propagates. The beam escaping from the top facet of the trumpet contains two orthogonal dipoles which have the polarizations H and V . These two dipoles go through the half-wave plate and their polarizations are rotated by the same angle θ (by rotating the half-wave plate an amount $\theta/2$). The two dipoles have the new polarizations H' and V' . The light then goes through the PBS, where the vertical polarized components of H' and V' will be reflected, and the horizontal polarized components will be transmitted.

Fig. 3.7 shows the PL spectra of the X and XX lines at three different angles θ : 0° ,

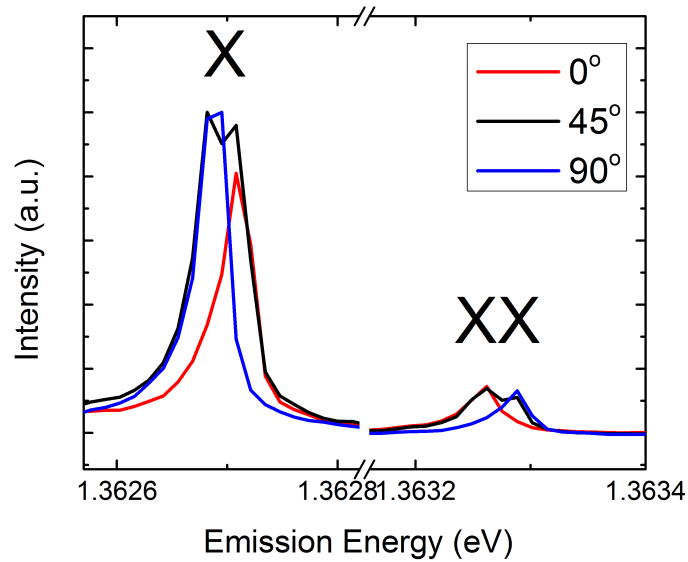


Figure 3.7 – Polarization dependence PL spectra of X and XX at different angles of the half wave plate - The PL emission is rotated in the step of 45° (by rotating the half-wave plate a step of 22.5°), three spectra correspond to three positions of the polarization dipoles emitted from the QDs, with respect to the vertical axis .

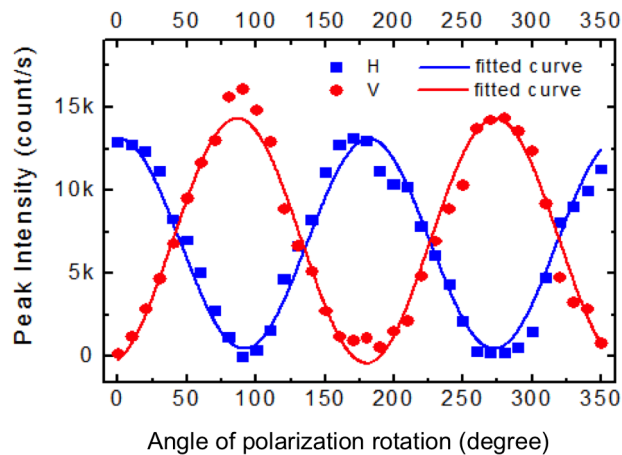


Figure 3.8 – The evolution of H and V polarization dipoles - By rotating the half-wave plate under the cross-polarized detection scheme, the PL intensity of the X line is fitted with two gaussians which represent the H and V fine-structure dipoles. The intensity of each dipole is then recorded for every position of the wave plate. The evolutions of H and V are then well fitted with sine functions.

45° and 90° (by rotating the half-wave plate by: 0°, 22.5° and 45°). It indicates clearly the mirror effect that is well demonstrated in Fig. 3.4. Fig. 3.8 shows the evolution of the intensities of the two polarization dipoles of X line when rotating the half-wave plate. The data is well fitted with sine functions. This result is the second evidence proving that the two X and XX lines under investigation are coming from the same QD. This identification process will serve as a basis to operate with a three-level system, as it will be presented in the following chapters.

The paragraphs above have focused on identifying the X and XX transitions. In general, PL spectra contain also emission lines which derive from charged exciton (X^\pm). Charged exciton can be assigned from the absence of fine-structure splitting. Fig. 3.9 shows the PL spectra for the polarization-sensitive measurement for three different positions of the half-wave plate. The splitting allows us to attribute the two emission lines at higher energy to neutral X and XX recombinations. The third line at lower energy is attributed to the charged exciton (CX). For this line, the optical asymmetry is not observed, which is a clear evidence of a charged X line.

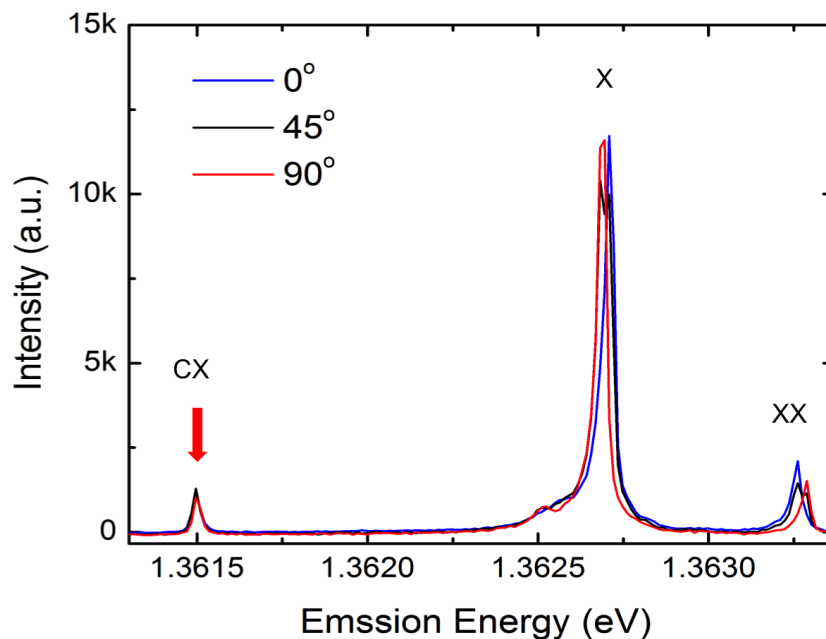


Figure 3.9 – PL spectra showing a charged exciton - A charged X is observed at 1.361 μeV . The charged X does not exhibit FSS, so when performing polarization sensitive measurement by rotating the half-wave plate, the charged X line remains unchanged.

3.2.2.2 Biexciton binding energy

Biexciton binding energy is defined as the energy difference between $2E_X$ and E_{XX} . Binding energy of XX results from the Coulomb interaction of four fermions (two electrons and two holes) localized in the confinement potential of the QD, which depends on the shape, size and strain of the QD. The Coulomb interaction of two localized excitons can be either attractive or repulsive, leading to either binding or anti-binding of the XX . For the QD that is shown in Fig. 3.2, the binding energy of -0.6 meV is obtained. Fig. 3.10(a) shows the PL spectra of the second QD (QD₂), which has a slightly higher emission energy compared to the first one (QD₁) presented above. Those two QDs are from the same trumpet. The XX binding energy for QD₂ is about -2.03 meV. Fig. 3.10(b) shows the PL spectra of the third QD (QD₃), which is embedded in another trumpet. QD₃ emits an exciton at rather low energy compared with the other two QDs. This time, the XX binding energy is positive at 2.2 meV. The fact that a QD emits at higher energy exhibits larger anti-binding energy is in good agreement with the report [102]. It was shown in [99, 102, 103] for InAs QD that depending on the recombination energy of X , the binding energy showed a linear dependence and could be vary from 1 meV to -6 meV when the X emission energy increased.

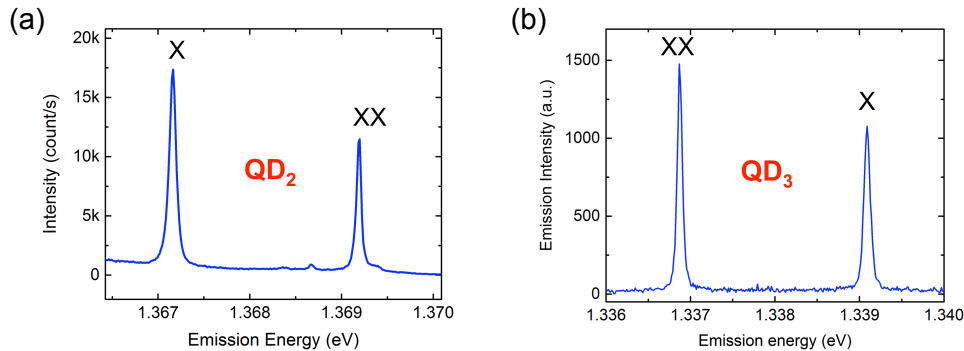


Figure 3.10 – PL spectra of other QDs - (a) PL spectra from QD₂, which emits at higher energy than QD₁ and features a larger anti-binding energy behavior. (b) PL spectra from QD₃, which emits at lower energy and features a positive binding energy.

The dependence of the XX binding energy on the emission energy of the X is plotted in Fig. 3.11, where the binding energy for a fourth QD is also taken into account. The plot indicates a wide variation of XX binding energy, including both binding and anti-binding behaviors. A clear trend is observed that the binding energy reduces with increasing the X emission energy. It was attributed in [102] that this decreasing of binding energy is due to a lower impact of correlation and exchange. That behavior relates to the size of the QD, the decreasing number of localized excited states in smaller QDs reduces the effect of exchange and correlation. Therefore decreasing QD size, the XX complex changes from

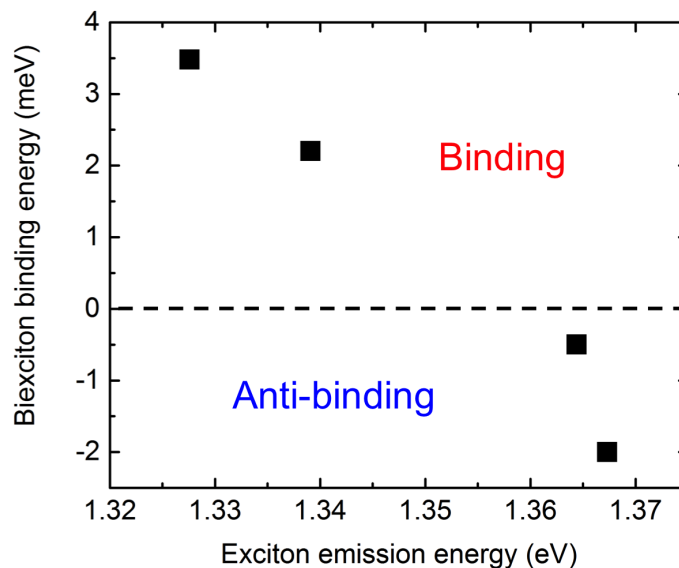


Figure 3.11 – Biexciton binding energy as a function of exciton energy - The binding energy reduces with higher X emission energy. At a certain X energy, the behavior switches from binding to anti-binding property.

binding to anti-binding.

3.2.3 Spectral drift

This section discusses the spectral drift of the PL, which is crucial in resonant spectroscopy. When performing optical spectroscopy measurements with the QD-trumpet system, unfortunately, a continuous temporal drift of the emission energy of QDs is always observed. The origin of the drift has been characterized in [95]. It was attributed to the sticking of oxygen molecules onto the trumpets, which modified the surface charge and hence the electric field seen by the QD. We observe blue-drift with all the QDs. Fig. 3.12 shows an example of the evolution of the PL spectra when we keep exciting the PW with times. Four PL lines are shown at different times.

A QD blue-drift depends on the QD distance from the surface. This can be used to identify a pair of X and XX from the same QD, because if the X and XX lines are from the same QD, they will drift with the same speed. Fig. 3.13 plots the energy drift for 4 different PL lines as a function of time. We can clearly identify two pairs of X and XX from two distinct QDs. The X and XX lines from the same QD drift at exactly the same speed. Hence, before analyzing in details the PL spectra of a QD, we can have a quick impression of the X and XX lines coming from the same QD just by checking the spectral drift.

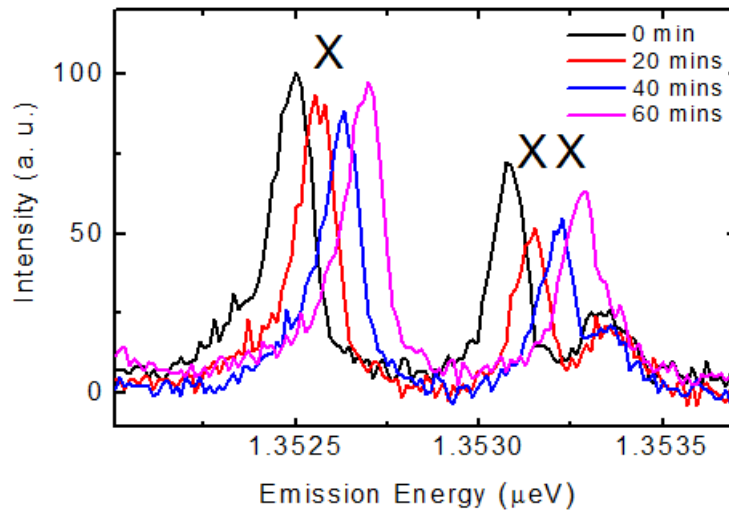


Figure 3.12 – PL spectra of a pair of X and XX lines taken at different time scales - the PW is excited continuously at the same power to see the stability of the spectrum. Both lines shift with the same speed and same direction toward higher energy region.

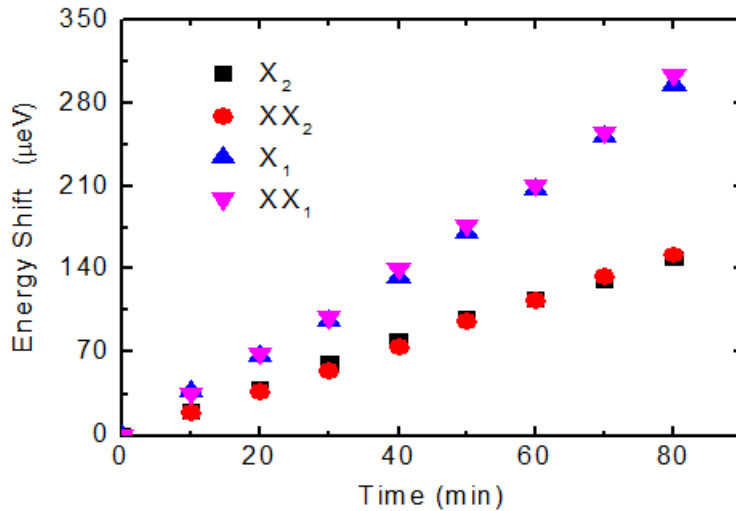


Figure 3.13 – The emission energy drift as a function of time for two pairs of X and XX from two different QDs - The X and XX from the same QD drift at exactly the same speed. One can take advantage of this in identifying the pair of X and XX transitions generated from one single QD.

It is very challenging to suppress this temporal drift problem, a treatment of the trumpet surface has been done in [95] by passivating the sidewall of the PW with a 20 nm thick Si_3N_4 layer. But unfortunately, it could not entirely suppress the drift and the

emission lines still shift during the measurement. The blue drift of the emission makes it much more difficult in performing the high precision resonant spectroscopy. In this study, we propose an alternative approach that may help to counteract the blue-drift, by introducing a very intense laser, with much lower energy than the band gap of the wetting layer. More details of this approach will be presented in appendix C.

3.2.4 Time-resolved photoluminescence measurement

3.2.4.1 Experimental setup

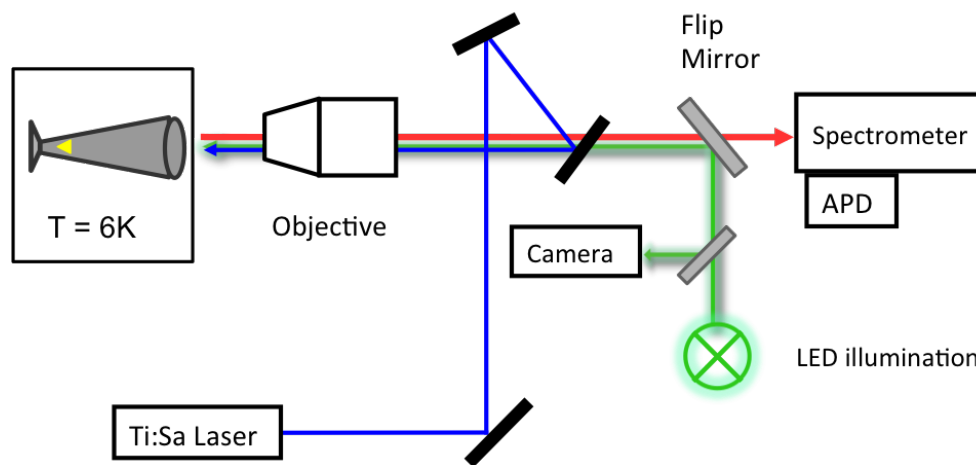


Figure 3.14 – Time-resolved PL experimental setup - the QD is excited by a pulsed Ti:Sa laser, the emission from the QD is then sent to the spectrometer and collected by a single-photon photon counting module

To study the lifetime of a QD inside the waveguide, we perform a time-resolved fluorescence measurement. The set up is described in Fig 3.14. The experiment is carried out at 6K. We use a pulsed source, which is a Tsunami titanium-Sapphire (Ti:Sa) laser (by Spectraphysics). The laser can operate in the wavelength range between 650nm ~980nm. The pump energy is supplied by a CW solid-state Millennia YAG laser, emitting at 532 nm. The pulsed duration is 1 ps and repetition rate is 80 MHz. The wavelength of the laser is tuned to be at 825 nm. The signal emitted from the QD is sent to the spectrometer (HORIBA iHR550). The light filtered by the spectrometer is then detected by an avalanche photodiode (APD) id100-50 (from idquantique). This APD has an active area diameter of 50 μm . It offers timing resolution of 55 ps, the dark count rate is $<200 \text{ s}^{-1}$. Afterward, the output pulse of the APD detector is sent to time to amplitude time-correlated single photon counting (TCSPC) module SPC-630 from Becker Hickl. This module has a time resolution of 8 ps.

3.2.4.2 Time-resolved photoluminescence spectroscopy

The measurement of X decay time is performed at very low power. The power used is at the level of 1% the non-resonant saturation power for the X transition, so that the population of the XX can be neglected. Fig.3.15 shows the results of the lifetime for X and XX . The results can be well-fitted with a single exponential decay function

$$I(t) = A \exp\left(-\frac{t}{\tau}\right) \quad (3.9)$$

where $I(t)$ is the PL intensity as a function of time t . A is the intensity for $t = 0$, and τ is the recombination lifetime. The exponential model results in a lifetime $\tau_X \approx 1.36$ ns for the exciton and $\tau_{XX} \approx 0.72$ ns for the biexciton. The mono-exponential behavior suggests that the obtained values correspond to the radiative lifetimes, and the non-radiative process can be negligible. The XX level decays roughly twice as fast as X ($\tau_X \approx 2\tau_{XX}$) since it has twice the number of radiative decay channels to the two bright states of the X . In the simplest picture, one should have $\tau_X = 2\tau_{XX}$. However because of the Coulomb interaction of the XX level, the ratio between the lifetimes of X and XX also depends on the confinement. The ratio τ_X/τ_{XX} also depends on the spin structure, the conversion of dark X to bright X via spin flip process contributes to the decay dynamic of the X lines [100, 101, 104]. In addition, it was shown in [105] that the ratio τ_X/τ_{XX} depends on the size of the QD, for example for the InGaAs/GaAs QDs, the ratio varies from approximately 2 down to 1.5, increasing the dot size reduces the recombination ratio.

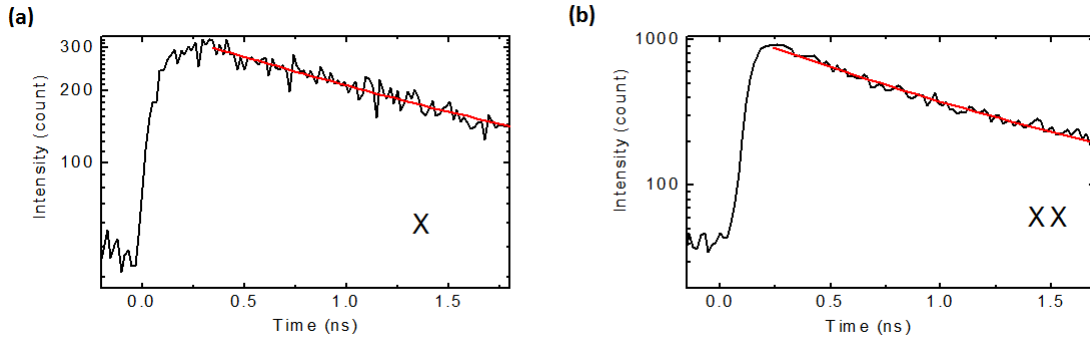


Figure 3.15 – Time-resolved PL spectra - (a) Time-resolved PL spectra of X line, which show the life time is 1.36 ns. (b) Time-resolved PL spectra of XX line, the life time of XX is 0.72 ns

The lifetime of the InAs/GaAs QD embedded inside a PW is comparable to the one obtained in bulk InAs/GaAs QD, where our colleagues (J. Claudon, J-M. Gérard from CEA/INAC) measured mean decay times for X and XX of 1.22 ± 0.25 ns and 0.76 ± 0.12 ns, respectively [106], the mean value of τ_X/τ_{XX} was reported to be 1.7. In the particular QD that is studying in this thesis, the ratio τ_X/τ_{XX} is found to be 1.89. The information of

X and XX lifetimes for a particular QD is important, because from that we can estimate the power of one photon per emitter lifetime, which is important in the next chapters.

3.3 Chapter summary

This chapter presented the basic characterizations of PL spectroscopy of self-assembled InAs QDs embedded in a GaAs conical shape PW. A detailed description of experimental configuration and optical elements was presented. Non-resonant PL measurements were performed. Power dependence analysis, polarization dependence PL measurement have been taken into account to help identify the neutral X and XX transitions of the same QD. The identification of X and XX lines paves a way to further investigations of the interesting optical effects based on a QD three-level one-dimensional system in the following chapters. The time-resolved PL measurement was also performed to study the life-time of the neutral X and XX in a single QD embedded in a PW. This chapter also briefly presented the temporal spectral drift of the emission energy of the QDs, which turned out to be a mean to quickly identify a pair of X and XX from the same QD.

Chapter 4

Single-mode giant non-linearity

This chapter will present a detailed model and experimental results of single-mode giant-nonlinearity. Chapter 3 has shown the use of photoluminescence (PL) spectroscopy to characterize optically active QDs. This chapter will address a study of resonant excitation and laser spectroscopy. Laser spectroscopy provides a sub- μeV resolution and therefore leads to the possibility to access the true lineshape of a transition. The chapter will begin with presenting a theoretical model of the interaction between a coherent driving field and an atom placed inside a one-dimensional waveguide. The model also includes the imperfection factors that could appear in the experiment. The chapter then continues with a presentation of resonant excitation experimental setup, including the establishment of cross-polarized detection to subtract the unwanted back-scattered laser background. The last sections will show the experimental results which will lead to the realization of a single-mode non-linearity at ultra-low power level.

Contents

4.1	Giant non-linearity of a one-dimensional atom	50
4.1.1	Introduction	50
4.1.2	Bloch equation of a coherent field interacting with a one-dimensional atom	51
4.2	Resonant excitation spectroscopy	60
4.2.1	Experimental setup	61
4.2.2	Cross-polarized detection	62
4.2.3	Resonant excitation spectroscopy	70
4.3	Ultra-low power single-mode giant non-linearity	76
4.3.1	A quantitative evaluation of all experimental parameters	76
4.3.2	Single-mode giant non-linearity	80
4.4	Chapter summary	84

4.1 Giant non-linearity of a one-dimensional atom

4.1.1 Introduction

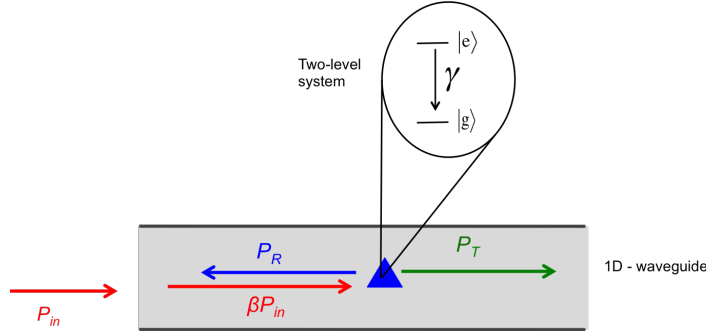


Figure 4.1 – Scheme of a one-dimensional atom interacts with an electromagnetic field - A laser field comes from one output of the one-dimensional waveguide. The field enters the waveguide and has β the chance of interacting with the quantum emitter. The non-linearity is characterized by the mean of a reflectivity measurement. The intensity of the reflected field P_R (emission of the two-level system propagating in the backward direction) is recorded. The reflectivity $R = P_R/P_{in}$ as a function of the incoming laser field power is expected to exhibit a non-linear behavior due to the saturation of the two-level system.

The optical behavior of a one-dimensional atom for arbitrary intensities of the incoming field has been theoretically discussed in the work of A. Auffèves et al. [25], based on the coupling of a two-level system quantum emitter with a one-dimensional continuum, mediated by a cavity. The giant non-linearity signature is based on the simplest non-linear effect, related to the saturation of a single two-level system excited by an incident coherent laser field that is on, or close to, resonance with the two-level transition. The system under consideration is depicted in Fig. 4.1 with an atom placed inside an optical one-dimensional waveguide. The transmission property of the driving field is governed by the two-level system depending on the incoming field power. At a power well below saturation, the quantum emitter features coherent scattering. Like a classical dipole, the two-level system oscillates at the incident laser frequency and radiates at the same wavelength with a well defined phase shift. In this regime, the light radiated by the emitter in the waveguide interferes with the incident field. This leads to a destructive interference in the field direction and cancel out the transmission. Therefore, at ultra-low excitation power lower than saturation, the driving field is entirely reflected. The non-linearity happens when increasing the incident laser power, the two-level system will be saturated at the power level of one photon per unit lifetime of the emitter, leading to a non-vanishing transmitted intensity. Increasing further the power, the laser field is entirely transmitted.

For an ideal one-dimensional system, the waveguide features a perfect coupling, which means every photon sent from the excitation source will enter, propagate through the

waveguide and finally interact with the two-level system with an optimum coupling efficiency. At the same time, every photon emitted is successfully coupled to the mode and collected at the output of the waveguide. However, reaching a perfect 100% efficiency is very challenging and the waveguide normally features imperfection. The light-matter coupling efficiency inside a waveguide is denoted as the factor β ,

$$\beta = \frac{\textit{spontaneous emission rate coupled to the waveguide mode}}{\textit{Total spontaneous emission rate}} \quad (4.1)$$

β indicates the quality of the one-dimensional waveguide. A perfect waveguide features $\beta = 1$. It should be noted here that in principle, one has to take into account also the mode-matching (the rate that an incoming photon could enter the waveguide) and the output-collection efficiency (the rate that a photon escaping the waveguide is successfully collected) (see section 2.2.4 for details). For simplicity, we consider these two factors ideal so that $\varepsilon_{in} = \varepsilon_{out} = \beta$.

4.1.2 Bloch equation of a coherent field interacting with a one-dimensional atom

In this section, we will derive Bloch equations for the interaction of a coherent input field and a two-level atom placed inside an optical waveguide. The input field is in a coherent state $|\alpha_L\rangle$ and has a frequency ω_L . The input power is $P_{in}=|\alpha|^2$ and is a unitless number representing the incoming photons per unit lifetime of the two-level system, we have $P_{in}=|\alpha|^2$.

The transition frequency between the ground state $|g\rangle$ and the excited state $|e\rangle$ is denoted as ω_0 . The coherent incoming field interacts and drives the atomic evolution via optical Bloch equations [107]. The time evolutions of the atomic operators are,

$$\langle \dot{S}_- \rangle = i\delta_L \langle S_- \rangle - \frac{\gamma + \gamma^*}{2} \langle S_- \rangle + \Omega \langle S_z \rangle, \quad (4.2)$$

$$\langle \dot{S}_z \rangle = -\gamma(\langle S_z \rangle + \frac{1}{2}) - \Omega \Re[\langle S_- \rangle],$$

Where $\langle S_- \rangle$ and $\langle S_z \rangle$ are expectation values of the atomic operators $S_- = e^{i\omega_L t} |g\rangle \langle e|$ and $S_z = \frac{1}{2}(|e\rangle \langle e| - |g\rangle \langle g|)$, respectively, δ_L is the detuning between the QD resonance and the laser field ($\delta_L = \omega_L - \omega_0 \ll \omega_0$), γ is the radiative-decay rate due to spontaneous emission of the two-level system, γ^* is the pure dephasing rate and Ω is the Rabi frequency of the excitation field inside the guided mode,

$$\Omega = \gamma \sqrt{\beta P_{in}}$$

Pure dephasing arises from fast fluctuations of the medium that cause rapid vibrations

of energy levels in a time scale faster than the recombination time of the emitter. Therefore this fluctuation is homogeneous and pure dephasing rate γ^* can appear in Bloch equations of the field-atom interaction.

In steady-state regime, where $\langle \dot{S}_- \rangle = \langle \dot{S}_z \rangle = 0$, we obtain a stationary solution for the population of the two-level system,

$$\langle S_- \rangle = - \left(\frac{\Omega}{(\gamma + \gamma^*) - 2i\delta_L} \right) \left(\frac{1}{1+x} \right) \quad (4.3)$$

$$\langle S_z \rangle + \frac{1}{2} = \frac{1}{2} \left(\frac{x}{1+x} \right)$$

where the saturation parameter x is defined as,

$$x = \left(\frac{\Omega^2/2}{(\frac{\gamma+\gamma^*}{2})^2 + (\delta_L)^2} \right) \left(\frac{\gamma + \gamma^*}{\gamma} \right), \quad (4.4)$$

Parameter x can be rewritten as,

$$x = 2P_{in}\beta \frac{1 + \gamma^*/\gamma}{(1 + \gamma^*/\gamma)^2 + (2\delta_L/\gamma)^2}, \quad (4.5)$$

4.1.2.1 Evolution of the fields and the interference between incoming and scattering fields

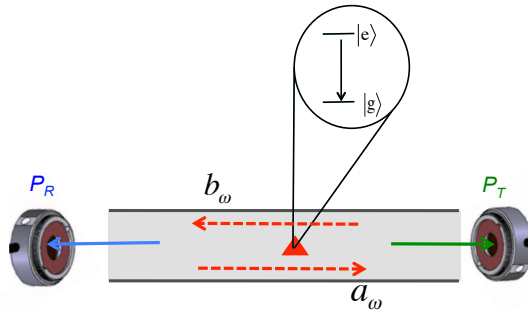


Figure 4.2 – Scheme of field propagations inside a one-dimensional waveguide - Considering a_ω and b_ω are the forward and backward propagating modes, respectively. Two detectors are placed at two outputs of the waveguide to measure the reflected (P_R) and transmitted (P_T) powers.

The non-linearity of a one-dimensional atom is realized based on the transmissivity or reflectivity of the field inside the waveguide. As described in Fig. 4.2, the driving laser field is assumed to propagate in the mode a_ω . The evolution of the quantized electric field in one-dimensional geometry in the Heisenberg picture is written as [108]

$$E(z, t) = E^{(+)}(z, t) + E^{(-)}(z, t) \quad (4.6)$$

where $E^{(-)}(z, t) = (E^{(+)}(z, t))^\dagger$ and

$$E^{(+)}(z, t) = i \sum_{\omega} \epsilon_{\omega} \left[a_{\omega}(t) e^{ikz} + b_{\omega}(t) e^{-ikz} \right] \quad (4.7)$$

Parameter ϵ_{ω} is the electric field per photon. The full electric field is a linear combination between the free and emitted fields, which is established as,

$$E^{(+)}(z, t) = E_{a,free}(z, t) + E_{b,free}(z, t) + \eta \{ S_{-}(t - z/c) \Theta(z) + S_{-}(t + z/c) \Theta(-z) \} \quad (4.8)$$

Where $\Theta(n)$ is the Heaviside step function indicating that, for a propagation in the mode a_{ω} , only the detection at $z > 0$ contains information about the atomic emitted field and analogously, detector at $z < 0$ can only measure the signal from an emitted field propagating in the opposite mode b_{ω} . Parameter η is the proportionality coefficient of the field, which depends on the atom-waveguide coupling factor β as,

$$\eta = i \epsilon_{\omega_L} \sqrt{\beta} \quad (4.9)$$

The reflected field $E_R(z, t)$ and transmitted field $E_T(z, t)$ correspond to the quantum operator,

$$E_R(z, t) \equiv E_{b,free}(z, t) + \eta [S_{-}(t + z/c) \Theta(-z)] \quad (4.10)$$

$$E_T(z, t) \equiv E_{a,free}(z, t) + \eta [S_{-}(t - z/c) \Theta(z)] \quad (4.11)$$

Since the laser is excited from left to right as in Fig. 4.2, we have $E_{b,free}(z, t) = 0$. One could see that the transmitted field in Eq. 4.11 features an interference between the incoming field and the radiated field from the two-level emitter. This interference is destructive and therefore induces a zero transmission, as will be shown in the following equations.

The power of the incoming field is [109],

$$P_{in} = \frac{\langle E_{a,free}^\dagger(z, t) E_{a,free}(z, t) \rangle}{\epsilon_{\omega_L}^2} = \frac{\varepsilon_{in}^{a*}(z, t) \varepsilon_{in}^a(z, t)}{\epsilon_{\omega_L}^2} = \alpha_L^2 \quad (4.12)$$

The reflection and transmission powers can be written as followings,

$$P_R = \frac{\langle E_R^\dagger(z, t) E_R(z, t) \rangle}{\epsilon_{\omega_L}^2} \quad (4.13)$$

$$P_T = \frac{\langle E_T^\dagger(z, t) E_T(z, t) \rangle}{\epsilon_{\omega_L}^2}$$

The reflection and transmission powers in the unit of photon per lifetime can be expressed as,

$$P_R = \frac{\eta^2 \langle S_- \rangle^2}{\epsilon_{\omega_L}^2} \quad (4.14)$$

$$P_T = P_{in} + \frac{2\alpha_L \epsilon_{\omega_L}(z, t) \eta \langle S_- \rangle}{\epsilon_{\omega_L}^2} + \frac{\eta^2 \langle S_- \rangle^2}{\epsilon_{\omega_L}^2}$$

We then have,

$$P_R = \beta \left(\langle S_z \rangle + \frac{1}{2} \right) \quad (4.15)$$

$$P_T = P_{in} + \frac{\Omega}{\gamma} \Re[\langle S_- \rangle] + \beta \left(\langle S_z \rangle + \frac{1}{2} \right)$$

Eqs. 4.15 show that both reflection and transmission channels carry the spontaneous emission. The transmission contains the incoming power P_{in} and the term $\frac{\Omega}{\gamma} \Re[\langle S_- \rangle]$ is the interference term between the atom and the driving field. This interference term plays a key role in this one-dimensional geometry.

From Eqs. 4.3, we have,

$$P_R = \frac{\beta}{2} \frac{x}{1+x} = \frac{\beta}{2} \left(1 - \frac{1}{1+x} \right) \quad (4.16)$$

$$P_T = P_{in} - \frac{1}{2} \frac{x}{1+x} + \frac{\beta}{2} \frac{x}{1+x} = P_{in} - P_R \left(\frac{1}{\beta} - 1 \right)$$

The reflected and transmitted powers P_R and P_T can be expressed as a function of incoming power P_{in} as,

$$P_R = \beta^2 \left(\frac{\gamma}{\gamma + \gamma^*} \right) \left(\frac{P_{in}}{1 + 2P_{in}\beta \frac{(\gamma + \gamma^*)/\gamma}{(\frac{\gamma + \gamma^*}{2})^2 + \delta_L^2}} \right) \quad (4.17)$$

$$P_T = P_{in} - P_R \left(\frac{1}{\beta} - 1 \right)$$

Finally, the transmission and reflection coefficients R and T have the the form [109],

$$R = \frac{P_R}{P_{in}} = \beta^2 \left(\frac{\gamma}{\gamma + \gamma^*} \right) \left(\frac{1}{1 + 2P_{in}\beta \frac{(\gamma + \gamma^*)/\gamma}{\left(\frac{\gamma + \gamma^*}{2}\right)^2 + (\delta_L^2)}} \right) \quad (4.18)$$

$$T = \frac{P_T}{P_{in}} = 1 - R \left(\frac{1}{\beta} - 1 \right)$$

At resonance when $\delta_L = 0$, R and T can be expressed as functions of the incoming field power,

$$R = \beta^2 \left(\frac{\gamma}{\gamma + \gamma^*} \right) \left(\frac{1}{1 + \beta \frac{\gamma}{\gamma + \gamma^*} 2P_{in}} \right) \quad (4.19)$$

$$T = (1 - \beta)^2 \left(\frac{\gamma}{\gamma + \gamma^*} \right) \left(\frac{1}{1 + \beta \frac{\gamma}{\gamma + \gamma^*} 2P_{in}} \right) + \frac{\frac{\gamma^*}{\gamma + \gamma^*} + \beta \frac{\gamma}{\gamma + \gamma^*} 2P_{in}}{1 + \beta \frac{\gamma}{\gamma + \gamma^*} 2P_{in}}$$

For an ideal system with $\beta = 1$ and $\gamma^* = 0$, Eqs. 4.19 are simplified as

$$R = \frac{1}{1 + 2P_{in}} \quad (4.20)$$

$$T = \frac{2P_{in}}{1 + 2P_{in}}$$

Fig. 4.3(a) plots the reflection coefficient (reflectivity) R and transmission coefficient (transmissivity) T as a function of excitation laser detuning in the unit of δ_L/γ in the case of a perfect waveguide. A perfect reflection obtained at low-excitation regime is because the fluorescence field emitted by the two-level system is phase shifted by an amount of π with respect to the driving field. This phenomena was pointed out in [25, 109–111]. The π phase shift induces a destructive interference between the driving field and the field emitted by the atom. This destructive interference results in a perfect reflection at very low driving power ($P_{in} \ll 1$ for an ideal system).

Fig. 4.3(b) plots the dependences of R and T as functions of excitation power P_{in} . At very low excitation power, the scattering fluorescence field interferes with the driving field in a purely coherent process, the field is therefore entirely reflected. Increasing further the power, the emitter becomes saturated and therefore induces a non-linearity. The non-linearity occurs at the power $P_{in} \simeq 1$. An experimental realization of this single-mode giant non-linearity behavior in reflectivity is the aim of this chapter, which will be presented in the following sections.

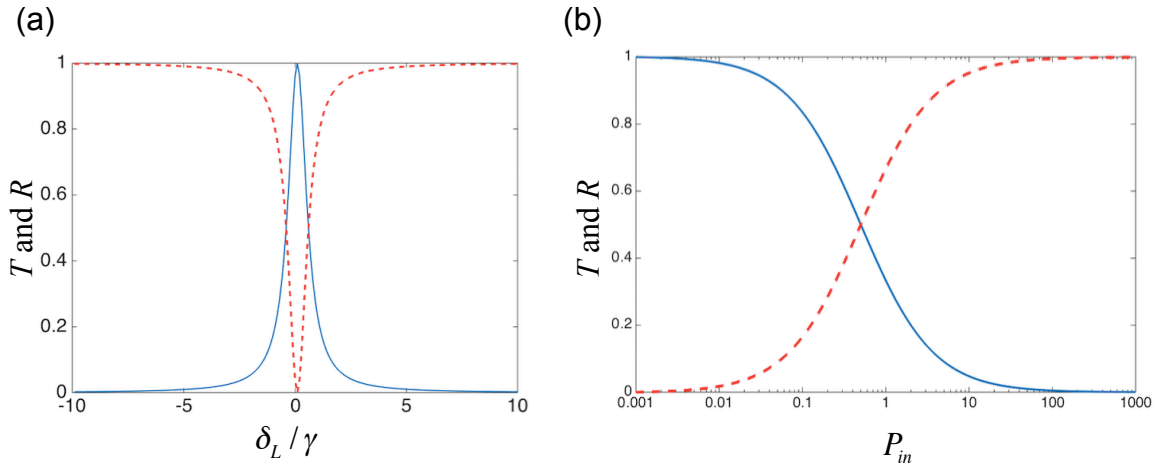


Figure 4.3 – (a) Reflection (blue curve) and transmission (red dots) coefficients for a vanishing power of the incoming field ($P_{in} \ll 1$) as a function of the field frequency detuning around resonance. (b) Reflection (blue curve) and transmission (red dots) coefficients as a function of incoming power P_{in} .

4.1.2.2 Impact of β factor and spectral broadening on the reflectivity of the one-dimensional two-level system

Eq. 4.18 shows the influences of the factors β and pure dephasing γ^* on the reflectivity of the system. At low excitation power $P_{in} \ll 1$, the reflectivity as a function of the laser frequency will have a Lorentzian distribution as,

$$R = \beta^2 \left(\frac{\gamma}{\gamma + \gamma^*} \right) \left(\frac{1}{1 + \frac{2\delta_L^2}{(\gamma + \gamma^*)^2}} \right) \quad (4.21)$$

One can see that a waveguide with a coupling factor β results in a change by β^2 in reflection compared with an ideal case. Regarding the pure dephasing rate γ^* , without pure dephasing, the emission linewidth of an ideal two-level system is broadened just by the radiative decay rate γ . The presence of pure dephasing leads to the decreasing of the resonant fluorescence by a factor of $\gamma/(\gamma + \gamma^*)$.

4.1.2.3 Effect of spectral diffusion

We have seen in the last section that the reflection lineshape is dynamically broadened by radiative lifetime and pure dephasing of the two-level system. This homogeneous lineshape is characterized by a Lorentzian profile. In practice, the resonant frequency of the emitter also suffers from fluctuations of the surrounding environment, which causes static random jumps and fluctuations of the resonant frequency. Such phenomenon is called spectral

diffusion or spectral wandering [112–114]. The fluctuation rate is in the nanosecond time scale (normally more than 10 ns, which is higher than the radiative lifetime of the two-level emitter). This rate is much shorter than the detection time of the usual CCD devices (which normally have the time resolution in the range of more than a few milliseconds). Thus, spectral diffusion results in an inhomogeneous broadening of the resonant excitation spectra.

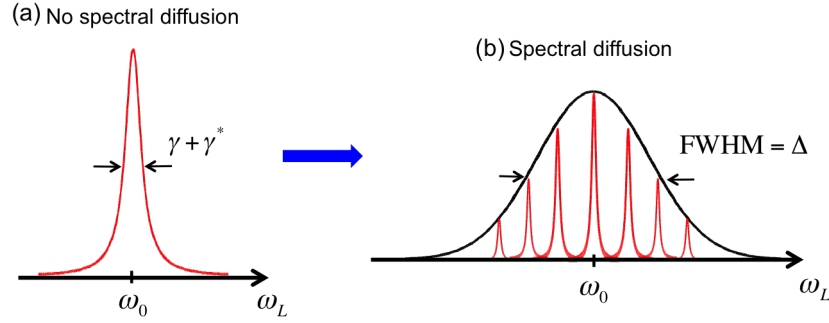


Figure 4.4 – Illustration of the emission linewidth of a quantum emitter as the presence of spectral diffusion - (a) Without spectral diffusion, the radiative-limit linewidth and pure dephasing features a homogeneous broadening, the spectrum is characterized by a Lorentzian shape. (b) Spectral diffusion: due to fluctuation of the environment surrounding the emitter, the original spectral fluctuates with the rate higher than the emission rate but much shorter than the detection limit of the CCD devices. Spectra diffusion induces an inhomogeneous broadening with a Gaussian shape.

It has been shown that such an inhomogeneous broadening features a Gaussian shape [113,115]. Fig. 4.4 illustrates the configuration taking into account the presence of spectral diffusion. Fig. 4.4(a) shows a reflection lineshape when there is no spectral diffusion. The line is dynamically broadened by rapid variations in the amplitude, phase, or orientation of the dipoles. Pure dephasing and lifetime contribute to that homogeneous broadening. When there appears fluctuations in the atomic frequency ω_0 on a time scale larger than the atomic lifetime, the line features a Gaussian broadening, as shown in Fig. 4.4(b). Due to spectral diffusion, the quantum emitter has different instantaneous frequencies $\omega_i(t)$, which evolves in time. The width Δ of the line represents the distribution of frequencies. The dependence of reflectivity on spectral diffusion can be expressed as,

$$R \propto \frac{1}{\sigma} e^{-\frac{\omega_L^2}{2\sigma^2}} \quad (4.22)$$

where parameter σ is the standard deviation of the distribution and is related to the full width at half maximum (FWHM) Δ by $\Delta = 2\sqrt{2\ln 2}\sigma$.

Spectral diffusion is an important issue in spectroscopy, because the observed spectral broadening prevents an access to the intrinsic line properties of the quantum emitter. Spectral diffusion can be measured based on photon correlations technique to access the

very short static time of the homogenous line. [112, 114, 116]. In resonant excitation spectroscopy, reducing the environment fluctuation effect is an important condition to be able to obtain a narrow lineshape. This issue will be discussed in the following experimental sections.

4.1.2.4 Coherent and incoherent scatterings of a two-level atom

This section aims at characterizing analytically the contribution of coherent and incoherent parts of the emission of a two level atom. The total intensity of the light scattered by the atom can be written as [107]

$$\langle I(t) \rangle = \eta^2 \langle S_+(t - (z/c)) \rangle \langle S_-(t - (z/c)) \rangle = \eta^2 \sigma_{gg}(t - (z/c)) \quad (4.23)$$

Dipole S_{\pm} can be written as a sum of the average dipole and the instantaneous difference of S_{\pm} from its average value $\langle S_{\pm} \rangle$ [107]

$$S_{\pm}(t - (z/c)) = \langle S_{\pm}(t - (z/c)) \rangle + \delta S_{\pm}(t - (z/c)) \quad (4.24)$$

In the steady-state regime, from the above equations, we have

$$\langle I \rangle = \eta^2 \langle S_+ \rangle \langle S_- \rangle + \eta^2 \langle \delta S_+ \delta S_- \rangle \quad (4.25)$$

The first term of Eq. 4.25 describes the contribution to $\langle I(t) \rangle$ of the mean dipole which represents the coherent part $\langle I_{coh} \rangle$. The radiation of the average dipole $\langle S_{\pm} \rangle$ is a radiation of a classical oscillating dipole with a phase that is well defined relative to the incident laser field. The light radiated by $\langle S_{\pm} \rangle$ can then interfere with the incident field, which is associated with a coherent scattering process. The second term corresponds to fluctuations of the dipole. Component δS_{\pm} radiates a field which does not have a well defined phase relative to the incident field because it comes from the fluctuating part of the atomic dipole and is related to spontaneous emission. This process is called incoherent scattering $\langle I_{incoh} \rangle$.

To see how the contributions of the coherent and incoherent scatterings depend on the incoming field, Bloch Eqs. 4.2 can be expressed in forms of three components of the ‘‘Bloch vector’’,

$$\begin{aligned} u &= \frac{1}{2}(S_+ + S_-) = \frac{1}{2}(\hat{\sigma}_{ge} + \hat{\sigma}_{eg}) \\ v &= \frac{1}{2i}(S_+ - S_-) = \frac{1}{2}(\hat{\sigma}_{ge} - \hat{\sigma}_{eg}) \\ w &= \frac{1}{2}(\hat{\sigma}_{ee} - \hat{\sigma}_{gg}) \end{aligned} \quad (4.26)$$

We then have,

$$\dot{u} = \delta_L v - \frac{\gamma + \gamma^*}{2} u \quad (4.27)$$

$$\dot{v} = -\delta_L u - \Omega w - \frac{\gamma + \gamma^*}{2} v$$

$$\dot{w} = \Omega v - \gamma w - \frac{\gamma}{2}$$

The steady-state solution for the Bloch Eqs. 4.27 is [107],

$$u_{st} = \frac{\delta_L}{\Omega} \frac{x}{x+1} \quad (4.28)$$

$$v_{st} = \frac{\gamma + \gamma^*}{2\Omega} \frac{x}{x+1} \quad (4.29)$$

$$w_{st} + \frac{1}{2} = \sigma_{ee}^{st} = \frac{1}{2} \frac{x}{x+1} \quad (4.30)$$

where x is the saturation parameter which was defined in Eq. 4.4. Eq. 4.30 gives information about the population of the excited state. At low intensity, the population increases linearly with x (or quadratically with the Rabi frequency Ω). Increasing x further, the population tends to reach a limit value equal to $\frac{1}{2}$ when Ω tends to infinity. Thus, a very strong excitation power results in the equalization of the populations of ground and excited states.

We then have,

$$\frac{1}{\eta^2} \langle I_{coh} \rangle = |\langle S_- \rangle|^2 = |u_{st} - i v_{st}|^2 \quad (4.31)$$

$$\frac{1}{\eta^2} \langle I_{incoh} \rangle = \langle S_+ S_- \rangle - |\langle S_- \rangle|^2$$

Finally, from Eqs.4.26, 4.25, we have the expressions for coherent and incoherent scatterings,

$$\frac{1}{\eta^2} \langle I_{coh} \rangle = \frac{1}{2} \frac{\gamma}{\gamma + \gamma^*} \frac{x}{(1+x)^2} \quad (4.32)$$

$$\frac{1}{\eta^2} \langle I_{incoh} \rangle = \frac{1}{2} \frac{x^2}{(1+x)^2} + \frac{1}{2} \frac{\gamma^*}{\gamma + \gamma^*} \frac{x}{(1+x)^2} \quad (4.33)$$

Fig. 4.5 shows the contributions of coherence and incoherence on the total scattering rate of a two-level atom, as a function of the saturation parameter x . The incident laser

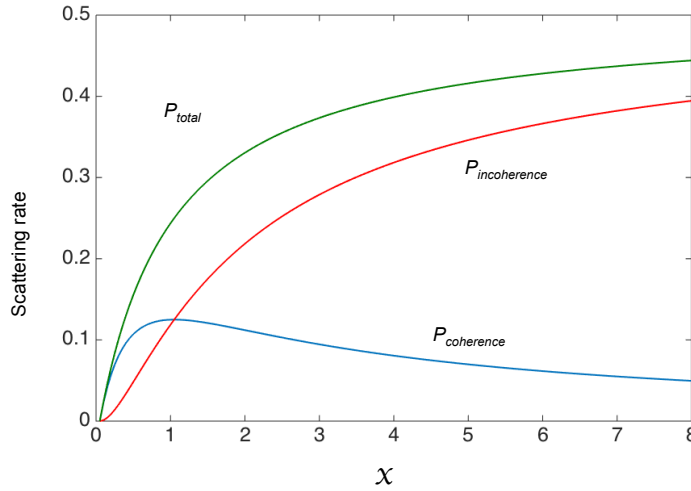


Figure 4.5 – Coherent and incoherent scattering contributions in total scattering rate as a function of saturation parameter x - The system is considered as a perfect system with $\beta = 1$ and $\gamma^* = 0$. The coherence is dominant at the power much less than saturation ($x = 1$).

intensity P_{in} is proportional to x . For a low laser power ($x \ll 1$), coherence scattering is dominant because the incoherence part is proportional to x^2 and can be neglected when $x \ll 1$. Thus, the total scattering is proportional to x . By contrast, for a high laser power ($x \gg 1$), P_{coh} tends to zero as a consequence of the two-level saturation. Thus, incoherent scattering dominates the total scattering and becomes almost independent of P_{in} .

For a non-ideal system, equations 4.31 and 4.33 indicates that at low-excitation regime, coherent scattering $\langle I_{coh} \rangle$ is proportional to $\gamma/(\gamma + \gamma^*)$ and incoherent scattering $\langle I_{incoh} \rangle$ is proportional to $\gamma^*/(\gamma + \gamma^*)$. Therefore, with the presence of a large pure dephasing ($\gamma^* > \gamma$), the coherent scattering rate is reduced drastically. The impact of these decoherence sources will be shown and discussed in more details in the following sections.

4.2 Resonant excitation spectroscopy

To have access to the giant non-linearity, one has to obtain the resonant reflection response of a two-level system. Therefore, the first step is performing resonant fluorescence measurement. Resonant fluorescence experiment consists of a two-level quantum emitter initially prepared in the ground state that is driven by an electromagnetic field. Resonance excitation spectra has been observed firstly for atom [117], then with dye molecules [118], superconducting macroscopic two-level system [119]. During the last ten years, resonant fluorescence of a single semiconductor QD has been intensively studied [120–127]. This chapter does not aim at characterizing in detail the resonance spectra. The main goal is to collect efficiently the resonant reflectivity in order to realize the giant non-linearity at

(such as wave plates, objective, beam splitters, ...). This unwanted laser background may cover up the resonant signal emitted by the QDs. Therefore, it is highly important to suppress as much as possible that back-scattered laser background on the resonant excitation spectra. This problem can be overcome by using a polarizing beam-splitter (PBS) to form a cross-polarized detection scheme, together with spatial filtering (by using a pin hole) to select only the light emitted from the QD to reach the spectrometer.

4.2.2 Cross-polarized detection

The principle of the laser rejection process is based on an orthogonal excitation/collection polarization. In this configuration, the PBS defines a linear vertical polarization for excitation and a linear horizontal polarization for detection. Therefore, the back-reflected laser signal on top of the trumpet is perpendicularly reflected by the PBS and is filtered out from the path to the spectrometer. To optimize the rejection rate, two linear film polarizers are placed at the input and output of the PBS (see Fig. 4.7). A polarizer is an optical filter that passes light of a specific polarization and blocks light of other polarizations. Two polarizers are mounted on high-precision rotation mounts PRM1/M from Thorlabs. This rotation mount is functioned with a locking screw, which engages micrometer for fine adjustment. When locked, the micrometer provides $\pm 7^\circ$ of rotation at the accuracy approximately 2.4 arcmin (0.04°) per micrometer division.

Fig. 4.7(a) describes the input configuration. The first polarizer placed before the input of the PBS optimizes a vertical polarization of the laser before reaching the PBS. After being reflected by the PBS, the laser vertically-polarized component passes through a half-wave plate, where its polarization can be rotated by an amount θ (by rotating the half-wave plate $\theta/2$). Since resonant excitation is a polarization sensitive process, we are able to control how the laser excites the orthogonal-polarized fine-structure dipoles of the QD. The dipole polarizations for X_x and X_y are denoted as H and V, respectively. H and V are supposed to be unchanged unless the sample's position is changed.

Concerning the light detection, as described in Fig. 4.7(b), the back-reflected laser signal and the light emitted by the dipoles hit the half-wave plate, where their polarizations are rotated by the same amount θ . The back-scattered laser signal is now polarized vertically again, while H and V are rotated to new positions H' and V'. The light then passes through the PBS where horizontal polarized components will be transmitted. The laser background is perpendicularly reflected and is now isolated from the detection channel. Afterwards, a second linear polarizer is placed with a chosen horizontally-polarized direction, to ensure the suppression of the laser background.

Fig. 4.8 describes three simple cross-polarized excitation-detection scenarios that could possibly happen when rotating the half-wave plate. Two worst cases are when the laser polarization coincides with the polarization of one dipole (Fig. 4.8(a)-(b)). That leads

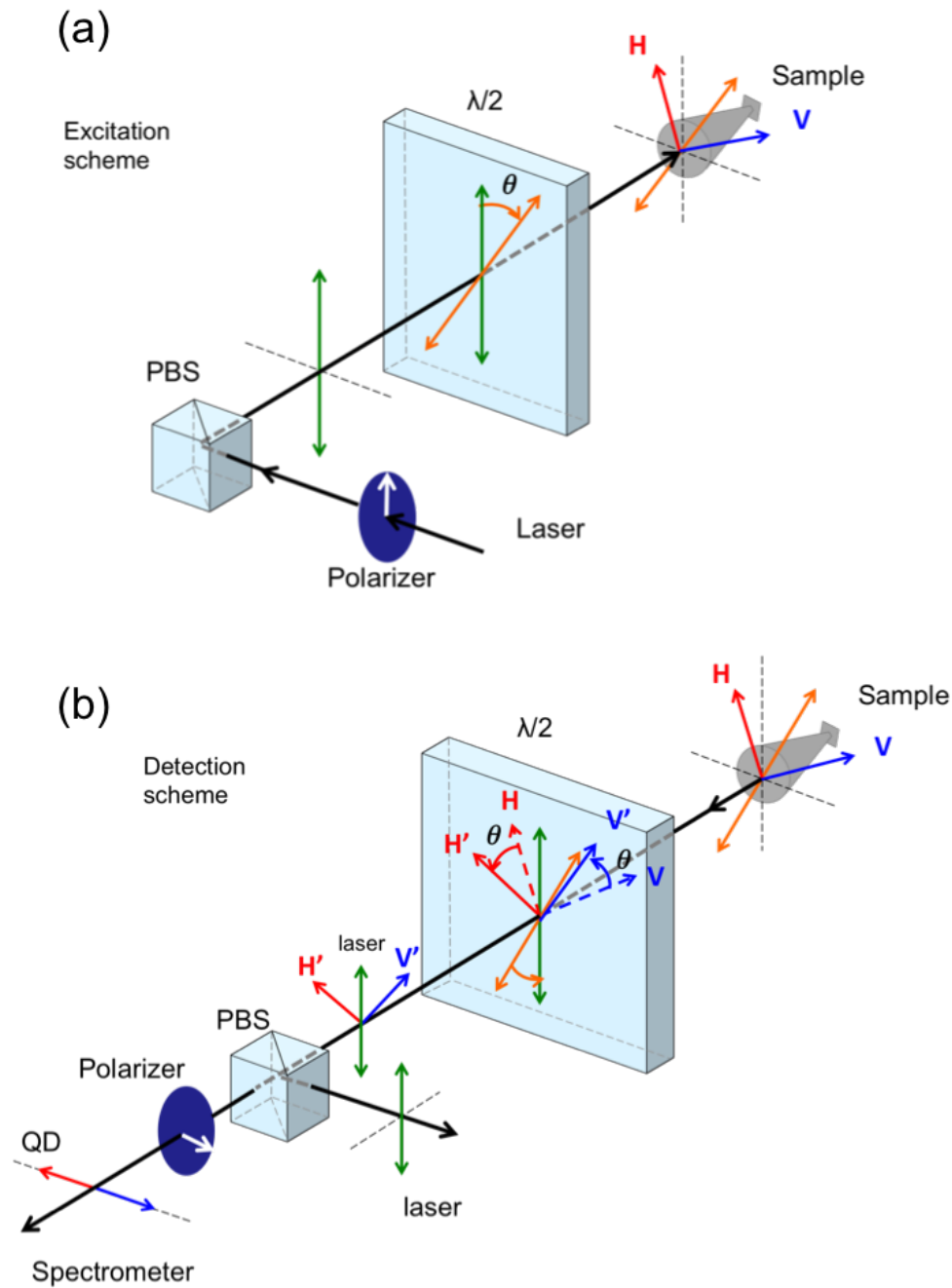


Figure 4.7 – Illustration of cross-polarized detection scheme - (a) An incoming laser beam passes through a polarizer at vertical polarization, reflected by the PBS. Then its polarization can be rotated by an angle θ by rotating an amount of $\theta/2$ on a half-wave plate ($\lambda/2$). The laser then excites two excitonic dipoles with orthogonal polarizations H and V . (b) Detection scheme: the polarizations of light emitted from the two dipoles and the back-scattered laser are then rotated by θ by the half-wave plate. The PBS reflects vertical components (including the back-scattered laser) and passes the horizontal components to the spectrometer (which in principle include only QD emission).

to a situation that one dipole is fully excited but is not at all detected whereas the other dipole is not at all excited. Therefore, the preferred scenario is the situation corresponding to Fig. 4.8(c), where the laser polarization is at a position in between the two dipoles.

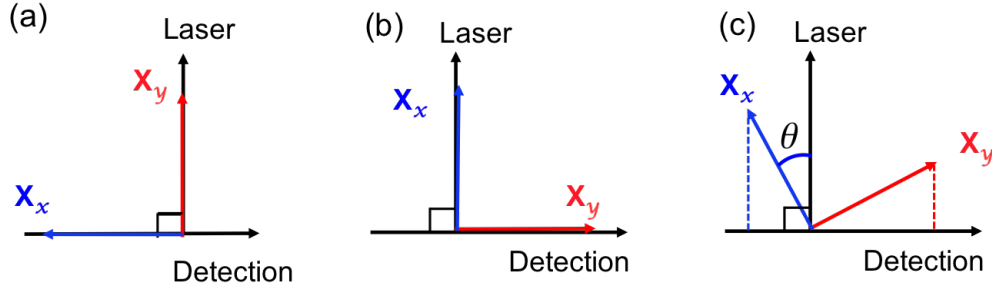


Figure 4.8 – Simple sketches of cross-polarized detection configurations - (a) and (b): The laser polarization is rotated by an angle respectively $\theta = 90^\circ$ and 0° with respect to X_x . (c) The angle θ is chosen so that the laser polarization is in between two dipole polarizations.

To understand how this configuration affect the detection signal, the schemes are described in Fig. 4.9 for the weak-excitation regime (a) and strong-excitation regime when the dipoles are saturated (b). Let us assume that the two excitonic dipoles have an equal strength. In the weak-excitation regime, consider the case that the laser with a power P_{in} is on resonance with X_x dipole. The laser polarization is at an angle θ with respect to X_x , as described in Fig. 4.9(a). In this case, the actual power applying on X_x is $P_{in_x} = P_{in} \cos^2(\theta)$. Under the excitation power P_{in_x} , the dipole emits an amount I_x . The projection of I_x on the horizontal detection channel is $I_{x-H} = I_x \sin^2(\theta)$. Overall, in the weak-excitation of the laser, assume I_0 is what the two level system emitted when $\theta = 0$ with the same power P_{in} , we then have,

$$I_{x-H} = [\cos^2(\theta) \sin^2(\theta)] I_0 \quad (4.34)$$

Similarly, for the X_y dipole with the same laser power P_{in} in a weak-excitation regime, we have,

$$I_{y-H} = [\sin^2(\theta) \cos^2(\theta)] I_0 \quad (4.35)$$

This indicates that at P_{in} well below saturation power, a spectrometer detects the same amount of photons for both FSS dipoles regardless of the angle θ . When increasing the laser power, the dipoles will be saturated. Fig. 4.9(b) illustrates this situation. Since two dipoles are identical, at saturation, they emit the same amount $I_{sat-x} = I_{sat-y}$. Therefore, the amount of photons emitted by the dipoles at saturation that are detected in the horizontal channel scales as

$$\frac{I_{sat-x-H}}{I_{sat-y-H}} = \frac{\sin^2(\theta)}{\cos^2(\theta)} = \tan^2(\theta) \quad (4.36)$$

Similarly, the laser powers P_{sat-x} and P_{sat-y} required to saturate the two dipoles scale as

$$\frac{P_{sat-x}}{P_{sat-y}} = \frac{\sin^2(\theta)}{\cos^2(\theta)} = \tan^2(\theta) \quad (4.37)$$

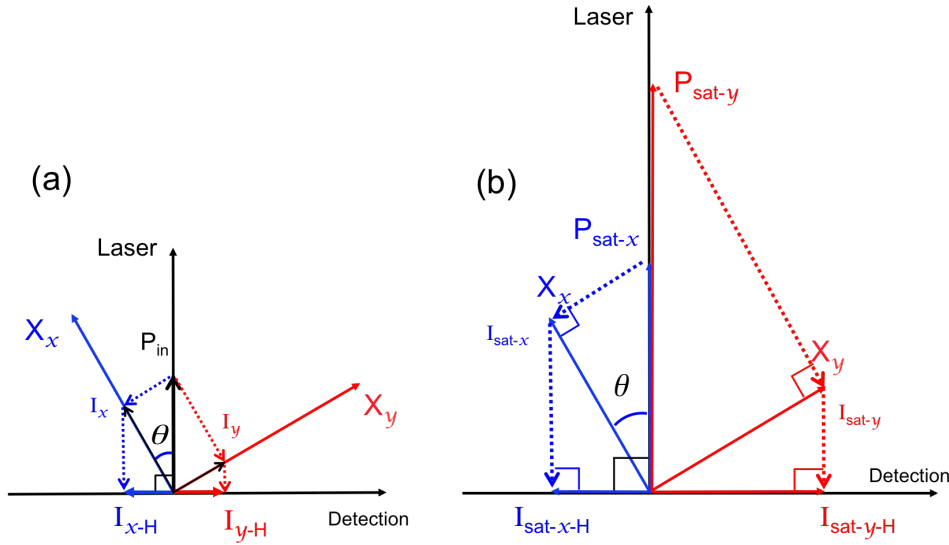


Figure 4.9 – Configuration of the resonant excitation in cross-polarization scheme - (a) Weak excitation regime in which P_{in} is well below saturation power P_{sat} . The amount of photons detected in horizontal channel is equal for two dipoles. (b) Strong excitation regime in which P_{in} is at the saturation level. In this situation, the saturation powers and the amount of photons detected from two dipoles both depend on the angle θ .

4.2.2.1 Quarter-wave plate

A quarter-wave plate ($\lambda/4$) is placed just before the microscope objective. The purpose of using a quarter-wave plate is to optimize the laser rejection following the idea proposed in [128]. In this report, the authors demonstrated that using a quarter-wave plate could compensate any distortion of the beam, thus it could help enhancing the back-reflected laser rejection rate. In addition, the quarter-wave plate behaves as a half-wave plate for the reflected laser light since the laser beam passes it twice. This possibility is useful at some alignment stages to visualize the laser beam on the screen. Because with a cross-polarization scheme, the laser is also isolated from the Watek camera used for imaging the sample.

The quarter-wave plate using in this setup is Thorlabs AQWP05M-980, which is op-

timized for the near-infrared region. The wave plate is mounted on a motorized precision rotation mount Thorlabs PRM1/MZ8. The rotation of the mount is driven via a DC servo motor that provides 1 arcsecond of resolution (2.8×10^{-3} degree). The motion of the motor can be driven by a software interface.

4.2.2.2 Laser extinction ratio

The laser suppression efficiency can be evaluated by the extinction ratio. Extinction ratio is defined as the ratio of the maximum and minimum transmissions of the laser back-reflection, when its polarization is respectively horizontal and vertical. The film polarizers used in this measurement are from Thorlabs, which offer the extinction ratio up to 10^3 (measured with a linear polarization CW laser). The extinction ratio of the PBS is announced to be 10^3 . In this setup, the best extinction ratio is achieved at 10^4 . The extinction is lower than expected, which can be attributed to the fact that the linear polarized laser induces some imperfections when traveling through many optical elements before reaching the polarizer and also to the internal reflections of the laser inside the optical elements. It will be shown in the following sections that a factor of 10^4 extinction is good enough to obtain the resonant excitation spectra from our sample.

4.2.2.3 Optical sources

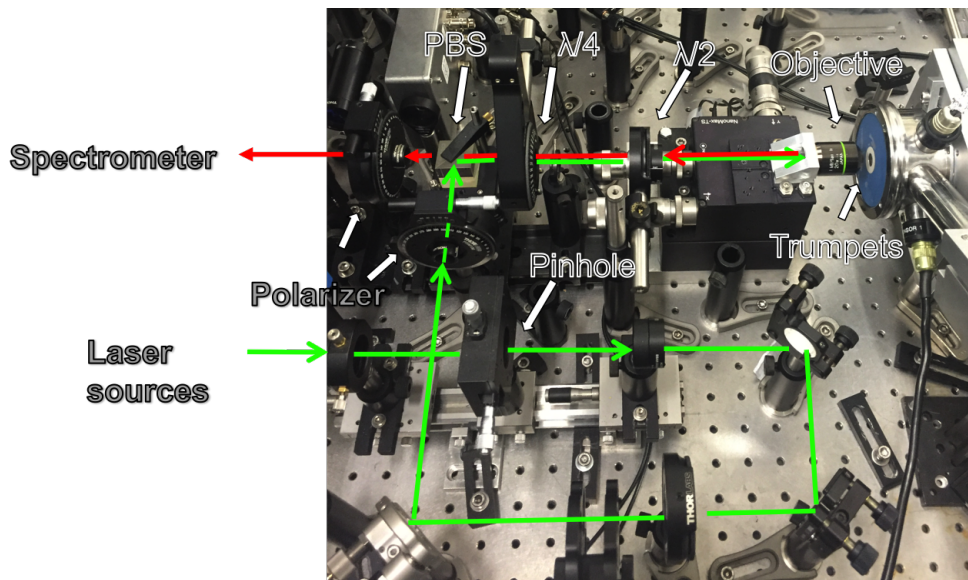


Figure 4.10 – A picture of essential optical elements in cross-polarized detection configuration.

A CW laser is used to perform resonant excitation, it is the Toptica DL 100 pro tunable diode laser. It offers a very wide wavelength coverage in the near-infrared region, with

a span from 900 - 960 nm. The maximum output power of the laser is 45 mW at the wavelength 935 nm, corresponding to a maximum current 140 mA. Coarse wavelength alignment of the laser can be done by hand with a micrometer screw. The fine tuning is obtained by a piezo actuator. The scan can be performed either internally or externally with a self-developed Labview program (by Edouard Wagner). The mode-hop free tuning range of this laser is up to 24 GHz ($100\mu\text{eV}$).

A second laser is the CW non-resonant laser that has been used in Chapter 3. This laser is used firstly to perform normal PL experiment to find the excitonic emission energies. In addition, it turns out that non-resonant laser plays a crucial role in efficiently retrieving the resonant signal from the QDs. Detail will be given in the following sections.

Fig. 4.10 shows a real photo taken in the laboratory. The photo captures the central part of the setup, including all the optical elements that contribute to the establishment of the cross-polarized detection.

4.2.2.4 Experimental procedure

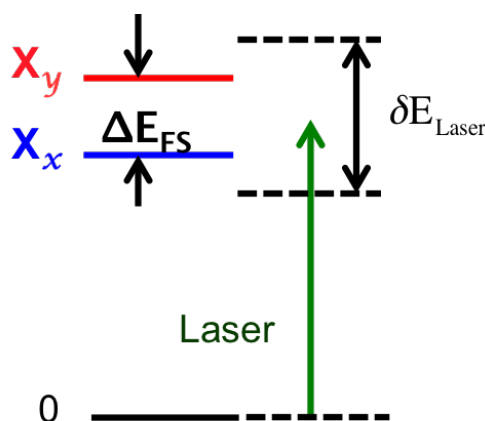


Figure 4.11 – Resonant excitation scheme - The frequency of a tunable laser with is scanned around one or both excitonic frequencies and a reflectivity measurement is performed. When the laser is out of resonance, no reflection signal is detected. By contrast, when it is on resonance with one of the dipoles, the emission from a dipole induces the reflection enhancement.

Resonant excitation spectroscopy requires a tuning of the laser energy to be exactly resonant with the emission energies of the X transitions of the QD. For that reason, the resonant laser energy is scanned with very small steps over the X emission energy to ensure obtaining the resonance during the scan. It has been shown in section 3.2.2.1 that the excitonic state contains two fine-structure splitting transitions separated in energy by ΔE_{FS} . In this case, the scan range is chosen to be able to cover one or both two X dipoles. The scheme in Fig. 4.11 shows the case when the laser energy is swept through both two

excitonic dipole energies.

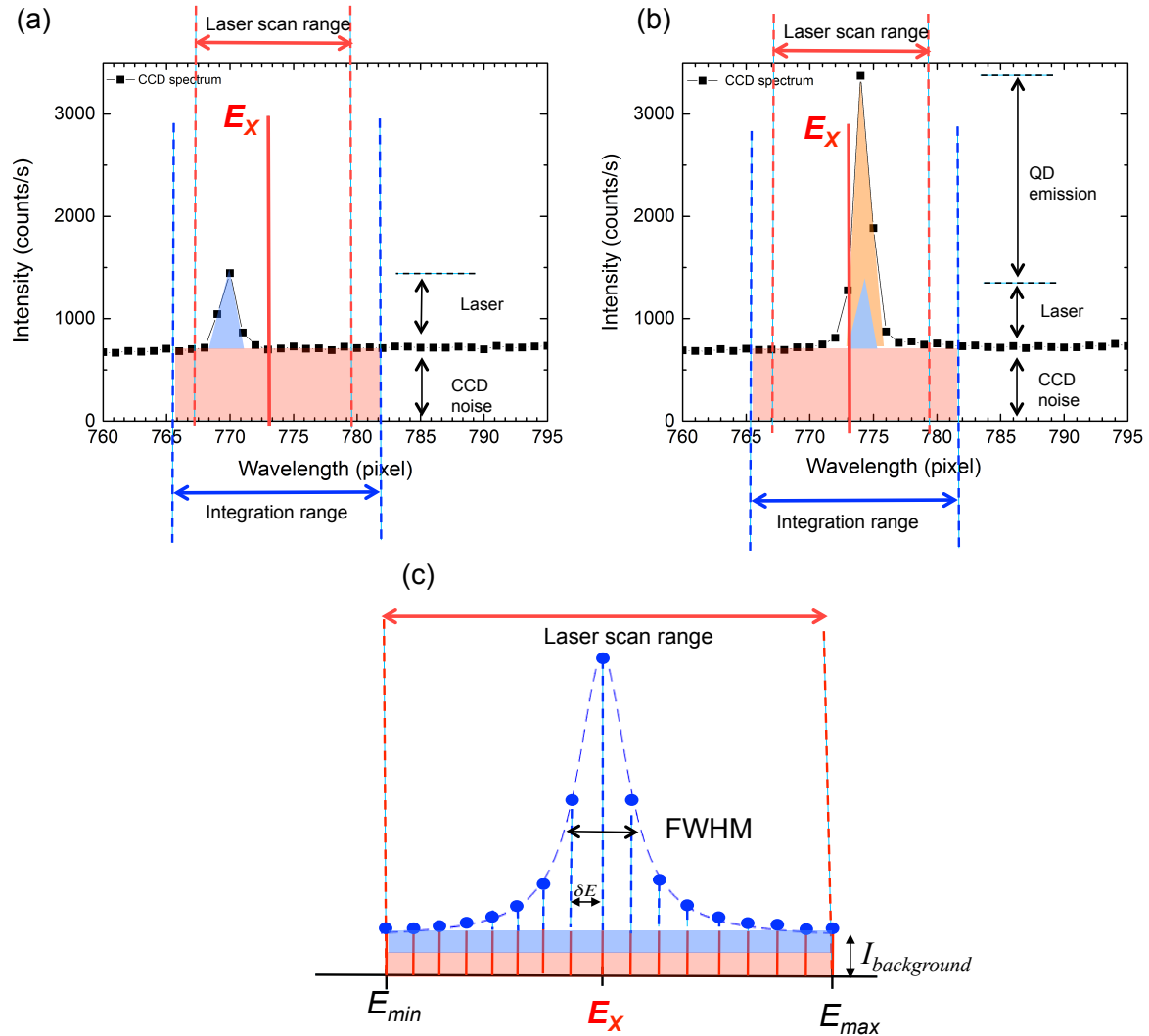


Figure 4.12 – Illustration of the data collection procedure in resonant excitation experiment - Consider the case when a laser is scanned over the X_x dipole. The vertical straight line corresponds to the wavelength of X_x transition. (a) CCD spectrum when the laser is off-resonant with excitonic levels, only the back-scattered laser background and the CCD background are detected. (b) CCD photoluminescence spectrum when the laser is very close to resonance, the X_x emission is detected on top of the laser background. The spectra in (a) and (b) is integrated in a range that covers both two excitonic dipoles. (c) Integrated values at each laser detuning are taken and then plotted to form a resonant excitation spectra.

The scan of a Toptica CW laser can be done directly with the Scan Control module SC110 on the controller. However, it is inconvenient to operate. Therefore, the scan is conducted externally by using a Labview program, in which we can easily control the range, the step size and the frequency of a scan. The experiment procedure contains several steps.

Firstly, the non-resonant PL spectra is taken to define the excitonic dipole wavelengths. Then the resonant laser wavelength is approximately set around those wavelengths to perform the scan.

We consider the case when the laser is scanned only over the X_x resonance. Fig. 4.12(a) shows a CCD spectrum when the laser wavelength is off-resonant. Each point corresponds to one pixel of the CCD. The scanning range is pointed out in the graph. One can see that even when the laser is off-resonant, there is a fraction of back-reflection laser signal that has not been rejected by the cross-polarized system and is therefore detected by the CCD. The linewidth of the laser spectrum is not infinitely narrow because it is limited and is equal to the spectrometer resolution (1 pixel $\approx 12.3 \mu eV$). In addition to this parasitics laser noise, the CCD camera always possesses a background, which is an accumulation of the CCD electronic noise and a pre-set offset. The background has a constant value for each pixel of the CCD (≈ 700 counts) as showing in Fig. 4.12(a). When the laser is very close to resonance, Fig. 4.12(b) plots the CCD spectrum in which the two-level system resonant PL shows up on top of the total background.

To produce resonant excitation (RE) spectra, at each step of the scan, an integrated value of the pixels within the integration range is recorded. As indicated in Fig. 4.12(a) and (b), an integration range is selected to make sure it contains the whole laser scan process. It should also be noted that the integration range always covers the spectra of both two excitonic dipoles. The integration time for each CCD spectrum is normally taken from 0.1s to 1s. This integrated value is the sum between the background and the resonant emission from the QD.

$$I_{Integrated} = I_{background} + I_X = I_{CCD} + I_{laser} + I_X \quad (4.38)$$

After each step ΔE of the scan, we obtain one integration value. Finally, the resonant spectrum can be created as described in Fig. 4.12(c). Each integration value corresponds to a circle. When the laser is off-resonant, $I_X = 0$. When the laser approaches the X_x transition wavelength as in Fig.4.12(b), the integration starts to grow because of resonant emission. Eventually, the final spectrum can be resolved by subtracting the flat background intensity. In practice, during the scan, the laser intensity changes linearly between E_{min} and E_{max} . Thus it still creates a flat background and within the small range around the linewidth of the X_x transition, the laser intensity can therefore be considered constant.

4.2.2.5 Reflectivity in cross-polarization scheme

In principle, with an ideal system, in which there is no back-scattered laser background, the optimum resonant reflectivity measurement has to be performed in co-polarization excitation. In such kind of excitation, the polarizations of the laser, the detection and

of the QD dipole are aligned in the same mode. In this case, the reflectivity can be understood as the reflection coefficient of an incoming laser in a single mode, as described in section 4.1. However, in practice, due to the large unwanted background, we have to establish the cross-polarized excitation. As shown in Fig. 4.9, one can see that the reflection obtained in the detection channel is actually the resonant back-scattering in a mode which is orthogonally polarized to the excitation mode. Therefore, in our cross-polarization scheme, the reflectivity definition can be considered as the ratio between the reflection power in the detection mode and the incoming power in the excitation mode.

4.2.3 Resonant excitation spectroscopy

As already discussed in the previous sections, a RE signal of a two-level quantum emitter consists of the superposition of the coherent resonant Rayleigh scattering and the incoherent resonant PL. Section 4.1.2.4 pointed out that coherent scattering dominates the RE spectrum when the excitation power is much smaller than the saturation power ($P \ll P_{sat}$). The realization of coherent signature has been done in [124, 129, 130]. At higher excitation power, the emitter is saturated leading to a reduction of the coherent term and incoherent scattering is dominant. Above saturation, the electron population of the two-level system will Rabi oscillate between ground and excited states. The result of Rabi oscillations is the formation of Mollow triplet [107, 131]. This high-excitation regime will be introduced and discussed in detail in the next chapter.

Regarding the spectral linewidth of a two-level system RE spectrum, at low-excitation regime, an ideal emitter is broadened just by radiative decay rate γ , where $\gamma = 1/\tau$ (τ is the radiative lifetime), namely radiative-limit broadening. In practice, although the strong confinement of electrons and holes in semiconductor QDs results in a discretization of their energy levels and leads to atomic like properties, a QD is still quite far from behaving like a perfect isolated atom and the radiative-limit linewidth is therefore hardly reached. The observed RE linewidths have been always larger than this radiative limit [124–126]. The additional sources of decoherence that contribute to the spectral broadening can come from pure dephasing and/or spectral diffusion, as has been introduced at the beginning of this chapter.

For the particular QD used in this study, the radiative lifetime has been measured as $\tau = 1.36$ ns (see section 3.2.4), which leads to the radiative decay $\gamma/2\pi = 120$ MHz. This corresponds to the homogeneous radiative-decay linewidth of $\gamma = 0.5\mu eV$. At the first stages of resonant fluorescence measurement, the single resonant laser is scanning firstly on one of the two fine-structure states (the scan range is around $35\mu eV$). The RE spectra is shown in Fig. 4.13. Each black circle corresponds to one step of the laser detuning, the gap between two steps is about $1.5\mu eV$. In this case, the optical and electronics background have been subtracted following the procedures explained above. The full-

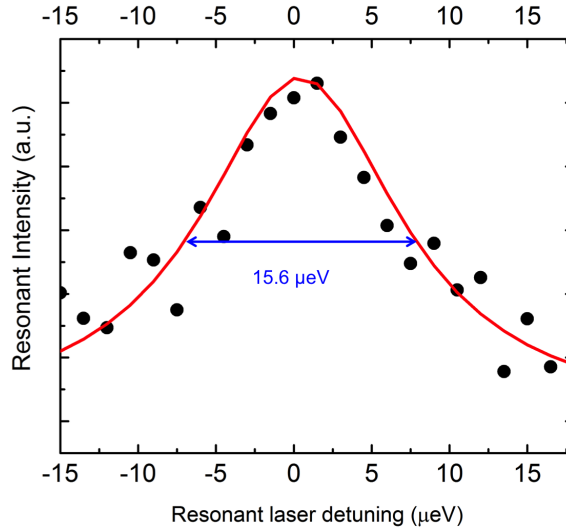


Figure 4.13 – Resonant excitation spectrum with a single resonant laser - Following the procedure described in Fig. 4.12, a RE spectrum is obtained (black circles) and fitted with a Gaussian function. The resonant laser power used is well below saturation ($P/P_{sat} = 0.1$). An unexpected broad linewidth is observed with FWHM $15.6 \mu eV$, which is much larger than the radiative-limit linewidth of this QD ($0.5 \mu eV$).

width-at-half-maximum (FWHM) obtained is $15.6 \mu eV$, which is much larger than the expected homogeneous linewidth. In general, the linewidth broadening may arise from pure dephasing [120, 122] and/or spectral diffusion [120, 132, 133]. Spectral diffusion is a process in which the QD transition frequency is randomly shifted during the measurement. This shift is thought to originate from a fluctuating charge environment of the QD [133] (see section 4.1.2.3). In [127], the authors reported a study on InAs/GaAs QDs and it was pointed out that the residual holes introduced by the non-intentional doping of the sample will preferably be trapped (de-trapped) in (from) the defect. The presence of this random trapping and untrapping of charges leads to spectral diffusion of the transition energy and also the quenching in RE intensity. As a result, broad and weak optical emission lines are obtained [114], similar to what we see in Fig. 4.13.

4.2.3.1 The effect of an additional ultra-weak non-resonant laser on resonant excitation spectra

To overcome the influence of spectral diffusion, it was proposed to use an ultra-weak non-resonant laser that plays a role as an optical gate for the RE process [126]. This non-resonant laser controls the QD ground state, neutralizes the QD and therefore contributes to a narrowing of the optical transition of the two-level system. This technique has been used efficiently in several groups to optimize RE signal [129, 134] and to minimize the

environment fluctuations to reduce the QD linewidth [22, 132].

Following this approach, we introduce a CW non-resonant laser to the set up. This additional laser has the wavelength of 825 nm. It has already been used in Chapter 3 for PL characterization. To avoid any influence of the non-resonant excitation on RE spectrum, the idea is to apply an ultra-weak power (at the level of $10^{-4} - 10^{-2}$ the saturation power) of this additional laser when performing resonant spectroscopy. Fig. 4.14 shows the RE spectra with the contribution of a non-resonant laser. The fit gives the FWHM of $4.5 \mu\text{eV}$, which is three times narrower than the RE spectra without using the non-resonant laser. In addition, the RE intensity also increases by a factor of 3. The result indicates a dramatic effect of the non-resonant laser on the RE spectrum.

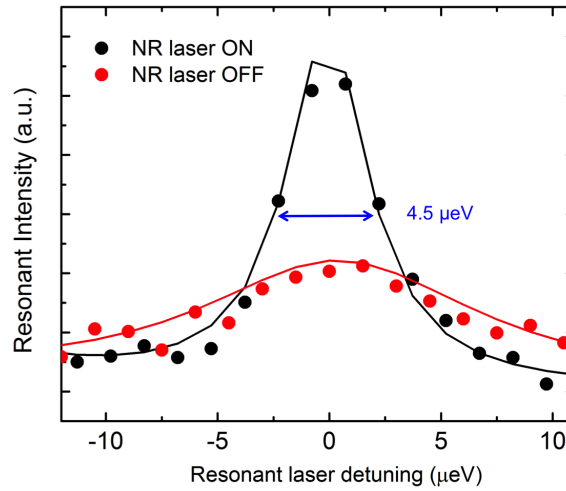


Figure 4.14 – Resonant excitation spectra with and without a non-resonant laser - The red circles are the data obtained in Fig. 4.13 by a single resonant laser. By introducing an ultra-weak non-resonant laser with an energy below the emitter energy ($P/P_{sat} \simeq 0.2\%$), the RE linewidth reduces drastically (black circles).

To have a better understanding of how the RE signal depends on a non-resonant laser, different non-resonant powers are applied. The dependence of the RE intensity on the non-resonant laser is plotted in Fig. 4.15. The resonant laser power is kept the same during the measurement. One can see that by increasing the non-resonant laser power slowly from 0, RE intensity starts to increase and reaches maximum when the non-resonant laser power is $P/P_{sat} \simeq 4 \cdot 10^{-3}$. Further increasing of the power leads to the reduction in RE intensity and at the same time the non-resonant PL contribution starts to be significant. Therefore, the strict condition of resonance excitation is no longer valid. This behavior is very similar to what was obtained in [127]. In our experiment, we decide to choose a non-resonant laser power around $P/P_{sat} \approx 10^{-3}$. At this level, the non-resonant excitation

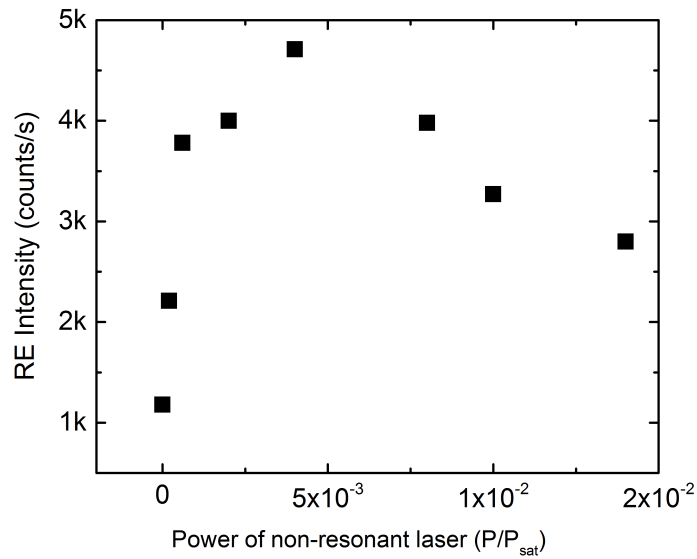


Figure 4.15 – Dependence of resonance intensity on the non-resonant laser power - The RE spectrum peak intensities for different non-resonant laser powers are taken and plotted as a function non-resonant power.

contribution to RE signal can be completely negligible. It should be also noted that from this points, all the RE measurement will always be performed with the presence of an ultra-weak CW non-resonant laser.

4.2.3.2 Saturation of a two-level system

It has been shown in section 4.1 that the non-linearity in reflectivity happens at the excitation power around saturation. Therefore, one important step toward realizing a non-linearity is to perform a resonant excitation power dependence experiment. In this measurement, the resonant laser is set to scan in a wide range of $\simeq 70 \mu\text{eV}$ to be able to cover both the fine-structure splitting (FSS) dipoles (the FSS energy of this QD is $25 \mu\text{eV}$ obtained with the normal PL spectra (see section 3.2.2.1)).

Fig. 4.16 shows the RE spectra when the resonant laser is scanned through both FSS states. Two RE peaks are observed, the distance between them is $\simeq 25.3 \mu\text{eV}$, which is equal to the the FSS value. Two peaks are fitted which give the linewidth about $\simeq 4.5 \mu\text{eV}$.

RE power dependence is performed by changing the power of the resonant laser. The RE peak intensities are plotted as a function of laser power in Fig. 4.17 for both two FSS dipoles. The saturation behaviors are observed when increasing the resonant laser power. One can see that the saturation intensities of two dipoles are different, this is because the laser polarization is in an asymmetrical position with respect to the polarizations of two

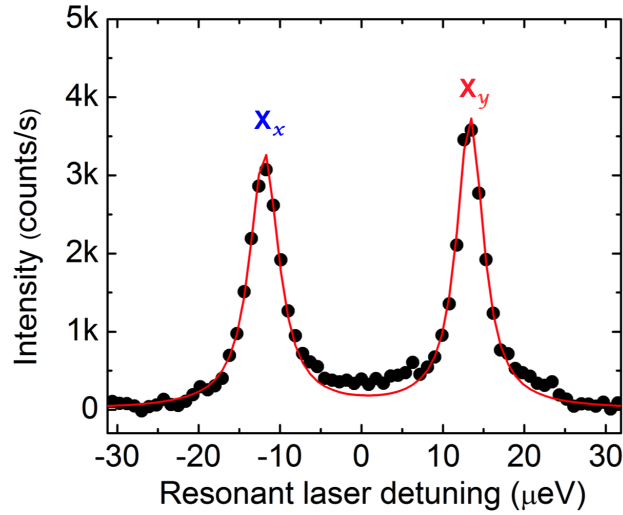


Figure 4.16 – Typical resonant excitation spectra for both two excitonic dipoles - A wide resonant scanning range is chosen to be coupled to both X_x and X_y . The distance between to RE peaks is $\approx 25\mu\text{eV}$, which is consistent with the FSS energy.

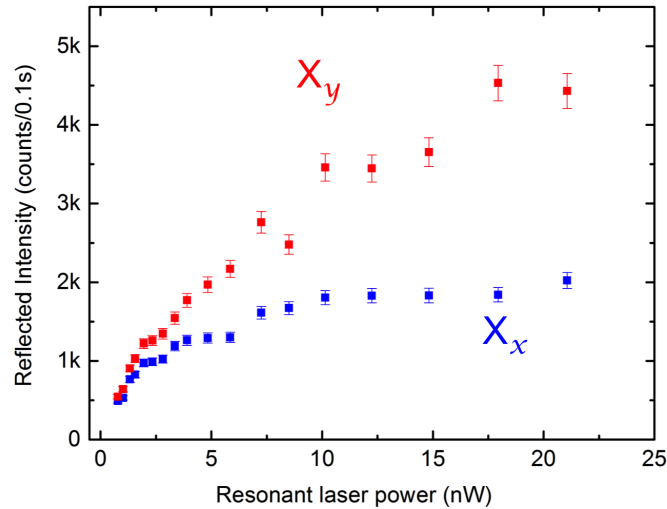


Figure 4.17 – Resonant excitation as a function of resonant laser - For each resonant laser power, RE spectra peak intensities of two dipoles are taken and plotted. A non-resonant laser with power $P/P_{sat} \approx 10^{-3}$ is always present in the measurement.

dipoles as explained section 4.2.2. The saturation intensities of two excitonic dipoles are scaled like $\frac{I_{sat-x-H}}{I_{sat-y-H}} = \tan^2(\theta) \approx 0.45$ in this situation, which gives $\theta \approx 33^\circ$. This value is consistent with the pre-selected value for θ by rotating the half-wave plate.

4.2.3.3 Calibration of input and output powers

Up to this point, we have introduced a resonant reflection measurement in which the incoming and reflected powers have been described by the raw units from the devices, which are nW (measured by a Thorlabs power meter PM100) for the excitation and count/s (by a CCD camera) for the detection. To have a meaningful physical demonstration of the non-linearity, the units are converted to photon per transition lifetime. For the incoming power, time-resolved measurement gave the radiative lifetime of the X level $\tau_X = 1.36$ ns. The power in photon/lifetime can be converted by

$$P(\text{photon/lifetime}) = \frac{\lambda\tau_X}{\hbar c} * P(\text{nW})$$

At the wavelength 920 nm ($\simeq 1.35$ eV), 1 nW corresponds to $\simeq 6.3$ photons/lifetime for this particular QD. In term of reflected intensity, the power is recorded by the CCD in photons/second, it is easy to convert to the photon/lifetime from $\tau_X = 1.36$ ns.

Ideally, input and output powers should be measured directly at the input/output of the trumpet. However, in the experimental condition, it is hardly possible to measure directly the amount of power coming in and out the trumpet. For the output power, the light escaping the trumpet is not detected directly by the CCD camera. As showing in the experimental setup, it has to travel through many optical elements and therefore loses many photons before reaching the CCD. The situation is shown in Fig. 4.18. For the incoming power, the power is measured just before the microscope objective in front of the cryostat. Given the transmission through the objective (78%), one can then easily infer the power at the input of the trumpet. Another important issue is to have a precise detection of power, because the effect is expected to be observed with just a few photons/lifetime. To do that, for low-power excitations, the laser is put on a higher power at first, then the power is filtered by multiple density filters. The transmissions of the filters are already well calibrated. Thus eventually, the low-power value can be inferred with high accuracy.

Concerning an estimation of the output power, the situation is more complicated. An ultra-low power reflected signal can not be measured with the resolution of typical power meters. Moreover, the reflected signal at the output of the trumpet contains not only the QD emission but also the back-reflection laser signal. Therefore, the power is only detected by the CCD camera after rejecting the background by the polarizing beam-splitter and the pin hole (Fig. 4.6). A careful calibration of each optical element is carried out (for objective, the beam splitters, the pinhole, the mirrors, the spectrometer, etc...) and the

total lost when a photon travels through the setup before reaching the CCD is estimated to be around 10^{-2} .

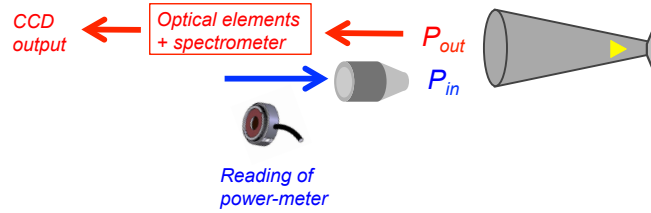


Figure 4.18 – Calibration of incoming and reflected powers.

4.3 Ultra-low power single-mode giant non-linearity

4.3.1 A quantitative evaluation of all experimental parameters

The previous section has demonstrated the resonant fluorescence of a QD two-level system. As already described in the first part of this chapter, the non-linearity is realized based on the reflectivity. The reflectivity R is the ratio between the reflected light coming out from the trumpet (the QD emission) and the light coming in (laser) the trumpet. In an ideal situation described in Fig. 4.3, one should expect a unity reflectivity at the laser power well below saturation. However, in the experimental condition, the one-dimensional atom is not perfect. The fundamental challenge for any optical waveguide is the light-matter coupling efficiency. As mentioned in chapter 2, the input and output coupling efficiencies, ε_{in} and ε_{out} , respectively, depend mostly on two factors. The first one is β , which determines the QD spontaneous emission rate that is coupled to the fundamental guided mode (HE_{11} in this case).

The light emitted by the QD is firstly coupled into the HE_{11} mode with a probability β and then propagates along the taper with symmetrical distributions upward and downward. The part moving upward propagates along the trumpet structure, with linearly increased diameter to induce a lateral expansion of the guided mode. Here we assume that all the photons that are coupled to this mode could travel toward the top facet with optimum efficiency, or in other words, the modal transmission $T_{HE_{11}} \simeq 1$ [23,135]. Finally, the light escaping the trumpet is collected in free-space by a microscope objective lens with a numerical aperture (NA=0.4), as illustrated in Fig. 4.19. The fraction of diffracted light could be collected by the lens is defined as ε_C . Similarly, for the input beam that is focused on top of the trumpet through a NA objective, ε_C defines the mode-matching efficiency. The mode-matching determines the amount of an incoming beam could enter the trumpet and couples to the fundamental guided mode HE_{11} . It then interacts with the QD with a probability β . We then have $\varepsilon_{in} = \varepsilon_{out} = \beta * \varepsilon_C$.

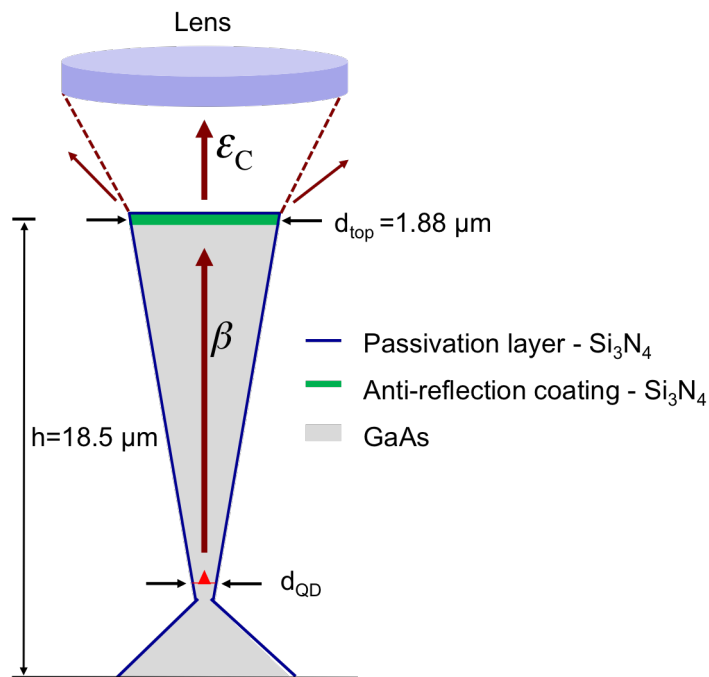


Figure 4.19 – Sketch of the trumpet in the measurement - The trumpet used in this study has the top facet diameter of $1.88 \mu\text{m}$, corresponds to a waist diameter around 550 nm where the QDs are located. The trumpet surface is covered with a 30 nm -thick Si_3N_4 passivation layer.

4.3.1.1 A non-circular symmetry at the waist where the quantum dots locate

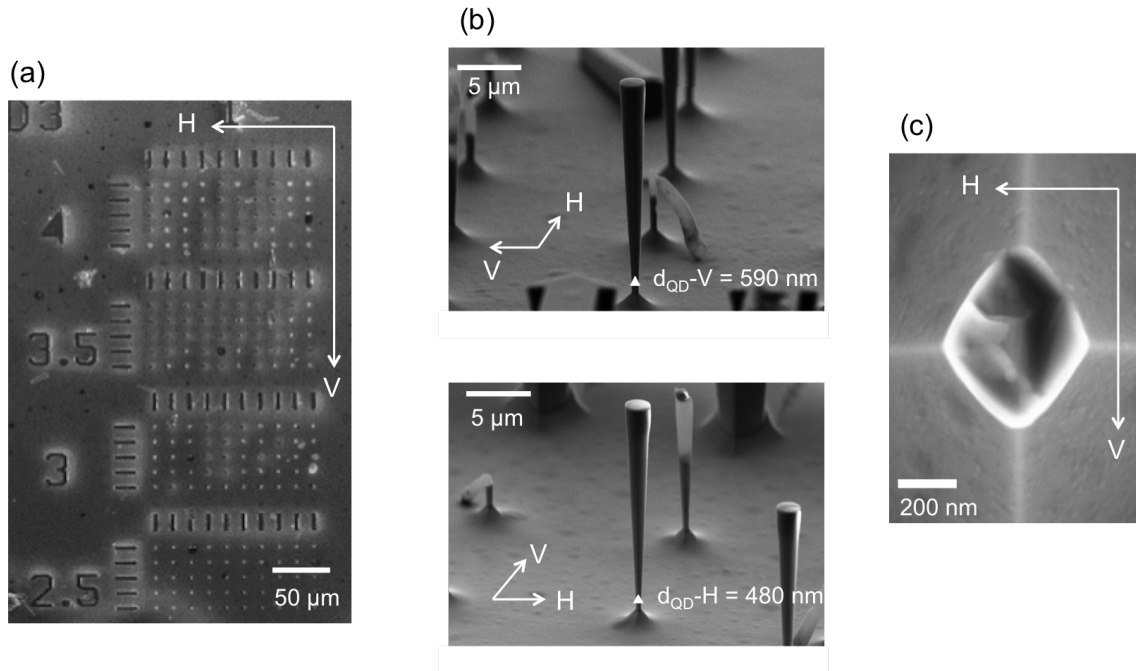


Figure 4.20 – SEM images showing the measurement of the waist diameters of the trumpet - (a) Top-view SEM image of a part of the whole sample. The sample contains several blocks of trumpets. Each block has 50 trumpets with different diameters with the step of 10 nm. The numbers on the left indicate the largest top diameter of the corresponding block. Two arrows indicate the horizontal and vertical directions that will be used to measure the QD-location diameter (b) SEM side-view images taken in H and V directions of the trumpet in this study, with the top diameter $1.88 \mu\text{m}$. (c) Top-view image of a “broken” trumpet with top diameter $1.88 \mu\text{m}$. The broken section is at exactly the QD-waist diameter, which shows a diamond shape with slightly asymmetrical axes.

In principle, the trumpet should have a uniform circular shape along the structure. But unfortunately, a SEM measurement taken by J. Claudon (INAC/CEA, Grenoble, who was in charge of the sample fabrication) indicates that the bottom of the trumpet where the QDs are located actually has a diamond-like shape. The SEM images are shown in Fig. 4.20. The horizontal and vertical directions are marked respectively as H and V in Fig. 4.20(a). The trumpet used in the study is measured from the side-view as shown in the SEM images on the center of Fig. 4.20. The diameters at the QDs height are measured in H and V directions. The results give d_{QD} in H is 480 nm and d_{QD} in V is 590 nm. The SEM image in Fig. 4.20(c) shows the top-view of a trumpet that was broken at exactly the waist, which shows clearly a non-circular shape.

In general, β factor depends strongly on the dimensions of the structure so that the asymmetry of the trumpet diameter at the location of the QDs may lead to different coupling efficiencies depending on the polarizations of the dipole emitter. An illustration

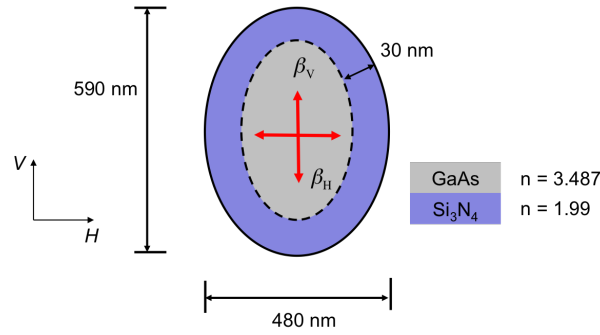


Figure 4.21 – Illustration of the cross-section at the QD-waist of the trumpet - The trumpet surface is covered with a 30 nm-thick Si_3N_4 passivation layer, which results in the GaAs part dimensions 420 nm and 530 nm for respectively H and V directions. The refractive indices of GaAs and Si_3N_4 are 3.487 and 1.99.

of QD location cross-section is described in Fig. 4.21. The β factor of this particular trumpet at the wavelength $\lambda = 920\text{nm}$ has been calculated by J. Claudon (INAC, CEA, Grenoble, France) and N. Gregersen (DTU Fotonik, Denmark). For a on-axis QD, the calculated β_H and β_V for horizontal and vertical directions are 33% and 32%, respectively. Thus, despite of the non-circular shape at the waist, this trumpet still gives a fairly similar coupling factor β for both directions. Therefore, we can still consider β as a polarization independent factor. In the upcoming sections, the fitting results of different emission polarizations with a universal β will confirm this approximation.

The factor ε_C for the amount of light escaping from this particular trumpet to be collected by a $\text{NA}=0.4$ objective is calculated to be 85%, for an on-axis QD. Moreover, the modal transmission $T_{HE_{11}}$ for the guided mode HE_{11} is calculated to be close to perfection ($\simeq 99\%$) along the vertical direction of the trumpet. This calculation gives the predicted coupling factor $\varepsilon_{in} = \varepsilon_{out} = \beta * \varepsilon_C = 0.26$, for an on-axis QD.

A theoretical model has been developed by Thomas Grange (theoretician from NanoPhysics and Semiconductors Group, Institut Néel, CNRS) considering all the imperfections this one-dimensional system. The parameters used in the theoretical calculation are: the angle θ between the X_x dipole and the laser polarization (vertically polarized), the universal input and output coupling efficiencies $\varepsilon_{in} = \varepsilon_{out}$, the homogenous broadening γ^* (pure dephasing broadening) and inhomogeneous broadening σ_X (spectral diffusion). The model also takes into account the presence of the other excitonic dipole X_y .

4.3.1.2 Polarizations of the excitonic dipoles with respect to the sample axes

The purpose of this brief section is to define the exciton dipole polarizations with respect to the sample axes, to have a better understanding of the sample. It has been shown in Fig. 4.20 that the two axes of the “diamond shape” bottom waist are coincided with the

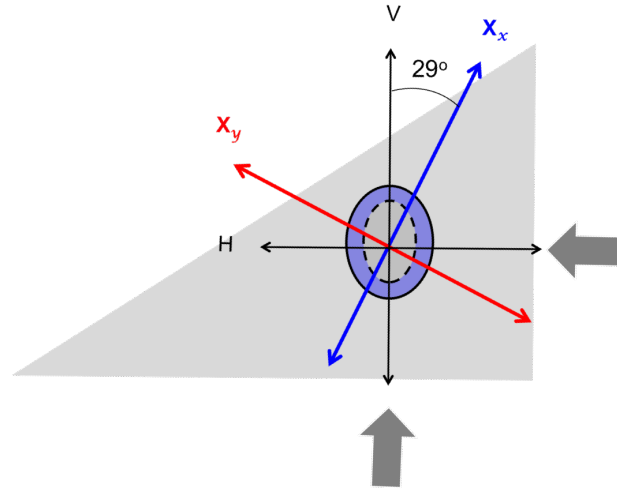


Figure 4.22 – Sketch showing the polarizations of the excitonic dipoles with respect to the axes of the sample - The excitonic polarizations are defined by rotating the half-wave plate in front of the sample.

axes of the whole sample. For the particular QD studying in this chapter, it turns out that the excitonic dipoles are polarized in two orthogonal directions that are $\approx 29^\circ$ away from sample's axes, as described in Fig. 4.22. The whole statistic for other QDs and other trumpets requires further investigation in the future.

4.3.2 Single-mode giant non-linearity

Given all the needed parameters, Fig. 4.23(a) describes the saturation curve of X_x dipole in the unit of photon/lifetime. Blue line is the fitted curve with the parameters given by the real experimental conditions. The total spectral broadening is $4 \mu eV$, which includes $1 \mu eV$ of homogeneous broadening (pure dephasing) and $3 \mu eV$ of inhomogeneous broadening (spectral diffusion). Those numbers are obtained through a careful fitting process based on the data given in chapter 5 for the same QD (see appendix A). The calculation also takes into account the presence of the other fine-structure dipole X_y with a FSS $25 \mu eV$ observed in chapter 3. The calculated values for input and output coupling efficiencies are respectively $\varepsilon_{in} = 0.26$ and $\varepsilon_{out} = 0.216$. The input coupling efficiency ε_{in} matches perfectly with the predicted value. While the output coupling efficiency is slightly mismatch. This is attributed to the uncertainty of the transmission of the experimental set up. This uncertainty comes mostly from the transmission rate through the pinhole located before the spectrometer, which is extremely sensitive.

The reflectivity of the dipole X_x is plotted in Fig. 4.23(b). The experimental data

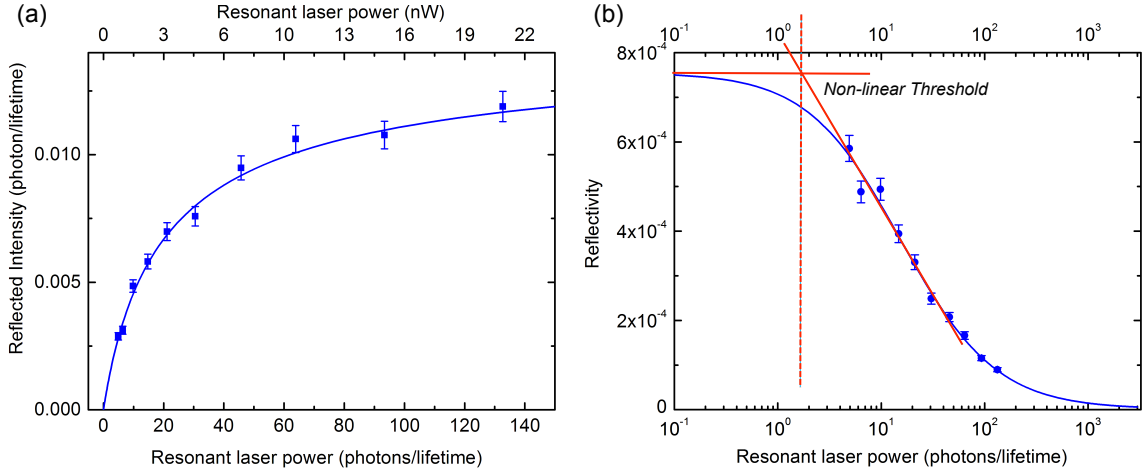


Figure 4.23 – Reflection intensity and reflectivity of X_x dipole - (a) The data in Fig. 4.17 is converted to the unit photon/lifetime and is fitted by the theoretical model. The angle θ is 33° . The broadening of the RE spectrum is $4.5 \mu\text{eV}$, including $0.5 \mu\text{eV}$ radiative limited linewidth (correspond to the X lifetime 1.36 ns) and $4 \mu\text{eV}$ broadening linewidth. (b) Reflectivity as a function of resonant laser power showing the non-linearity signature of the two-level system. The non-linear threshold is obtained at only 2 photons/lifetime, demonstrating a single-mode giant non-linearity.

again shows a good agreement with the fitted curve. The non-linear behavior is observed, when increasing the power, the laser reflectivity is switched from reflection to transmission. The non-linear threshold (the point where the non-linearity starts to occur [14]) is observed at $\simeq 2$ photons/lifetime. A comparison of state of the art single-mode giant non-linearity obtained with different one-dimensional structures will be presented in section 5.7.

4.3.2.1 Broad-band operation properties in single-mode giant non-linearity

Fig. 4.24 shows reflected intensity and reflectivity as a function of resonant laser power for both excitonic dipoles X_x and X_y . As mentioned above, the asymmetrical excitation between the laser polarization and two orthogonal polarized dipoles leads to different saturations and reflectivities. X_x dipole is more efficiently coupled to the laser and therefore it requires less photons to reach the non-linear threshold.

The result is also an evidence of the broadband operation feature of the photonic trumpet. Two excitonic dipoles at two different frequencies can be coupled at the same time with high efficiency. This feature is confirmed by a good agreement with theoretical calculation for both dipoles.

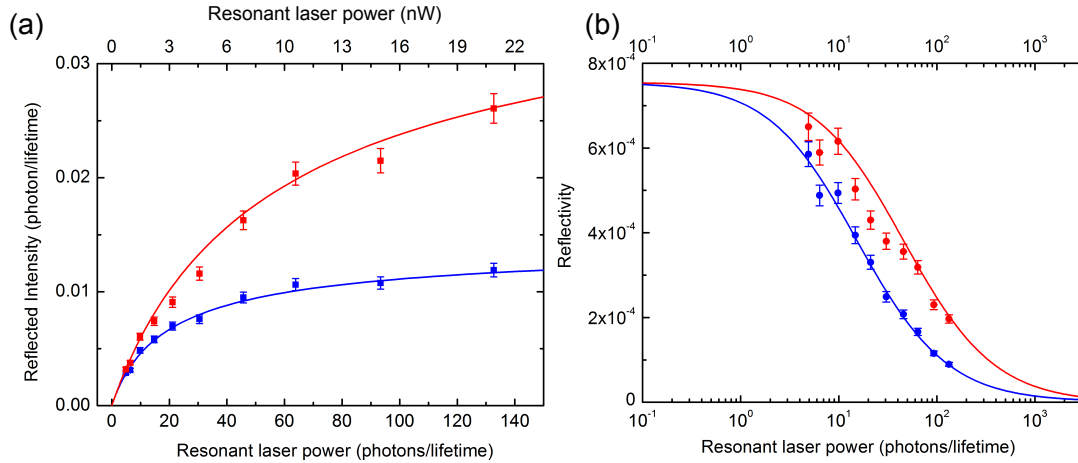


Figure 4.24 – (a) Reflected power and (b) Reflectivity for two dipoles X_x and X_y with an angle 33° between X_x and laser polarization. Blue circles and red squares correspond to X_x and X_y , respectively. Section 4.2.2 have pointed out that, in cross-polarized detection scheme, for an incoming laser power P_{in} much less than the saturation power, the amount of photons detected is the same for two dipoles regardless of the angle θ . As a result, the reflectivities of two excitonic dipoles at vanishing power of resonant laser are equal. A high agreement obtained between experimental and theoretical results show the high coupling efficiency of the trumpet over a broadband energy.

4.3.2.2 Single-mode giant non-linearity of an ideal system in cross-polarization scheme

One could notice in Fig. 4.24 that even though a non-linearity is observed at the level of just a few photons/lifetime, the maximum reflectivity obtained is less than 10^{-3} . This rather low reflectivity comes from many reasons which have been partially discussed in the first theory sections of this chapter. The first reason is the spectral broadening of the emission linewidth, which originates from pure dephasing and spectral diffusion. Eqs. ?? indicate that pure dephasing reduces the reflection by a factor of $(\gamma + \gamma^*)/\gamma$. Eq. 4.22 shows that the reflectivity decreases linearly with spectral diffusion broadening. The second reason is the non-optimum input and output coupling efficiencies of the one-dimensional waveguide. With $\varepsilon_{in} = \varepsilon_{out}$, the reflectivity obtained in the real system is lower by a factor of ε_{in}^2 compared with that of an ideal system. The third reason comes from the cross-polarized configuration, which reduces the reflectivity by a factor of $1/\cos^2(\theta) \sin^2(\theta)$ as pointed out in Eq. 4.34.

Considering an ideal system in cross-polarization scheme, the reflectivity calculation is plotted in Fig. 4.25 for the dipole X_x . It turns out that the optimum reflectivity could be observed is ≈ 0.105 . This value is still low because of the cross-polarized detection. In the weak excitation regime, the emitted power from the two-level system is decreased by a factor of $1/\cos^2(\theta) \sin^2(\theta)$ compared with the power emitted in co-polarized excitation.

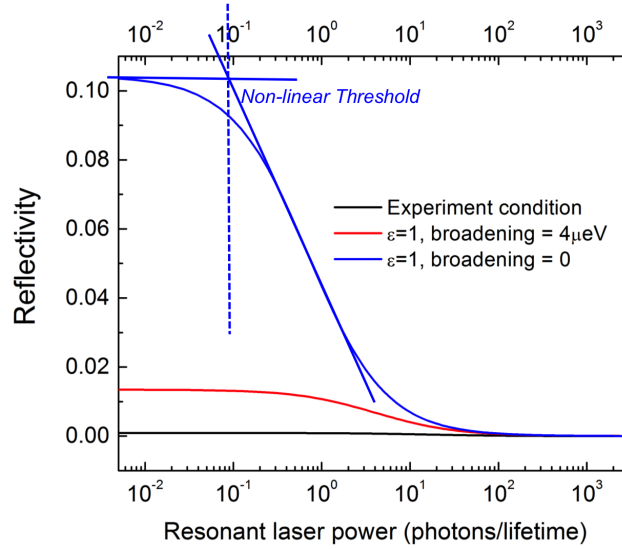


Figure 4.25 – Calculated reflectivity - The calculation is performed in cross-polarized detection scheme with an angle $\theta = 33^\circ$. The black curved is the calculated reflectivity in the real experimental condition that was shown in Fig. 4.23(b). The red curve is the calculated reflectivity for a perfect coupling waveguide but the quantum emitter still has a spectral broadening of $4\mu eV$. The blue curve corresponds to an ideal QD-trumpet system.

In addition, half of the photons emitted by the QD is directed to the downward direction of the trumpet. Therefore, the maximum reflectivity could be obtained in this case is,

$$R_{cross-polarization} = 0.5 \{ \cos^2(\theta) \sin^2(\theta) \} \quad (4.39)$$

For $\theta = 33^\circ$, $R_{cross-polarization} = 0.104$, which is in highly agreement with the calculation. It is easily to see that for $\theta = 45^\circ$, we can have $R_{cross-polarization}^{MAX} = 0.125$.

4.3.2.3 Coherent versus incoherent scattering

Probing and controlling quantum coherence have been considered as the major issues in quantum information science. As has been demonstrated in section 4.1.2.4, for an ideal system broadened by radiative decay rate γ , the spectra and temporal properties of the scattered photons depend strongly on the Rabi frequency Ω of the laser. When $\Omega \ll \gamma$, most of the light is scattered coherently. Whereas increasing Ω gives rise to incoherent scattering [136]. A quantum emitter in reality is always affected by surrounding environment and spectral broadening sources, which induce a huge influence on the spectral and temporal characteristics of the scattering process compared to the ideal two-level system [129]. Fig. 4.26 illustrates the calculation of the scattered photons intensity from a perfect-guided one-dimensional atom ($\varepsilon_{in} = 1$) without (solid lines) and with (trashed lines) pure dephasing and spectral diffusion. The black curves show the total reflected

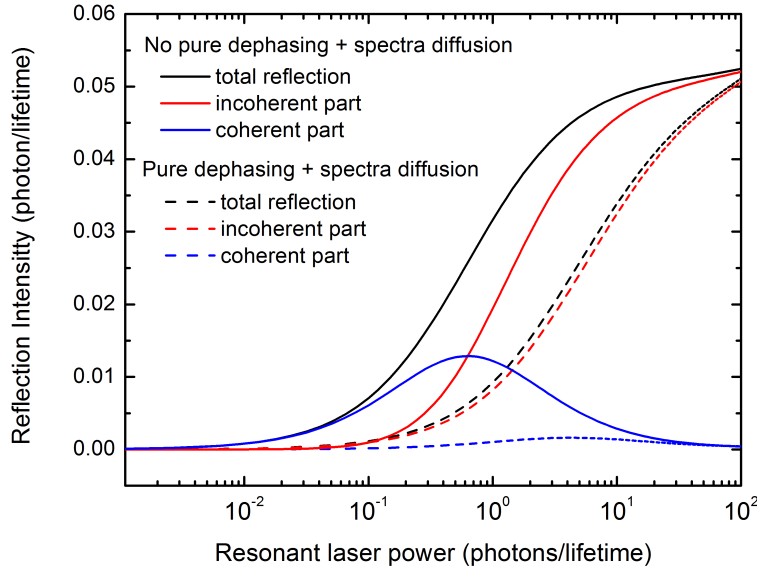


Figure 4.26 – Calculation plots of total reflected light intensity from QD two-level system, including the fractions of coherent and incoherent parts, for an ideal one-dimensional two-level atom (solid lines) and for a one-dimensional two-level atom $4 \mu eV$ broadening (dashed lines). The polarization of the laser is the same with experimental conditions ($\theta = 33^\circ$).

light intensity. The blue and red curves show respectively the contribution of the coherent and incoherent scatterings.

4.4 Chapter summary

This chapter presented a detailed study of single-mode optical giant non-linearity of a laser beam coupled to a QD-waveguide system. A giant non-linearity is realized by characterizing the laser reflectivity. A detailed model including imperfection conditions was demonstrated in the first sections. The chapter continued with the results of resonant fluorescence spectroscopy on a single semiconductor QD embedded in a photonic trumpet. To perform the resonant excitation measurement, a cross-polarized polarization setup was established to subtract efficiently the back-scattered laser background. A ultra-weak non-resonant laser was used to reduce the effect of spectral diffusion. From the resonant emission signal, the reflectivity was plotted and a giant non-linearity was observed with just 2 photons/lifetime at non-linear threshold, thanks to the excellent one-dimensional waveguide property of the trumpet. This power level is within the same order of magnitude with the state of the art obtained with a QD-pillar micro-cavity system. The data was well fitted with a theoretical model, which indicated an excellent waveguide property as well as an efficient broadband operation feature of the trumpet.

Chapter 5

Two-mode giant non-linearity

The previous chapter has demonstrated the single-mode giant non-linearity of a one-dimensional artificial atom, in which the reflection of a single laser beam is modified by a two-level quantum emitter. This chapter aims at a cross giant non-linearity, based on a three-level system coupled with two laser beams at two different frequencies. We will show that the reflection of one beam can be controlled by the presence of another beam at a level of tens of photons, thus realizing an ultra-low power all-optical switch.

Contents

5.1	Introduction	87
5.1.1	Dressed states	87
5.1.2	Observation of dressed states	90
5.1.3	Dressed states of a three-level system via Bloch equations	93
5.1.4	Two-mode giant non-linearity with a quantum dot three-level system - Autler-Townes splitting approach	99
5.1.5	Two-mode giant non-linearity with a quantum dot three-level system - population switch approach	100
5.1.6	Evaluation of all-optical switch performances	101
5.1.7	Electromagnetically induced transparency versus Autler-Townes splitting	102
5.2	Experimental setup	105
5.2.1	Experimental procedure	106
5.3	Two-mode giant-nonlinearity: Autler-Townes splitting approach	107
5.3.1	Autler-Townes splitting	107
5.3.2	Autler-Townes splitting as a function of control laser power	109
5.3.3	A full scan over two excitonic fine-structure dipoles	112

5.3.4	Autler-Townes optical switch	115
5.4	Two-mode giant non-linearity: Population switch approach	123
5.4.1	Reflection measurement	124
5.4.2	Ultra-low power optical witch	125
5.5	Contributions of coherence and incoherence in total probe reflectivity	133
5.5.1	Autler-Townes splitting approach	134
5.5.2	Population switch approach	135
5.6	Switching time	135
5.7	A comparison with state of the art giant non-linearity	136
5.7.1	Single-mode giant non-linearity	136
5.7.2	Two-mode giant non-linearity	137
5.8	Chapter summary	140

5.1 Introduction

Chapter 4 has described the realization of a single-mode giant non-linearity with a two-level quantum dot (QD). In this chapter, we take into account a third energy level of a QD, the biexciton level, to form a “ladder” or “cascade” three-level system. To experimentally realize a two-mode non-linearity, a second laser beam is added to the system. We then have two laser beams coupled to two different transitions of the QD. One beam plays the role of controlling beam, its function is to modify and control the reflection of the other beam, considered as probe beam in a reflectivity measurement.

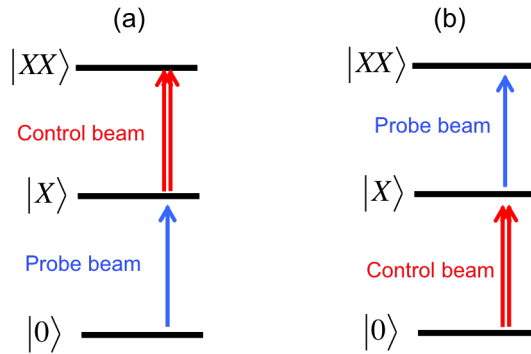


Figure 5.1 – Simple sketches describing the goal of this chapter: observing the modification of a probe beam in the presence of a control beam. Two approaches are considered: (a) the probe beam is coupled to the $0 \leftrightarrow X$ transition and the control beam is coupled to the $X \leftrightarrow XX$ transition; (b) reversed approach, the probe beam is coupled to the $X \leftrightarrow XX$ transition and the control beam is coupled to the $0 \leftrightarrow X$ transition.

In this chapter, two different approaches will be considered to realize a all-optical switch, by coupling the probe beam either to the lower or the upper transition of a three-level emitter. The first case as described in Fig. 5.1(a) is based on the dressed-atom approach [107], through an effect so called Autler-Townes splitting [137]. The second approach considers the case where the roles of two beams are inverted (Fig. 5.1(b)). The switch is then obtained due to a population effect. In both two approaches, taking advantage of the broadband high coupling efficiency of the photonic trumpets, we will show in the next sections the experimental realization a two-mode giant non-linearity at ultra-low level of power.

5.1.1 Dressed states

5.1.1.1 Rabi oscillations of the atomic system

Rabi oscillation is the direct consequence of interactions of light with discrete energy levels and is a fundamental example of non-linear light-matter interaction. We consider a classical field with frequency ω_C , coupled with a two-level system with ground state $|2\rangle$

and excited state $|3\rangle$ (the states are encoded like that because in the next sections, we will introduce the third state $|1\rangle$ to the system.). The transition frequency of the two-level system is ω_0 . The driving frequency is put on or close to resonance with the atom $|\delta_C| = |\omega_C - \omega_0| \ll \omega_0$. The general behavior of resonance fluorescence from the two-level system depends on the amplitude of the driving field. At low excitation regime, the two-level atom operates as a passive scatterer. The excited-state population is small and coherent scattering process dominates the emission. Increasing the excitation amplitude eventually saturates the emitter leading to inelastic scattering and to a decrease of the coherent term, as has been introduced in the previous chapter. The interaction between a two-level system and a quasi-resonant electromagnetic field leads to Rabi oscillations [138]: the population of the two-level system will Rabi oscillate between the ground and excited states at the generalized Rabi frequency [107]:

$$\Omega_1 = \sqrt{\delta_C^2 + \Omega^2} \quad (5.1)$$

where Ω is the Rabi frequency of the driving field $\Omega = \mathbf{d}E/\hbar$ (\mathbf{d} is the electric dipole moment and E is the field amplitude). The damping of Rabi oscillations is due to the spontaneous emission rate γ and the pure dephasing rate γ^* of the two-level atom. Thus Rabi oscillations decay at the dipole decoherence rate. Therefore, in order to spectrally resolve Rabi oscillations, the condition $\Omega_1 \geq (\gamma + \gamma^*)$ must be met. Rabi oscillations introduce the frequency Ω_1 into the dynamics of the system. This effect can be observed spectrally in absorption measurement in Autler-Townes approach [137], under the influence of a strong resonant pump. The following sections will explain in details how we can use this approach to obtain two-mode giant non-linearity.

5.1.1.2 A two-level atom interacts with a quantized field: Dressed states approach

Considering the interaction of the atom with a coherent electromagnetic field, the Rabi results can be seen from the point of view of the dressed states picture. Rabi oscillations can be described by Jaynes-Cummings model which describes the interaction of the two-level atom with a single mode quantum laser field [139]. The laser field can be considered as a coherent source. Following the assumption of C. Cohen-Tannoudji in [107], to simplify the quantum description of the laser field, the laser is considered as a cavity without losses, having only one mode with frequency ω_C (in the real experiment, the atom is not in a cavity, but instead interacts in free space with an incident laser). The laser mode has an average number of photons N . The energy density of the mode is N/V where V is the volume of the interaction region. N and V can be considered very large since only the ratio N/V is significant because it is related to the energy density.

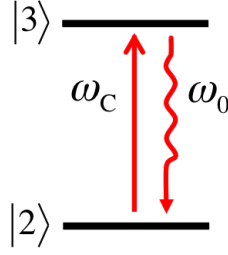


Figure 5.2 – An electromagnetic field coupled to a two-level quantum emitter with ground state $|2\rangle$ and excited state $|3\rangle$.

The laser frequency ω_C is put on or close to resonance with the atom $|\delta_C| = |\omega_C - \omega_0| \ll \omega_0$. The atom in the state $|2\rangle$ can absorb one photon and go to state $|3\rangle$. Two states $|2, N+1\rangle$ and $|3, N\rangle$ are very close to each other near resonance, they form a manifold. Similarly, in another manifold, the state $|2, N\rangle$ is coupled to $|3, N-1\rangle$. In the rotating wave approximation, the total Hamiltonian of the atom-laser system is the sum of laser Hamiltonian, atomic excitation Hamiltonian, and the Jaynes-Cummings interaction Hamiltonian:

$$H_{JC} = H_{laser} + H_{atom} + V_{AL} \quad (5.2)$$

$$H_{JC} = \hbar\omega_C a^\dagger a + \frac{1}{2}\hbar\omega_0 \sigma_z + \hbar g(a\sigma^+ + a^\dagger\sigma^-) \quad (5.3)$$

Where a^\dagger and a are the creation and operation operators. $\sigma^+ = |3\rangle\langle 2|$ and $\sigma^- = |2\rangle\langle 3|$ and $\sigma_z = |3\rangle\langle 3| - |2\rangle\langle 2|$ are the atomic operators. g is the coupling constant [107].

Eq. 5.3 can be rewritten as

$$H_{JC} = \hbar\omega_C(a^\dagger a + \frac{\sigma_z}{2}) + \frac{1}{2}\hbar\delta_C \sigma_z + \hbar g(a\sigma^+ + a^\dagger\sigma^-) \quad (5.4)$$

Under the rotating wave approximation, the first term of Eq. 5.4 possesses the total number of excitation $N = a^\dagger a + \frac{\sigma_z}{2}$ which is the constant of motion. We consider a basis that contains only two states $|2, N+1\rangle$ and $|3, N\rangle$. The Hamiltonian matrix can be decomposed into blocks of 2×2 matrices, each block contains a particular N .

The interaction Hamiltonian V_{AL} couples the two state $|2, N+1\rangle$ and $|3, N\rangle$ to each other. The corresponding matrix element is written

$$v_N = \langle 3, N | V_{AL} | 2, N+1 \rangle = \hbar g \sqrt{N+1} = \hbar \mathbf{d} E \quad (5.5)$$

then the sub-matrix can be obtained as

$$\begin{aligned}
H_N &= \hbar \begin{pmatrix} N\omega_C + \frac{\omega_0}{2} & g\sqrt{N+1} \\ g\sqrt{N+1} & (N+1)\omega_C - \frac{\omega_0}{2} \end{pmatrix} \\
&= \hbar \left(N + \frac{1}{2}\right) \omega_L \begin{pmatrix} 1 & 0 \\ 0 & 1 \end{pmatrix} + \hbar \begin{pmatrix} \delta_C/2 & g\sqrt{N+1} \\ g\sqrt{N+1} & -\delta_C/2 \end{pmatrix}
\end{aligned} \tag{5.6}$$

By diagonalizing this matrix, we find the two eigen values

$$\begin{aligned}
E_{|+,N\rangle} &= \hbar \left(N + \frac{1}{2}\right) \omega_C + \frac{1}{2} \hbar \Omega_N \\
E_{|-,N\rangle} &= \hbar \left(N + \frac{1}{2}\right) \omega_C - \frac{1}{2} \hbar \Omega_N
\end{aligned} \tag{5.7}$$

With the generalized Rabi frequency

$$\Omega_N = \sqrt{\delta_C^2 + 4g^2(N+1)} = \sqrt{\delta_C^2 + \Omega^2} \tag{5.8}$$

where the value $\Omega = 2g\sqrt{N+1}$ can be called quantum electrodynamic Rabi frequency, or just Rabi frequency of the driving field [107]. Since $N \gg 1$, the Rabi frequency can be simplified as $\Omega = 2g\sqrt{N}$

The eigenstates $|+, N\rangle$ and $|-, N\rangle$ associated with the eigenenergies are given by

$$\begin{aligned}
|+, N\rangle &= \sin(\theta_R) |2, N+1\rangle + \cos(\theta_R) |3, N\rangle \\
|-, N\rangle &= \cos(\theta_R) |2, N+1\rangle - \sin(\theta_R) |3, N\rangle
\end{aligned} \tag{5.9}$$

where the angle θ_R is defined by

$$\tan 2\theta_R = -\frac{\Omega_N}{\delta_C} \quad 0 \leq 2\theta_R \leq \pi \tag{5.10}$$

These two eigenstates $|+, N\rangle$ and $|-, N\rangle$ are called the dressed states, which are separated by an interval $\hbar\Omega_N = \hbar\sqrt{\delta_C^2 + \Omega^2}$. The illustration of dressed states are described in Fig. 5.3, the two initial uncoupled states $|2, N+1\rangle$ and $|3, N\rangle$ is dressed and split when taken into account the coupling. Two new states $|+, N\rangle$ and $|-, N\rangle$ are formed and symmetrically located with respect to the uncoupled states.

5.1.2 Observation of dressed states

We have seen in the previous section that the resonant interaction between a laser beam with frequency ω_L and a two-level atom results in the formation of dressed states which are separated by $\hbar\sqrt{\delta_C^2 + \Omega^2}$. The splitting depends on the detuning of the laser frequency and on the power of the incoming laser field, namely the control laser field. The dressed

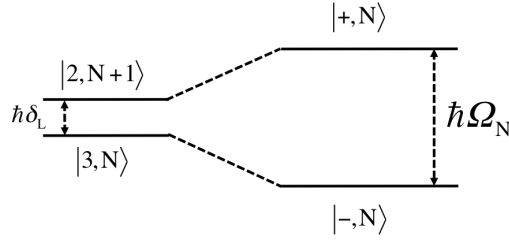


Figure 5.3 – Dressed states scheme between an atom and an excitation field: uncoupled states in the left-hand side and dressed states in the right-hand side in manifold N .

states under the presence of a control field can be observed spectrally by measuring the absorption spectrum of a second weak probe field. The weak probe field intensity is considered very low compared to the saturation power, to make sure it does not introduce any perturbation to the atom dressed by the control field. The two most common cases are when the probe field couples to the same or to a different transition as the control field. The following sections will discuss these two cases.

5.1.2.1 Mollow triplet

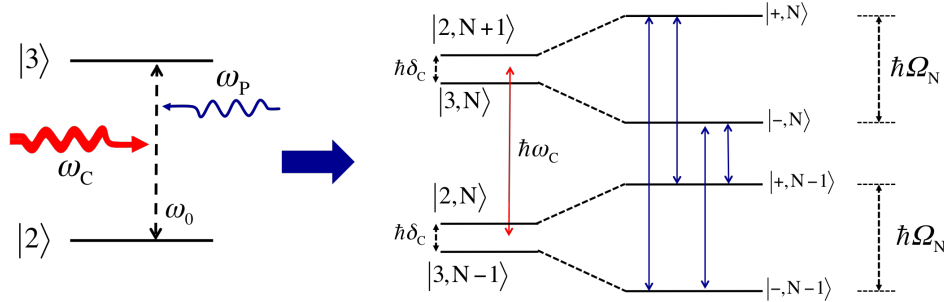


Figure 5.4 – The second laser beam couples the transition and leads to the formation of the Mollow triplet.

In the first case, the second weak probe beam is on resonance with the same transition $|2\rangle$ and $|3\rangle$ of the atom. The configuration is presented in Fig. 5.4. The configuration is described in the left scheme, the probe beam has the frequency ω_P and not far from the atomic frequency ω_0 that $|\omega_P - \omega_0| \ll \omega_0$. Without atom-field interaction, the two uncoupled states $|2, N+1\rangle$ and $|3, N\rangle$ have almost the same energy and form a manifold. The dressed states are created when taking into account the light-matter interaction. The result of the coupling is the generation of the dressed states $|+, N-1\rangle$ and $|- , N-1\rangle$ as can be seen in the right scheme of Fig. 5.4. Since N is large, $g\sqrt{N+1} \approx g\sqrt{N}$, the splittings are therefore similar in different manifolds. Under a strong control field, four dressed states are formed. The absorption of the weak probe field is now measured. The transitions between the two dressed states within the same manifold are not allowed .

Four transitions connecting the two dressed states of two adjacent manifolds are allowed at frequencies ω_C and $\omega_C \pm \Omega_N$. Thus, in the absorption spectrum of the probe field, a triplet is formed, which is called Mollow triplet [117, 131]. The two transitions between $|+, N\rangle$, $|+, N-1\rangle$ and $|-, N\rangle$, $|-, N-1\rangle$ have the same frequency ω_C and correspond to the central and the dominant peak of the emission spectra. Two other satellite emission peaks are positioned symmetrically around the central peak with a distance $\pm\Omega_N$. Mollow triplet was observed firstly with atom [117] and then with semiconductor QDs in several experiments [121, 122, 140].

5.1.2.2 Autler-Townes doublet

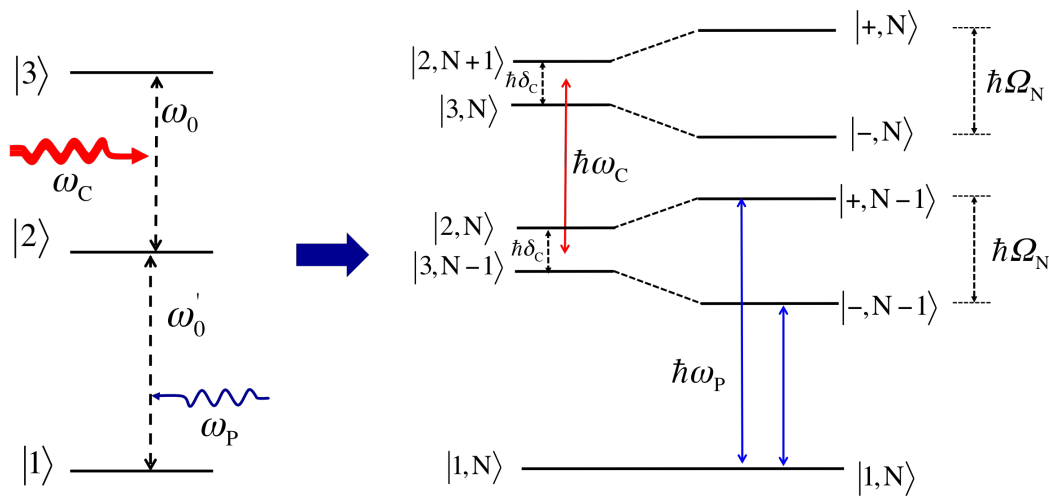


Figure 5.5 – Pump-Probe experiment of a three-level system, AT doublet.

The second approach concerns a pump-probe experiment of a three-level atom, where the weak probe beam is now coupled to a different transition sharing a common level with the initial transition, as described on the left of Fig. 5.5. The third level $|1\rangle$ is introduced to the atom and is positioned below level $|2\rangle$. The frequency of this lower transition is ω'_0 and we assume that $\omega'_0 - \omega_0$ is large enough so we can ignore any perturbation produced by an intense control beam (with frequency ω_C) on the level $|1\rangle$. Under a strong resonant control field, dressed states are formed. Assuming that $|1, N\rangle$ remains unchanged in the presence of the control field, the transition with frequency close to ω'_0 is probed by the second weak beam. This transition is limited to $|1, N\rangle \leftrightarrow |2, N\rangle$ without the control field ($\Omega = 0$). When $\Omega > 0$, the dressed states $|+, N-1\rangle$ and $|-, N-1\rangle$ appear, leading to two possible probe probe transitions $|1, N\rangle \leftrightarrow |+, N-1\rangle$ and $|1, N\rangle \leftrightarrow |-, N-1\rangle$ with frequencies $\omega'_0 - \frac{\delta_C}{2} - \frac{\Omega_N}{2}$ and $\omega'_0 - \frac{\delta_C}{2} + \frac{\Omega_N}{2}$, respectively. The corresponding doublet is called Autler-Townes doublet [137].

The energy difference between the Autler-Townes doublet is equal to Ω_N . So, if we keep

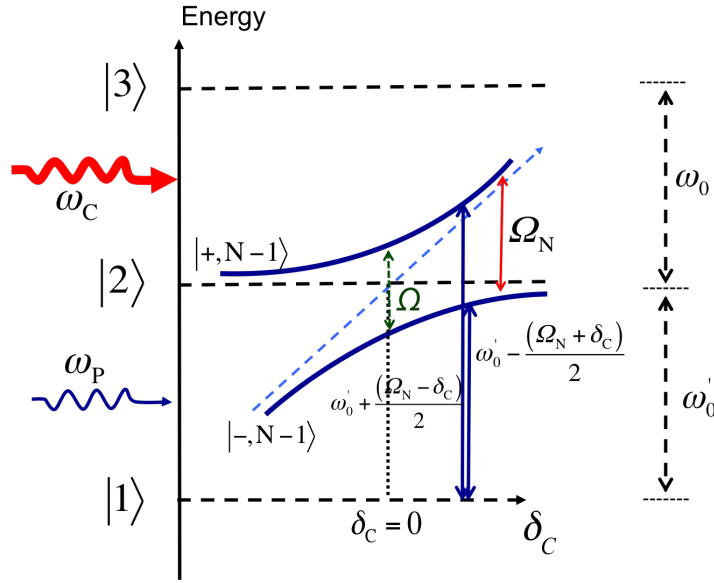


Figure 5.6 – Energy evolution of the dressed states as a function of the pump laser detuning δ_C .

the same control laser intensity (Ω is constant) and vary the control frequency detuning δ_C , the evolution of the absorption field is therefore similar to the evolution of the two dressed states $|+, N-1\rangle$ and $|-, N-1\rangle$, with an anti-crossing characteristic as illustrated in Fig. 5.6. The minimum distance between two branches is equal to the Rabi frequency of the strong control beam Ω and that occurs when $\omega_C = \omega_0$. Two solid arrows represent two components of the Autler-Townes doublet, at resonance ($\delta_C = 0$), we obtain two lines at frequencies $\omega'_0 \pm \Omega/2$.

The Autler-Townes doublet indicates that, for a three-level system, the absorption line of a weak probe laser beam tuned over the transition $|1\rangle \longleftrightarrow |2\rangle$ is split into two components if the transition $|2\rangle \longleftrightarrow |3\rangle$ is resonantly coupled to an intense control laser beam. Thus, an optical switch can be obtained if we look at the transmission or reflection of the probe field ω_P , with and without the presence of the control field ω_C .

5.1.3 Dressed states of a three-level system via Bloch equations

This section will give detailed analytical discussions of the non-linear effect resulting from the interaction between a three-level atom and two electromagnetic fields. We consider a three-level ladder system with the state $|1\rangle$, $|2\rangle$ and $|3\rangle$, forming a cascade. Three states have energies $\hbar\omega_{11}$, $\hbar\omega_{22}$ and $\hbar\omega_{33}$, respectively. The Hamiltonian for a three-level atom is

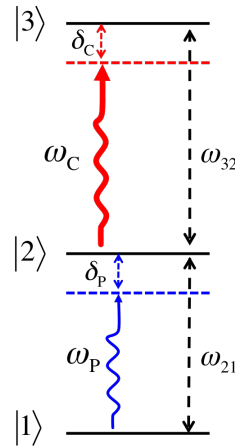


Figure 5.7 – A cascade three-level system is coupled simultaneously with two different fields, namely probe and control fields. The probe field with frequency ω_P is tuned around the transition $|1\rangle \longleftrightarrow |2\rangle$ frequency ω_{21} with detuning δ_P . The control field with frequency ω_C is tuned around the transition $|2\rangle \longleftrightarrow |3\rangle$ frequency ω_{32} with detuning δ_C . The goal is to see how the presence of the control field affects the absorption spectra of the probe field.

$$H_A = \hbar \begin{pmatrix} \omega_{11} & 0 & 0 \\ 0 & \omega_{22} & 0 \\ 0 & 0 & \omega_{33} \end{pmatrix} \quad (5.11)$$

The transition $|1\rangle \longleftrightarrow |2\rangle$ and $|2\rangle \longleftrightarrow |3\rangle$ have transition frequencies $\omega_{21} = \omega_{22} - \omega_{11}$ and $\omega_{32} = \omega_{33} - \omega_{22}$, respectively. Two electromagnetic fields are applied to the upper and lower transitions of the system: ε_P tuned around the transition $|1\rangle \longleftrightarrow |2\rangle$ and ε_C around the transition $|2\rangle \longleftrightarrow |3\rangle$. The scheme is described in Fig. 5.7, ε_P and ε_C are called as probe and control fields, respectively.

The Hamiltonian for the three-level system and the two fields is,

$$H = H_A + V_P + V_C \quad (5.12)$$

Where the interactions of atom with probe and control fields are,

$$V_P = -\mathbf{d}_P \cdot \mathbf{E}_P \cos(\omega_P t) \quad (5.13)$$

$$V_C = -\mathbf{d}_C \cdot \mathbf{E}_C \cos(\omega_C t)$$

with \mathbf{d} is the atomic dipole, ω_P and ω_C are respectively the frequencies of the probe and control fields. Consider the probe field, for the transition between states $|1\rangle$ and $|2\rangle$,

the atomic dipole is given by

$$\mathbf{d}_P = \mathbf{d}_{12} (|2\rangle \langle 1| + |1\rangle \langle 2|) \quad (5.14)$$

The interaction V_P can be rewritten in the terms of the raising and lowering operators,

$$V_P = \frac{\hbar\Omega_P}{2} (|2\rangle \langle 1| e^{i\omega_P t} + |2\rangle \langle 1| e^{-i\omega_P t} + |2\rangle \langle 1| e^{i\omega_P t} + |2\rangle \langle 1| e^{-i\omega_P t}) \quad (5.15)$$

where,

$$\hbar\Omega_P = -\mathbf{d}_{12} \cdot \mathbf{E}_P \quad (5.16)$$

$$\mathbf{d}_{12} = \langle 1| \mathbf{d} |2\rangle \quad (5.17)$$

with Ω_P (Ω_C) the Rabi frequency of the probe (control) laser field. Similar transformation is done for the interaction V_C . In the rotating wave approximation, we have [107]

$$V_P = \frac{\hbar\Omega_P}{2} (|2\rangle \langle 1| e^{i\omega_P t} + |1\rangle \langle 2| e^{-i\omega_P t}) \quad (5.18)$$

$$V_C = \frac{\hbar\Omega_C}{2} (|3\rangle \langle 2| e^{i\omega_C t} + |2\rangle \langle 3| e^{-i\omega_C t})$$

The Hamiltonian for V_P and V_C can be written in the form

$$V = V_P + V_C = \hbar \begin{pmatrix} 0 & (\Omega_P/2) e^{-i\omega_P t} & 0 \\ (\Omega_P/2) e^{i\omega_P t} & 0 & (\Omega_C/2) e^{-i\omega_C t} \\ 0 & (\Omega_C/2) e^{i\omega_C t} & 0 \end{pmatrix} \quad (5.19)$$

The resulting total Hamiltonian of the system is,

$$H = \hbar \begin{pmatrix} \omega_{11} & (\Omega_P/2) e^{-i\omega_P t} & 0 \\ (\Omega_P/2) e^{i\omega_P t} & \omega_{22} & (\Omega_C/2) e^{-i\omega_C t} \\ 0 & (\Omega_C/2) e^{i\omega_C t} & \omega_{33} \end{pmatrix} \quad (5.20)$$

The density matrix ρ for the three-level system is a 3×3 matrix in which the matrix elements $\rho_{12} = \rho_{21}^*$ and $\rho_{23} = \rho_{32}^*$ describe the coherences for the dipole transitions. The matrix element $\rho_{13} = \rho_{31}^*$ describes the two-photon non-radiative coherence and $\rho_{11}, \rho_{22}, \rho_{33}$ represent the populations of three levels.

We want to derive the equations of motion for the density matrix elements, based on Liouville equation [141],

$$\dot{\rho}_{mn} = \frac{i}{\hbar} [\rho, H]_{mn} - (\gamma\rho)_{mn} \quad (5.21)$$

where we have

$$[\rho, H]_{mn} = \sum_k (\rho_{mk} H_{kn} - H_{mk} \rho_{kn}) \quad (5.22)$$

$$(\gamma\rho)_{mn} = \gamma_{mn} \rho_{mn}$$

Here the decay rate γ_{mn} is introduced to the system. For simplification, we assume that we have an ideal three-level system, without any spectral broadening (like pure dephasing or spectral diffusion).

The “slow” density matrix elements, after removing the rapidly varying components of the dipole coherences are written as:

$$\rho_{12} = \tilde{\rho}_{12} e^{-i\omega_P t} \quad (5.23)$$

$$\rho_{23} = \tilde{\rho}_{23} e^{-i\omega_C t}$$

$$\rho_{13} = \tilde{\rho}_{13} e^{-i(\omega_P + \omega_C)t}$$

We also make the replacements:

$$\rho_{11} = n_1 \quad (5.24)$$

$$\rho_{22} = n_2$$

$$\rho_{33} = n_3$$

where the total population of the system is normalized so that $n_1 + n_2 + n_3 = 1$.

In the rotating-wave approximation, we then obtain the following set of optical Bloch equations:

$$\dot{\tilde{\rho}}_{12} = (i\delta_P - \gamma_{21})\tilde{\rho}_{12} - \frac{i\Omega_P}{2}(n_2 - n_1) + \frac{i\Omega_C}{2}\tilde{\rho}_{13} \quad (5.25)$$

$$\dot{\tilde{\rho}}_{23} = (i\delta_C - \gamma_{32})\tilde{\rho}_{23} - \frac{i\Omega_C}{2}(n_3 - n_2) - \frac{i\Omega_P}{2}\tilde{\rho}_{13} \quad (5.26)$$

$$\dot{\tilde{\rho}}_{13} = [i(\delta_P + \delta_C) - \gamma_{31}]\tilde{\rho}_{13} - \frac{i\Omega_P}{2}\tilde{\rho}_{23} + \frac{i\Omega_C}{2}\tilde{\rho}_{12} \quad (5.27)$$

where $\delta_P = \omega_P - \omega_{21}$, $\delta_C = \omega_C - \omega_{32}$ are the detunings of the probe and control fields, respectively, around the frequencies of the lower and upper transitions.

Assuming that $|1\rangle$ is the ground state of the system and that the probe field Ω_P is very small, so that most of the population is in the state $|1\rangle$ while the two other states are unoccupied. Eqs. 5.25 become,

$$\dot{\tilde{\rho}}_{12} = (i\delta_P - \gamma_{21})\tilde{\rho}_{12} + \frac{i\Omega_P}{2} + \frac{i\Omega_C}{2}\tilde{\rho}_{13} \quad (5.28)$$

$$\dot{\tilde{\rho}}_{23} = (i\delta_C - \gamma_{32})\tilde{\rho}_{23} - \frac{i\Omega_P}{2}\tilde{\rho}_{13} \quad (5.29)$$

$$\dot{\tilde{\rho}}_{13} = [i(\delta_P + \delta_C) - \gamma_{31}]\tilde{\rho}_{13} - \frac{i\Omega_P}{2}\tilde{\rho}_{23} + \frac{i\Omega_C}{2}\tilde{\rho}_{12} \quad (5.30)$$

One could see from Eq. 5.31 that in the absence of the control field ($\Omega_C = 0$), we end up with the usual Bloch equation for a laser and a two-level system interaction, so that the third level can be ignored.

In the steady-state regime, $\dot{\tilde{\rho}}_{12} = \dot{\tilde{\rho}}_{23} = \dot{\tilde{\rho}}_{13} = 0$, we then have,

$$\frac{i\Omega_C}{2}\tilde{\rho}_{13} = -(i\delta_P - \gamma_{21})\tilde{\rho}_{12} - \frac{i\Omega_P}{2} \quad (5.31)$$

$$\frac{i\Omega_P}{2}\tilde{\rho}_{13} = (i\delta_C - \gamma_{32})\tilde{\rho}_{23} \quad (5.32)$$

$$\frac{i\Omega_C}{2}\tilde{\rho}_{12} = -[i(\delta_P + \delta_C) - \gamma_{31}]\tilde{\rho}_{13} + \frac{i\Omega_P}{2}\tilde{\rho}_{23} \quad (5.33)$$

Since the amplitude of the probe field is very small, its Rabi frequency $\Omega_P \ll \gamma_{21}, \Omega_C$ (which is consistent with the conditions for Autler-Townes splitting considered in the above section) so that the last term in Eq. 5.33 can be neglected. Substitute Eq.5.33 into Eq. 5.31, we then have the final expression

$$\tilde{\rho}_{12} = -\frac{i\Omega_P}{2} \left[(i\delta_P - \gamma_{21}) + \frac{\Omega_C^2/4}{i(\delta_P + \delta_C) - \gamma_{31}} \right]^{-1} \quad (5.34)$$

Eq. 5.34 can be rewritten as

$$\tilde{\rho}_{12} = \frac{-\frac{i\Omega_P}{2}[i(\delta_P + \delta_C) - \gamma_{31}]}{(i\delta_P - \gamma_{21})[i(\delta_P + \delta_C) - \gamma_{31}] + \frac{\Omega_C^2}{4}} \quad (5.35)$$

The absorption A_P of the probe beam scanned across the transition $|1\rangle \longleftrightarrow |2\rangle$ is proportional to the imaginary part of the coherence $\tilde{\rho}_{21}$:

$$A_P \propto \text{Im} \left[\frac{\tilde{\rho}_{12}}{\Omega_P} \right] \quad (5.36)$$

Fig. 5.8 plots the absorption of the transition $|1\rangle \longleftrightarrow |2\rangle$. Firstly, in the absence of the control field as shown in Fig. 5.8(a), the system behave as a two-level system driven by a single field. When the strong second field ($\Omega_C = 5\gamma_{21}$) is introduced to couple with the upper transition $|2\rangle \longleftrightarrow |3\rangle$, the absorption of the lower transition $|1\rangle \longleftrightarrow |2\rangle$ changed drastically. The anti-crossing feature obtained in Fig. 5.8(b) is described by dressed atom approach in the section above and is a clear evidence of Autler-Townes effect. The

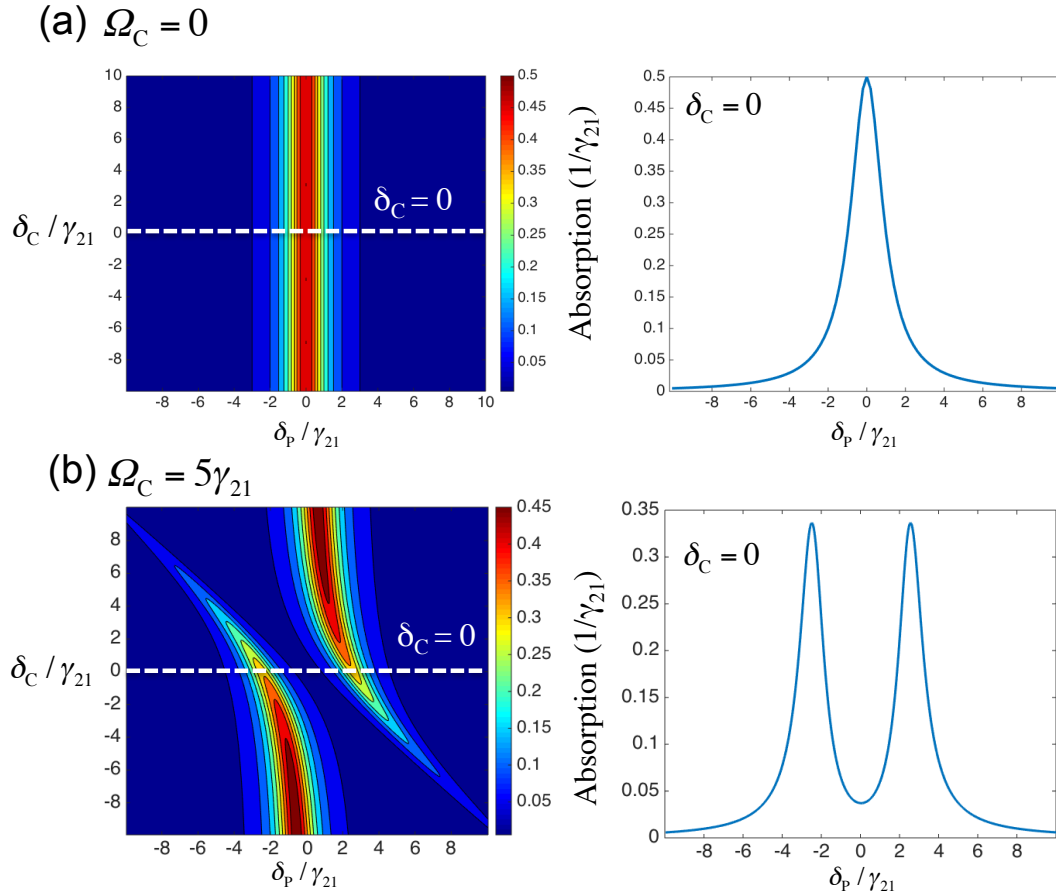


Figure 5.8 – Absorption of transition $|1\rangle \leftrightarrow |2\rangle$ as a function of field detunings - In this case, we consider $\gamma_{31} = 0.5\gamma_{21}$. The Rabi frequency of probe field $\Omega_P = 10^{-3} \times \gamma_{21}$. Two values of Rabi frequency are plotted: (a) $\Omega_C = 0$ and (b) $\Omega_C = 5\gamma_{21}$. The two figures in the left show the absorption as a function of δ_P/γ_{21} at $\delta_C = 0$ (correspond to the dash line of the two-dimensional figures in the left).

absorption of a resonant probe beam is thus dramatically changed by the presence of the control beam.

In the weak control field limit ($\Omega_C < \gamma_{21}$), it will be seen in section 5.1.7 that for a three-level system under two-photon resonance condition and if $\gamma_{31} = 0$ (which means transition $|1\rangle \longleftrightarrow |3\rangle$ is forbidden and there is no dephasing), we will obtain the interference effect which suppresses the absorption even under very weak control field Rabi frequency (so called electromagnetically induced transparency effect).

5.1.4 Two-mode giant non-linearity with a quantum dot three-level system - Autler-Townes splitting approach

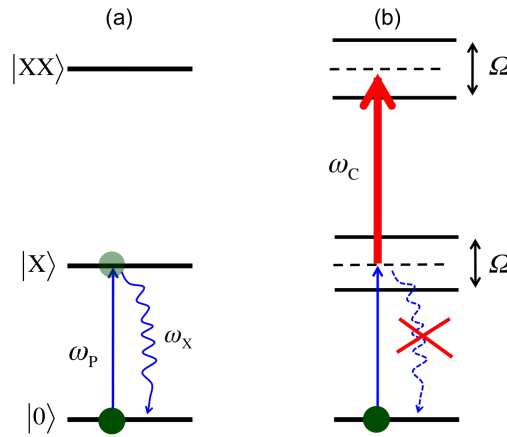


Figure 5.9 – A scheme of two-mode giant non-linearity for a QD three-level cascade system in Autler-Townes approach - Assuming that the system is placed inside a photonic trumpet. The reflectivity measurement is performed similar to what has been done in chapter 4 by looking at the reflection of an incoming beam at the output of the trumpet. (a) The ground, exciton (X), and biexciton (XX) states of a QD resemble a cascade three-level system. A probe beam is coupled the $0 \longleftrightarrow X$ transition. Without the presence of the control beam, the emitter behaves like a two-level system interacting with a resonant field. Assuming the power of the probe beam is very weak compared to the saturation power of $0 \longleftrightarrow X$ transition, then X level will absorb and re-emit all the photons. Thus, maximum reflection will be detected at the output. (b) A control beam is turned on and coupled resonantly to $X \longleftrightarrow XX$. At the power level of the control beam much larger than the linewidth of the transition (well above the saturation power), X and XX levels will be split into new dressed states. If the frequency of the probe beam is kept unchanged $\omega_P = \omega_X$, it will probe an empty level due to splitting. Thus, no emission is induced and zero reflection is obtained at the output. As a result, a all-optical switch is realized.

A semiconductor quantum dot (QD) can be considered as an artificial three-level atom, in which the ground, exciton (X) and biexciton (XX) states form a cascade system as illustrated in Fig. 5.9(a). We assume that the QD is perfectly symmetrical, so that there is no X fine-structure splitting (FSS) in this case. Without the presence of external fields, all the QD population is initially prepared in the ground state. This is consistent with the

assumption of the theoretical model above.

To obtain a all-optical switch, two laser beams are coupled to the system. A probe beam with frequency ω_P excites the $0 \longleftrightarrow X$ transition, whereas a control beam with frequency ω_C excites the $X \longleftrightarrow XX$ transition. The Rabi frequency Ω_P of the probe beam is kept very weak $\Omega_P \ll \gamma_X$ ($\gamma_X \equiv \gamma_{21}$). Without the presence of the control beam, one can ignore the XX level. The situation is then similar to the case presented in chapter 4 for a single beam coupled to a two-level system. In particular, if $P_{probe} \ll P_{saturation-X}$, at $\delta_P = 0$, the probe field is entirely absorbed by the $0 \longleftrightarrow X$ transition. X state reflects all the photons it absorbed owing to the one-dimensional structure of the waveguide. The emission can be detected in a reflectivity measurement as demonstrated in chapter 4. The reflectivity has a maximum value at vanishing probe power.

When the control beam is introduced to the system and is coupled to the $X \longleftrightarrow XX$ transition, at high enough power, Rabi oscillations give rise to the formation of X dressed states. As a result, at $\delta_P = 0$, X state splits and becomes transparent to a resonant probe beam and a suppression in absorption is obtained, realizing a all-optical switch.

5.1.5 Two-mode giant non-linearity with a quantum dot three-level system - population switch approach

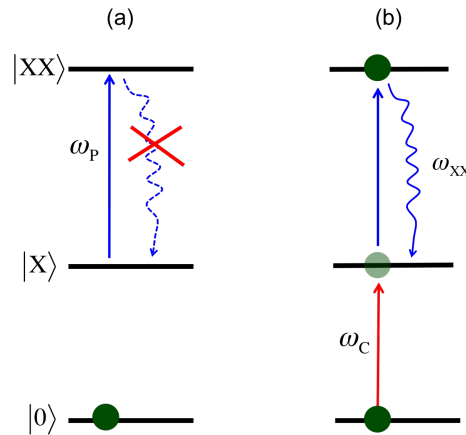


Figure 5.10 – A scheme of two-mode giant non-linearity for a QD three-level cascade system in a reversed approach - (a) In this approach, the probe beam is now coupled to $X \longleftrightarrow XX$ transition. Without a control beam, the probe beam is pumping an empty transition and therefore no emission is induced. The beam is completely transmitted. (b) A control beam with an arbitrary power less than saturation is turned on and resonantly coupled to $0 \longleftrightarrow X$ transition. X level is now populated so that the upper transition is no longer transparent. As a result, the probe beam is absorbed by $X \longleftrightarrow XX$ transition and the reflection is switched. We call this approach population switch.

In this section, we consider an alternative approach using the same system, but the roles of the control and probe fields are inverted. As showing in Fig. 5.10, $X \longleftrightarrow XX$

transition is now coupled to a weak probe beam while the $0 \longleftrightarrow X$ transition is coupled to a control beam.

Fig. 5.10(a) illustrates to the case when the control beam is absent. The initial X and XX states are unoccupied and have no population. Therefore, transition $X \longleftrightarrow XX$ is completely transparent and thus the probe beam is entirely transmitted. As a result, no reflection is detected.

However, as soon as a control beam is introduced to the system (Fig. 5.10(b)), X state will be populated due to an absorption of the control beam. In this case, the probe beam will be absorbed by $X \longleftrightarrow XX$ transition. For the probe beam with a power less than saturation of $X \longleftrightarrow XX$ transition, all the photons of the probe field will be absorbed and re-emitted. Part of this emission is guided to the output of the waveguide and detected. As a result, a all-optical switch is realized. This approach using population effect is called “population switch”. The switching contrast is obtained by comparing the reflection when the control laser is OFF and ON, one should notice that the contrast is always 100%, that $(P_{RON} - P_{ROFF}) / (P_{RON} + P_{ROFF}) = 1$, regardless of the control beam amplitude.

5.1.6 Evaluation of all-optical switch performances

We have proposed two approaches to realize a all-optical switch, based on two-mode giant non-linearity of a one-dimensional three-level system. The power of the probe beam is always ultra-weak, while the control beam power can be arbitrarily large. A switch is obtained by looking at the reflection of a probe beam in the absence or presence of a control beam. When the control beam is turned on, the first phenomenological difference between two approaches is that, in Autler-Townes approach, the probe beam is switched from reflection to transmission, whereas in population approach, the probe is switched from transmission to reflection.

For any potential low-power switch application, the power required to obtain a switch is a crucial factor that affects the performance of the device. For the Autler-Townes switch based on the splitting of dressed states under the pumping of a strong control beam (section 5.1.4), the higher the power amplitude, the larger the splitting is induced. Therefore, a switch would require the control beam power at least equal to the saturation power of the transition. By contrast, in the population switch approach (section 5.1.5), the condition to realize a switch is just a non-zero control power. In addition, this approach offers a switch with maximum contrast since the reflection is always zero without the presence of the control beam. For an ultra-weak probe power, its reflectivity depends on the population of the X intermediate state and is maximal at saturation of the control beam. One then should realize that for a control power higher than saturation, X state will be dressed and split due to Rabi oscillations. As a result, the X state becomes transparent to the probe beam, the reflection is then switched again from reflection to transmission.

5.1.7 Electromagnetically induced transparency versus Autler-Townes splitting

This section will discuss a special case of the interaction between a three-level system and two distinct laser fields that has been presented in section 5.1.3. By looking at Eq. 5.31, one could predict a destructive interference effect. The term $\frac{i\Omega_C}{2}\tilde{\rho}_{13}$ can counteract with the absorption coming from the term $\frac{i\Omega_P}{2}$. This interference effect would require the two-photon resonance condition for the non-radiative coherence $\tilde{\rho}_{13}$ in Eq. 5.30 [142]. For Ω_P infinitively small, the non-radiative coherence gives a two-photon resonance with a width γ_{31} centered at $\delta_P = -\delta_C$. Considering this two-photon resonance condition $\delta_P + \delta_C = 0$, from Eq. 5.35, the absorption has the form

$$A_P \propto \text{Im} \left[\frac{\tilde{\rho}_{12}}{\Omega_P} \right] = \gamma_{31} \frac{\gamma_{21}\gamma_{31} + \frac{\Omega_C^2}{4}}{\left(\gamma_{21}\gamma_{31} + \frac{\Omega_C^2}{4}\right)^2 + \delta_P^2\gamma_{31}^2} \quad (5.37)$$

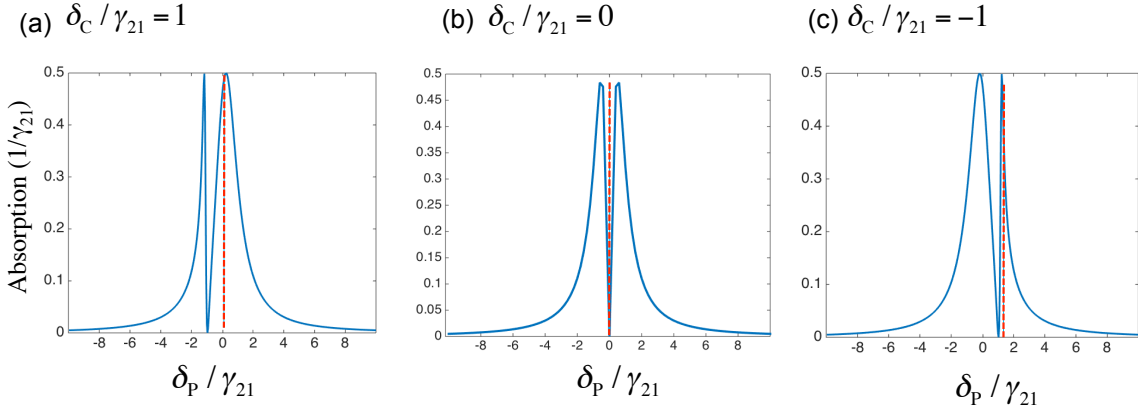


Figure 5.11 – Electromagnetically induced transparency effect - Absorption as a function of the probe field detuning δ_P for different control field detunings for the case $\gamma_{31} = 0$. The control field Rabi frequency $\Omega_C = \gamma_{21}$: (a) $\delta_C/\gamma_{21} = 1$, (b) $\delta_C/\gamma_{21} = 0$ and (c) $\delta_C/\gamma_{21} = -1$. At the probe field detuning δ_P satisfying the two-photon resonance condition $\delta_P + \delta_C = 0$, the interference effect causes the total suppression of the absorption.

One could see that if $\gamma_{31} = 0$, which means the dipole transition $|1\rangle \longleftrightarrow |3\rangle$ is forbidden, there is no absorption and transition $|1\rangle \longleftrightarrow |2\rangle$ is entirely transparent. Fig. 5.11 plots the absorption of transition $|1\rangle \longleftrightarrow |2\rangle$ as a function of probe field detuning for three different detunings of the control field. In all cases, when $\delta_P = -\delta_C$, a dip in absorption is observed. This dramatic change in absorption is the signature of electromagnetically induced transparency (EIT) effect. As has been pointed out above, the reason for the dip in absorption is the destructive interference (also called as Fano interference [143]) between two transitions $|1\rangle \longleftrightarrow |2\rangle$ and $|2\rangle \longleftrightarrow |3\rangle$. This interference thus induces the suppression in absorption even with a weak control field, leading to the transparency in

reflection spectrum. Thus, Fano interference effect discriminates EIT from Autler-Townes splitting. In the absence of Fano interference, we have seen that strong control field induces dressed states with frequency separation proportional to the control-field Rabi frequency Ω_C . This field-induced splitting also causes the reduction in absorption but exhibits no interference effect and corresponds to Autler-Townes splitting. In other words, one could say that the effect of EIT resembles a combination of Autler-Townes splitting and the Fano interference.

It was pointed out in [144, 145] that the strict condition to obtain Fano interference for a three-level system (for “lambda” and “ladder” system with control field coupled to the upper transition) at weak-control field is that, the third transition $|1\rangle \longleftrightarrow |3\rangle$ must be dipole forbidden, as in those plots in Fig. 5.8 with $\gamma_{31} = 0$. This is similar with what is predicted in Eq. 5.37. Under this condition, as soon as the control field with an arbitrarily power is introduced to the system, the absorption is canceled out and EIT is observed.

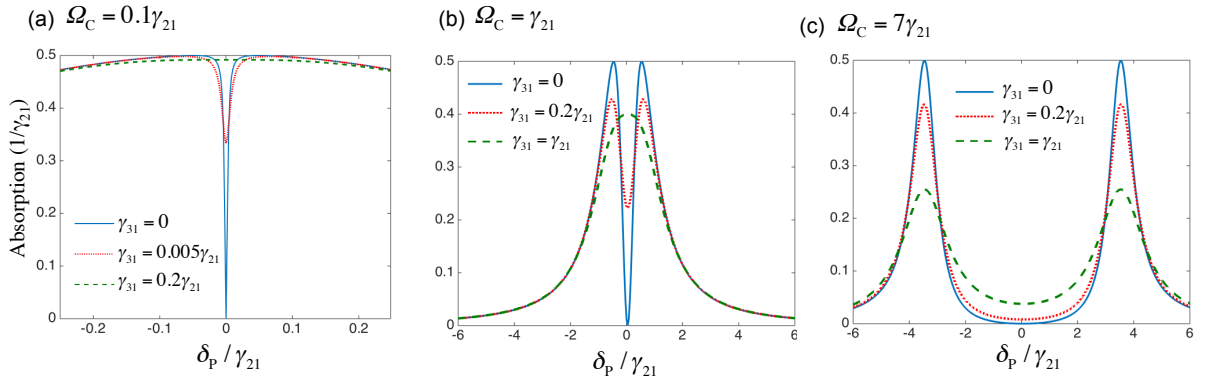


Figure 5.12 – Absorption spectra of transition $|1\rangle \longleftrightarrow |2\rangle$ at zero detuning of the control field $\delta_C = 0$ - The probe field Rabi frequency is kept very weak at $\Omega_P = 10^{-3} \times \gamma_{21}$. Different decay terms of transition $|1\rangle \longleftrightarrow |3\rangle$ γ_{31} is applied for each Rabi frequency of the control field: (a) $\Omega_C = 0.1\gamma_{21}$ (in this figure the detuning range of the probe field is zoomed to a short range since the EIT dip is very narrow), (b) $\Omega_C = \gamma_{21}$ and (c) $\Omega_C = 7 \times \gamma_{21}$.

In practice, with artificial atoms, especially semiconductor QDs, having a system with such EIT condition is very challenging. Because the system most of the time exhibits pure dephasing and other sources of spectral broadening due to the surrounding environment, so that for QDs, we always has $\gamma_{31} \neq 0$. Therefore, observing purely EIT with QDs is hardly possible.

To see how the factor γ_{31} affects the absorption of transition $|1\rangle \longleftrightarrow |2\rangle$, we consider a simple case where the control field detuning $\delta_C = 0$. From Eq. 5.35, the absorption becomes

$$A_P \propto \text{Im} \left[\frac{\tilde{\rho}_{12}}{\Omega_P} \right] = \frac{\delta_P^2 \gamma_{21} + \gamma_{31} \left(\frac{\Omega_C^2}{4} + \gamma_{21} \gamma_{31} \right)}{\left(\frac{\Omega_C^2}{4} - \delta_P^2 + \gamma_{21} \gamma_{31} \right)^2 + \delta_P^2 (\gamma_{21} + \gamma_{31})^2} \quad (5.38)$$

One could see that if $\gamma_{31} = 0$, zero absorption is obtained at the probe field detuning $\delta_P = \delta_C = 0$, regardless of the control field amplitude. However, for a non-zero γ_{31} , the absorption is no longer totally suppressed at two-photon resonance condition. Fig. 5.12 plots the absorption at $\delta_C = 0$ with different decay terms γ_{31} , for three different Rabi frequencies of the control field. When Ω_C is very small with respect to the decay rate of transition $|1\rangle \longleftrightarrow |2\rangle$ (Fig. 5.12(a)), the interference effect is observed when $\gamma_{31} = 0$. The interference is reduced when increasing γ_{31} as expected. The similar behavior is observed when $\Omega_C = \gamma_{21}$ (Fig. 5.12(b)).

At high control field Rabi frequency Ω_C as in Fig. 5.12(c), Fano interference is negligible since the intermediate state is dressed by a strong control field which leads to the emerging of dressed states with large frequency splitting. It leads to the reduction in absorption even with $\gamma_{31} > \gamma_{21}$ since EIT effects are dominated by Autler-Townes effect at that power level.

To conclude, the difference between EIT and Autler-Townes splitting is significant at low Rabi frequency range of the control field $\Omega_C \leq \gamma_{21}$, due to Fano interference effect. And it should be noted that the destructive interference is obtained efficiently only when the third transition $|1\rangle \longleftrightarrow |3\rangle$ decay rate $\gamma_{31} = 0$. Because of this tightly EIT restriction, experimental realization of the narrow absorption dip at weak control field has just been observed for limited systems. There have been a few reports which demonstrated the observation of narrow EIT transmission window, with atom [40, 146], nitrogen-vacancy centers in diamond [147], nanoscale optomechanical crystal [148] or with whispering-gallery-mode resonators [149]. Concerning semiconductor QDs, EIT has not been observed experimentally. This is because of the large dephasing in QDs transitions that inhibits the destructive interference needed for EIT. Proposals have been made to overcome this obstacle [150–152]. For example, it has been proposed that using hybrid system by placing QDs as optical emitters near a single plasmonic resonator could modify the lifetime and efficiency of the emitter and could induce a transparency dip in the surface-plasmon spectrum [152]. Purcell effect boosts radiative effects so that the system becomes less sensitive to dephasing.

With our system, due to the limit decoherence properties of the semiconductor QDs, narrow absorption dip in EIT is not expected to be observed. The strategy to obtain a all-optical switch will rely on the Autler-Townes approach that has been discussed in section 5.1.4.

5.2 Experimental setup

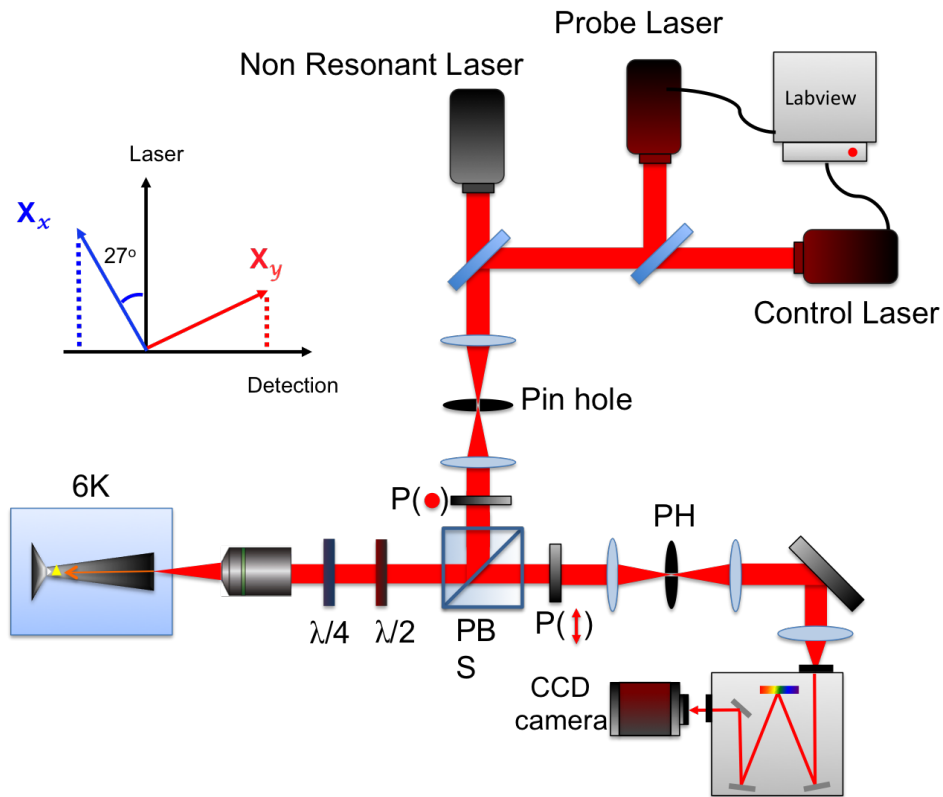


Figure 5.13 – Experimental setup of the two-mode giant non-linearity measurement - The same configuration as in chapter 4 is used. One more Toptica CW laser is added to the setup and it shares the path with other lasers toward the first pin hole and toward the sample. An ultra-weak non-resonant laser is always present in resonant excitation as explained in section 4.2.3.1. The cross-polarized detection is established with an angle 27° with respect to the X_x dipole polarization axis.

The setup configuration using cross-polarized detection is exactly the same as the single-mode giant non-linearity experiment, except for the addition of a second CW TOP-TICA laser, as can be seen in Fig. 5.13. This additional laser is also directed to the same pin hole and has the same optical path and polarization with two other lasers used in chapter 4. Two tunable Toptica lasers play the roles of control and probe beams as has been demonstrated in the previous sections.

It should be noted here that in this cross-polarized scheme, the angle θ is chosen to excite non-symmetrically two excitonic dipoles ($\theta = 27^\circ$ in this case) because the study will focus on one dipole of which the polarization (X_x) is closer to the laser polarization. Eq. 4.37 shows that the saturation powers of X_x and X_y scale as $\tan^2(\theta)$, which means having a smaller θ results in a smaller power needed to saturate X_x (see Fig. 4.24 for the single-mode giant non-linearities of two non-symmetrically excited dipoles in which the

power required to saturate X_x (blue curve) is smaller than that of the other one).

5.2.1 Experimental procedure

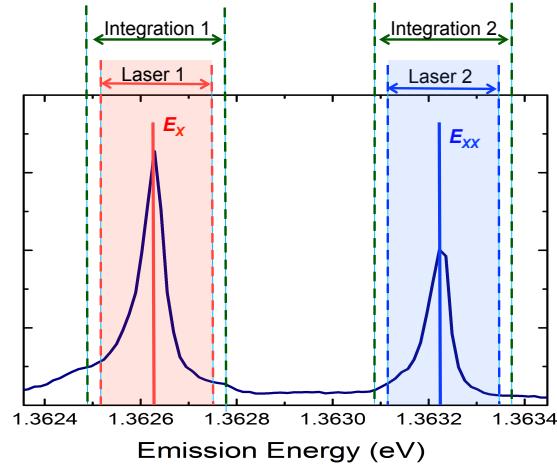


Figure 5.14 – Illustration of two-laser scan process - The scan ranges are defined by the PL spectra of the QD. The FSS of the excitonic level is $25 \mu eV$, so the range is set between a few tens of μeV to $85 \mu eV$, depending if we want to study one or both to FSS dipoles. The PL spectrum at each scanning step is recorded with the CCD camera and is integrated (see section 4.2.2.4 for more details) in a fixed range (normally more than $100 \mu eV$) that always covers the emission from both two FSS dipoles. Both the integrated reflections of two lasers are integrated and can be plotted as a function of two detunings in the form of a two-dimensional map.

The general goal of the experiment is to see how the reflection of a weak probe beam coupled to one transition is changed by the presence of a control beam coupled to a different transition. Such measurement requires that two beams are simultaneously resonant with different transitions. To be able to do that, the idea is to scan at the same time the frequencies of two beams around resonances, in which the effect should be observed during the scan.

We use the very same QD as in chapter 3 and 4, with FSS energy $25 \mu eV$. As described in Fig. 5.14, two lasers are scanned simultaneously around the X and XX energies (see section 3.3 and 3.2.3 for an identification of X and XX lines from a single QD). The idea is to sweep one laser, for example Laser 1 within its range while keeping the frequency of the Laser 2. After one sweep of Laser 1, the frequency of Laser 2 is changed by one step. Or in other words, in this measurement, the scan with a single laser is repeated several times (see section 4.2.2.4 for the full description of the single-laser scan), each time with a progression in frequency of the second laser until the second laser could cover its range. At each step of the scan, the CCD spectra are recorded and two integrations are made for two emission lines, as described in Fig. 5.14. Eventually, we can plot the reflected intensity of

one laser (usually the probe laser) as a function of both laser detunings, similar to what is plotted in Fig. 5.8. These two-dimensional maps contain the information of the reflection for every detuning of two lasers. The reflected intensity of the other laser is also recorded but is usually not of great interest.

The typical integration time of each point is 0.1s. The scanning range of the laser beam normally varies between a few tens of μeV to $85 \mu\text{eV}$, which is able to cover both two FSS dipoles when needed. The integration range is always large enough to integrate both the emissions from two fine-structure dipoles. The polarization angle θ between X_x and laser polarizations is set to be at 27° .

The following sections will demonstrate in details the results obtained following the Autler-Townes and the population approaches.

5.3 Two-mode giant-nonlinearity: Autler-Townes splitting approach

5.3.1 Autler-Townes splitting

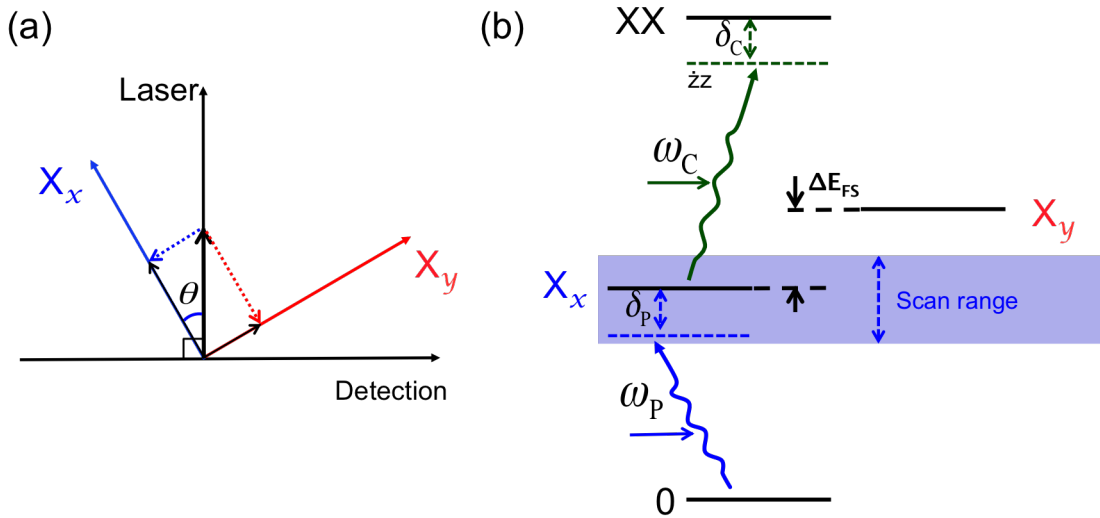


Figure 5.15 – Probe laser scans over X_x state - (a) Cross-polarization scheme showing that the dipole X_x chosen for a short scan has its polarization closer to the laser polarization (the angle θ is 27° compared with 63° of the other dipole). Thus, it will require less laser power to saturate X_x . (b) A full configuration describing a four-level quantum emitter. Firstly, the scan range is set that it is just enough to cover dipole X_x . In this case, the scan range for the probe beam is about $40 \mu\text{eV}$. Meanwhile, the scan range for the control beam is $80 \mu\text{eV}$, to make sure that the Autler-Townes effect is captured in the two-dimensional map.

In this approach, the probe laser is coupled to the lower transition (ground and X states), while the control laser is coupled to the upper transitions (X and XX states).

With the absence of the control laser, the situation is exactly the single-mode giant non-linearity where we have one single probe beam coupled to a two-level artificial atom. At first, we focus on the X_x dipole of the FSS doublet. The polarization of this FSS state is closer to the laser polarization as described in Fig. 5.15, the probe laser scan range is just enough to scan across the X_x line.

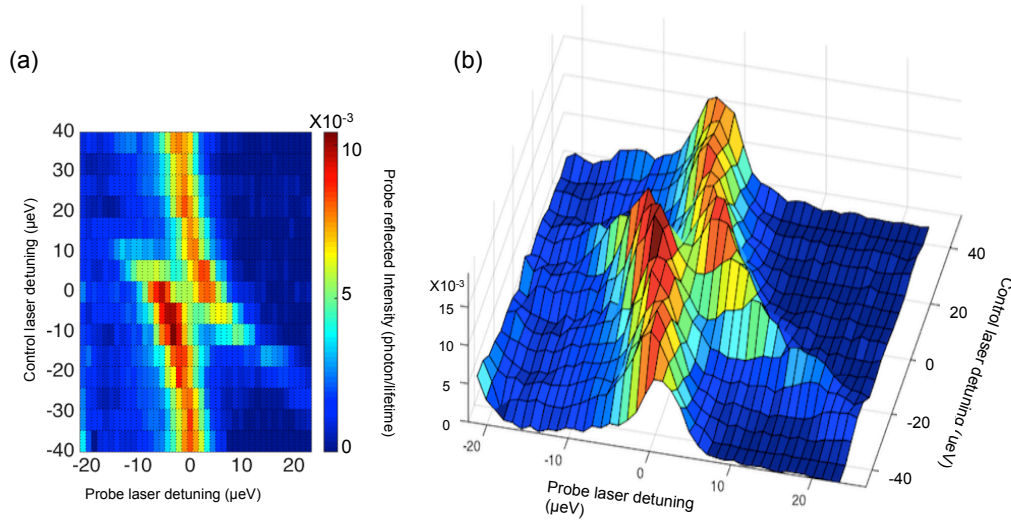


Figure 5.16 – Autler-Townes splitting of X_x transition - (a) Two-dimensional map with the horizontal and the vertical axes showing respectively the scanning of the probe and the control beam across the resonances. In this measurement, the power of the probe laser is put below the saturation power of the X_x level. The color scale indicates the reflected intensity of the probe laser. The power of the control laser is far above saturation so that it induces a significant Autler-Townes splitting

Fig. 5.16 shows a typical result for a two-laser scan. In the two-dimensional plot in Fig. 5.16(a), typical anti-crossing curves are observed. When the control laser is far detuned from resonance, one can see that there is no splitting and a single line is observed at the probe resonance, just like single probe laser resonant excitation in chapter 4. When the intense control laser approaches the resonance, it starts to give rise to Rabi oscillations and two new dressed states appear. Fig. 5.16(b) shows more clearly the evolution of the probe reflection in a three-dimensional point of view.

Fig. 5.17 shows in detail the resonant spectra of the X_x transition at different detunings of the control beam. Probe reflection spectra shows a normal single resonance peak when the control laser is far-detuned from resonance. When the control frequency is closer to resonance, a Autler-Townes doublet is formed. The relative amplitudes and the splitting of these two dressed states are controlled by the control detuning δ_C . The positions of two peaks with respect to the control laser detuning δ_C are $(\delta_C \pm \Omega_1)/2$ where Ω_1 is the

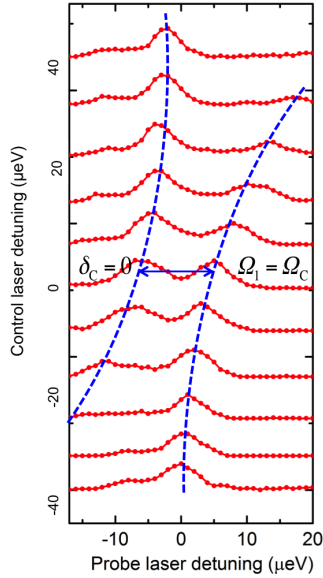


Figure 5.17 – Cross-section of probe reflection for different control detunings δ_C . One could see the formation of two dressed states when the control beam is scanned toward the resonance. The blue dashed lines give a guide to the eye for the anti-crossing feature of a Autler-Townes doublet.

generalized Rabi frequency as presented in section 5.1.1.2

$$\Omega_1 = \sqrt{\delta_C^2 + \Omega_C^2} \quad (5.39)$$

with Ω_C the Rabi frequency of the control laser. The quantity Ω_1 also gives the splitting between the Autler-Townes doublet, therefore we also call Ω_1 the Autler-Townes splitting. At zero detuning $\delta_C = 0$, the dressed states have an equal admixture of the X state and the ground state, resulting in the two equal amplitude peaks, and the Autler-Townes splitting of the two peaks is $\Omega_1 = \Omega_C$.

5.3.2 Autler-Townes splitting as a function of control laser power

To understand the dependence of the Autler-Townes splitting when changing the power of the control laser, several scans are performed with different control laser powers and the results are shown in Fig. 5.18. At the power of the control laser 19.5 nW, a slight spectral broadening is observed indicating that the excitonic state starts to be split. Increasing further the control laser power, Autler-Townes splitting becomes significant and two dressed states are well resolved with an anti-crossing feature when changing the control laser detuning. To have a closer look of the effect, Fig. 5.19(a) shows the probe reflection (black circles) for different control laser powers at zero detuning $\delta_C = 0$. The red lines are the

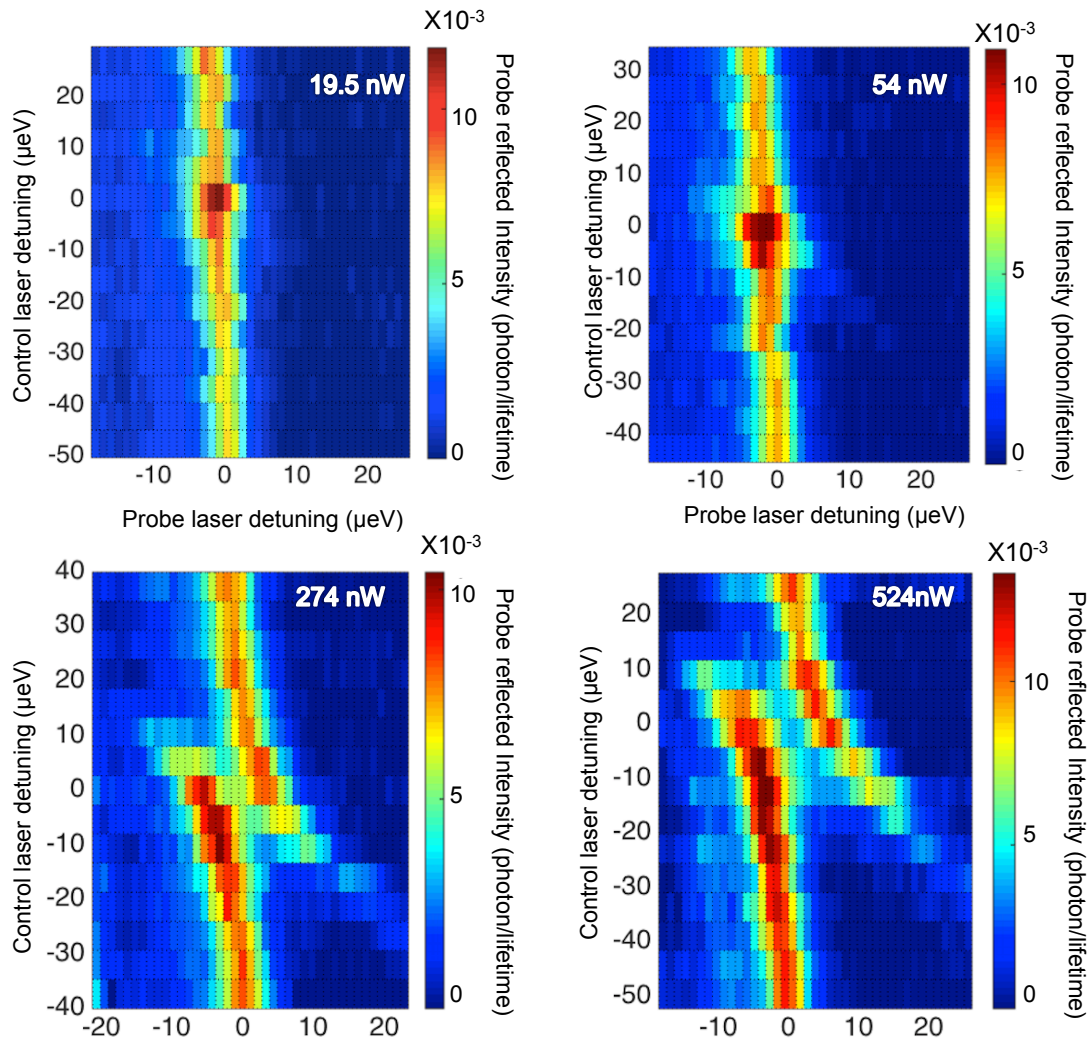


Figure 5.18 – Two-laser scan of probe reflection with different powers of control laser powers - The probe laser power is kept at the power below the saturation power ($P_{probe}/P_{sat} = 0.2$). The probe and control laser scanning ranges are 40 μeV and 80 μeV , respectively.

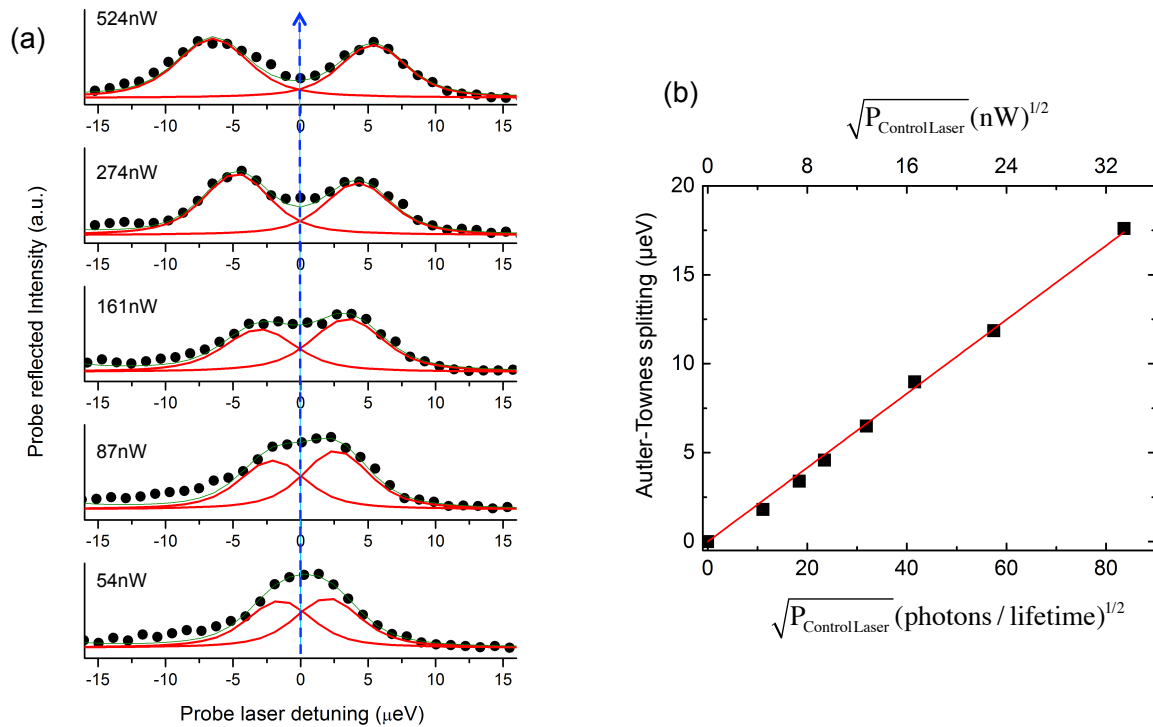


Figure 5.19 – Probe reflected intensity at zero detuning of control laser - (a) Probe reflection with increasing the control laser power at $\delta_C = 0$. The experimental data (black circles) is fitted showing the contribution of two dressed states (red curves). The dashed arrow at the zero detuning of probe laser shows the reduction in probe reflection when increasing the control power, which is the indication of two-mode giant optical non-linearity and all-optical switch. (b) The Autler-Townes splitting at $\delta_C = 0$ between two dressed state (the distance between two fitted curves) with different control powers is plotted as a function of square root of the control power (which is proportional to the field amplitude of the beam). A linear dependence is observed.

fitted curves, which represents two dressed states.

The Autler-Townes splitting for each control laser power is taken by taking the peak to peak distance of the two fitted curves. Fig. 5.19(b) shows the plot of the Autler-Townes splitting as a function of square root of the control laser power (proportional to the Rabi frequency Ω_C) at zero detuning $\delta_C = 0$. A linear dependence is observed confirming the relation $\Omega_1 = \Omega_C$. When the control laser is switched off $\Omega_C = 0$, we have no splitting as expected.

5.3.3 A full scan over two excitonic fine-structure dipoles

To have a complete picture of the behavior of two FSS dipoles, we carry out a broad probe beam scan that could cover both X_x and X_y states. The FSS energy is $25 \mu eV$, the scan range for both control and probe beams is $80 \mu eV$.

Fig. 5.20 and Fig. 5.21 show a systematic measurement for different powers of the control beam where the reflections of both two dipoles are observed within the probe laser detuning range. The scans in the left (right) show the experimental data (theoretical calculated data). Similar to chapter 4, the full theoretical model done by T. Grange considers all the imperfections of the QD-waveguide coupling system, including the other excitonic FSS dipole forming a four-level system. The fitting parameters for the spectral broadening (pure dephasing γ^* and spectra diffusion σ) and the input-output coupling efficiency are chosen so that they reproduce best the experimental two-dimensional plot. In addition, for a more precise fit, one could base on the slope of Autler-Townes splitting in Fig. 5.19(b) or base on the reflectivity plots in the next sections to adjust the parameters of the system. A detailed fitting method will be presented in appendix A.

Because of the asymmetry of the laser polarization with respect to the FSS dipoles, one can see different behaviors and splittings between X_x and X_y reflections. At zero detuning of both two beams $\delta_P = \delta_C = 0$, the splittings of X_x and X_y can be expressed as:

$$\frac{\Omega_x}{\Omega_y} = \frac{\Omega_C \cos(\theta)}{\Omega_C \sin(\theta)} = \tan^{-1}(\theta) \quad (5.40)$$

This equation indicates that the Rabi frequency of the laser applying on a dipole depends on the angle θ , the dipole closer to the laser polarization is dressed more efficient by the laser thus its Autler-Townes splitting is larger than the other one. For $\theta = 27^\circ$, the Autler-Townes splitting Ω_x is larger than Ω_y by $\tan^{-1}(27) \approx 2$.

One could see from experiment results that the X frequency suffers slightly from temporal drift (see section 3.2.3). The lines are thus shifted with the speed approximately $1 \mu eV/\text{minute}$. The total scan takes 4 minutes to finish (for 0.1s integration time per each point), therefore the emission energies are shifted by $4 \mu eV$ when the scan finishes. The

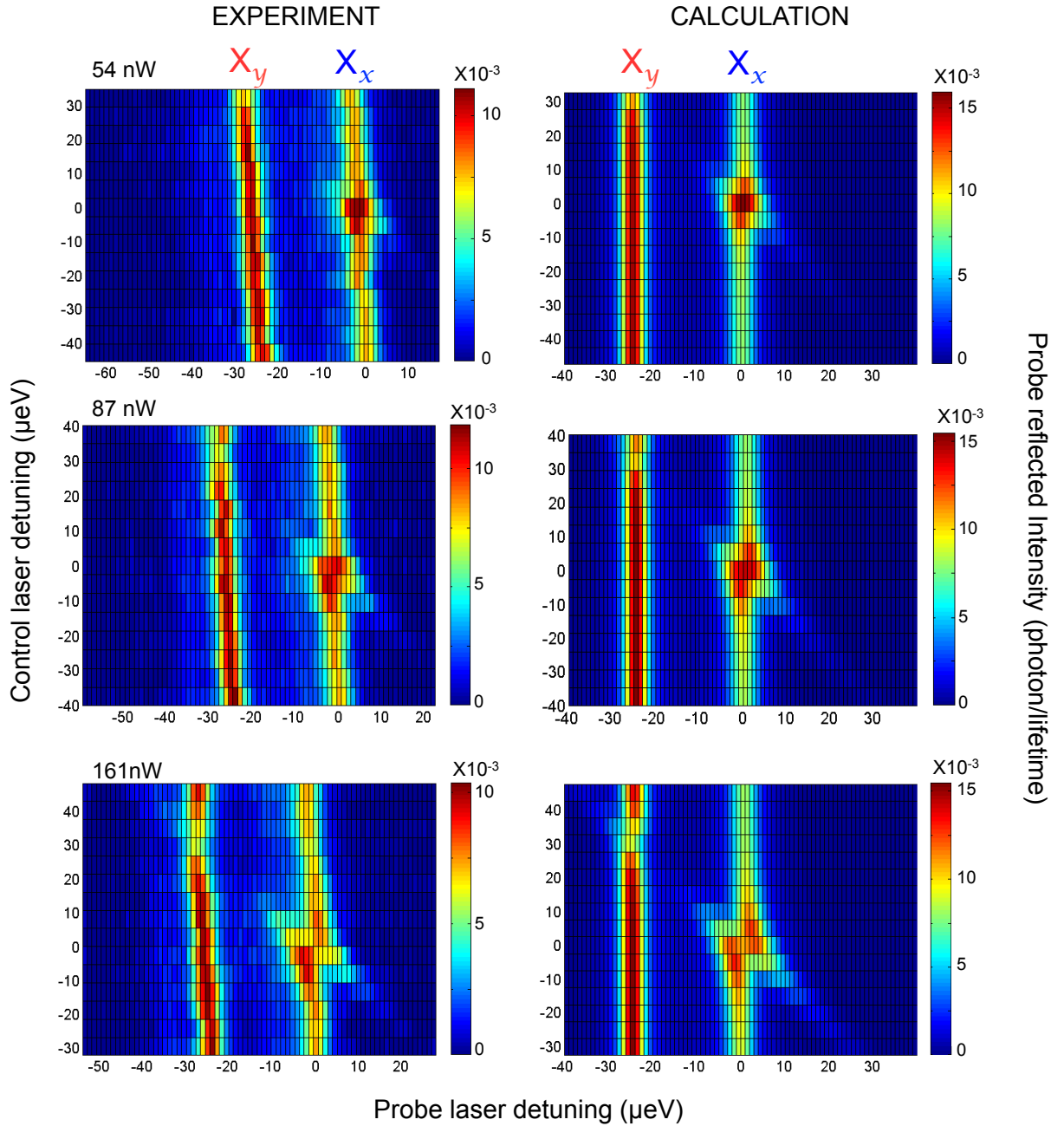


Figure 5.20 – Probe reflection of X transitions in a broad scan - Experimental (left) and theoretical (right) results of the broad scans are shown for different powers of the control laser beam where the reflections of both two FSS dipoles are visible. The experiment is performed on the same QD that has been used in chapter 4 (section 4.3.2), so the linewidth broadening factors used in the model are the ones used in section 4.3.2. The total spectral broadening is $4 \mu\text{eV}$, including $1 \mu\text{eV}$ of due to pure dephasing and $3 \mu\text{eV}$ due to spectral diffusion. The input and output coupling factors are $\varepsilon_{in} = \varepsilon_{out} = 0.26$. The angle θ between the polarization of dipole X_x and the lasers is $\theta = 27^\circ$.

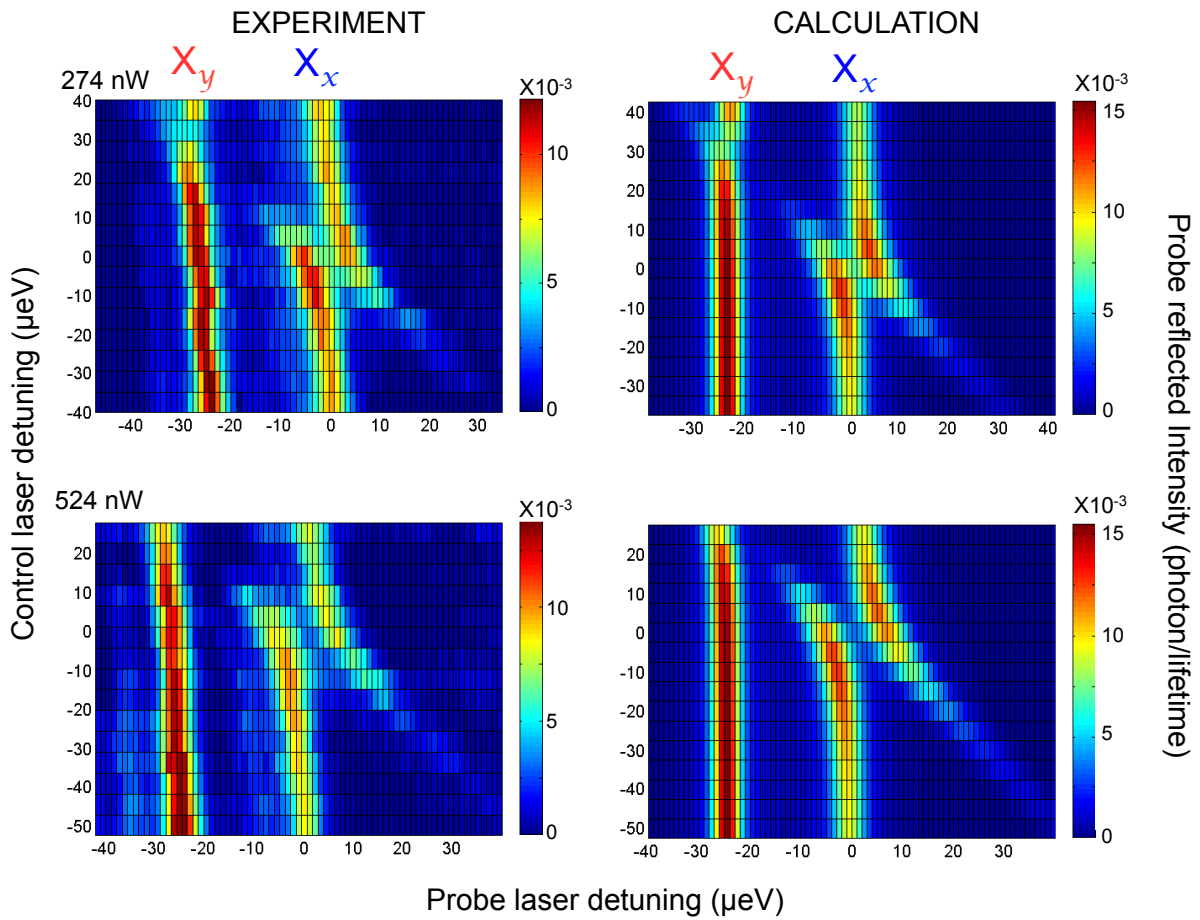


Figure 5.21 – Probe reflection of X transitions, theory and experimental plots for control laser power 274 nW and 524 nW.

effect of temporal drift can be reduced by decreasing the integration time of the scan. In this case, the integration time is fairly short, just 0.1s per point.

5.3.4 Autler-Townes optical switch

5.3.4.1 Probe reflection as a function of control power

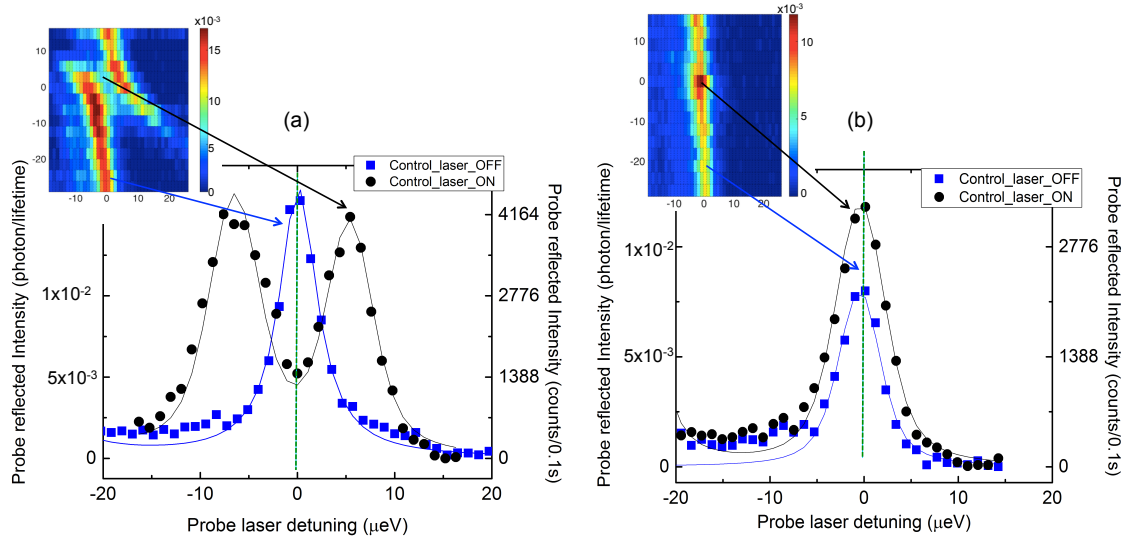


Figure 5.22 – Probe laser reflectivity when the control laser is ON and OFF resonance - (a) For control power 19.5 nW, which is not too far above saturation power, when the control beam is turned on (black circles), one could see an enhancement in reflection compared with when the control beam is turn off (blue square). For a constant probe power ($P_{probe}/P_{sat} = 0.2$), this enhancement is because of the presence of the other excitonic dipole, which will be explained in details in the next section. (b) The control power is far above saturation power at 524 nW. When the control beam is turned on, Autler-Townes splitting is well established. At zero probe detuning $\delta_P = 0$, a switch in reflection is obtained.

Previous section has demonstrated how the reflection of a probe beam can be modified by the presence of a control beam dressing the upper transition of a QD three-level system. This section aims at estimating quantitatively this two-mode giant non-linearity all-optical switch and how the switching contrast depends on the power of the control beam. Fig. 5.22(a) and 5.22(b) show the probe reflection of X_x level when the control beam is on resonance and when it is far away from resonance (off), respectively.

These two plots show clearly the switch at the zero probe detuning $\delta_P = 0$, as indicated by the green dashed-lines. When the control laser power is large as in Fig. 5.22(a), two dressed states are well separated and the reflection of the probe laser is reduced drastically. This is the experimental demonstration of a all-optical switch in which the modification of probe reflection is triggered by the control beam.

Interestingly, one could notice from Fig. 5.22(b) that, with a control laser power not

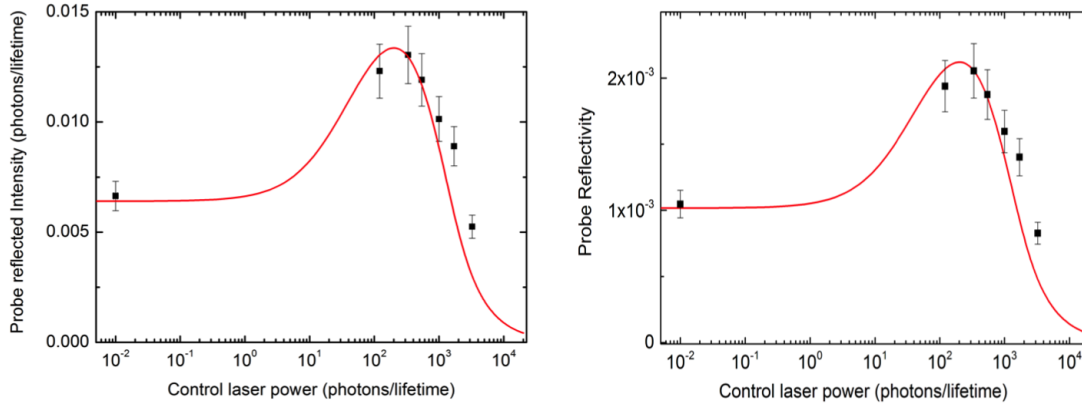


Figure 5.23 – Probe reflection intensity and probe reflectivity as a function of the control laser power - (a) The dependence of probe reflection intensity (black square) on the control power. The probe power $P_{probe}/P_{sat} = 0.2$. (b) Probe reflectivity (defined as the ratio between the probe reflected intensity and the probe laser power) as a function of control power.

very intense, we have slightly more reflection at $\delta_P = \delta_C = 0$. This is surprising because with a purely three-level system, in principle, the X_x state can not emit an amount of photons more than what is populated by the probe laser, which means the presence of the control laser can not induce the enhancement in reflection of the probe beam. To be able to understand it, we have to take into account the contribution of other FSS dipole X_y in a four-level system picture. This reflection enhancement will be discussed in the coming section.

Fig. 5.23(a) plots the measured probe reflection intensity (black squared) as a function of control laser power, together with the fit obtained from the theory. The data is taken at resonances of both two beams ($\delta_C = \delta_P = 0$). When the control power is infinitely small, the probe reflection is constant because of the negligible contribution of the control beam. However, when increasing the control power, a surprising enhancement in reflection is observed. The probe reflection intensity increases and reaches the maximum at control power ≈ 200 photons/lifetime. Increasing further the control power, the reflection intensity reduces rapidly because of Autler-Townes effect. Fig. 5.23(b) plots the probe reflectivity as a function of control power. Because probe power is kept constant for the whole measurement, so the reflectivity is proportional to the reflection intensity. The probe reflectivity for an ideal system will be discussed in section 5.3.4.4.

5.3.4.2 Enhancement of probe reflection

To be able to explain the enhancement of the probe reflection, we have to consider a full picture of the system, in which the other FSS dipole is taken into account and the

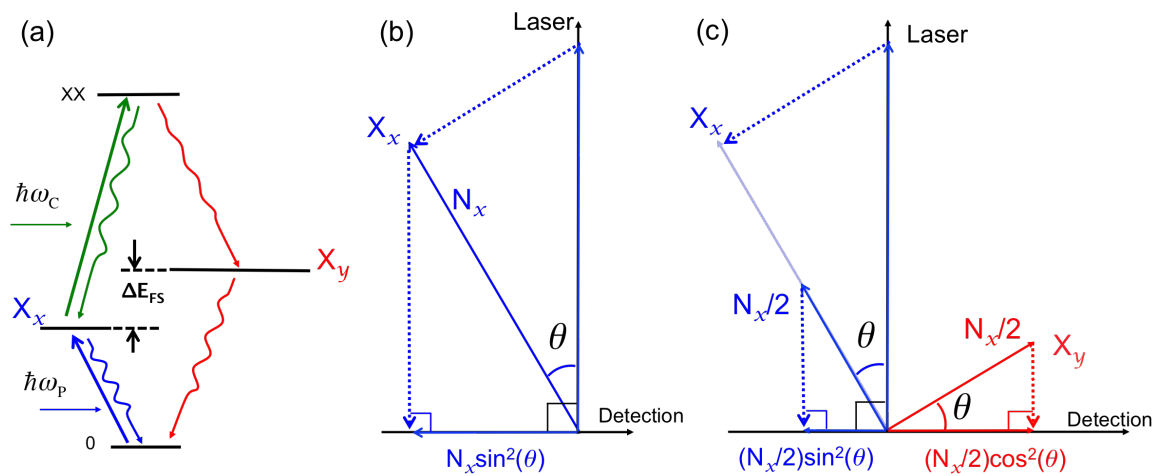


Figure 5.24 – Schema of a four level system that explains the enhancement in probe reflection - (a) A QD four-level system: X_x level is chosen to be resonantly coupled with the lasers. (b) Without the presence of a control laser, one can neglect the other excitonic dipole X_y . The probe laser excites dipole X_x (whose polarization is away from the polarization of the laser by an angle θ). For a probe power below saturation ($P_{probe} < P_{sat}$), the amount of probe reflection is proportional to power. Assuming that X_x emits N_x photons, then the amount of photons detected is $N_x \sin^2(\theta)$. (c) A control laser is turned on and coupled to $X_x - XX$ transition. XX level has also the decay path to X_y , thus when increasing the control power, the population of X_x will be gradually transferred to X_y . Therefore, the population of two excitonic levels will eventually be equalized. At this stage, each level will emit equally $N_x/2$ photons, but depending on the angle θ , the actual amount of photons detected for each level will be different.

system has to be seen in cross-polarized detection scheme (as explained in section 4.2.2). Fig. 5.24(a) sketches a four-level system. We consider the case in which the lasers are on resonance with X_x dipole ($\delta_P = \delta_C = 0$). When the control beam is absent, for a probe beam with a power much less than saturation, X_x state absorbs and emits an amount N_x photons, as illustrated in Fig. 5.24(b). Assuming that the FSS energy ΔE_{FS} is large enough that dipole X_y is not affected by the laser beam and therefore can be neglected in this case. Because of cross-polarized detection, the amount of photons that will be detected is $N_x \sin^2(\theta)$.

When a control laser is introduced into the system, since XX level always has two possible decay channels to X_x and X_y , thus X_x level has to share its population with X_y . As a result, for a control power high enough, eventually, two FSS levels will have equal population and two FSS dipole will emit equally $N_x/2$ photons. Therefore, in cross-polarization scheme, as can be seen in Fig. 5.24(c), the total photons that will be detected in horizontal channel is $(N_x/2) \sin^2(\theta) + (N_x/2) \cos^2(\theta) = N_x/2$.

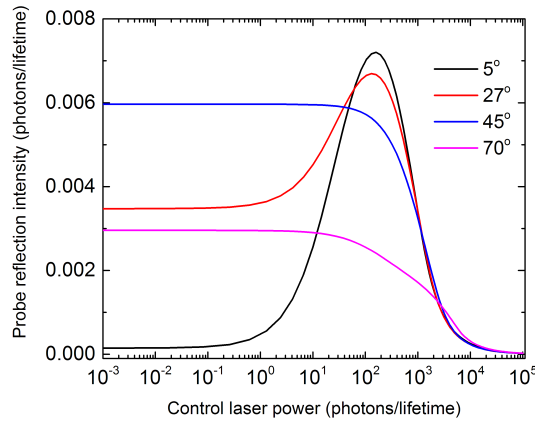


Figure 5.25 – Calculated probe reflection intensity as a function of control power, for different angle θ between dipole X_x and laser polarizations - The power of the probe laser is kept to be the same at 6 photons/lifetime ($P_{probe}/P_{sat} = 0.15$). The FSS is considered large enough to well isolate the dipole X_y from direct influence of the control laser. One could see that at an infinitely small control power, the probe reflections are very different, this is because for a constant probe power, the excitation efficiency of the beam depends strongly on the angle θ , as explained in section 4.2.2. For $\theta < 45^\circ$, $N_x \sin^2(\theta) < N_x/2$ so the enhancement in probe reflection is obtained. Reversely for $\theta > 45^\circ$, no enhancement is observed.

Therefore, in the cross-polarized detection scheme, the behavior of probe reflection intensity with or without the presence of the control beam depends strongly on the angle θ . Fig. 5.25 plots the probe reflection intensity for different angles θ . One could see that the enhancement in probe reflection with the presence of the control laser is obtained only when θ satisfies the condition $N_x \sin^2(\theta) < N_x/2$, which means when $\theta < 45^\circ$. That

explains the probe reflection enhancement in our measurement (Fig. 5.23) because the angle θ is set at 27° .

It should be noted here that if the data collection process integrates only the range of dipole X_x , this enhancement should not be observed because in this case the reflection from X_y is not taken into account. In our measurement the data collection process integrates the whole spectral range that covers both two X dipoles (see section 4.2.2.4 and 5.2.1), so that the reflections from both of them is always collected. The integration range has to be large because on one hand, the large range is needed to obtain the full anti-crossing signature of Autler-Townes splitting. On the other hand, the temporal drift makes it very challenging to integrate the spectrum at an exact single frequency. As a result, we eventually collect also the light emitted from X_y , which leads to the observed reflection enhancement.

5.3.4.3 Probe laser switching contrast

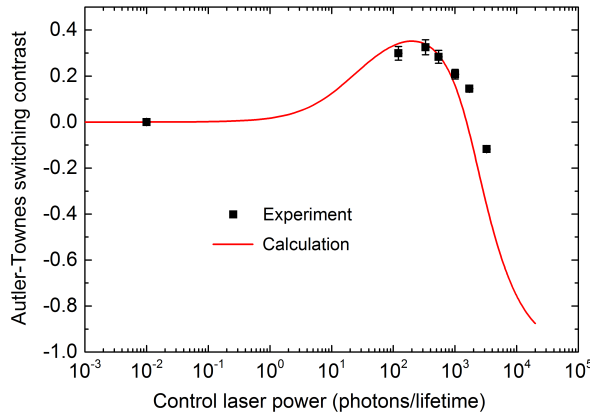


Figure 5.26 – Probe laser switching contrast as a function of control laser power - The angle $\theta = 27^\circ$. The data is fitted by the theory. Due to the enhancement in probe reflection, the contrast is firstly switched to positive values at the control power less than 200 photons/lifetime. Increasing further the control laser power far above saturation, the contrast starts to decrease as expected and finally becomes negative. In this configuration with the experimental conditions, the level of control power required to have the most efficient switch (switching contrast close to -1) is rather large (in the order of larger than 10^4 photons/lifetime).

From the probe reflection in Fig. 5.23, one can induce the switching contrast. The probe switching contrast C_P can be defined as

$$C_P = \frac{P_R(on) - P_R(off)}{P_R(on) + P_R(off)}$$

Where $P_R(on)$ and $P_R(off)$ are the probe reflected intensity when the control laser is

ON and OFF, respectively. The switching contrast is plotted in Fig. 5.26(b) as a function of the control laser power. The black squares are the experimental results, the red curve is the calculation. Basically, the behavior of the contrast is similar to the probe reflection in Fig. 5.23. From the curve, we can see that the switching contrast starts to have a non-zero value when the control laser power is just in the order of 10 photons/lifetime. The contrast gets to the maximum value when the control laser power is at the level $\simeq 2.10^2$ photons/lifetime. When the control laser power keeps increasing, the switching contrast turns from positive to negative because of Autler-Townes splitting. It is worth mentioning here that for $\theta > 45^\circ$, as explained in the previous section, the contrast will start from zero and go negative without any positive value.

5.3.4.4 Probe reflectivity for an ideal system in Autler-Townes approach

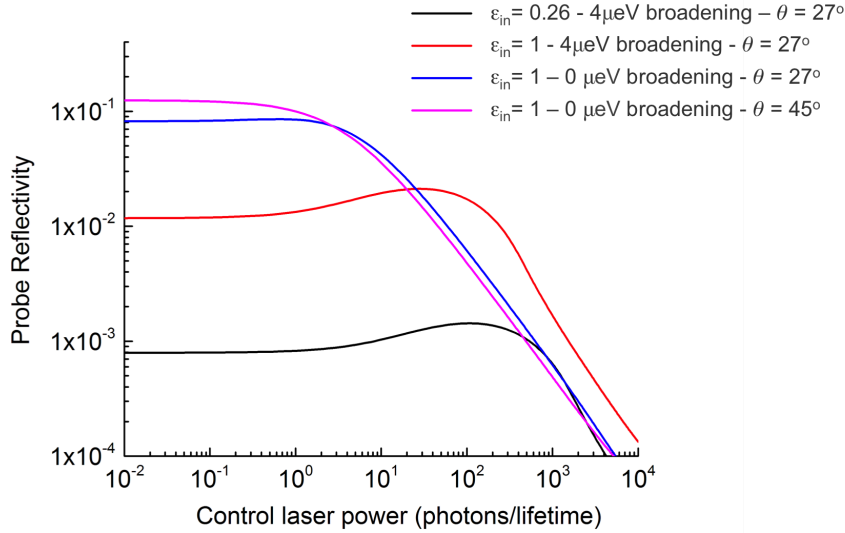


Figure 5.27 – Probe reflectivity for optimized parameters of the system in cross-polarized configuration - The probe power is set at $P_{Probe}/P_{sat} = 0.01$. The black curve plots the fitted reflectivity for the experimental condition (Fig. 5.23(b)), in which $\varepsilon_{in} = \varepsilon_{out} = 0.26$, $\theta = 27^\circ$, pure dephasing rate $\gamma^* = 1 \mu eV$, spectral diffusion width $3 \mu eV$. The red curve plots the calculated reflectivity for the same spectral broadening as the black one ($4 \mu eV$ in total), but with optimum coupling rates $\varepsilon_{in} = \varepsilon_{out} = 1$. The blue curve shows the ideal cross-polarized probe reflectivity at $\theta = 27^\circ$ for a perfect system with zero broadening and $\varepsilon_{in} = \varepsilon_{out} = 1$. The pink curve shows also the ideal cross-polarized probe reflectivity for a perfect system with zero broadening and $\varepsilon_{in} = \varepsilon_{out} = 1$, but with $\theta = 45^\circ$.

This section will show the calculation of probe reflectivity obtained with an ideal three-level system in crossed-polarization and co-polarization excitation schemes. Firstly, we consider a cross-polarized detection with an angle $\theta = 27^\circ$ similar to the experiment. Section 4.3.2.2 and 4.1.2 have discussed in detail the scaling laws for the impacts of im-

perfection parameters on the probe reflectivity (including the input and output coupling efficiencies, spectral broadening factors and also the angle θ), for a vanishing probe and control powers. Fig. 5.27 plots the calculated probe reflectivity in three different cases. Firstly, the black curve shows the case for real parameters in the experiment. The red curve shows the case for a system with perfect coupling efficiency $\varepsilon_{in} = \varepsilon_{out} = 1$ but the line width is broadened as in the real condition ($4 \mu eV$). In this case, compare to the real experimental condition, the reflectivity is enhanced by a factor of $0.26^{-2} \approx 15$. In this case, pure dephasing rate γ^* induces a reduction of $(\gamma + \gamma^*)/\gamma$ and spectral diffusion induces a reduction of σ (see Eq. 4.22) in probe reflectivity compared with an ideal case with no broadening, as represented by the blue curve (for $\theta = 27^\circ$, with unity coupling efficiencies). At a control laser power well below saturation, similar to the ideal case in the single-mode giant non-linearity in section 4.3.2.2, an ideal reflectivity R_P in cross-polarized scheme could be obtained is $0.5 \cos^2(\theta) \sin^2(\theta)$. For $\theta = 27^\circ$, $R_P \approx 0.08$. One can see that the cross-polarized reflectivity can reach the maximum $R_P = 0.125$ when $\theta = 45^\circ$ (the pink curve in Fig. 5.27). As discussed in section 5.3.4.2, at $\theta = 45^\circ$ we can also avoid an unexpected enhancement in probe reflection.

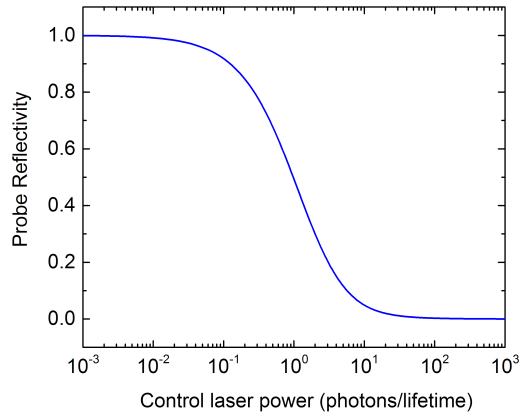


Figure 5.28 – Ideal probe reflectivity in co-polarized excitation configuration - In this case, the angle θ is 0° , the excitation and detection have the same polarization. Assuming that the probe power is very low ($P_{probe} \ll P_{sat}$). In this scenario, without the presence of the control beam (or with an infinitely small control power), we can obtain a unity probe reflectivity. At the power of the control laser 1 photon/lifetime, the reflectivity is reduced by a factor of 2 and eventually total transmission is induced at control power larger than 10 photons/lifetime.

Ideal probe reflectivity in co-polarized excitation scheme In cross-polarization scheme, the maximum probe reflectivity could be obtained for an ideal system is 0.125 for an angle $\theta = 45^\circ$ (Fig. 5.27). One then would wonder the reflectivity could be reached if we

perform a co-polarized excitation, assuming that there is no laser background. Fig. 5.28 plots the optimum reflectivity as a function of control laser power. When the control laser is absent, the reflectivity is equal to 1. A unity reflectivity could be reached in co-polarized excitation because at ultra-low probe power, it has been shown in section 4.1.2.1 that the destructive interference between half of the photons emitted in the forward direction and the incoming laser cancels out the transmission. Therefore, one could obtain a maximum reflectivity. In this case, the reflection could be reduced by a factor of 2 by a control power just 1 photon/lifetime.

5.3.4.5 Optical switch with laser background

As already mentioned in the beginning of chapter 4. One of the biggest obstacles in performing resonant spectroscopy is the presence of the scattered light from the excitation laser, because the laser has the same frequency as the emitter's frequency. For that reason, we used a cross-polarized detection scheme to reject the unwanted laser background. Unfortunately, a small fraction of laser background is still present. Fig. 5.29(a) and (b) show respectively the probe reflection intensity and the probe switching contrast with the presence of the probe laser background. In practice, the background of the laser can be reduced if the anti-reflection coating layer is improved and if we can enhance the efficiency of cross-polarized laser rejection scheme (the rejection rate is 10^4 at the moment).

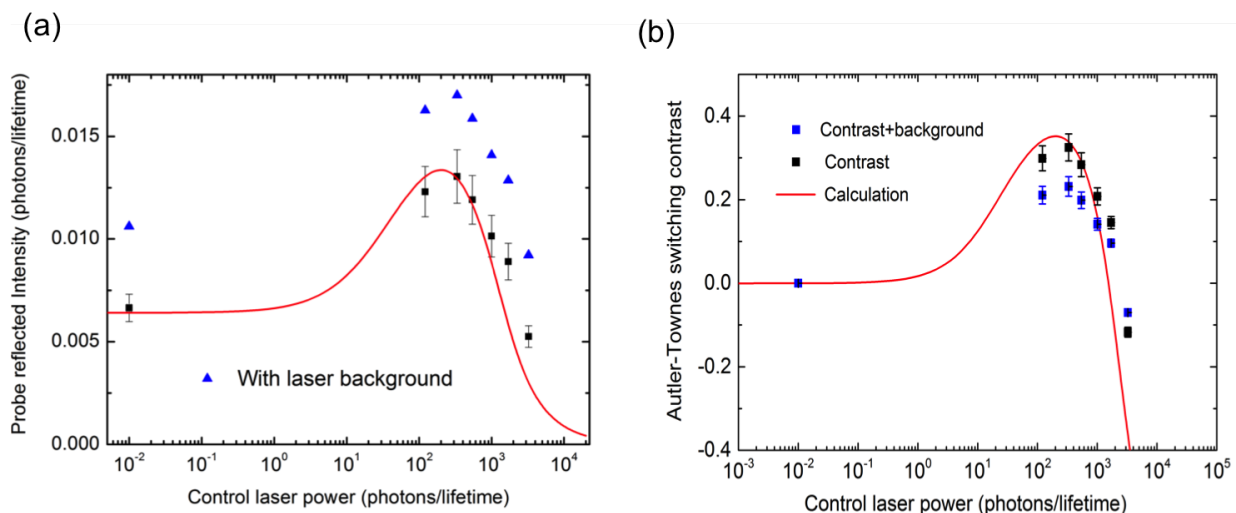


Figure 5.29 – (a) Probe reflection and (b) probe switching contrast as the presence of probe laser background.

For a conclusion of this section, we have presented an experimental realization of an all-optical switch based on Autler-Townes splitting approach. The result indicated that the switch could be obtained at a control power around 200 photons/lifetime for the excitonic

dipole with a polarization $\theta = 27^\circ$ with respect to the laser polarization. However, it has been pointed out that the reflection enhancement at that control power comes from the contribution of another excitonic fine-structure dipole with a different frequency. In addition, the reflectivity obtained in the experiment is far below unity ($\approx 10^{-3}$). Those results are not favorable for a real all-optical switch application in optical or quantum computing. Nevertheless, we have also shown that by performing a co-polarized excitation, a unity reflectivity could be achieved. Furthermore, it will also be discussed in section 5.5.1 that this co-polarized excitation based on Autler-Townes splitting approach also preserves the coherent nature of the system at low control power.

5.4 Two-mode giant non-linearity: Population switch approach

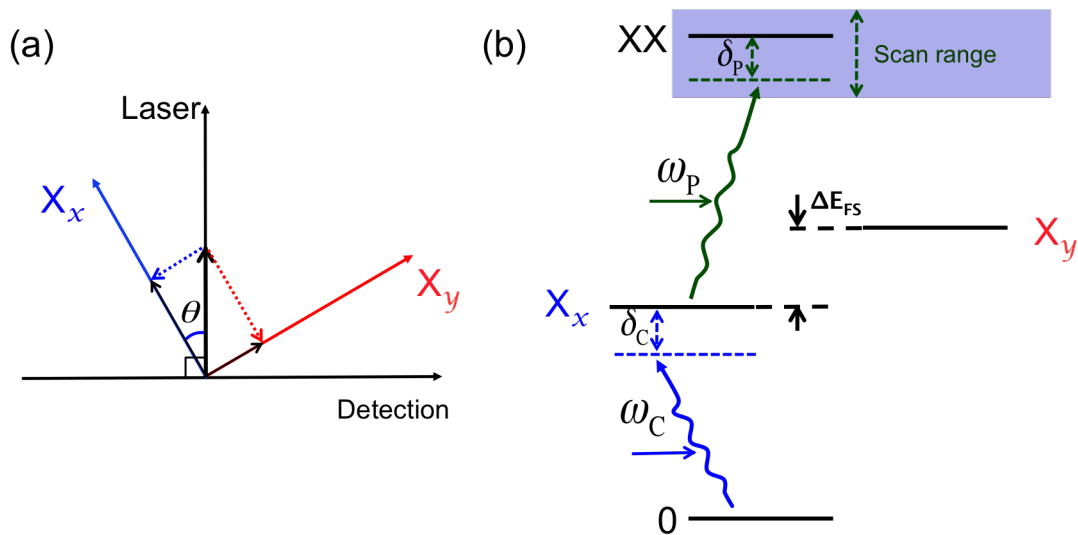


Figure 5.30 – Population switch geometry - Very similar experimental configuration in Autler-Townes approach is established. The only different is the swapping of probe and control beams. (a) Cross-polarized detection scheme with an angle $\theta = 27^\circ$. (b) Sketch of a QD four-level system. The excitonic dipole X_x is chosen to form a three-level cascade. A control beam is tuned around $0 \leftrightarrow X_x$ resonance with a detuning δ_C . A probe beam is tuned around $X_x \leftrightarrow XX$ resonance with a detuning δ_P .

In this section, we aim at realizing an all-optical switch in a reversed approach, with the probe beam coupled to the upper transition and the control beam coupled to the lower one. Fig. 5.30 illustrates the configuration. One important notice is that in this section, the term “control laser beam” and “probe laser beam” will be used reversely compared with the previous section. It has been stated in section 5.1.5 that without the presence of the control beam, the X level is empty, so that a probe beam coupled to the upper

levels will be totally transmitted. By contrast, if the control beam, with a power below the saturation of the X level, is turned on, the X level is populated. As a result, the probe beam will then be absorbed and exhibit a non-vanishing reflectivity. The nature of the switch is based on the population of the intermediate state, so we call this approach “population switch”. This switch is very efficient because the reflection is really zero when the control laser is off.

5.4.1 Reflection measurement

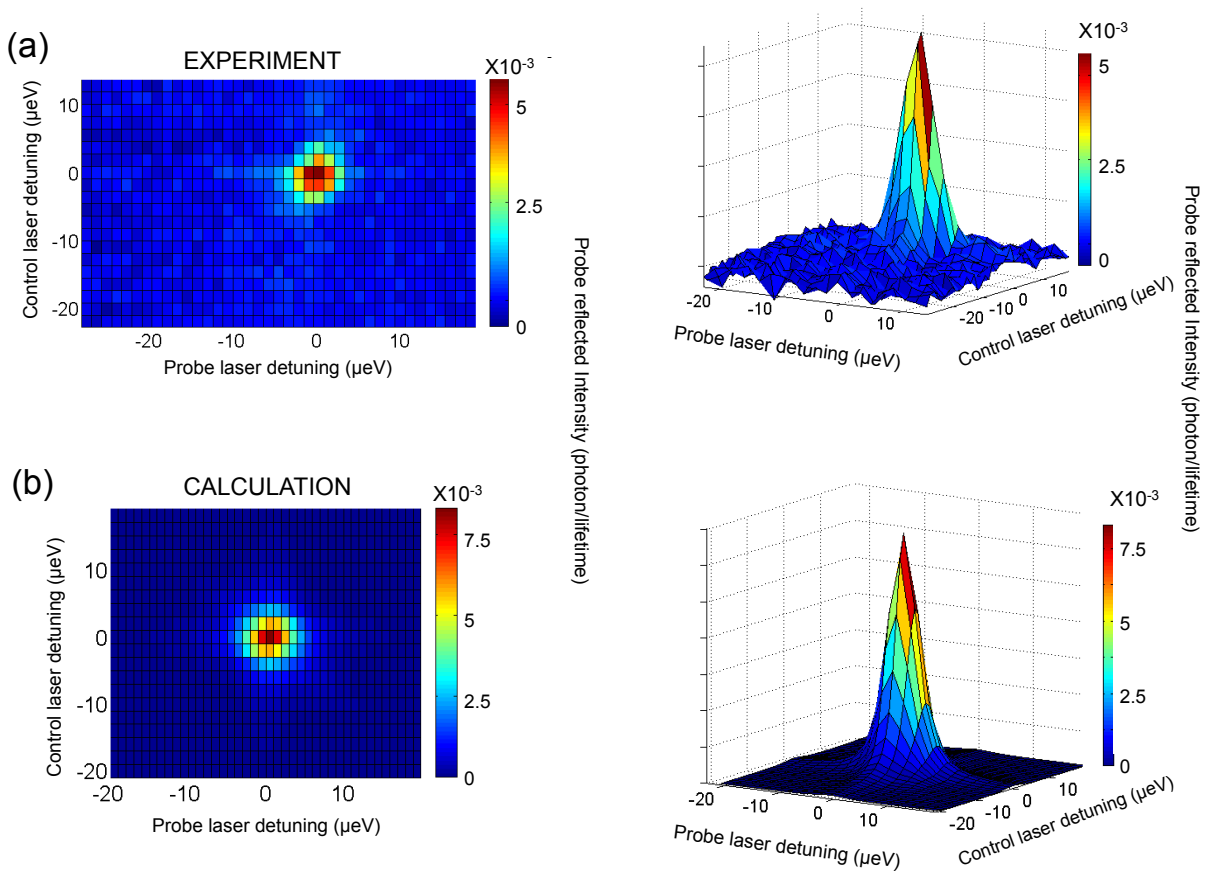


Figure 5.31 – Two-laser scan in the population switch approach - (a) Experimental and (b) theoretical results showing top-view (left) and side-view (right) of the two-dimensional maps. The horizontal and vertical axes show the detuning of the probe and control lasers, respectively. The color bar shows the probe reflection intensity. The detuning range for both control and probe lasers is around $40 \mu\text{eV}$, which is enough to cover just the X_x dipole. The probe and control powers are respectively $P_{\text{probe}}/P_{\text{sat}} = 0.1$ and $P_{\text{control}}/P_{\text{sat}} = 0.5$. The angle θ is always set at 27° . In the calculation, the input-output coupling efficiencies are $\varepsilon_{\text{in}} = \varepsilon_{\text{out}} = 0.26$. The total spectral broadening is $4 \mu\text{eV}$, including $1 \mu\text{eV}$ due to pure dephasing and $3 \mu\text{eV}$ due to spectral diffusion (see appendix A for more details of fitting method).

The experiment is carried out for the same QD that has been studied in Autler-Townes splitting approach. The measurement follows the same procedure as in section 5.2.1. It should be noted here that the angle θ in cross-polarization scheme is kept at 27° . A two-dimensional scan is performed by sweeping the probe beam frequency over XX frequency. The control beam frequency is put around the X_x level. After each sweep, the frequency of the control beam is tuned by one step. We want to observe the modification of probe beam reflection as the presence of the control beam, therefore this time the reflection frequency of interest is the frequency of $X_x \leftrightarrow XX$ transition.

Following this procedure, Fig. 5.31(a) shows the experimental result of a typical two-laser scan. One can see that when the control beam is far from resonance ($\delta_C = 0$), the probe beam is entirely transmitted and no reflection is detected. By contrast, when the control beam approaches very close to resonance, the presence of the control laser populates X_x state and therefore, the probe beam is absorbed only for $\delta_P = 0$ and thus reflected by the $X_x - XX$ transition. Fig. 5.31(b) shows the calculation plots given the same parameters as in Fig. 5.20.

5.4.2 Ultra-low power optical witch

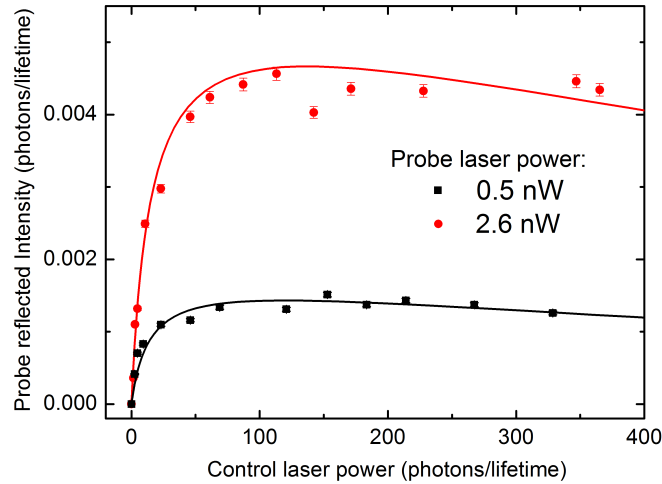


Figure 5.32 – Probe reflected intensity as a function of the control laser power - Several two-laser scans are performed with varying control powers for two different probe laser powers: 0.5 nW ($P_{probe}/P_{sat} = 0.1$) and 2.6 nW ($P_{probe}/P_{sat} = 0.5$). For a probe power below saturation power, the probe reflected intensity is proportional to the probe power.

The previous section has shown an experimental demonstration of an all-optical switch in population approach. The next step is to see how the control power modifies the reflection of the probe beam, the control power is varied from ultra-low to well above

saturation of the X_x level. Two different probe powers (at $P_{probe}/P_{sat} = 0.1$ and 0.5) are taken to perform the measurement. Fig. 5.32 plots the results of probe reflection. The resonant reflection of each scan is taken to plot the probe reflection intensity (the value at $\delta_P = \delta_C = 0$ in Fig. 5.31). The black squares and red circles are the data for two probe powers. The black and red curves are calculation fits.

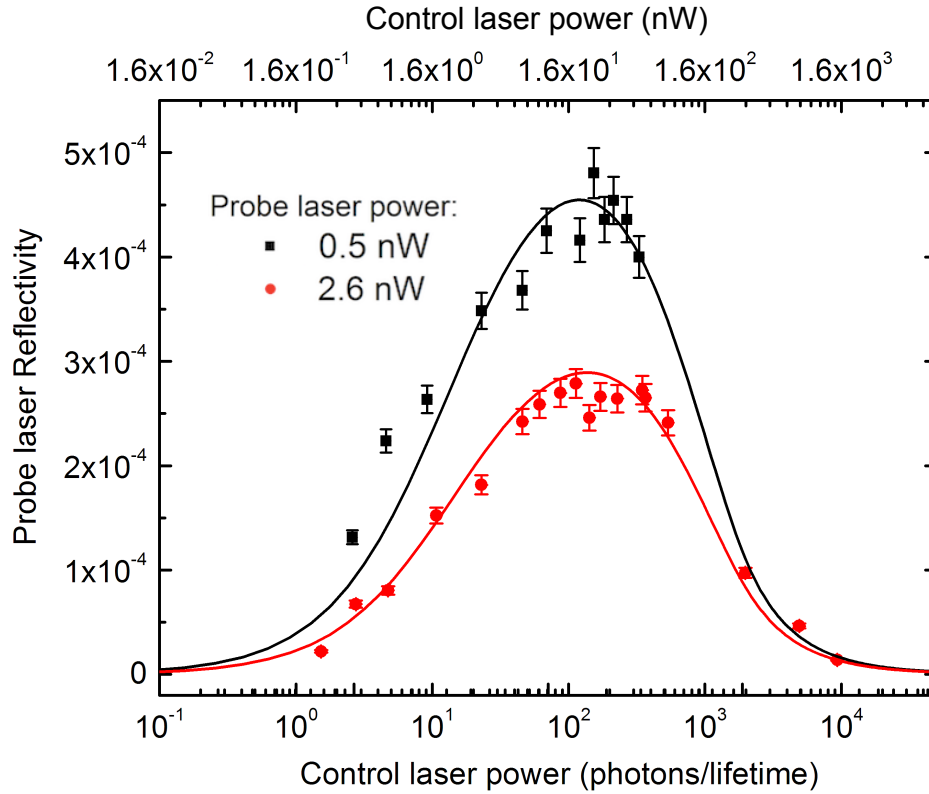


Figure 5.33 – Probe reflectivity of the probe laser in 4 orders of magnitude of the control laser power - The reflectivity is taken as the ratio between the probe reflected intensity in Fig. 5.32 and the probe power. The symbols are experimental data, and the curves are the theoretical calculations. At the weak control power level, the probe reflectivity increases progressively with control power until it reaches the maximum due to saturation. For the probe power 2.6 nW ($P_{probe}/P_{sat} = 0.5$), the probe reflection is also measured for the control power well above saturation. At this level of control power, X_x state will be split due to the formation of dressed states. Thus, keep increasing the control power will lead to less and less coupling of the probe beam at zero detuning $\delta_P = 0$. As a result, the reflectivity is reduced and eventually reaches zero reflection.

From the reflection intensity, the reflectivity can be plotted in Fig. 5.33 as a function of control laser power. The reflectivity is defined as the ratio of the probe reflection and probe power. The figure indicates that with ultra-weak control power, in the order of less than 0.1 photon/lifetime, no probe reflectivity is induced. When the control power increases by one and two orders of magnitude at 1 and 10 photons/lifetime. The reflectivity starts

to increase and the optical switch can already be realized at such power level. Increasing further the control laser power, the reflectivity reaches the maximum at $\simeq 100$ photons/lifetime. One interesting remark that has already been pointed out is that, for any power of the control laser, the switching contrast $C_P = [P_R(on) - P_R(off)] / [P_R(on) + P_R(off)]$ is always maximum because $P_R(off)$ is always equal to zero.

One could notice that when increasing the control power above 100 photons/lifetime, the reflectivity starts to reduce quickly and finally reaches the minimum. This is because when two beams are on exact resonances with the transitions ($\delta_C = \delta_P = 0$), X_x state is dressed and split with the amplitude proportional to the control power. Therefore, X_x level becomes more and more transparent to the probe beam. The full behavior of probe reflection for above-saturation control power range will be discussed in section 5.4.2.1.

Fig. 5.33 can be considered as the most important result of this thesis. A reflectivity of the probe beam is switched on and off by the presence of the control beam with a power from just a few photons/lifetime. The probe reflectivity reaches a maximum value with a control power as low as ≈ 100 photons/lifetime (≈ 16 nW). In addition, for any control power, the probe switching contrast always has a unity value. Keep increasing the probe power, the probe reflectivity is switched off again. Although the high control range is not at a great interest in this approach, a variation of control power in a four orders of magnitude range gives a complete picture of the probe reflectivity response and shows a high agreement between experimental results and theoretical model. Finally, it should be mentioned again that this two-mode giant non-linearity confirms the exceptional broadband operation property of the photonic trumpet, which allows simultaneous couplings of two different beams to two different transitions of the emitter.

Probe reflectivity for different probe laser powers One could see in Fig. 5.33 that the reflectivities for two probe powers are not the same, this is because one of the two powers is close to the saturation power. Fig. 5.34 plots the probe reflectivity for different probe powers. The plots show that when the probe power is well below saturation power, the reflectivity remains constant because the absorption of XX transition is still in linear regime and it increases progressively with the probe power. When the probe power reaches saturation, the absorption is no longer proportional to the power, thus the reflectivity decreases rapidly with increasing probe power.

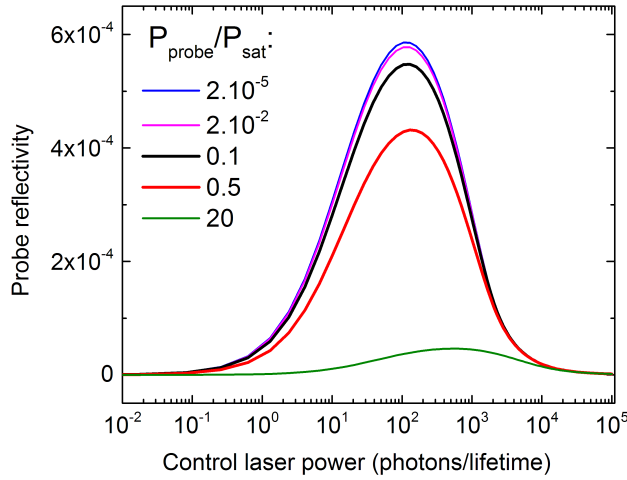


Figure 5.34 – Calculated probe reflectivity as a function of control power for different probe powers P_{probe}/P_{sat} : 2.10^{-5} (10^{-4} nW), 2.10^{-2} (0.1 nW), 0.1 (0.5 nW), 0.5 (2.6 nW) and 20 (100 nW). The black and red curves with P_{probe}/P_{sat} respectively 0.1 and 0.5 correspond to the two powers using in the experiment. The dependence of probe reflectivity on probe power explains different reflectivity obtained in Fig. 5.33 .

5.4.2.1 Observation of Autler-Townes splitting at high control laser power

We have seen in the previous section that when increasing the control power, because of Rabi oscillations, X levels will be dressed and leads to the formation of an Autler-Townes doublet. Fig. 5.35 shows two-dimensional scans for two different powers of the control beam. Both experiment and calculation results are shown. The scan ranges of both lasers are large enough ($80 \mu eV$) to cover efficiently two FSS dipoles. As expected, the anti-crossing signature of Autler-Townes effect is observed. One can see that the splitting is not equal for two excitonic dipoles, which is because of the asymmetry of the excitation polarization with respect to two orthogonal polarizations of the dipoles, as explained in section 5.3.3.

Fig. 5.36(a) shows the cross-section of probe reflection when the control laser is on exact resonance at $\delta_C = 0$, for different control powers. The behavior is the same as in section 5.3, the Autler-Townes splitting increase progressively with the control field amplitude and is equal to Rabi frequency of control beam at zero detuning. The splitting as a function of square root of power is also plotted in Fig. 5.36(b).

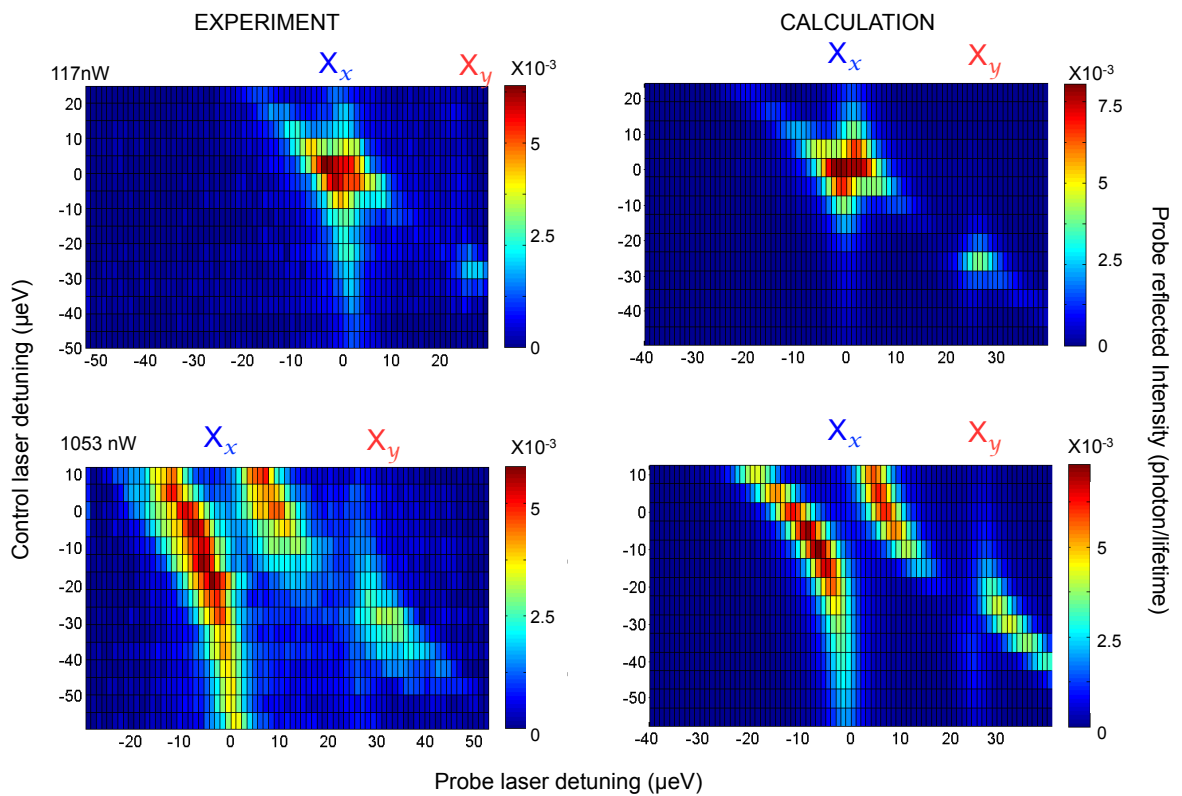


Figure 5.35 – Two-dimensional map of the probe reflection when control power is far above saturation - Experimental (left) and theoretical (right) results showing two-dimensional map of the probe reflection in the reversed situation (population switch) for two different powers of the control beam well above saturation. The scan range for the probe beam is $80 \mu\text{eV}$.

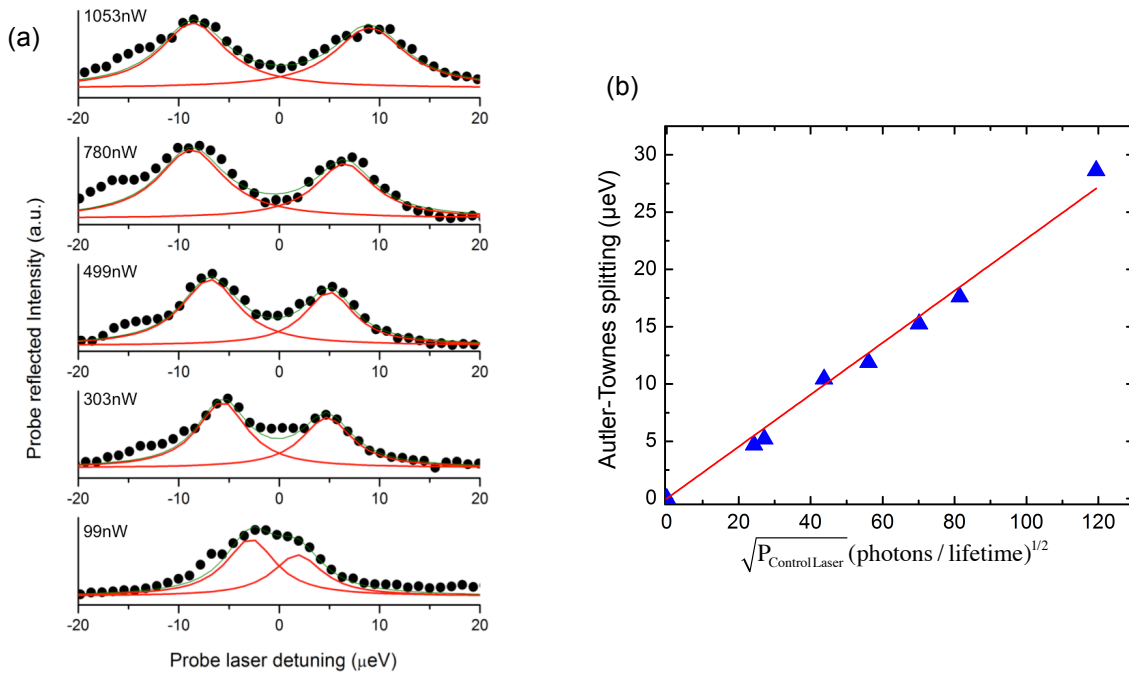


Figure 5.36 – Autler-Townes splitting for different control laser power in reversed approach - (a) The probe reflected intensity is plotted as a function of probe detuning δ_P for different powers of the control beam (coupled to $0 \leftrightarrow X_x$ transition), the experiment data (black circle) is fitted as red curves showing the Autler-Townes splitting between dressed states. (b) Autler-Townes splitting for each control power is plotted as a function of square root of control power. The data (blue triangles) shows a linear dependence as expected.

5.4.2.2 Probe reflectivity with optimum parameters

The probe reflectivity observed in population switch approach is relatively far below 1, which is similar to the single-mode giant non-linearity in chapter 4 and also two-mode giant non-linearity in Autler-Townes approach in section 5.3.4. The main reasons have been discussed in section 4.3.2.2. The first reason is the linewidth broadening $4 \mu eV$ (due to pure dephasing ($1 \mu eV$) and spectral diffusion ($3 \mu eV$)). The second reason is the non-optimum input and output coupling efficiencies of the one-dimensional waveguide ($\varepsilon_{in} = \varepsilon_{out} = 0.26$ for the trumpet in this measurement). The third reason comes from the cross-polarized configuration, which reduces the amount of photons detected. Finally, the saturation results in the fact that just half the population is established in the X_x state, while the other half stays in the ground state. The presence of the other excitonic dipole X_y also influences the reflection.

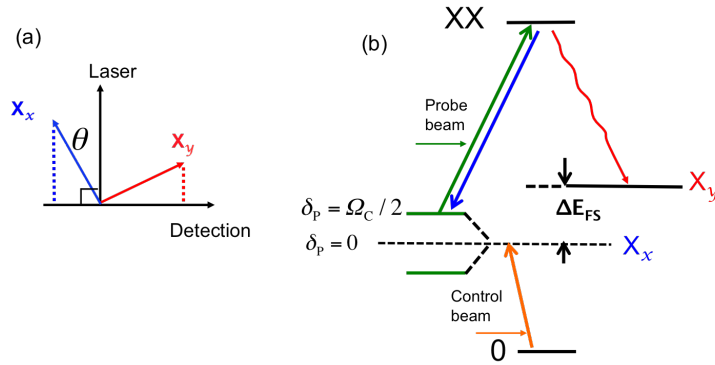


Figure 5.37 – Illustration of the population switch in cross-polarized detection scheme - (a) X_x state is at a polarization θ away from laser polarization. (b) When the power of the control beam is higher than saturation power, at $\delta_C = 0$, X_x state will be split into two new dressed states with frequencies $\pm\Omega_C/2$. There are two strategies to probe the upper transition $X_x - XX$, by either probing at the original X_x resonance frequency ($\delta_P = 0$) or by probing at one of the two dressed state frequencies ($\delta_P = \pm\Omega_C/2$).

In principle, as shown in Fig. 5.33, the maximum reflectivity is obtained when the X_x state is saturated. At saturation, X_x and ground states share each state a half of the total population. Thus, we lose a factor of 2 in reflectivity. Then, due to saturation (even in co-polarized excitation), destructive interference effect in the forward direction between the emission and the laser is canceled out. Therefore, the photons emitted are separately guided into forward and backward directions of the trumpet guided mode, another factor of 2 is lost. Next, we have to take into account the presence of the other FSS dipole X_y (Fig. 5.37). As soon as the XX level is populated due to coupling with the probe beam, the photons will decay through $XX \longleftrightarrow X_y$ transition. If the probe power is vanishingly small, one can neglect the contribution of X_y . But for a probe power high enough, eventually, half of the population of the X_x level will be transferred to level X_y .

In the following, we will consider an ideal one-dimensional three-level atom and show the calculated probe reflectivity in two excitation-detection scenarios: cross-polarization and co-polarization.

Ideal reflectivity in cross-polarized excitation At the control power level above saturation and with the control detuning $\delta_C = 0$, X is split by an amount equal to Rabi frequency of the control beam Ω_C (see Fig. 5.37(b)). For that reason, precise estimation can be made if we probe at the frequency of one of the two dressed states, as described in Fig. 5.37(b). However, in this case, only one dressed state is probed so that a factor of two in reflectivity will be lost. In the population switch approach, the probe beam is coupled to the $X_x \longleftrightarrow XX$ transition which makes the situation more complicated than coupling with the a real ground state. Because of those complications, the calculated probe reflectivity for both two geometries is plotted in Fig. 5.38 for an ideal-system in cross-polarized excitation scheme. The results indicate that for both cases, the ideal probe reflectivity can reach to around 0.03, which is still far below the unity reflectivity.

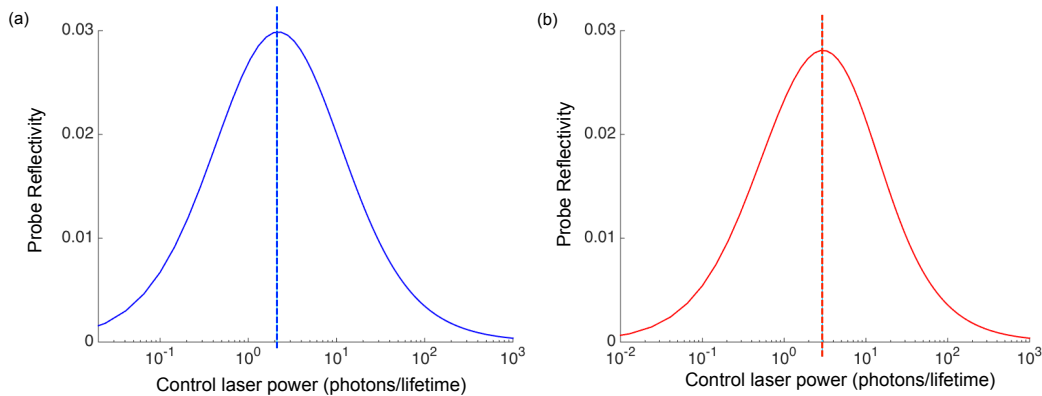


Figure 5.38 – Calculated probe reflectivity in cross-polarized at 27° excitation for the population switch approach - The control laser is always put at resonance frequency $\delta_C = 0$, (a) The probe beam is put on resonance with the original X_x state ($\delta_P = 0$). (b) The probe beam is put on resonance with one of the two Autler-Townes doublet ($\delta_P = \Omega_C/2$).

Ideal reflectivity in co-polarized excitation Given the same approach, if we excite in co-polarized scheme by assuming that there is no scattered laser background. In this case, the polarizations of excitation, detection and of X_x level are identical. It should be noted that the destructive interference effect between half the emission into the forward direction and the laser field is only valid for a power much lower than saturation. The effect is no longer valid for a control power above saturation. In addition, half of the population is lost at saturation. Fig. 5.39 plots the calculated probe reflectivity for two cases similar to the cross-polarization geometry above.

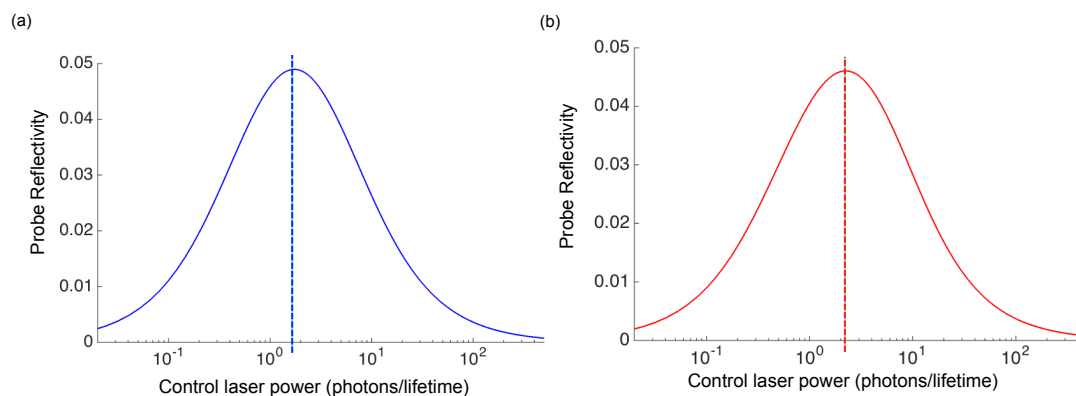


Figure 5.39 – Calculated probe reflectivity in co-polarized excitation for the population switch approach - The control laser is always put at resonance frequency $\delta_C = 0$, (a) The probe beam is put on resonance with the original X_x state. (b) The probe beam is put on resonance with one of the two Autler-Townes doublet.

Overall, even for a perfect three-level system in this approach, the reflectivity of a probe beam could be switched from 0 to only 0.05, the power required to obtain a maximum switch is ≈ 2 photons/lifetime. In comparison with the Autler-Townes approach, it has been presented in section 5.3.4.4 that the probe reflectivity could be switched from 1 to zero. In that case, with the control power 1 photon/lifetime, the reflectivity can be switched only from 1 to 0.5. It will require more than 10 photons/lifetime to switch the reflectivity close to zero.

For a short conclusion of this section, we have presented experimental results of two-mode giant non-linearity based on population switch approach. With the presence of a control beam coupled to the upper transition of a cascade three-level system, the reflectivity of a probe beam coupled to the lower transition can be switched to maximum with a control power as low as 100 photons/lifetime. This approach offers a unity switch contrast regardless of control power. Similar to Autler-Townes switch approach, the maximum reflectivity could be experimentally observed is also far below unity ($\approx 5 \cdot 10^{-4}$). It has been shown that even for an ideal case in this approach, the probe reflectivity can not be achieved more than 0.05, which is much worse than a unity reflectivity in the ideal case for Autler-Townes approach (see section 5.3.4.4).

5.5 Contributions of coherence and incoherence in total probe reflectivity

For any possible application in quantum information and computation, preserving the quantum coherent nature of the system is an important aspect. Section 4.1.2.4 and 4.3.2.3 in chapter 4 have discussed the contributions of coherent and incoherent scatterings in the

single-mode giant non-linearity case. Eqs. 4.5 describe the contribution of imperfections of the system on the incoherent part even at very low excitation power. In two-mode giant non-linearity with the same system, a similar behavior is observed and the calculation results will be presented in this section, for both two approaches.

5.5.1 Autler-Townes splitting approach

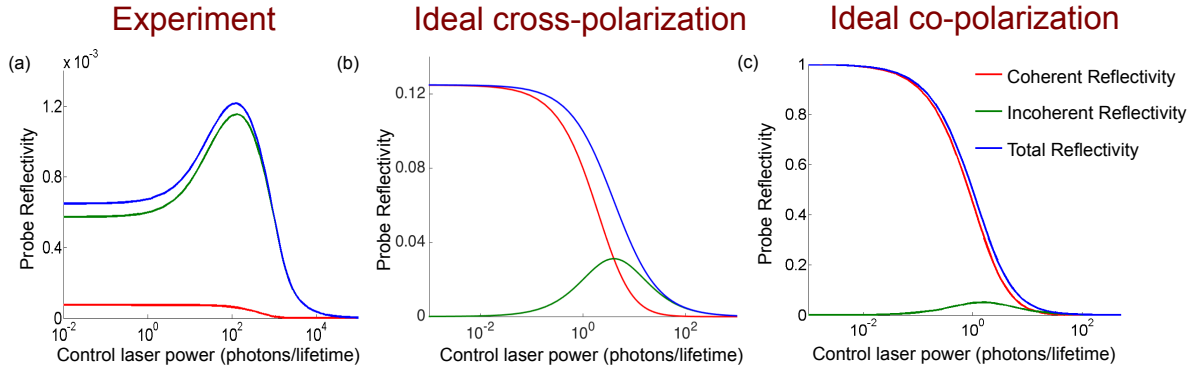


Figure 5.40 – Calculated coherent and incoherent contributions in total probe reflectivity in Autler-Townes splitting approach - The probe power is vanishingly small ($P_{Probe}/P_{sat} = 10^{-6}$). Three different cases are considered: (a) Probe reflectivity as a function of control power in cross-polarization detection scheme with $\theta = 27^\circ$, $\varepsilon_{in} = \varepsilon_{out} = 0.26$, total linewidth broadening $4 \mu eV$. (b) Probe reflectivity in cross-polarization detection scheme with $\theta = 45^\circ$, for an ideal system with no loss, $\varepsilon_{in} = \varepsilon_{out} = 1$, zero linewidth broadening. (c) Probe reflectivity in co-polarization excitation-detection scheme ($\theta = 0^\circ$) for an ideal system.

Fig. 5.40 plots the calculated probe reflectivity as a function of control power for the real experimental condition (Fig. 5.40(a)) with an angle $\theta = 27^\circ$ and for an ideal one-dimensional system in two excitation-detection scenarios: cross-polarization with $\theta = 45^\circ$ (Fig. 5.40(b)) and co-polarization (Fig. 5.40(c)). One could see that besides the dramatic differences in reflectivity between an ideal and a real perfect systems that has been discussed in section 5.3.4.4, coherent scattering also depends strongly on the imperfections of the system. In cross-polarization scheme, an ideal probe reflectivity can be reached up to 0.125. For an infinitely low control power, coherent scattering dominates the reflection. However, as discussed in section 5.3.4.2, increasing the control power results in an enhancing contribution of the other excitonic dipole, which is a source of decoherence.

The best scenario is obtained with an ideal system in co-polarized excitation scheme in Fig. 5.40(c). In this case, one can ignore the presence of the other excitonic dipole polarized in a perpendicular direction with respect to excitation and detection directions. Thus, coherent contribution is well preserved at control power below saturation. This feature together with a unity reflectivity at low control power are favorable conditions for the realization of a single-photon optical transistor.

5.5.2 Population switch approach

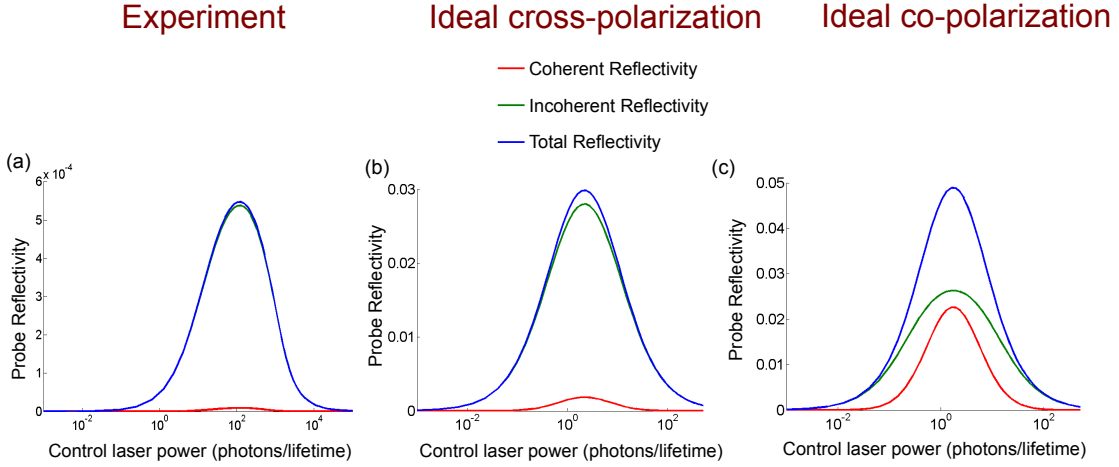


Figure 5.41 – Calculated coherent and incoherent contributions in total probe reflectivity in population switch approach - The probe power is vanishingly small ($P_{Probe}/P_{sat} = 10^{-6}$). Three different cases are considered: (a) Probe reflectivity as a function of control power in cross-polarization detection scheme with $\theta = 27^\circ$, $\varepsilon_{in} = \varepsilon_{out} = 0.26$, total linewidth broadening $4 \mu eV$. (b) Probe reflectivity in cross-polarization detection scheme with $\theta = 27^\circ$, for an ideal system with no loss, $\varepsilon_{in} = \varepsilon_{out} = 1$, zero linewidth broadening. (c) Probe reflectivity in co-polarization excitation-detection ($\theta = 0^\circ$) scheme for an ideal system.

In this approach, similar set of calculation is plotted in Fig. 5.41, for the probe reflectivity of the real system as well as for an ideal system in crossed-polarized and co-polarized detection schemes. One could see that incoherent scattering is dominant even with an ideal system in cross-polarization scheme. This is because in this approach, the probe beam is coupled to the $X_x \longleftrightarrow XX$ transition and thus it makes the situation more complicated than coupling with the ground state. In addition, the presence of the other fine-structure splitting level X_y also impacts the probe reflectivity of level X_x .

This section has shown that even though the experimental data for a all-optical switch in Autler-Townes splitting approach is not as good as that in population switch approach, it turns out that for an ideal system, Autler-Townes approach out-performs the other in which unity parameters required for a all-optical transistor could be reached.

5.6 Switching time

We have shown that a all-optical switch can be realized at the levels of just a few photons per emitter lifetime. In practice, another crucial factor that determines the performance of an optical transistor is the amount of time needed to perform a switch.

Firstly, we consider the Autler-Townes switch approach. Let us assume that the lower transition is always excited by a continuous wave (CW) probe laser. The presence of a

strong control beam coupled to the upper transition dresses the intermediate state and switches the probe reflection. Therefore, in principle, the time required to obtain this switch is the time it takes to establish the two new dressed states. In principle, when a control pulse is coupled to the upper transition, the levels will Rabi oscillate with a damping rate equal to the decay rate of the transition. Therefore, the time required to establish an Autler-Townes doublet is equal to the decay rate of the emitter.

Secondly, in the population switch approach, the probe beam is coupled to the upper transition. Without the control beam, no reflection is induced. When the control beam coupled to the lower transition is turned on, the intermediate state is populated and thus the probe reflection is switched. In this case, one has to firstly consider the time needed to populate the intermediate level. Imagine if we excite the lower transition with a π -pulse. In this case, the time to populate the lower transition will be inversely proportional to the pulse amplitude ($\Omega t = \pi$). There is a trade-off between time and amplitude. A short population time requires a strong control pulse and vice versa, a low-power control pulse leads to longer population time.

Finally, it should be noted that in any case, even for a single-mode giant non-linearity with a two-level system coupled with a single field, it always takes a time $1/\gamma$ to establish the reflection.

5.7 A comparison with state of the art giant non-linearity

5.7.1 Single-mode giant non-linearity

Single-mode giant non-linearity in which a quantum emitter can change the transmission of an incoming electromagnetic field at ultra-low power has been reported in several systems, mostly with QDs inside one-dimensional photonic structures. Table 5.1 shows a short summary of the results obtained with the common QD - photonic structure systems. For a QD-pillar-cavity system, giant non-linearity has been reported by the group of P. Senellart from *Laboratoire de Photonique et Nanostructures*, LPN/CNRS in 2012 [14] and recently in 2015 [130]. Owing to the high input-output coupling efficiencies, together with high spontaneous emission enhancement, a giant non-linearity threshold was obtained with just 8 photons/pulse in [14] and less than 1 photon/pulse in [130]. With photonic crystal cavity, the non-linearity was shown to be achieved with a few average cavity photon numbers [30], by the group of J. Vucković from *Stanford University, USA*. However, the actual power required at the input of the system was larger since the input coupling efficiency was only 1.8%. For photonic crystal waveguide, in 2015, the group of P. Lodahl from *Niels Bohr Institute, University of Copenhagen*, demonstrated a giant non-linearity at a level of less than one critical average photon per lifetime with a system having 23% input-coupling efficiency [31].

Apart from semiconductor QDs, strong light-matter non-linear interaction has also been reported with superconducting transmon qubit [32], ultra cold atom gas [33, 34], which will be shown in the coming section.

Photonic structure	Excitation method	Input %	Output %	Power at threshold	Year	Broadband property
Pillar MC	CW/Pulse	95%	16%	8 photons/pulse	[14] 2012	No
Pillar MC	CW/Pulse	95%	70%	0.7 photon/pulse*	[130] 2015	No
PC Waveguide	CW	23%	N/A	2 nW	[31] 2015	20 nm
PC cavity	CW	1.8%	N/A	200nW*	[30] 2007	No
Waveguide ¹	CW	26%	26%	2 photons/lifetime		>100 nm

MC: Micro-cavity.

CW: Continuous wave.

PC: Photonic crystal.

N/A: Not available.

* : Value inferred from given parameters.

¹ : QD-trumpet system studied in this thesis.

Table 5.1 – Common QD - photonic structure systems that have been reported to show single-mode giant non-linearity.

5.7.2 Two-mode giant non-linearity

We have shown in this chapter a all-optical switch based on a three-level system with two distinct probe and control beams coupled to two transitions of the system. In literature, the investigation of dressed excitonic states based on a QD three-level system has been reported in several articles [153–155]. Autler-Townes splittings were observed in [153] considering a cascade three-level system similar to our study and in [154] considering a “V” system. In [155], the authors reported a cascade three-level QD in which both two switching approaches (control beam coupled to either upper or lower transition) were considered. However, all of those articles were done with bulk QDs, which were not embedded in any photonic structure. Thus none of them has observed the effect at ultra-low power level and therefore a giant non-linearity has not been addressed.

Autler-Townes splitting approach has also been used for different types of artificial

atom. In [156], the authors have observed the Autler-Townes splitting on a superconducting loop interrupted by Josephson junctions (superconducting qubit). Io-Chun Hoi et.al. [32] demonstrated a single-photon router in the microwave regime, their artificial atom is a multi-level superconducting transmon qubit, strongly coupled to a superconducting one-dimensional transmission line. By coupling two optical fields on three energy levels of the transmon, one strong control field splits the original intermediate state into a doublet due to Autler-Townes splitting. In this work, the system was seen as a single-photon router, where the probe field in the single-photon regime is reflected without the control field (routed to one port) and transmitted with the presence of the control field (routed to another port).

Photonic structure	Excitation method	Input %	Output %	power of CB	Year	Broadband property
PC cavity	Pulse	0.8%	N/A	140-400 photons/pulse	[43] 2012	No
PC cavity	Pulse	3%	N/A	3.4 nW ¹	[82] 2012	No
PC cavity	Pulse	2%	N/A	120 photons/pulse	[42] 2012	No
waveguide ²	CW	26%	26%	10-100 photons/lifetime		> 100nW

CB: Control beam.

MC: Micro-cavity.

CW: Continuous wave.

PC: Photonic crystal.

N/A: Not available.

* : Value inferred from given parameters.

¹ : With 40 ps pulse duration and 80 MHz pulse repetition rate

² : QD-trumpet system studied in this thesis.

Table 5.2 – Quantum dot - photonic structure systems that have been reported to show two-mode giant non-linearity.

All-optical switch and transistor can also be obtained with ultra-cold atom [33, 34, 40, 157]. In [33], the group of G. Rempe from *Max-Planck-Institut für Quantenoptik, Germany* a combination of electromagnetically induced transparency (EIT) (see section 5.1.7 for EIT) with Rydberg states and Rydberg blockade was used to create large nonlinearities. The “average” gate photon number required to switch one or more source photons was in the order of one photon. However, in this type of approach, a strong control field

is always required to provide EIT effect. Another approach using a four-state N-type laser-cooled cesium atom was reported in [157] by the group of M.D. Lukin from *Harvard University, USA*, they demonstrated a all-optical transistor device in which one stored gate photon controlled the resonator transmission of subsequently applied source photons, this approach also needed a control laser to induces transparency (through EIT) for the gate photons.

Another method to obtain low-power all-optical switching is to exploit the strong atom-light interactions between a QD and a photonic crystal cavity. Cavity-QD interactions can enable the strong coupling regime where a cavity and a QD mix to form new polariton states. In this strong coupling regime, the system can exhibit a large nonlinear optical response at low optical powers [25, 41, 43, 158]. Therefore, controlling these nonlinearities could enable all-optical switching at low energy. In addition, this approach also offers fast switching time scale, in the ps regime. In particular, R. Bose and co-workers from *University of Maryland, USA* reported a nonlinear all-optical switch by utilizing strong coupling between a single QD and a planar photonic crystal cavity structure [43]. The response of the strongly coupled system is modulated by a picosecond pump laser pulse that induces a large nonlinear response, resulting in an observed modification of the transmission and scattering amplitude of a second incident probe pulse. The pump energy required for optical switching ranges from 140 to more than 440 photons. The same protocol has been addressed by the group of J. Vucković. Their non-linear optical medium consisted of a three-hole-defect photonic crystal cavity with a layer of self-assembled InAs QD [82]. In [42], the group of A. Imamoglu from *Institute of Quantum Electronics, ETH Zurich* also reported a similar study based on a strongly coupled QD-cavity system. A control laser was tuned to one of the two polariton resonances, and a signal laser pulse was scanned across the spectrum. The presence of the control laser reduced the polariton signal and thus induced the non-linearity. The power of the control laser was ~ 120 photons/pulse. A short summary of those QD-cavity strong coupling system is shown in table 5.2. Although this kind of method is different from our approach, it is worth to have a comparison because of the similarity of the systems.

Alternatively, a single-photon transistor can be realized using nanoscale surface plasmons system proposed by M.D. Lukin and coworkers [46]. Surface plasmons are propagating electromagnetic modes confined to the surface of a conductor-dielectric interface. Their unique properties make it possible to confine them to sub-wavelength dimensions [44, 45]. Therefore, it was proposed that a non-linear effect can be exploited by the strong coupling between individual optical emitters and propagating surface plasmons confined to a conducting nanowire to perform a two-photon switch, leading to the realization of a single-photon transistor.

5.8 Chapter summary

This chapter presented a detailed study of two-mode giant non-linearity with two distinct lasers coupled to a QD three-level system embedded in a photonic trumpet. A all-optical switch was obtained by looking at the reflection of a probe beam coupled to one transition, depending on the presence or absence of a second control beam coupled to the other transition of a three-level system. Two approaches were considered with probe beam coupled to upper or lower transition. In both two approaches, all-optical switches were realized at the level starting from just a few photons/lifetime. The conclusion was that the most efficient switch was achieved when the probe beam is coupled to the upper transition, with a control power of just ≈ 100 photons/lifetime to obtain maximum reflectivity. This chapter once again confirmed the excellent one-dimensional waveguide property of the photonic trumpet, as well as its efficient broadband operation feature. The results of two-mode giant optical non-linearity presented in this chapter have not reached the unity conditions for the realization of a single-photon transistor. However, it was also shown that an ideal all-optical switch could be obtained in Autler-Townes approach with an optimized system.

Chapter 6

Summary and Perspectives

This thesis work focused on a realization of two-mode optical giant non-linearity using a InAs quantum dot (QD) embedded in a GaAs photonic trumpet, which paves a way in obtaining an ultra-low-power all-optical switch. At the end of the thesis, the initial goal has been achieved. We have demonstrated a all-optical switch in which the reflection of a probe beam was modified by the presence of a control beam at the level of just a few tens of photons per emitter lifetime. This is the lowest switch power level that has been reported for a QD-waveguide system. In addition, the fact that the switch was realized by two distinct optical beams is an experimental confirmation of the excellent broadband operation feature of the photonic trumpet. The following paragraphs will briefly summarize the main content of this thesis.

At the beginning of the thesis, chapter 2 gave an overview about semiconductor QDs and photonic nanostructures. General properties, applications, multi-exciton levels and fabrication process of self-assembled InAs QDs embedded in a GaAs photonic trumpet were presented.

The following chapter presented the basic characterizations of PL spectroscopy of QDs embedded in a photonic trumpet. A detailed description of experimental configuration was presented. Non-resonant PL measurement was performed. Power dependence analysis and polarization dependence PL measurement were taken into account to help identify the neutral exciton (X) and biexciton (XX) transitions of a single QD. Time-resolved PL measurement was also carried out to study the lifetime of the neutral X and XX in a single QD embedded in a trumpet.

The last two chapters are dedicated to the presentation of optical giant non-linearity of the one-dimensional system. Firstly, in chapter 4, single-mode giant non-linearity was investigated. The giant non-linearity was experimentally realized by characterizing the reflectivity of a one-dimensional system based on the saturation effect of a two-level system. The reflectivity measurement was done by performing resonant fluorescence spectroscopy.

To perform the resonant excitation measurement, a cross-polarized detection scheme was established to subtract the laser background. A ultra-weak non-resonant laser was added to the setup to reduce the spectra diffusion caused by the fluctuating charge environment surrounding the QDs. The reflectivity as a function of excitation power was plotted showing a non-linear behavior. Thanks to the excellent one-dimensional waveguide property of the trumpet, the single-mode giant non-linearity was observed with just 2 photons/lifetime at non-linear threshold.

The thesis then went on with chapter 5 considering a QD with three-level (or four-level taking into account the exciton fine-structure dipoles) in a one-dimensional system, to realize two-mode giant non-linearity. The idea was to use two distinct laser beams coupled to two different transitions sharing a common level. One beam played the role of the probe beam, the reflection of which was expected to change depending on the presence or absence of a second beam, who played the role of the control beam. Two approaches were considered with probe beam coupled to upper or lower transitions of the three-level ladder system. This chapter firstly begun with introducing some basic theoretical backgrounds of dressed atom pictures and Autler-Townes effect on a three-level system. In both two approaches, all-optical two-photon switches were realized at the level starting from just a few photons per lifetime. Eventually, the most efficient two-mode giant non-linearity was achieved when the probe beam is coupled to the upper transition. In particular, a control beam could switch a probe beam efficiently from zero reflection to maximum reflection. This demonstration is due to the excellent one-dimensional waveguide property of the photonic trumpet. In addition, the fact that two laser beams with different frequencies could be well coupled to two different transitions of a three-level system can only be of the efficient broadband operation feature of the trumpet. Overall, those results provide a very promising candidate for ultra-low power all-optical transistors and switches or eventually to possible quantum information and computation applications.

For the future works, as discussed in section 5.5.1, for an ideal system, unity reflectivity and highly preservation of coherence can be obtained by performing a co-polarized excitation in Autler-Townes switch approach. To improve the system, firstly, it has been stated in the previous chapters that the QD-waveguide coupling efficiency can be enhanced by optimizing the dimensions of the trumpet. As shown in Fig. 2.13 and 2.14(b), for an on-axis QD emitting at $\lambda = 950$ nm, a trumpet with a bottom diameter around 240-260 nm features a spontaneous emission coupling rate $\beta \approx 95\%$. For the first-lens input-output coupling efficiencies, in [23], M. Munsch and co-workers reported a study on the far-field emission of these photonic trumpets showing that the transmission into a numerical aperture 0.75 objective lens could reach 95% for a trumpet with top diameter around $2.5 \mu\text{m}$ and an opening angle around 10° . Combining those parameters can result in the total input-output coupling efficiencies $\varepsilon_{in} = \varepsilon_{out} \approx 90\%$.

Another possibility of improvement is to minimize the effect of spectral broadening. In particular, one idea to reduce the influence of pure dephasing is to implement a low-Q cavity into the trumpet structure and take advantage of a fairly weak Purcell effect of the cavity to enhance the spontaneous emission rate. Thus, the impact of pure dephasing will be reduced. Although this approach will decrease the broadband operation property of the trumpet, such a two-mode giant non-linearity experiment does not require an 100 nm broadband feature. For example, 1 nm broadband operation is enough to perform the two-color resonant excitation with the QD in our study. In addition, reducing the sensitivity of the system to decoherence sources like pure dephasing also enhances the coherent scattering rate of the emitter.

A realization of a single-photon transistor would be an important step toward the realization of optical computing and eventually quantum computing. Nevertheless, the question whether or not quantum computation could really be achieved has been still controversial. For example, in [159, 160], the authors have proved the impossibility of realizing a quantum logic based on single-photon Kerr nonlinearities to achieve cross-phase-modulation between two optical fields.

Besides the context of giant optical non-linearity, another interesting perspective is to combine quantum optics and mechanical properties of this one-dimensional system. It has been shown that the photonic trumpet can be considered as a mechanical oscillator [96], where the influence of the mechanical motion on the fluorescence properties of the emitter was evidenced. The system with a quantum emitter coupled to a mechanical oscillator is a hybrid system. In [161], it was proposed that a two-level quantum emitter under a modulated resonant optical excitation could behave like an optomechanical transducer and create constructive interferences of classical phonon fields in the oscillator. Thus, optically resonant driving of the QD results in the excitation of large amplitude mechanical oscillations. This mechanism could open up interesting applications, for example a single-shot measurement of a QD state with high signal to noise ratio or a temperature manipulation of the mechanical mode.

Appendix A

Fitting method for the unknown parameters of the quantum dot-waveguide system

This appendix will briefly show the fitting method to find the parameters of the real system. As has been showing in chapter 4 and 5, the unknown parameters of a QD-waveguide system are the input-coupling efficiencies ε_{in} , ε_{out} and the origins of the resonant spectra linewidth broadening. One of the ways to find those parameters is to rely on Autler-Townes splitting measurement. From section 5.1.1, we know that when the intermediate state of a three-level atom is dressed by a strong control field, it will be split into two new states with the Autler-Townes splitting $\Omega = \sqrt{\delta_C^2 + \Omega_1^2}$. For a non-perfect system, Ω_1 is defined as the Rabi frequency of the control field inside the waveguide before coupling with the QD. At zero detuning of the control field, $\Omega = \Omega_1 = \sqrt{\varepsilon_{in}}\Omega_0$ with Ω_0 is the real Rabi frequency of the control field before entering the waveguide, which can be measured with normal power detectors. Therefore, with a given Ω_0 and knowing the Autler-Townes splitting from the two-laser scan, one can firstly infer the input coupling efficiency of the waveguide.

The next unknown parameters are the contributions of homogeneous broadening (pure dephasing factor γ^*) and inhomogeneous broadening (spectral diffusion factor σ_X) on the total linewidth of the resonant spectrum. Pure dephasing arises from fast fluctuations of the medium that causes rapid vibrations of energy levels in a time scale faster than the recombination time of the emitter. Therefore this fluctuation is homogeneous and pure dephasing rate γ^* can be appeared in Bloch equations of the field-atom interaction (see section 4.1.2). By contrast, spectral diffusion arises due to fluctuation of the environment surrounding the emitter at a rate higher than the spontaneous emission rate but much shorter than the detection limit of the CCD devices. This results in an inhomogeneous

broadening of the spectrum. The question is what are the weights of these two types of broadening in the total spectral width. From the resonant spectrum, a total spectral width $4.5 \mu eV$ is easily to be extracted, in which it includes $0.5 \mu eV$ radiative-limit linewidth (see section 4.2.3). Thus the total spectral broadening is $4 \mu eV$. Fig. A.1 shows an example of a fitting process based on the experimental result in a two-mode giant non-linearity based on Autler-Townes approach. Fig. A.1(a) plots the experimental result of a two-laser scan with control power 274 nW. As mentioned above, the first step is to find ε_{in} , which is 0.26 in this case. Fig. A.1(a), (b) and (c) show the theoretical plots for different values of γ^* . Comparing them to the experimental plot, one can see that Fig. A.1(c) is the best fit to the measurement. Eventually, the homogeneous and inhomogeneous linewidth are selected to be respectively $1 \mu eV$ and $3 \mu eV$.

One can also base on the probe reflectivity experimental results in population switch approach to find the unknown spectral broadening parameters. From the experiment data in section 5.4.2 for two different probe powers, different values of homogeneous and inhomogeneous broadenings are applied in the theoretical calculation to obtain the best fit. The fitting plots are shown in Fig. A.2. One could see that similar to the above fitting process, the most suitable fit is for a pure dephasing $\gamma^* = 1 \mu eV$, as showing in Fig. A.2(b). The good agreement between two fitting approaches gives the final reliable broadening parameters, as well as the coupling coefficients.

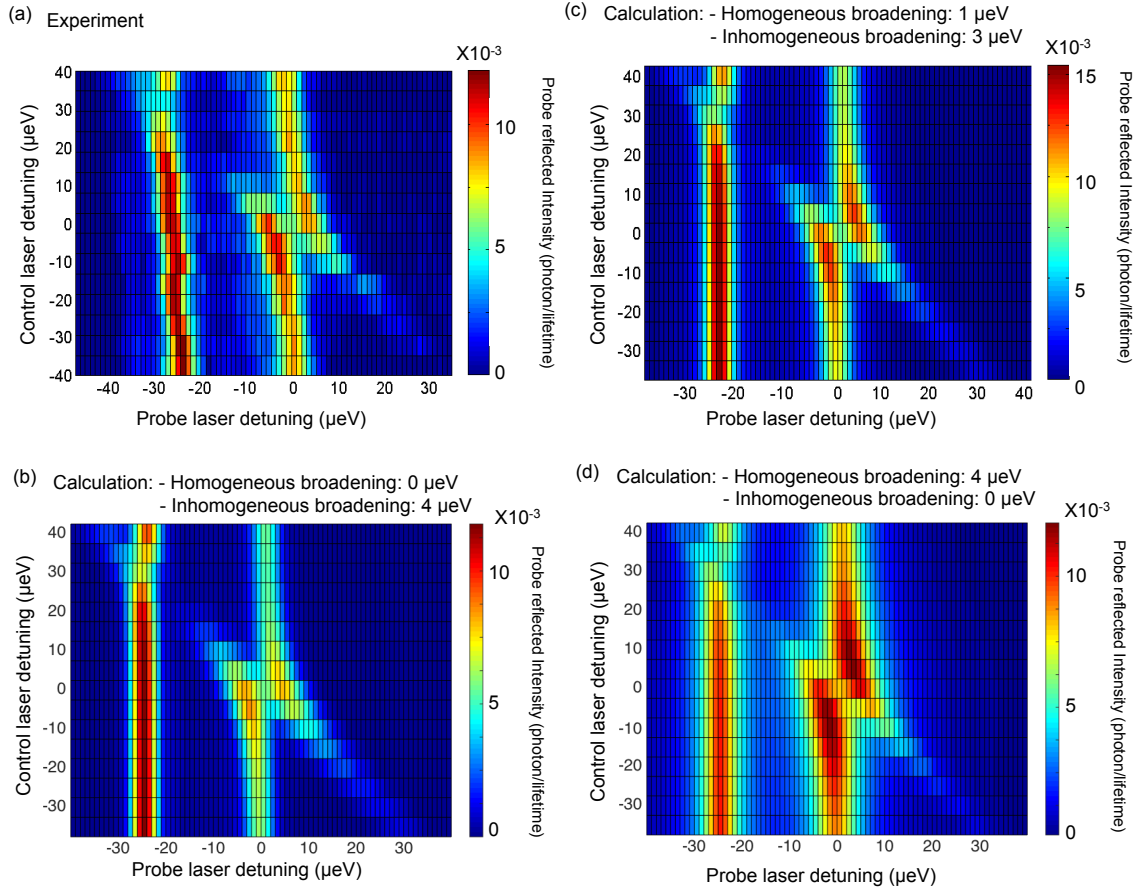


Figure A.1 – Two-laser scan in Autler-Townes approach with a probe beam coupled to $0 \leftrightarrow X$ transition - The probe power $P_{Probe}/P_{sat} = 0.2$. The control power is 274 nW in this case (see Fig. 5.21 in the main text). In the calculation, the total linewidth broadening is always 4 μeV , the input and output coupling efficiencies $\varepsilon_{in} = \varepsilon_{out} = 0.26$. (a) Experimental data. (b) Theoretical calculation for homogeneous broadening (pure dephasing) $\gamma^* = 0\mu\text{eV}$ and inhomogeneous broadening (spectral diffusion) $\sigma_X = 4\mu\text{eV}$. (c) Theoretical calculation for $\gamma^* = 1\mu\text{eV}$ and $\sigma_X = 3\mu\text{eV}$. (d) Theoretical calculation for $\gamma^* = 4\mu\text{eV}$ and $\sigma_X = 0\mu\text{eV}$.

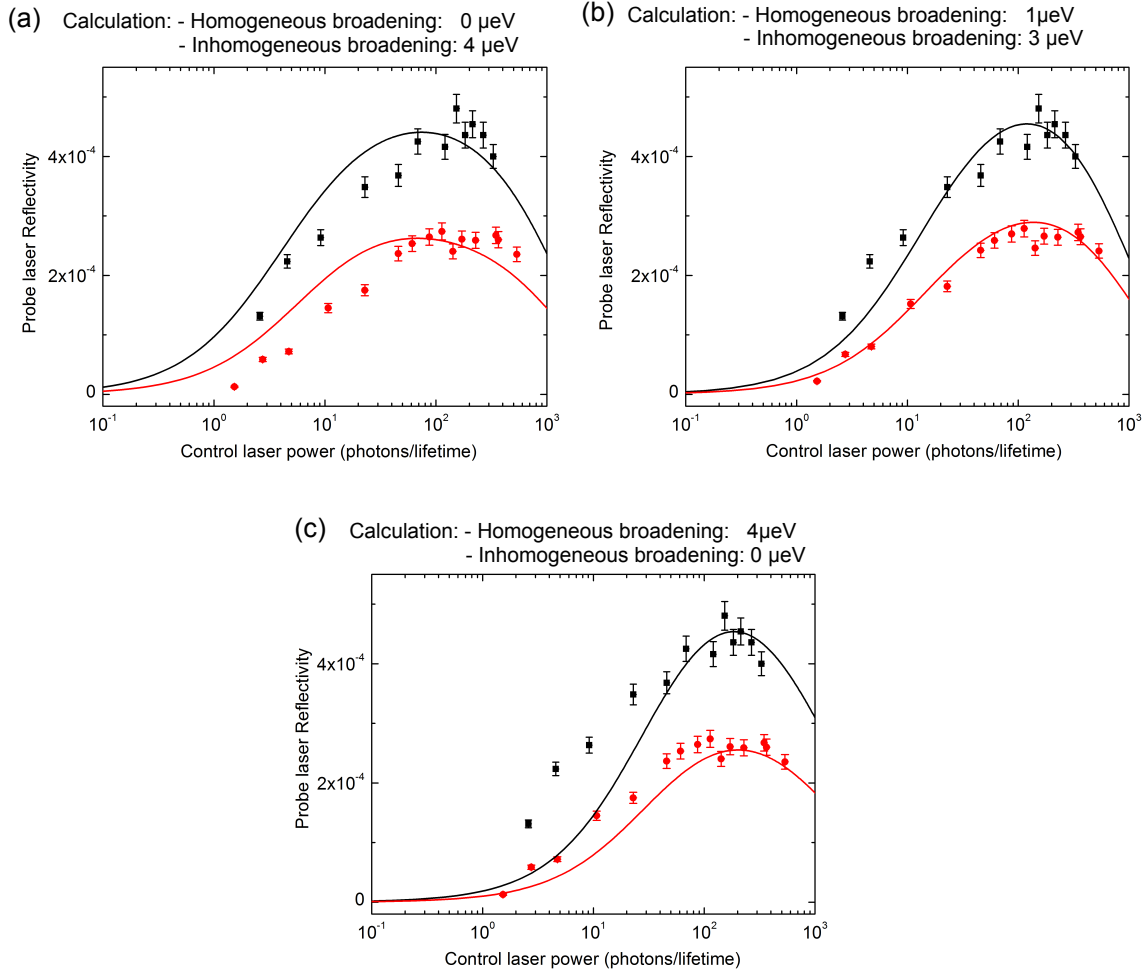


Figure A.2 – Calculated probe reflectivity for different homogeneous broadenings
- The experimental data obtained for two different probe powers 0.5 nW ($P/P_{sat} = 0.1$) and 2.6 nW ($P/P_{sat} = 0.5$) is fitted with different combinations of homogeneous (γ^*) and inhomogeneous (σ_X) broadenings, the total linewidth broadening is always $4 \mu\text{eV}$ in the calculation. (a) $\gamma^* = 0$, (b) $\gamma^* = 1 \mu\text{eV}$ and (c) $\gamma^* = 4 \mu\text{eV}$.

Appendix B

Observation of suspended and giant trumpets

In this thesis, we also perform the measurements for other types of trumpet, namely “suspended” and “giant” trumpets. Both of them were fabricated by J. Claudon and J-M. Gérard in CEA/INAC. This appendix will briefly introduce the structures and also present the basic optical spectroscopy measurements of these two trumpet families .

B.1 Suspended trumpet

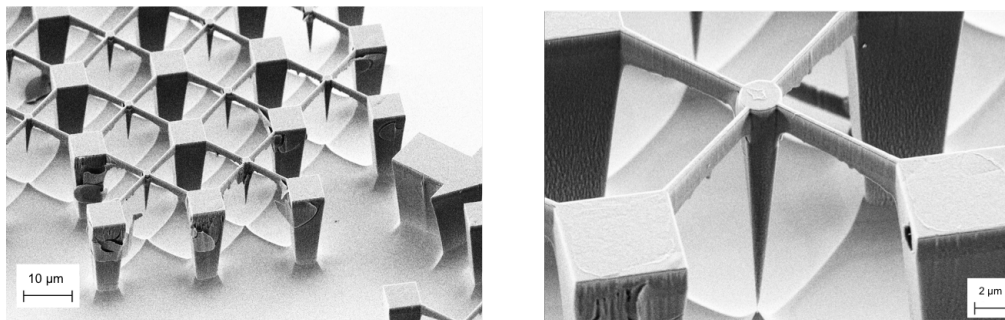


Figure B.1 – Scanning electron microscope views of suspended trumpets. The top diameter ranges from 1.5 to 3.3 μm with 20 nm step. The opening angle of the taper is 8.5° .

Scanning electron microscope (SEM) images of suspended trumpet are shown in Fig. B.1. The main difference of this sample compared to the “free-standing” trumpets presented in the main part of the thesis is that the trumpets are held by the pillars. The bottom of the trumpet is not connected to the substrate. This structure offers improved mechanical stability and robustness.

Besides the round-shape top facet samples, this set of suspended trumpets also comes up with elliptical-shape top facet samples. .

B.2 Giant trumpet

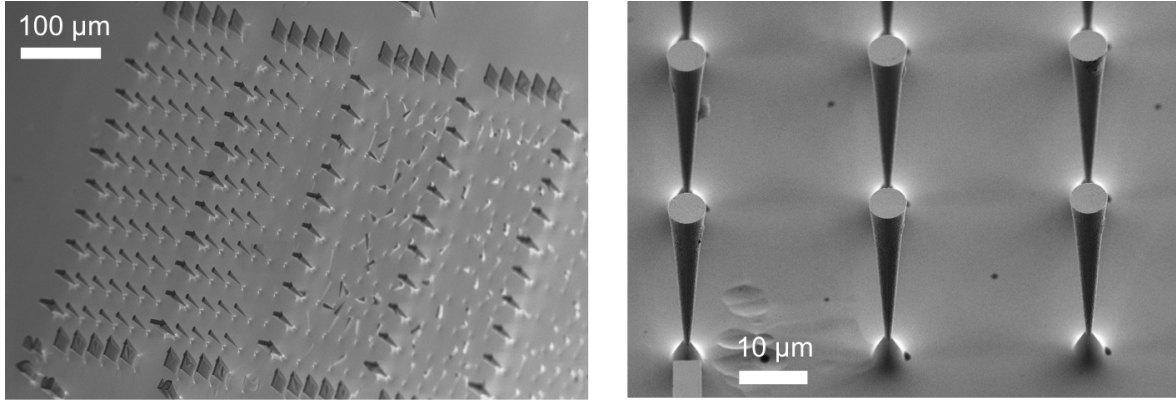


Figure B.2 – SEM images of giant trumpets. The maximum top diameter is $7 \mu\text{m}$.

This family of “free-standing” trumpet is considered “giant” because in comparison of the normal trumpets presented, the top facet diameter can reach up to $7 \mu\text{m}$. This set of trumpets has an opening angle up to 10.5° (compared with 5° of the normal ones), the height is $26.8 \mu\text{m}$ (compared with $17 \mu\text{m}$ of the normal ones). The purpose of fabricating a large top facet trumpet is to improve the output beam directivity and thus obtain highly Gaussian far-field emission [135].

B.3 Photoluminescence spectra of quantum dots embedded in a suspended trumpet

In the following sections, we will show the preliminary results of the photoluminescence (PL) and resonant excitation (RE) spectra from suspended trumpets. The study of PL spectroscopy is carried out in the same configuration as the normal free-standing trumpets. We focus just on the trumpets which have circular top diameter. The most efficient PL is observed with the trumpets with top diameter around $2.5\text{-}2.7 \mu\text{m}$ (which corresponds around 500 nm base diameter where QDs are located). The percentage of the “alive” trumpets, which means the trumpets that emit efficient PL, is relatively higher compared with the normal trumpets. In addition, each suspended trumpet contains many active QDs. Fig.B.3 shows a typical PL spectra of a suspended trumpet, with a top diameter $2.66 \mu\text{m}$. The non-resonant excitation power is $7 \mu\text{W}$. A high density of emission lines is observed. In general, the emission energy is similar to the QDs embedded in free-standing trumpets.

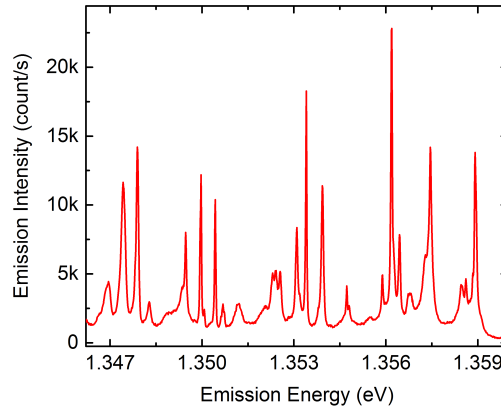


Figure B.3 – An example of PL spectra from QDs embedded in a suspended photonic wire - Many emission lines are observed. The emission linewidth is different from QD to QD, which is in the range from a few tens of μeV to more than $100 \mu\text{eV}$.

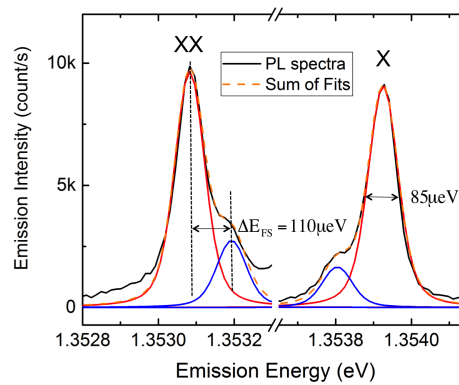


Figure B.4 – Exciton and biexciton lines of an InAs quantum dot embedded in a suspended trumpet - The X and XX lines are well fitted two curves (blue and red lines), which represent two linearly polarized emission lines.

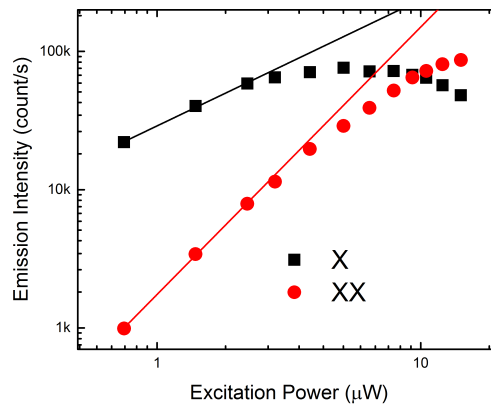


Figure B.5 – Exciton and biexciton power dependence of a QD in a suspended trumpet.

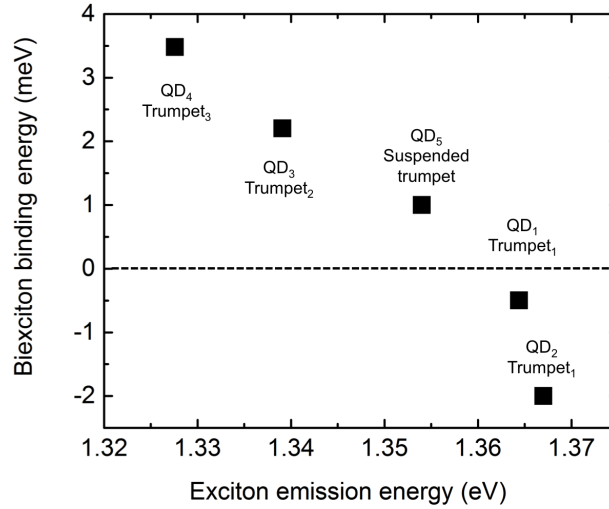


Figure B.6 – Biexciton Binding energy as a function of exciton energy for InAs QDs in suspended and free-standing trumpets - The binding energy of InAs QDs embedded in suspended trumpet matches the dependency of the ones embedded in free-standing trumpets.

Fig.B.4 shows a typical PL spectra of a pair of X and XX emission lines from a QD inside a suspended trumpet. Two orthogonal-polarized lines are clearly observed. The fine-structure splitting (FSS) energy of this X level is $110 \mu eV$, the linewidth of the lines is about $85 \mu eV$. Investigating other QDs gives linewidths which are in the same range of the QDs embedded inside the free-standing trumpets. The non-resonant excitation power dependence of the X and XX lines is also plotted in Fig. B.5. The linear and quadratic dependence are observed for X and XX lines, with the exponents 0.92 and 1.93, respectively.

For this QD, the XX binding energy is close to $1 meV$, with the X emission energy $\sim 1.354 eV$. If we place this value together with the binding energies obtained for free-standing trumpets, the plot is shown in Fig. 3.11. A good trend is still observed confirming the linear dependence of binding energy on the X emission energy.

B.4 Resonant excitation spectra of suspended trumpet

RE measurement of the suspended trumpets is carried out in exactly the same manner as with the free-standing trumpets. A weak non-resonant laser is also introduced to help reducing any possible spectral diffusion process. Fig. B.7 shows the PL spectrum for the X states of a InAs QD embedded in a suspended trumpet with top diameter $2.62 \mu m$. Two FSS dipoles are observed with the linewidth about $27 \mu eV$, the FSS energy is found out to

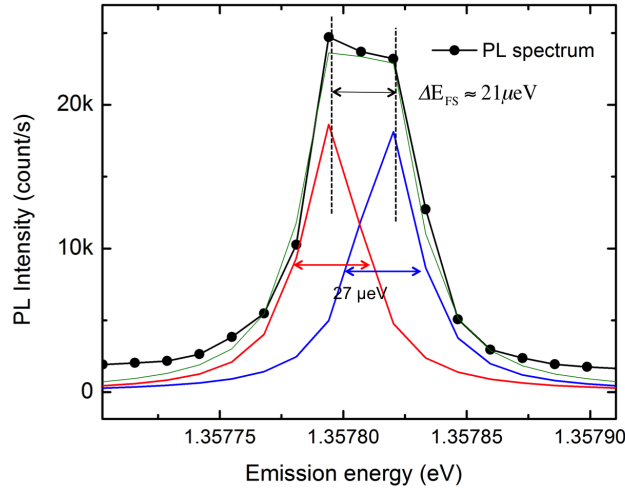


Figure B.7 – Photoluminescence spectrum of the excitonic level of a QD in a suspended trumpet used for the resonant excitation measurement.

be about $21 \mu\text{eV}$. In principle, narrow PL linewidths promise to obtain very narrow RE linewidths of these transitions. Unfortunately, in our measurement, we observe very large resonant spectra linewidths with this QD, as showing in Fig. B.8(a). The black circles are the experimental data. The data was fitted with the black and blue curves, which corresponds to the two FSS dipoles. The black curve is the sum of the two individual fitted curves. Various amount of the weak non-resonant laser has been used in an effort to reduce the spectral linewidth. However, the narrowest linewidth observed is $15.6 \mu\text{eV}$, which is more than 3 times larger than the linewidth obtained with free-standing trumpet. The FSS energy observed by scanning the resonant laser is in the good agreement with the value obtained by PL spectrum. Many resonant excitation measurements have been performed for various QDs from different trumpets, unfortunately, the same rather large linewidth is observed.

For giant trumpets, the very similar behavior is obtained for both PL spectroscopy and RE measurement. Fig. B.8(b) shows the RE spectra for a giant trumpet with top facet diameter of $5.32 \mu\text{m}$. Two RE peaks are observed with the large linewidth of $15.8 \mu\text{eV}$, the exciton FSS energy is $12.7 \mu\text{eV}$. The large amount of linewidth broadening observed for both two new sets of samples can be attributed to some intrinsic properties of the samples or to the fabrication process. For example, the effect of spectral diffusion is too intense and it can not be reduced by the weak non-resonant laser. Further study and measurement would be required to fully understand and to be able to efficiently reduce the spectral broadening of these two samples.

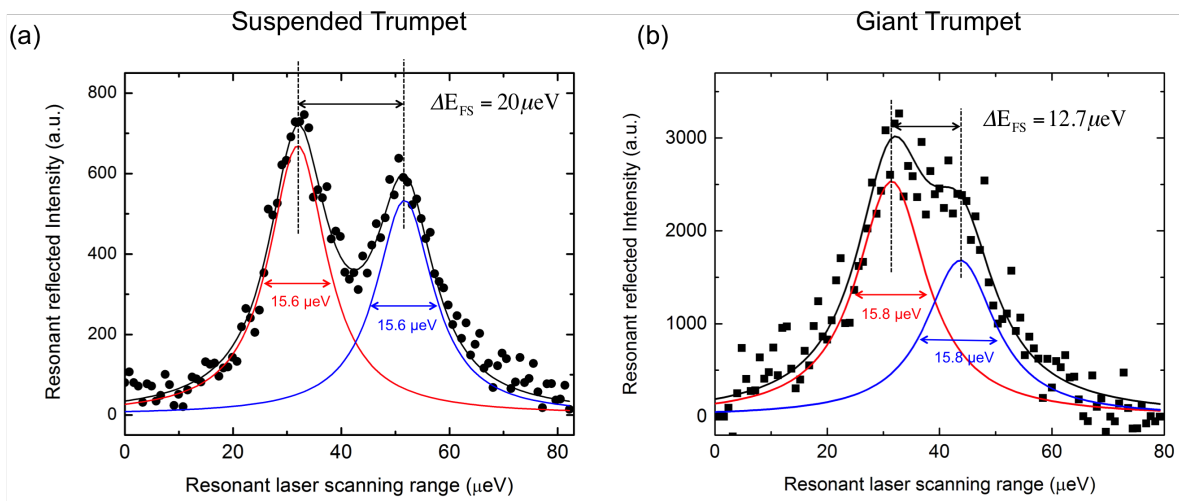


Figure B.8 – Resonant excitation spectra of the QD embedded in (a) a suspended trumpet and (b) a giant trumpet. Two fine-structure dipoles are observed with the expected splitting, however, the linewidth of the resonant spectra are broad even with the presence of a weak non-resonant laser.

Appendix C

An alternative to counteract the temporal spectral drift

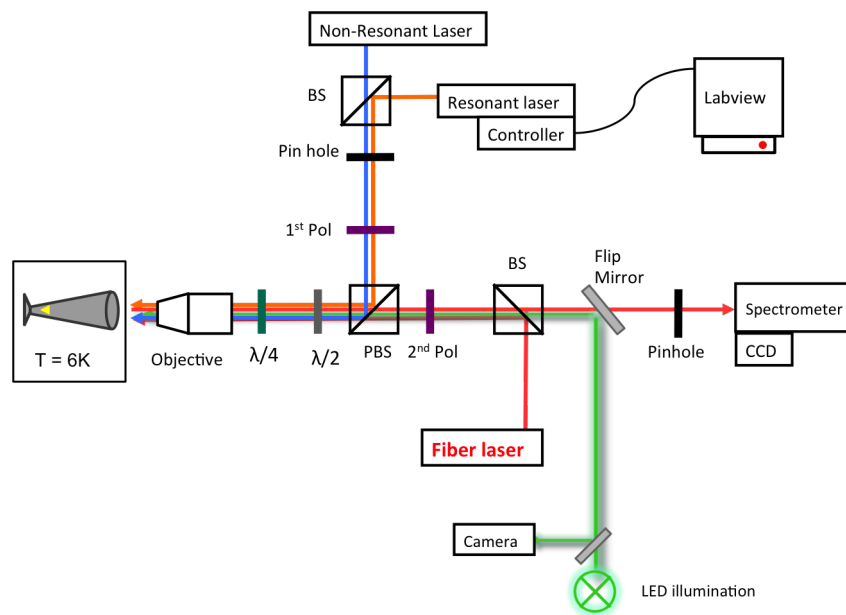


Figure C.1 – Experimental setup of the resonant excitation with the presence of an intense fiber laser. The fiber laser has the energy much lower than the emission energy of the QD.

As has been mentioned in the main part of this thesis, temporal spectral blue-drift has been an obstacle which causes many difficulties in performing the measurements. In particular, the emission energies of the X and XX states tend to blue-shift with time. The drift was attributed to the sticking of oxygen molecules onto the wire, which modified the surface charge and hence the electric field seen by the QD [95]. Since the resonant fluorescence measurements requires a setup with as high stability as possible, the fact the target transition frequencies move with time leads to the unavoidable re-alignment and

calibration of the lasers to be in the optima scanning ranges. For that reason, it would be ideal if the temporal drift problem could be resolved. In this context, we propose an alternative to partially counter the blue-drift, by using an extra intense laser beam, with an energy much lower than the QD transition energies, to red-shift the emission lines with a speed exactly equal to the natural blue-drift speed. Hence, it would help to stabilize the emission lines.

It is commonly known that temperature of the QD affects its emission energies, like it was investigated in [52] for InAs QD embedded in GaAs photonic trumpet. Increasing the temperature of the system could cause surface effects on the trumpet environment surrounding the QDs. This leads to the red-shift of the emission lines. Base on that temperature effect, we come up with an idea of using an intense laser, to heat up the trumpet and red-shift the emission lines to encounter with the natural blue-drift. Fig. C.1 describes the setup of the resonant excitation measurement. The experimental setup is the same as described in chapter 4, with an additional fiber laser introduced to the setup (Thorlabs laser diode BL976-PAG500). The laser has maximum power up to 600 mW and it has a wavelength of 976 nm (1.27 eV), which is much higher than the emission wavelengths of the X and XX of InAs QDs. This laser is set to be horizontally polarized to pass through the PBS. The power of the laser is monitored with a controller (Thorlabs CLD1015).

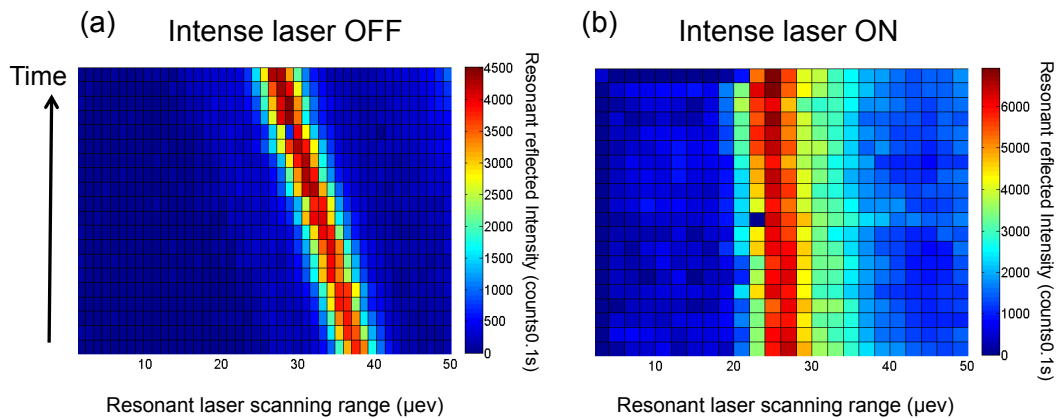


Figure C.2 – Temporal resonant spectra without (a) and with (b) the presence of the intense fiber laser. With a proper tuning of power, the red-shift caused by the fiber laser counteracts perfectly with the natural drift, thus a stable spectrum is obtained.

Fig. C.2 demonstrates the effect of the additional intense laser. In Fig. C.2(a), the temporal evolution of a normal resonant spectra is illustrated, which shows clearly how the emission energy of the X transition changes with time. In Fig. C.2(b), the fiber laser is turned on. The red-shift speed induced by the intense fiber laser increases progressively with laser power. Therefore, by carefully tuning the power, the red-shift speed can be set

exactly equal to that of the natural blue-drift. As a result, a stable emission energy is obtained.

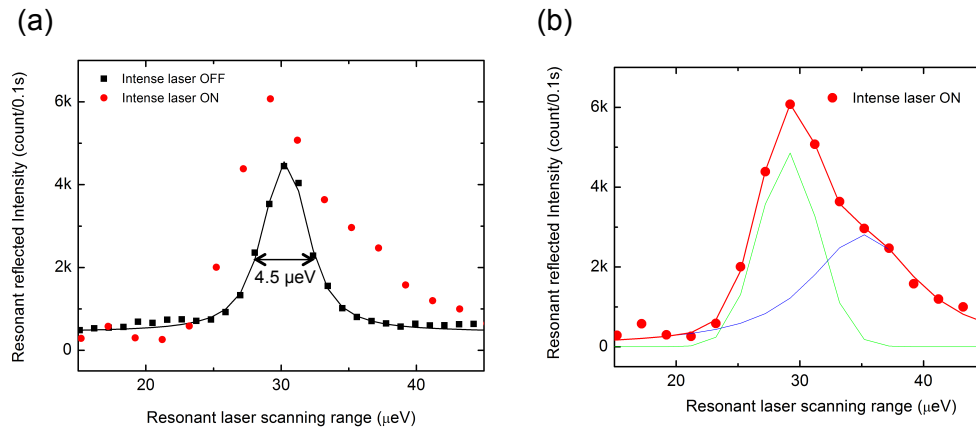


Figure C.3 – (a) Resonant spectra with and without the presence of the intense fiber laser. (b) Resonant spectrum with the presence of the fiber laser, the spectrum shows the possibility of containing one more transition.

This technique brings a way to stabilize the emission lines. However, it also induces a broadening of the resonant spectrum. This broadening is probably a result of thermal effects. For example, thermal fluctuations of charges around the quantum dots may induce the spectral jittering and leads to a broader spectrum. Fig. C.3(a) shows the resonant spectra when the intense fiber laser is turned ON and OFF. The resonant spectrum in the presence of the intense fiber laser is broader and it has an asymmetrical shape. This spectral shape can be fitted as shown in Fig. C.3(b), which appears to be the sum of two individual peaks. The additional transition may come from the fluctuation of the charges surrounding the QD. To fully understand and have better control of the spectral width, a more systematic study is required to have a better understanding of this phenomenon.

In our experiment, although this technique has not been used simultaneously with a resonant excitation measurement, it can be useful to red-shift the emission lines back to preferred regions (in case of a QD nature blue-drift). For example, in a two-laser scan measurement in chapter 5, it is not so easy to set up the lasers to scan in single-mode in the QD emission ranges. Therefore, having the possibility to bring back the emission lines to well-prepared laser scanning ranges makes it more convenient to perform the measurement.

References

- [1] G. G. Claude Cohen-Tannoudji, Jacques Dupont-Roc, *Photons and Atoms: Introduction to Quantum Electrodynamics*. Claude Cohen-Tannoudji, Jacques Dupont-Roc, Gilbert Grynberg, 1989.
- [2] N. Gisin and R. Thew, “Quantum communication,” *Nat Photon*, vol. 1, no. 3, pp. 165–171, 03 2007. [Online]. Available: <http://dx.doi.org/10.1038/nphoton.2007.22>
- [3] E. Knill, R. Laflamme, and G. J. Milburn, “A scheme for efficient quantum computation with linear optics,” *Nature*, vol. 409, no. 6816, pp. 46–52, 01 2001. [Online]. Available: <http://dx.doi.org/10.1038/35051009>
- [4] J. L. O’Brien, “Optical quantum computing,” *Science*, vol. 318, no. 5856, pp. 1567–1570, 2007. [Online]. Available: <http://www.sciencemag.org/content/318/5856/1567.abstract>
- [5] H. J. Caulfield and S. Dolev, “Why future supercomputing requires opticscomputer,” *Nat Photon*, vol. 4, no. 5, pp. 261–263, 05 2010. [Online]. Available: <http://dx.doi.org/10.1038/nphoton.2010.94>
- [6] Q. A. Turchette, C. J. Hood, W. Lange, H. Mabuchi, and H. J. Kimble, “Measurement of conditional phase shifts for quantum logic,” *Phys. Rev. Lett.*, vol. 75, pp. 4710–4713, Dec 1995. [Online]. Available: <http://link.aps.org/doi/10.1103/PhysRevLett.75.4710>
- [7] P. A. Z. Dr. Dirk Bouwmeester, Prof. Artur Ekert, Ed., *The Physics of Quantum Information*. Springer Berlin Heidelberg, 2000.
- [8] P. Lambropoulos and D. Petrosyan, *Fundamentals of Quantum Optics and Quantum Information*.
- [9] N. Gisin, G. Ribordy, W. Tittel, and H. Zbinden, “Quantum cryptography,” *Rev. Mod. Phys.*, vol. 74, pp. 145–195, Mar 2002. [Online]. Available: <http://link.aps.org/doi/10.1103/RevModPhys.74.145>

- [10] H. J. Kimble, M. Dagenais, and L. Mandel, “Photon antibunching in resonance fluorescence,” *Phys. Rev. Lett.*, vol. 39, pp. 691–695, Sep 1977. [Online]. Available: <http://link.aps.org/doi/10.1103/PhysRevLett.39.691>
- [11] T. Basché, W. E. Moerner, M. Orrit, and H. Talon, “Photon antibunching in the fluorescence of a single dye molecule trapped in a solid,” *Phys. Rev. Lett.*, vol. 69, pp. 1516–1519, Sep 1992. [Online]. Available: <http://link.aps.org/doi/10.1103/PhysRevLett.69.1516>
- [12] C. Kurtsiefer, S. Mayer, P. Zarda, and H. Weinfurter, “Stable solid-state source of single photons,” *Phys. Rev. Lett.*, vol. 85, pp. 290–293, Jul 2000. [Online]. Available: <http://link.aps.org/doi/10.1103/PhysRevLett.85.290>
- [13] N. Gregersen, T. R. Nielsen, J. Mørk, J. Claudon, and J.-M. Gérard, “Designs for high-efficiency electrically pumped photonic nanowire single-photon sources,” *Opt. Express*, vol. 18, no. 20, pp. 21 204–21 218, Sep 2010. [Online]. Available: <http://www.opticsexpress.org/abstract.cfm?URI=oe-18-20-21204>
- [14] V. Loo, C. Arnold, O. Gazzano, A. Lemaître, I. Sagnes, O. Krebs, P. Voisin, P. Senellart, and L. Lanco, “Optical nonlinearity for few-photon pulses on a quantum dot-pillar cavity device,” *Phys. Rev. Lett.*, vol. 109, p. 166806, Oct 2012. [Online]. Available: <http://link.aps.org/doi/10.1103/PhysRevLett.109.166806>
- [15] M. Bayer, O. Stern, P. Hawrylak, S. Fafard, and A. Forchel, “Hidden symmetries in the energy levels of excitonic /‘artificial atoms/’,” *Nature*, vol. 405, no. 6789, pp. 923–926, 06 2000. [Online]. Available: <http://dx.doi.org/10.1038/35016020>
- [16] P. Michler, A. Kiraz, C. Becher, W. V. Schoenfeld, P. M. Petroff, L. Zhang, E. Hu, and A. Imamoglu, “A quantum dot single-photon turnstile device,” *Science*, vol. 290, no. 5500, pp. 2282–2285, 2000. [Online]. Available: <http://www.sciencemag.org/content/290/5500/2282.abstract>
- [17] N. Akopian, N. H. Lindner, E. Poem, Y. Berlatzky, J. Avron, D. Gershoni, B. D. Gerardot, and P. M. Petroff, “Entangled photon pairs from semiconductor quantum dots,” *Phys. Rev. Lett.*, vol. 96, p. 130501, Apr 2006. [Online]. Available: <http://link.aps.org/doi/10.1103/PhysRevLett.96.130501>
- [18] W. Barnes, G. Björk, J. Gérard, P. Jonsson, J. Wasey, P. Worthing, and V. Zwiller, “Solid-state single photon sources: light collection strategies,” *The European Physical Journal D - Atomic, Molecular, Optical and Plasma Physics*, vol. 18, no. 2, pp. 197–210, 2002. [Online]. Available: <http://dx.doi.org/10.1140/epjd/e20020024>

- [19] J. Claudon, J. Bleuse, N. S. Malik, M. Bazin, P. Jaffrennou, N. Gregersen, C. Sauvan, P. Lalanne, and J.-M. Gerard, “A highly efficient single-photon source based on a quantum dot in a photonic nanowire,” *Nat Photon*, vol. 4, no. 3, pp. 174–177, 03 2010. [Online]. Available: <http://dx.doi.org/10.1038/nphoton.2009.287>
- [20] M. E. Reimer, G. Bulgarini, N. Akopian, M. Hocevar, M. B. Bavinck, M. A. Verheijen, E. P. A. M. Bakkers, L. P. Kouwenhoven, and V. Zwiller, “Bright single-photon sources in bottom-up tailored nanowires,” *Nat Commun*, vol. 3, p. 737, 03 2012. [Online]. Available: <http://dx.doi.org/10.1038/ncomms1746>
- [21] P. Lodahl, A. Floris van Driel, I. S. Nikolaev, A. Irman, K. Overgaag, D. Vanmaekelbergh, and W. L. Vos, “Controlling the dynamics of spontaneous emission from quantum dots by photonic crystals,” *Nature*, vol. 430, no. 7000, pp. 654–657, 08 2004. [Online]. Available: <http://dx.doi.org/10.1038/nature02772>
- [22] O. Gazzano, S. Michaelis de Vasconcellos, C. Arnold, A. Nowak, E. Galopin, I. Sagnes, L. Lanco, A. Lemaître, and P. Senellart, “Bright solid-state sources of indistinguishable single photons,” *Nat Commun*, vol. 4, p. 1425, 02 2013. [Online]. Available: <http://dx.doi.org/10.1038/ncomms2434>
- [23] M. Munsch, N. S. Malik, E. Dupuy, A. Delga, J. Bleuse, J.-M. Gérard, J. Claudon, N. Gregersen, and J. Mørk, “Dielectric gaas antenna ensuring an efficient broadband coupling between an inas quantum dot and a gaussian optical beam,” *Phys. Rev. Lett.*, vol. 110, p. 177402, Apr 2013. [Online]. Available: <http://link.aps.org/doi/10.1103/PhysRevLett.110.177402>
- [24] K. M. Birnbaum, A. Boca, R. Miller, A. D. Boozer, T. E. Northup, and H. J. Kimble, “Photon blockade in an optical cavity with one trapped atom,” *Nature*, vol. 436, no. 7047, pp. 87–90, 07 2005. [Online]. Available: <http://dx.doi.org/10.1038/nature03804>
- [25] A. Auffèves-Garnier, C. Simon, J.-M. Gérard, and J.-P. Poizat, “Giant optical nonlinearity induced by a single two-level system interacting with a cavity in the purcell regime,” *Phys. Rev. A*, vol. 75, p. 053823, May 2007. [Online]. Available: <http://link.aps.org/doi/10.1103/PhysRevA.75.053823>
- [26] N. Imoto, H. A. Haus, and Y. Yamamoto, “Quantum nondemolition measurement of the photon number via the optical kerr effect,” *Phys. Rev. A*, vol. 32, pp. 2287–2292, Oct 1985. [Online]. Available: <http://link.aps.org/doi/10.1103/PhysRevA.32.2287>
- [27] I. Fushman, D. Englund, A. Faraon, N. Stoltz, P. Petroff, and J. Vučković, “Controlled phase shifts with a single quantum dot,” *Science*, vol. 320, no. 5877,

- pp. 769–772, 2008. [Online]. Available: <http://www.sciencemag.org/content/320/5877/769.abstract>
- [28] D. A. B. Miller, “Optical interconnects to silicon,” *IEEE J. Selected Topics in Quantum Electronics*, vol. 6, pp. 1312–1317.
- [29] D. Miller, “Device requirements for optical interconnects to silicon chips,” *Proc. IEEE*, vol. 97, pp. 1166–1185, 2009.
- [30] D. Englund, A. Faraon, I. Fushman, N. Stoltz, P. Petroff, and J. Vuckovic, “Controlling cavity reflectivity with a single quantum dot,” *Nature*, vol. 450, no. 7171, pp. 857–861, 12 2007. [Online]. Available: <http://dx.doi.org/10.1038/nature06234>
- [31] A. Javadi, I. Sollner, M. Arcari, S. L. Hansen, L. Midolo, S. Mahmoodian, G. Kirsanske, T. Pregnolato, E. H. Lee, J. D. Song, S. Stobbe, and P. Lodahl, “Single-photon non-linear optics with a quantum dot in a waveguide,” *Nat Commun*, vol. 6, 10 2015. [Online]. Available: <http://dx.doi.org/10.1038/ncomms9655>
- [32] I.-C. Hoi, C. M. Wilson, G. Johansson, T. Palomaki, B. Peropadre, and P. Delsing, “Demonstration of a single-photon router in the microwave regime,” *Phys. Rev. Lett.*, vol. 107, p. 073601, Aug 2011. [Online]. Available: <http://link.aps.org/doi/10.1103/PhysRevLett.107.073601>
- [33] S. Baur, D. Tiarks, G. Rempe, and S. Dürr, “Single-photon switch based on rydberg blockade,” *Phys. Rev. Lett.*, vol. 112, p. 073901, Feb 2014. [Online]. Available: <http://link.aps.org/doi/10.1103/PhysRevLett.112.073901>
- [34] D. Tiarks, S. Baur, K. Schneider, S. Dürr, and G. Rempe, “Single-photon transistor using a förster resonance,” *Phys. Rev. Lett.*, vol. 113, p. 053602, Jul 2014. [Online]. Available: <http://link.aps.org/doi/10.1103/PhysRevLett.113.053602>
- [35] R. W. Boyd, *Nonlinear Optics*. Academic Press, 1992.
- [36] H. J. Caulfield and S. Dolev, “Why future supercomputing requires optics,” *Nat Photon*, vol. 4, no. 5, pp. 261–263, 05 2010. [Online]. Available: <http://dx.doi.org/10.1038/nphoton.2010.94>
- [37] H. Schmidt and A. Imamoglu, “Giant kerr nonlinearities obtained by electromagnetically induced transparency,” *Opt. Lett.*, vol. 21, no. 23, pp. 1936–1938, Dec 1996. [Online]. Available: <http://ol.osa.org/abstract.cfm?URI=ol-21-23-1936>

- [38] S. E. Harris and Y. Yamamoto, “Photon switching by quantum interference,” *Phys. Rev. Lett.*, vol. 81, pp. 3611–3614, Oct 1998. [Online]. Available: <http://link.aps.org/doi/10.1103/PhysRevLett.81.3611>
- [39] M. Fleischhauer, A. Imamoglu, and J. P. Marangos, “Electromagnetically induced transparency: Optics in coherent media,” *Rev. Mod. Phys.*, vol. 77, pp. 633–673, Jul 2005. [Online]. Available: <http://link.aps.org/doi/10.1103/RevModPhys.77.633>
- [40] H. Gorniaczyk, C. Tresp, J. Schmidt, H. Fedder, and S. Hofferberth, “Single-photon transistor mediated by interstate rydberg interactions,” *Phys. Rev. Lett.*, vol. 113, p. 053601, Jul 2014. [Online]. Available: <http://link.aps.org/doi/10.1103/PhysRevLett.113.053601>
- [41] E. Waks and J. Vuckovic, “Dispersive properties and large kerr nonlinearities using dipole-induced transparency in a single-sided cavity,” *Phys. Rev. A*, vol. 73, p. 041803, Apr 2006. [Online]. Available: <http://link.aps.org/doi/10.1103/PhysRevA.73.041803>
- [42] T. Volz, A. Reinhard, M. Winger, A. Badolato, K. J. Hennessy, E. L. Hu, and A. Imamoglu, “Ultrafast all-optical switching by single photons,” *Nat Photon*, vol. 6, no. 9, pp. 605–609, 09 2012. [Online]. Available: <http://dx.doi.org/10.1038/nphoton.2012.181>
- [43] R. Bose, D. Sridharan, H. Kim, G. S. Solomon, and E. Waks, “Low-photon-number optical switching with a single quantum dot coupled to a photonic crystal cavity,” *Phys. Rev. Lett.*, vol. 108, p. 227402, May 2012. [Online]. Available: <http://link.aps.org/doi/10.1103/PhysRevLett.108.227402>
- [44] D. E. Chang, A. S. Sørensen, P. Hemmer, and M. D. Lukin, “Quantum optics with surface plasmons,” *Phys. Rev. Lett.*, vol. 97, p. 053002, Aug 2006. [Online]. Available: <http://link.aps.org/doi/10.1103/PhysRevLett.97.053002>
- [45] D. E. Chang, A. S. Sørensen, P. R. Hemmer, and M. D. Lukin, “Strong coupling of single emitters to surface plasmons,” *Phys. Rev. B*, vol. 76, p. 035420, Jul 2007. [Online]. Available: <http://link.aps.org/doi/10.1103/PhysRevB.76.035420>
- [46] D. E. Chang, A. S. Sorensen, E. A. Demler, and M. D. Lukin, “A single-photon transistor using nanoscale surface plasmons,” *Nat Phys*, vol. 3, no. 11, pp. 807–812, 11 2007. [Online]. Available: <http://dx.doi.org/10.1038/nphys708>
- [47] N. S. Malik, “Les fils photoniques : une géométrie innovante pour la réalisation de sources de lumière quantique brillantes,” Ph.D. dissertation, Université de Grenoble, 2011. [Online]. Available: <https://tel.archives-ouvertes.fr/tel-00681846>

- [48] S. Lee, O. L. Lazarenkova, P. von Allmen, F. Oyafuso, and G. Klimeck, “Effect of wetting layers on the strain and electronic structure of InAs self-assembled quantum dots,” *Phys. Rev. B*, vol. 70, p. 125307, Sep 2004. [Online]. Available: <http://link.aps.org/doi/10.1103/PhysRevB.70.125307>
- [49] R. Heitz, A. Kalburge, Q. Xie, M. Grundmann, P. Chen, A. Hoffmann, A. Madhukar, and D. Bimberg, “Excited states and energy relaxation in stacked InAs/GaAs quantum dots,” *Phys. Rev. B*, vol. 57, pp. 9050–9060, Apr 1998. [Online]. Available: <http://link.aps.org/doi/10.1103/PhysRevB.57.9050>
- [50] S. Trumm, M. Wesseli, H. J. Krenner, D. Schuh, M. Bichler, J. J. Finley, and M. Betz, “Spin-preserving ultrafast carrier capture and relaxation in InGaAs quantum dots,” *Applied Physics Letters*, vol. 87, no. 15, pp. –, 2005. [Online]. Available: <http://scitation.aip.org/content/aip/journal/apl/87/15/10.1063/1.2103399>
- [51] M. Wesseli, C. Ruppert, S. Trumm, H. J. Krenner, J. J. Finley, and M. Betz, “Nonlinear optical response of a single self-assembled InGaAs quantum dot: A femtojoule pump-probe experiment,” *Applied Physics Letters*, vol. 88, no. 20, pp. –, 2006. [Online]. Available: <http://scitation.aip.org/content/aip/journal/apl/88/20/10.1063/1.2205722>
- [52] I. Yeo, “Une boîte quantique dans un fil photonique : spectroscopie et optomécanique,” Ph.D. dissertation, Université de Grenoble, 2012. [Online]. Available: <https://hal.archives-ouvertes.fr/tel-00809344>
- [53] P. Michler, Ed., *Single Semiconductor Quantum Dots*. Springer, 2009.
- [54] P. Lelong and G. Bastard, “Binding energies of excitons and charged excitons in GaAs(In)As quantum dots,” *Solid State Communications*, vol. 98, no. 9, pp. 819 – 823, 1996. [Online]. Available: <http://www.sciencedirect.com/science/article/pii/0038109896000245>
- [55] D. Gammon, E. S. Snow, B. V. Shanabrook, D. S. Katzer, and D. Park, “Fine structure splitting in the optical spectra of single GaAs quantum dots,” *Phys. Rev. Lett.*, vol. 76, pp. 3005–3008, Apr 1996. [Online]. Available: <http://link.aps.org/doi/10.1103/PhysRevLett.76.3005>
- [56] R. Seguin, A. Schliwa, S. Rodt, K. Pötschke, U. W. Pohl, and D. Bimberg, “Size-dependent fine-structure splitting in self-organized InAs/GaAs quantum dots,” *Phys. Rev. Lett.*, vol. 95, p. 257402, Dec 2005. [Online]. Available: <http://link.aps.org/doi/10.1103/PhysRevLett.95.257402>

- [57] M. Bayer, G. Ortner, O. Stern, A. Kuther, A. A. Gorbunov, A. Forchel, P. Hawrylak, S. Fafard, K. Hinzer, T. L. Reinecke, S. N. Walck, J. P. Reithmaier, F. Klopff, and F. Schäfer, “Fine structure of neutral and charged excitons in self-assembled in(ga)as/(al)gaas quantum dots,” *Phys. Rev. B*, vol. 65, p. 195315, May 2002. [Online]. Available: <http://link.aps.org/doi/10.1103/PhysRevB.65.195315>
- [58] A. S. Lenihan, M. V. Gurudev Dutt, D. G. Steel, S. Ghosh, and P. K. Bhattacharya, “Raman coherence beats from entangled polarization eigenstates in inas quantum dots,” *Phys. Rev. Lett.*, vol. 88, p. 223601, May 2002. [Online]. Available: <http://link.aps.org/doi/10.1103/PhysRevLett.88.223601>
- [59] K. Kowalik, O. Krebs, A. Lemaître, S. Laurent, P. Senellart, P. Voisin, and J. A. Gaj, “Influence of an in-plane electric field on exciton fine structure in inas-gaas self-assembled quantum dots,” *Applied Physics Letters*, vol. 86, no. 4, pp. –, 2005. [Online]. Available: <http://scitation.aip.org/content/aip/journal/apl/86/4/10.1063/1.1855409>
- [60] A. I. Tartakovskii, M. N. Makhonin, I. R. Sellers, J. Cahill, A. D. Andreev, D. M. Whittaker, J.-P. R. Wells, A. M. Fox, D. J. Mowbray, M. S. Skolnick, K. M. Groom, M. J. Steer, H. Y. Liu, and M. Hopkinson, “Effect of thermal annealing and strain engineering on the fine structure of quantum dot excitons,” *Phys. Rev. B*, vol. 70, p. 193303, Nov 2004. [Online]. Available: <http://link.aps.org/doi/10.1103/PhysRevB.70.193303>
- [61] W. Langbein, P. Borri, U. Woggon, V. Stavarache, D. Reuter, and A. D. Wieck, “Control of fine-structure splitting and biexciton binding in $\text{in}_x\text{ga}_{1-x}\text{As}$ quantum dots by annealing,” *Phys. Rev. B*, vol. 69, p. 161301, Apr 2004. [Online]. Available: <http://link.aps.org/doi/10.1103/PhysRevB.69.161301>
- [62] G. Bester, S. Nair, and A. Zunger, “Pseudopotential calculation of the excitonic fine structure of million-atom self-assembled $\text{in}_{1-x}\text{ga}_x\text{As}/\text{GaAs}$ quantum dots,” *Phys. Rev. B*, vol. 67, p. 161306, Apr 2003. [Online]. Available: <http://link.aps.org/doi/10.1103/PhysRevB.67.161306>
- [63] A. Högele, S. Seidl, M. Kroner, K. Karrai, R. J. Warburton, B. D. Gerardot, and P. M. Petroff, “Voltage-controlled optics of a quantum dot,” *Phys. Rev. Lett.*, vol. 93, p. 217401, Nov 2004. [Online]. Available: <http://link.aps.org/doi/10.1103/PhysRevLett.93.217401>
- [64] J. J. Finley, D. J. Mowbray, M. S. Skolnick, A. D. Ashmore, C. Baker, A. F. G. Monte, and M. Hopkinson, “Fine structure of charged and neutral excitons in

- inas-al_{0.6}ga_{0.4}As quantum dots,” *Phys. Rev. B*, vol. 66, p. 153316, Oct 2002. [Online]. Available: <http://link.aps.org/doi/10.1103/PhysRevB.66.153316>
- [65] A. J. Bennett, M. A. Pooley, R. M. Stevenson, M. B. Ward, R. B. Patel, A. B. de la Giroday, N. Skold, I. Farrer, C. A. Nicoll, D. A. Ritchie, and A. J. Shields, “Electric-field-induced coherent coupling of the exciton states in a single quantum dot,” *Nat Phys*, vol. 6, no. 12, pp. 947–950, 12 2010. [Online]. Available: <http://dx.doi.org/10.1038/nphys1780>
- [66] T. Kuroda, T. Mano, N. Ha, H. Nakajima, H. Kumano, B. Urbaszek, M. Jo, M. Abbarchi, Y. Sakuma, K. Sakoda, I. Suemune, X. Marie, and T. Amand, “Symmetric quantum dots as efficient sources of highly entangled photons: Violation of bell’s inequality without spectral and temporal filtering,” *Phys. Rev. B*, vol. 88, p. 041306, Jul 2013. [Online]. Available: <http://link.aps.org/doi/10.1103/PhysRevB.88.041306>
- [67] G. Juska, V. Dimastrodonato, L. O. Mereni, A. Gocalinska, and E. Pelucchi, “Towards quantum-dot arrays of entangled photon emitters,” *Nat Photon*, vol. 7, no. 7, pp. 527–531, 07 2013. [Online]. Available: <http://dx.doi.org/10.1038/nphoton.2013.128>
- [68] R. J. Young, R. M. Stevenson, P. Atkinson, K. Cooper, D. A. Ritchie, and A. J. Shields, “Improved fidelity of triggered entangled photons from single quantum dots,” *New Journal of Physics*, vol. 8, no. 2, p. 29, 2006. [Online]. Available: <http://stacks.iop.org/1367-2630/8/i=2/a=029>
- [69] A. Dousse, J. Suffczynski, A. Beveratos, O. Krebs, A. Lemaitre, I. Sagnes, J. Bloch, P. Voisin, and P. Senellart, “Ultrabright source of entangled photon pairs,” *Nature*, vol. 466, no. 7303, pp. 217–220, 07 2010. [Online]. Available: <http://dx.doi.org/10.1038/nature09148>
- [70] M. A. M. Versteegh, M. E. Reimer, K. D. Jöns, D. Dalacu, P. J. Poole, A. Gulinatti, A. Giudice, and V. Zwiller, “Observation of strongly entangled photon pairs from a nanowire quantum dot,” *Nat Commun*, vol. 5, 10 2014. [Online]. Available: <http://dx.doi.org/10.1038/ncomms6298>
- [71] P. Lodahl, S. Mahmoodian, and S. Stobbe, “Interfacing single photons and single quantum dots with photonic nanostructures,” *Rev. Mod. Phys.*, vol. 87, pp. 347–400, May 2015. [Online]. Available: <http://link.aps.org/doi/10.1103/RevModPhys.87.347>
- [72] K. J. Vahala, “Optical microcavities,” *Nature*, vol. 424, no. 6950, pp. 839–846, 08 2003. [Online]. Available: <http://dx.doi.org/10.1038/nature01939>

- [73] E. Purcell, “Proceedings of the american physical society,” *Phys. Rev.*, vol. 69, pp. 674–674, Jun 1946. [Online]. Available: <http://link.aps.org/doi/10.1103/PhysRev.69.674>
- [74] J. M. Gérard, B. Sermage, B. Gayral, B. Legrand, E. Costard, and V. Thierry-Mieg, “Enhanced spontaneous emission by quantum boxes in a monolithic optical microcavity,” *Phys. Rev. Lett.*, vol. 81, pp. 1110–1113, Aug 1998. [Online]. Available: <http://link.aps.org/doi/10.1103/PhysRevLett.81.1110>
- [75] E. Moreau, I. Robert, J. M. Gérard, I. Abram, L. Manin, and V. Thierry-Mieg, “Single-mode solid-state single photon source based on isolated quantum dots in pillar microcavities,” *Applied Physics Letters*, vol. 79, no. 18, pp. 2865–2867, 2001. [Online]. Available: <http://scitation.aip.org/content/aip/journal/apl/79/18/10.1063/1.1415346>
- [76] M. Pelton, C. Santori, J. Vučković, B. Zhang, G. S. Solomon, J. Plant, and Y. Yamamoto, “Efficient source of single photons: A single quantum dot in a micropost microcavity,” *Phys. Rev. Lett.*, vol. 89, p. 233602, Nov 2002. [Online]. Available: <http://link.aps.org/doi/10.1103/PhysRevLett.89.233602>
- [77] L. Lanco and P. Senellart, “A highly efficient single photon-single quantum dot interface,” *arXiv*, vol. 1502.01062, 2015. [Online]. Available: <http://arxiv.org/abs/1502.01062>
- [78] J. M. Gérard, B. Sermage, B. Gayral, B. Legrand, E. Costard, and V. Thierry-Mieg, “Enhanced spontaneous emission by quantum boxes in a monolithic optical microcavity,” *Phys. Rev. Lett.*, vol. 81, pp. 1110–1113, Aug 1998. [Online]. Available: <http://link.aps.org/doi/10.1103/PhysRevLett.81.1110>
- [79] R. J. P., G. Sek, A. Löffler, C. Hofmann, S. Kuhn, S. Reitzenstein, L. V. Keldysh, V. D. Kulakovskii, T. L. Reinecke, and A. Forchel, “Strong coupling in a single quantum dot-semiconductor microcavity system,” *Nature*, vol. 432, no. 7014, pp. 197–200, 11 2004. [Online]. Available: <http://dx.doi.org/10.1038/nature02969>
- [80] A. Predojević, M. W. Mitchell, L. Lanco, and P. Senellart, *Nano-Optics and Nanophotonics*. Springer International Publishing, 2015, pp. 39–71. [Online]. Available: http://dx.doi.org/10.1007/978-3-319-19231-4_2
- [81] A. Dousse, L. Lanco, J. Suffczyński, E. Semenova, A. Miard, A. Lemaître, I. Sagnes, C. Roblin, J. Bloch, and P. Senellart, “Controlled light-matter coupling for a single quantum dot embedded in a pillar microcavity using far-field optical lithography,” *Phys. Rev. Lett.*, vol. 101, p. 267404, Dec 2008. [Online]. Available: <http://link.aps.org/doi/10.1103/PhysRevLett.101.267404>

- [82] D. Englund, A. Majumdar, M. Bajcsy, A. Faraon, P. Petroff, and J. Vucković, “Ultrafast photon-photon interaction in a strongly coupled quantum dot-cavity system,” *Phys. Rev. Lett.*, vol. 108, p. 093604, Mar 2012. [Online]. Available: <http://link.aps.org/doi/10.1103/PhysRevLett.108.093604>
- [83] Y. Akahane, T. Asano, B.-S. Song, and S. Noda, “High-q photonic nanocavity in a two-dimensional photonic crystal,” *Nature*, vol. 425, no. 6961, pp. 944–947, 10 2003. [Online]. Available: <http://dx.doi.org/10.1038/nature02063>
- [84] J. P. Zhang, D. Y. Chu, S. L. Wu, S. T. Ho, W. G. Bi, C. W. Tu, and R. C. Tiberio, “Photonic-wire laser,” *Phys. Rev. Lett.*, vol. 75, pp. 2678–2681, Oct 1995. [Online]. Available: <http://link.aps.org/doi/10.1103/PhysRevLett.75.2678>
- [85] V. S. C. Manga Rao and S. Hughes, “Single quantum-dot purcell factor and β factor in a photonic crystal waveguide,” *Phys. Rev. B*, vol. 75, p. 205437, May 2007. [Online]. Available: <http://link.aps.org/doi/10.1103/PhysRevB.75.205437>
- [86] T. Lund-Hansen, S. Stobbe, B. Julsgaard, H. Thyrrestrup, T. Sünner, M. Kamp, A. Forchel, and P. Lodahl, “Experimental realization of highly efficient broadband coupling of single quantum dots to a photonic crystal waveguide,” *Phys. Rev. Lett.*, vol. 101, p. 113903, Sep 2008. [Online]. Available: <http://link.aps.org/doi/10.1103/PhysRevLett.101.113903>
- [87] M. Arcari, I. Söllner, A. Javadi, S. Lindskov Hansen, S. Mahmoodian, J. Liu, H. Thyrrestrup, E. H. Lee, J. D. Song, S. Stobbe, and P. Lodahl, “Near-unity coupling efficiency of a quantum emitter to a photonic crystal waveguide,” *Phys. Rev. Lett.*, vol. 113, p. 093603, Aug 2014. [Online]. Available: <http://link.aps.org/doi/10.1103/PhysRevLett.113.093603>
- [88] I. Friedler, C. Sauvan, J. P. Hugonin, P. Lalanne, J. Claudon, and J. M. Gérard, “Solid-state single photon sources: the nanowire antenna,” *Opt. Express*, vol. 17, no. 4, pp. 2095–2110, Feb 2009. [Online]. Available: <http://www.opticsexpress.org/abstract.cfm?URI=oe-17-4-2095>
- [89] J. Bleuse, J. Claudon, M. Creasey, N. S. Malik, J.-M. Gérard, I. Maksymov, J.-P. Hugonin, and P. Lalanne, “Inhibition, enhancement, and control of spontaneous emission in photonic nanowires,” *Phys. Rev. Lett.*, vol. 106, p. 103601, Mar 2011. [Online]. Available: <http://link.aps.org/doi/10.1103/PhysRevLett.106.103601>
- [90] V. V. Klimov and M. Ducloy, “Spontaneous emission rate of an excited atom placed near a nanofiber,” *Phys. Rev. A*, vol. 69, p. 013812, Jan 2004. [Online]. Available: <http://link.aps.org/doi/10.1103/PhysRevA.69.013812>

- [91] A. V. Maslov, M. I. Bakunov, and C. Z. Ning, “Distribution of optical emission between guided modes and free space in a semiconductor nanowire,” *Journal of Applied Physics*, vol. 99, no. 2, pp. –, 2006. [Online]. Available: <http://scitation.aip.org/content/aip/journal/jap/99/2/10.1063/1.2164538>
- [92] Nowicki-Bringuier, Y.-R., Hahner, R., Claudon, J., Lecamp, G., Lalanne, P., and Gérard, J. M., “A novel high-efficiency single-mode single photon source,” *Ann. Phys. Fr.*, vol. 32, no. 2-3, pp. 151–154, 2007. [Online]. Available: <http://dx.doi.org/10.1051/anphys:2008030>
- [93] N. Gregersen, T. R. Nielsen, J. Claudon, J.-M. Gérard, and J. Mørk, “Controlling the emission profile of a nanowire with a conical taper,” *Opt. Lett.*, vol. 33, no. 15, pp. 1693–1695, Aug 2008. [Online]. Available: <http://ol.osa.org/abstract.cfm?URI=ol-33-15-1693>
- [94] M. Munsch, J. Claudon, J. Bleuse, N. S. Malik, E. Dupuy, J.-M. Gérard, Y. Chen, N. Gregersen, and J. Mørk, “Linearly polarized, single-mode spontaneous emission in a photonic nanowire,” *Phys. Rev. Lett.*, vol. 108, p. 077405, Feb 2012. [Online]. Available: <http://link.aps.org/doi/10.1103/PhysRevLett.108.077405>
- [95] I. Yeo, N. S. Malik, M. Munsch, E. Dupuy, J. Bleuse, Y.-M. Niquet, J.-M. Gérard, J. Claudon, É. Wagner, S. Seidelin, A. Auffèves, J.-P. Poizat, and G. Nogues, “Surface effects in a semiconductor photonic nanowire and spectral stability of an embedded single quantum dot,” *Applied Physics Letters*, vol. 99, no. 23, pp. –, 2011. [Online]. Available: <http://scitation.aip.org/content/aip/journal/apl/99/23/10.1063/1.3665629>
- [96] I. Yeo, P.-L. de Assis, A. Gloppe, E. Dupont-Ferrier, P. Verlot, N. S. Malik, E. Dupuy, J. Claudon, J.-M. Gerard, A. Auffeves, G. Nogues, S. Seidelin, J.-P. Poizat, O. Arcizet, and M. Richard, “Strain-mediated coupling in a quantum dot-mechanical oscillator hybrid system,” *Nat Nano*, vol. 9, no. 2, pp. 106–110, 02 2014. [Online]. Available: <http://dx.doi.org/10.1038/nnano.2013.274>
- [97] S. Jung, H. Yeo, I. Yun, J. Leem, I. Han, J. Kim, and J. Lee, “Size distribution effects on self-assembled inas quantum dots,” *Journal of Materials Science: Materials in Electronics*, vol. 18, no. 1, pp. 191–194, 2007. [Online]. Available: <http://dx.doi.org/10.1007/s10854-007-9205-9>
- [98] J. S. Kim, B. S. Ko, J.-I. Yu, and I.-H. Bae, “Temperature- and excitation-power-dependent optical properties of inas/gaas quantum dots by comparison of photoluminescence and photorefectance spectroscopy,” *Journal of the Korean Physical Society*, vol. 55, no. 2, pp. 640–645, august 2009.

- [99] D. Sarkar, H. P. van der Meulen, J. M. Calleja, J. M. Becker, R. J. Haug, and K. Pierz, “Exciton fine structure and biexciton binding energy in single self-assembled inasalas quantum dots,” *Journal of Applied Physics*, vol. 100, no. 2, 2006. [Online]. Available: <http://scitation.aip.org/content/aip/journal/jap/100/2/10.1063/1.2209089>
- [100] S. Bounouar, C. Morchutt, M. Elouneq-Jamroz, L. Besombes, R. André, E. Bellet-Amalric, C. Bougerol, M. Den Hertog, K. Kheng, S. Tatarenko, and J. P. Poizat, “Exciton-phonon coupling efficiency in cdse quantum dots embedded in znse nanowires,” *Phys. Rev. B*, vol. 85, p. 035428, Jan 2012. [Online]. Available: <http://link.aps.org/doi/10.1103/PhysRevB.85.035428>
- [101] G. Sallen, A. Tribu, T. Aichele, R. André, L. Besombes, C. Bougerol, S. Tatarenko, K. Kheng, and J. P. Poizat, “Exciton dynamics of a single quantum dot embedded in a nanowire,” *Phys. Rev. B*, vol. 80, p. 085310, Aug 2009. [Online]. Available: <http://link.aps.org/doi/10.1103/PhysRevB.80.085310>
- [102] S. Rodt, R. Heitz, A. Schliwa, R. L. Sellin, F. Guffarth, and D. Bimberg, “Repulsive exciton-exciton interaction in quantum dots,” *Phys. Rev. B*, vol. 68, p. 035331, Jul 2003. [Online]. Available: <http://link.aps.org/doi/10.1103/PhysRevB.68.035331>
- [103] S. Rodt, A. Schliwa, K. Pötschke, F. Guffarth, and D. Bimberg, “Correlation of structural and few-particle properties of self-organized InAsGaAs quantum dots,” *Phys. Rev. B*, vol. 71, p. 155325, Apr 2005. [Online]. Available: <http://link.aps.org/doi/10.1103/PhysRevB.71.155325>
- [104] G. Bacher, R. Weigand, J. Seufert, V. D. Kulakovskii, N. A. Gippius, A. Forchel, K. Leonardi, and D. Hommel, “Biexciton versus exciton lifetime in a single semiconductor quantum dot,” *Phys. Rev. Lett.*, vol. 83, pp. 4417–4420, Nov 1999. [Online]. Available: <http://link.aps.org/doi/10.1103/PhysRevLett.83.4417>
- [105] M. Wimmer, S. V. Nair, and J. Shumway, “Biexciton recombination rates in self-assembled quantum dots,” *Phys. Rev. B*, vol. 73, p. 165305, Apr 2006. [Online]. Available: <http://link.aps.org/doi/10.1103/PhysRevB.73.165305>
- [106] M. Feucker, R. Seguin, S. Rodt, A. Hoffmann, and D. Bimberg, “Decay dynamics of neutral and charged excitonic complexes in single inasgaas quantum dots,” *Applied Physics Letters*, vol. 92, no. 6, pp. –, 2008. [Online]. Available: <http://scitation.aip.org/content/aip/journal/apl/92/6/10.1063/1.2844886>
- [107] C. Cohen-Tannoudji, J. Dupont-Roc, and G. Grynberg, *Atom-Photon Interactions*. Wiley, 2008.

- [108] D. Valente, S. Portolan, G. Nogues, J. P. Poizat, M. Richard, J. M. Gérard, M. F. Santos, and A. Auffèves, “Monitoring stimulated emission at the single-photon level in one-dimensional atoms,” *Phys. Rev. A*, vol. 85, p. 023811, Feb 2012. [Online]. Available: <http://link.aps.org/doi/10.1103/PhysRevA.85.023811>
- [109] D. Valente, “Quantum Optics with Semiconducting Artificial Atoms,” Theses, Université de Grenoble, Oct. 2012. [Online]. Available: <https://tel.archives-ouvertes.fr/tel-00859710>
- [110] K. Kojima, H. F. Hofmann, S. Takeuchi, and K. Sasaki, “Efficiencies for the single-mode operation of a quantum optical nonlinear shift gate,” *Phys. Rev. A*, vol. 70, p. 013810, Jul 2004. [Online]. Available: <http://link.aps.org/doi/10.1103/PhysRevA.70.013810>
- [111] H. F. Hofmann, K. Kojima, S. Takeuchi, and K. Sasaki, “Optimized phase switching using a single-atom nonlinearity,” *Journal of Optics B: Quantum and Semiclassical Optics*, vol. 5, no. 3, p. 218, 2003. [Online]. Available: <http://stacks.iop.org/1464-4266/5/i=3/a=304>
- [112] G. Sallen, A. Tribu, T. Aichele, R. André, L. Besombes, C. Bougerol, M. Richard, S. Tatarenko, K. Kheng, and J. P. Poizat, “Subnanosecond spectral diffusion measurement using photon correlation,” *Nat Photon*, vol. 4, no. 10, pp. 696–699, 10 2010. [Online]. Available: <http://dx.doi.org/10.1038/nphoton.2010.174>
- [113] H. Kamada and T. Kutsuwa, “Broadening of single quantum dot exciton luminescence spectra due to interaction with randomly fluctuating environmental charges,” *Phys. Rev. B*, vol. 78, p. 155324, Oct 2008. [Online]. Available: <http://link.aps.org/doi/10.1103/PhysRevB.78.155324>
- [114] G. Sallen, A. Tribu, T. Aichele, R. André, L. Besombes, C. Bougerol, M. Richard, S. Tatarenko, K. Kheng, and J.-P. Poizat, “Subnanosecond spectral diffusion of a single quantum dot in a nanowire,” *Phys. Rev. B*, vol. 84, p. 041405, Jul 2011. [Online]. Available: <http://link.aps.org/doi/10.1103/PhysRevB.84.041405>
- [115] A. Berthelot, I. Favero, G. Cassabois, C. Voisin, C. Delalande, P. Roussignol, R. Ferreira, and J. M. Gerard, “Unconventional motional narrowing in the optical spectrum of a semiconductor quantum dot,” *Nat Phys*, vol. 2, no. 11, pp. 759–764, 11 2006. [Online]. Available: <http://dx.doi.org/10.1038/nphys433>
- [116] S. Bounouar, A. Trichet, M. Elouneq-Jamroz, R. André, E. Bellet-Amalric, C. Bougerol, M. Den Hertog, K. Kheng, S. Tatarenko, and J.-P. Poizat, “Extraction of the homogeneous linewidth of the spectrally diffusing line of a cdse/zns

- quantum dot embedded in a nanowire,” *Phys. Rev. B*, vol. 86, p. 085325, Aug 2012. [Online]. Available: <http://link.aps.org/doi/10.1103/PhysRevB.86.085325>
- [117] F. Y. Wu, R. E. Grove, and S. Ezekiel, “Investigation of the spectrum of resonance fluorescence induced by a monochromatic field,” *Phys. Rev. Lett.*, vol. 35, pp. 1426–1429, Nov 1975. [Online]. Available: <http://link.aps.org/doi/10.1103/PhysRevLett.35.1426>
- [118] G. Wrigge, I. Gerhardt, J. Hwang, G. Zumofen, and V. Sandoghdar, “Efficient coupling of photons to a single molecule and the observation of its resonance fluorescence,” *Nat Phys*, vol. 4, no. 1, pp. 60–66, 01 2008. [Online]. Available: <http://dx.doi.org/10.1038/nphys812>
- [119] O. Astafiev, A. M. Zagoskin, A. A. Abdumalikov, Y. A. Pashkin, T. Yamamoto, K. Inomata, Y. Nakamura, and J. S. Tsai, “Resonance fluorescence of a single artificial atom,” *Science*, vol. 327, no. 5967, pp. 840–843, 2010. [Online]. Available: <http://www.sciencemag.org/content/327/5967/840.abstract>
- [120] A. Muller, E. B. Flagg, P. Bianucci, X. Y. Wang, D. G. Deppe, W. Ma, J. Zhang, G. J. Salamo, M. Xiao, and C. K. Shih, “Resonance fluorescence from a coherently driven semiconductor quantum dot in a cavity,” *Phys. Rev. Lett.*, vol. 99, p. 187402, Nov 2007. [Online]. Available: <http://link.aps.org/doi/10.1103/PhysRevLett.99.187402>
- [121] S. Ates, S. M. Ulrich, S. Reitzenstein, A. Löffler, A. Forchel, and P. Michler, “Post-selected indistinguishable photons from the resonance fluorescence of a single quantum dot in a microcavity,” *Phys. Rev. Lett.*, vol. 103, p. 167402, Oct 2009. [Online]. Available: <http://link.aps.org/doi/10.1103/PhysRevLett.103.167402>
- [122] E. B. Flagg, A. Muller, J. W. Robertson, S. Founta, D. G. Deppe, M. Xiao, W. Ma, G. J. Salamo, and C. K. Shih, “Resonantly driven coherent oscillations in a solid-state quantum emitter,” *Nat Phys*, vol. 5, no. 3, pp. 203–207, 03 2009. [Online]. Available: <http://dx.doi.org/10.1038/nphys1184>
- [123] C. Santori, D. Fattal, J. Vučković, G. S. Solomon, E. Waks, and Y. Yamamoto, “Submicrosecond correlations in photoluminescence from inas quantum dots,” *Phys. Rev. B*, vol. 69, p. 205324, May 2004. [Online]. Available: <http://link.aps.org/doi/10.1103/PhysRevB.69.205324>
- [124] C. Matthiesen, A. N. Vamivakas, and M. Atatüre, “Subnatural linewidth single photons from a quantum dot,” *Phys. Rev. Lett.*, vol. 108, p. 093602, Feb 2012. [Online]. Available: <http://link.aps.org/doi/10.1103/PhysRevLett.108.093602>

- [125] H. S. Nguyen, G. Sallen, C. Voisin, P. Roussignol, C. Diederichs, and G. Cassabois, “Ultra-coherent single photon source,” *Applied Physics Letters*, vol. 99, no. 26, pp. –, 2011. [Online]. Available: <http://scitation.aip.org/content/aip/journal/apl/99/26/10.1063/1.3672034>
- [126] H. S. Nguyen, G. Sallen, M. Abbarchi, R. Ferreira, C. Voisin, P. Roussignol, G. Cassabois, and C. Diederichs, “Photoneutralization and slow capture of carriers in quantum dots probed by resonant excitation spectroscopy,” *Phys. Rev. B*, vol. 87, p. 115305, Mar 2013. [Online]. Available: <http://link.aps.org/doi/10.1103/PhysRevB.87.115305>
- [127] H. S. Nguyen, G. Sallen, C. Voisin, P. Roussignol, C. Diederichs, and G. Cassabois, “Optically gated resonant emission of single quantum dots,” *Phys. Rev. Lett.*, vol. 108, p. 057401, Jan 2012. [Online]. Available: <http://link.aps.org/doi/10.1103/PhysRevLett.108.057401>
- [128] A. V. Kuhlmann, J. Houel, D. Brunner, A. Ludwig, D. Reuter, A. D. Wieck, and R. J. Warburton, “A dark-field microscope for background-free detection of resonance fluorescence from single semiconductor quantum dots operating in a set-and-forget mode,” *Review of Scientific Instruments*, vol. 84, no. 7, pp. –, 2013. [Online]. Available: <http://scitation.aip.org/content/aip/journal/rsi/84/7/10.1063/1.4813879>
- [129] K. Konthasinghe, J. Walker, M. Peiris, C. K. Shih, Y. Yu, M. F. Li, J. F. He, L. J. Wang, H. Q. Ni, Z. C. Niu, and A. Muller, “Coherent versus incoherent light scattering from a quantum dot,” *Phys. Rev. B*, vol. 85, p. 235315, Jun 2012. [Online]. Available: <http://link.aps.org/doi/10.1103/PhysRevB.85.235315>
- [130] V. Giesz, N. Somaschi, G. Hornecker, T. Grange, B. Reznichenko, L. D. Santis, J. Demory, C. Gomez, I. Sagnes, A. Lemaitre, O. Krebs, N. D. Lanzillotti-Kimura, L. Lanco, A. Auffeves, and P. Senellart, “Coherent control of a solid-state quantum bit with few-photon pulses,” *ArXiv*, vol. 1512.04725, 2015. [Online]. Available: <http://arxiv.org/abs/1512.04725>
- [131] B. R. Mollow, “Absorption and emission line-shape functions for driven atoms,” *Phys. Rev. A*, vol. 5, pp. 1522–1527, Mar 1972. [Online]. Available: <http://link.aps.org/doi/10.1103/PhysRevA.5.1522>
- [132] A. Majumdar, E. D. Kim, and J. Vučković, “Effect of photogenerated carriers on the spectral diffusion of a quantum dot coupled to a photonic crystal cavity,” *Phys. Rev. B*, vol. 84, p. 195304, Nov 2011. [Online]. Available: <http://link.aps.org/doi/10.1103/PhysRevB.84.195304>

- [133] A. Högele, S. Seidl, M. Kroner, K. Karrai, R. J. Warburton, B. D. Gerardot, and P. M. Petroff, “Voltage-controlled optics of a quantum dot,” *Phys. Rev. Lett.*, vol. 93, p. 217401, Nov 2004. [Online]. Available: <http://link.aps.org/doi/10.1103/PhysRevLett.93.217401>
- [134] A. Reinhard, T. Volz, M. Winger, A. Badolato, K. J. Hennessy, E. L. Hu, and A. Imamoglu, “Strongly correlated photons on a chip,” *Nat Photon*, vol. 6, no. 2, pp. 93–96, 02 2012. [Online]. Available: <http://dx.doi.org/10.1038/nphoton.2011.321>
- [135] P. Stepanov, A. Delga, N. Gregersen, E. Peinke, M. Munsch, J. Teissier, J. Mázrk, M. Richard, J. Bleuse, J.-M. Gã©rard, and J. Claudon, “Highly directive and gaussian far-field emission from âgiantâ photonic trumpets,” *Applied Physics Letters*, vol. 107, no. 14, 2015. [Online]. Available: <http://scitation.aip.org/content/aip/journal/apl/107/14/10.1063/1.4932574>
- [136] B. R. Mollow, “Power spectrum of light scattered by two-level systems,” *Phys. Rev.*, vol. 188, pp. 1969–1975, Dec 1969. [Online]. Available: <http://link.aps.org/doi/10.1103/PhysRev.188.1969>
- [137] S. H. Autler and C. H. Townes, “Stark effect in rapidly varying fields,” *Phys. Rev.*, vol. 100, pp. 703–722, Oct 1955. [Online]. Available: <http://link.aps.org/doi/10.1103/PhysRev.100.703>
- [138] I. I. Rabi, “Space quantization in a gyrating magnetic field,” *Phys. Rev.*, vol. 51, pp. 652–654, Apr 1937. [Online]. Available: <http://link.aps.org/doi/10.1103/PhysRev.51.652>
- [139] E. Jaynes and F. Cummings, “Comparison of quantum and semiclassical radiation theories with application to the beam maser,” *Proceedings of the IEEE*, vol. 51, no. 1, pp. 89–109, Jan 1963.
- [140] A. Nick Vamivakas, Y. Zhao, C.-Y. Lu, and M. Atatüre, “Spin-resolved quantum-dot resonance fluorescence,” *Nat Phys*, vol. 5, no. 3, pp. 198–202, 03 2009. [Online]. Available: <http://dx.doi.org/10.1038/nphys1182>
- [141] M. Fleischhauer, A. Imamoglu, and J. P. Marangos, “Electromagnetically induced transparency: Optics in coherent media,” *Rev. Mod. Phys.*, vol. 77, pp. 633–673, Jul 2005. [Online]. Available: <http://link.aps.org/doi/10.1103/RevModPhys.77.633>
- [142] M. C. Phillips, “Electromagnetically induced transparency in semiconductors,” Ph.D. dissertation, Graduate School of the University of Oregon, 2002. [Online]. Available: <http://pages.uoregon.edu/hailin/MCPthesis.pdf>

- [143] U. Fano, “Effects of configuration interaction on intensities and phase shifts,” *Phys. Rev.*, vol. 124, pp. 1866–1878, Dec 1961. [Online]. Available: <http://link.aps.org/doi/10.1103/PhysRev.124.1866>
- [144] G. S. Agarwal, “Nature of the quantum interference in electromagnetic-field-induced control of absorption,” *Phys. Rev. A*, vol. 55, pp. 2467–2470, Mar 1997. [Online]. Available: <http://link.aps.org/doi/10.1103/PhysRevA.55.2467>
- [145] P. M. Anisimov, J. P. Dowling, and B. C. Sanders, “Objectively discerning autler-townes splitting from electromagnetically induced transparency,” *Phys. Rev. Lett.*, vol. 107, p. 163604, Oct 2011. [Online]. Available: <http://link.aps.org/doi/10.1103/PhysRevLett.107.163604>
- [146] K.-J. Boller, A. Imamoglu, and S. E. Harris, “Observation of electromagnetically induced transparency,” *Phys. Rev. Lett.*, vol. 66, pp. 2593–2596, May 1991. [Online]. Available: <http://link.aps.org/doi/10.1103/PhysRevLett.66.2593>
- [147] C. Santori, P. Tamarat, P. Neumann, J. Wrachtrup, D. Fattal, R. G. Beusoleil, J. Rabeau, P. Olivero, A. D. Greentree, S. Praver, F. Jelezko, and P. Hemmer, “Coherent population trapping of single spins in diamond under optical excitation,” *Phys. Rev. Lett.*, vol. 97, p. 247401, Dec 2006. [Online]. Available: <http://link.aps.org/doi/10.1103/PhysRevLett.97.247401>
- [148] A. H. Safavi-Naeini, T. P. M. Alegre, J. Chan, M. Eichenfield, M. Winger, Q. Lin, J. T. Hill, D. E. Chang, and O. Painter, “Electromagnetically induced transparency and slow light with optomechanics,” *Nature*, vol. 472, no. 7341, pp. 69–73, 04 2011. [Online]. Available: <http://dx.doi.org/10.1038/nature09933>
- [149] B. Peng, Ş. K. Özdemir, W. Chen, F. Nori, and L. Yang, “What is and what is not electromagnetically induced transparency in whispering-gallery microcavities,” *Nat Commun*, vol. 5, 10 2014. [Online]. Available: <http://dx.doi.org/10.1038/ncomms6082>
- [150] A. Hatef, S. M. Sadeghi, and M. R. Singh, “Plasmonic electromagnetically induced transparency in metallic nanoparticle–quantum dot hybrid systems,” *Nanotechnology*, vol. 23, no. 6, p. 065701, 2012. [Online]. Available: <http://stacks.iop.org/0957-4484/23/i=6/a=065701>
- [151] J. Q. Shen, “Electromagnetically-induced-transparency plasmonics: Quantum-interference-assisted tunable surface-plasmon-polariton resonance and excitation,” *Phys. Rev. A*, vol. 90, p. 023814, Aug 2014. [Online]. Available: <http://link.aps.org/doi/10.1103/PhysRevA.90.023814>

- [152] X. Wu, S. K. Gray, and M. Pelton, “Quantum-dot-induced transparency in a nanoscale plasmonic resonator,” *Opt. Express*, vol. 18, no. 23, pp. 23 633–23 645, Nov 2010. [Online]. Available: <http://www.opticsexpress.org/abstract.cfm?URI=oe-18-23-23633>
- [153] G. Jundt, L. Robledo, A. Högele, S. Fält, and A. Imamoglu, “Observation of dressed excitonic states in a single quantum dot,” *Phys. Rev. Lett.*, vol. 100, p. 177401, Apr 2008. [Online]. Available: <http://link.aps.org/doi/10.1103/PhysRevLett.100.177401>
- [154] X. Xu, B. Sun, P. R. Berman, D. G. Steel, A. S. Bracker, D. Gammon, and L. J. Sham, “Coherent optical spectroscopy of a strongly driven quantum dot,” *Science*, vol. 317, no. 5840, pp. 929–932, 2007. [Online]. Available: <http://www.sciencemag.org/content/317/5840/929.abstract>
- [155] B. D. Gerardot, D. Brunner, P. A. Dalgarno, K. Karrai, A. Badolato, P. M. Petroff, and R. J. Warburton, “Dressed excitonic states and quantum interference in a three-level quantum dot ladder system,” *New Journal of Physics*, vol. 11, no. 1, p. 013028, 2009. [Online]. Available: <http://stacks.iop.org/1367-2630/11/i=1/a=013028>
- [156] A. A. Abdumalikov, O. Astafiev, A. M. Zagoskin, Y. A. Pashkin, Y. Nakamura, and J. S. Tsai, “Electromagnetically induced transparency on a single artificial atom,” *Phys. Rev. Lett.*, vol. 104, p. 193601, May 2010. [Online]. Available: <http://link.aps.org/doi/10.1103/PhysRevLett.104.193601>
- [157] W. Chen, K. M. Beck, R. Bücker, M. Gullans, M. D. Lukin, H. Tanji-Suzuki, and V. Vuletić, “All-optical switch and transistor gated by one stored photon,” *Science*, vol. 341, no. 6147, pp. 768–770, 2013. [Online]. Available: <http://www.sciencemag.org/content/341/6147/768.abstract>
- [158] K. Srinivasan and O. Painter, “Linear and nonlinear optical spectroscopy of a strongly coupled microdisk-quantum dot system,” *Nature*, vol. 450, no. 7171, pp. 862–865, 12 2007. [Online]. Available: <http://dx.doi.org/10.1038/nature06274>
- [159] J. H. Shapiro, “Single-photon kerr nonlinearities do not help quantum computation,” *Phys. Rev. A*, vol. 73, p. 062305, Jun 2006. [Online]. Available: <http://link.aps.org/doi/10.1103/PhysRevA.73.062305>
- [160] J. Gea-Banaacloche, “Impossibility of large phase shifts via the giant kerr effect with single-photon wave packets,” *Phys. Rev. A*, vol. 81, p. 043823, Apr 2010. [Online]. Available: <http://link.aps.org/doi/10.1103/PhysRevA.81.043823>

-
- [161] A. Auffèves and M. Richard, “Optical driving of macroscopic mechanical motion by a single two-level system,” *Phys. Rev. A*, vol. 90, p. 023818, Aug 2014. [Online]. Available: <http://link.aps.org/doi/10.1103/PhysRevA.90.023818>

Résumé

Contrôler la lumière avec de la lumière au niveau du photon unique est un objectif fondamental dans le domaine de l'information quantique, ou de l'ordinateur optique à très basse puissance. Un émetteur quantique constitué d'un unique système à deux niveaux est un milieu très non-linéaire, pour lequel l'interaction avec un photon peut modifier la transmission d'un photon suivant. Dans ce scénario, le défi pour obtenir une telle non-linéarité géante est d'optimiser l'interaction lumière-matière. Une solution à ce défi est d'insérer l'émetteur quantique dans une structure photonique. Ce système est appelé "atome uni-dimensionnel": la collection de la lumière, tout comme la probabilité d'absorber un photon se propageant dans la structure est maximum.

Dans ce travail, nous avons utilisé ce type de système pour réaliser une non-linéarité géante à deux modes, dans laquelle la réflexion d'un des modes est contrôlée par un autre mode au niveau du photon unique. Le système est constitué d'une boîte quantique semi-conductrice InAs/GaAs, qui peut être considéré comme un atome artificiel, insérée dans un fil photonique en GaAs opérant comme un guide d'onde. Le fil photonique définit un mode spatial unique autour de l'émetteur et offre une interaction lumière-matière avec une efficacité quasi-idéale. De plus, ce fil photonique présente cette propriété sur une large bande spectrale. Grâce à ces deux propriétés, nous avons démontré expérimentalement une non-linéarité géante à un mode et à deux modes à un niveau de quelques dizaines de photons par durée de vie de l'émetteur. Cela permet de réaliser un interrupteur tout optique intégré, à très faible seuil.

Mots-clés: Nanophotonique, boîte quantique, semi-conducteur, nanophysique, optique non-linéaire.

Abstract

Controlling light by light at the single photon level is a fundamental quest in the field of quantum computing, quantum information science and classical ultra-low power optical computing. A quantum light emitter made of a single two-level system is a highly non-linear medium, where the interaction of one photon with the medium can modify the transmission of another incoming photon. In this scenario, the most challenging issue to obtain a giant optical non-linearity is to optimize photon-emitter interaction. This issue can be overcome by inserting the quantum emitter inside a photonic structure. This system is known as "one-dimensional atom": the light collection efficiency as well as the probability for an emitter to absorb a photon fed into the structure is maximal.

In this study, we aim at using such kind of system to experimentally realize a two-mode giant non-linearity, in which the reflection of one light mode is controlled by another light mode at the single-photon level. The system consists of a semiconductor InAs/GaAs quantum dot, which can be considered as an artificial atom, embedded inside a GaAs photonic wire, which is an optical waveguide. The photonic wire defines a single spatial mode around the emitter and offers a close to unity light-emitter interaction efficiency. In addition, the photonic wire also possesses a spectrally broadband operation range. Thanks to these two excellent features of the system, we experimentally demonstrate in this thesis a single-mode and a two-mode giant non-linearity obtained at the level of just a few tens of photons per emitter lifetime. This realizes an integrated ultra-low power all-optical switch.

Keywords: Nanophotonics, quantum dot, semiconductor, nanophysics, non-linear optics.